DISSERTATION

THE ACTIVE COMPLEX ELECTRODE (ACE1) ELECTRICAL IMPEDANCE TOMOGRAPHY SYSTEM & ANATOMICALLY INSPIRED MODELING OF ELECTRODE-SKIN CONTACT IMPEDANCE

Submitted by

Michelle M. Mellenthin

Graduate Degree Program in Bioengineering

In partial fulfillment of the requirements

For the Degree of Doctor of Philosophy

Colorado State University

Fort Collins, Colorado

Summer 2016

Doctoral Committee:

Advisor: Jennifer L. Mueller

Kevin Lear
Diego Krapf
Ali Pezeshki

Copyright by Michelle M. Mellenthin 2016

All Rights Reserved

ABSTRACT

THE ACTIVE COMPLEX ELECTRODE (ACE1) ELECTRICAL IMPEDANCE TOMOGRAPHY SYSTEM & ANATOMICALLY INSPIRED MODELING OF ELECTRODE-SKIN CONTACT IMPEDANCE

Electrical Impedance Tomography (EIT) is a technique used to image the varying electrical properties of biological tissues or tissue conductivity and permittivity. There are many clinical uses of EIT, but as a newer imaging modality, there is interest in improving hardware to acquire EIT data, creating models of the system and generating high quality images. The two main contributions of this work include: (1) EIT hardware advancements and (2) software modeling to simulate measured human subject data. Specifically, this dissertation includes the design and testing of Colorado State University's first EIT system, the pairwise current injection active complex electrode (ACE1) system for phasic voltage measurement. The ACE1 system was primarily designed for thoracic EIT applications, and its performance and limitations were tested through a variety of experiments. Additionally, the EIT forward problem was used to investigate electrode-skin contact impedance.

ACKNOWLEDGEMENTS

I am grateful for the many people that have supported me during my academic pursuits. Firstly, I would like to thank my parents, Jim and Mary Mellenthin for supporting me throughout the entirety of my education. I also would like to thank my husband, Christopher Huizenga, for his encouragement.

I thank Jennifer Mueller for her efforts and assistance as my advisor. Not only has she taught me about the field of Electrical Impedance Tomography (EIT), but also about life. Additionally, I'd like to acknowledge the other members of my committee Kevin Lear, Diego Krapf and Ali Pezeshki. A special thanks are extended to my Colorado State University (CSU) colleagues in the EIT lab, especially Melody Alsaker and Rashmi Murphy.

During 2012-2013, the International Institute of Education Whitaker Fellowship Program gave me the opportunity to collaborate internationally. I am extremely grateful to present and former members of the EIT lab at the Universidade de São Paulo (USP): Raul Gonzalez Lima, Fernando Silva de Moura, Erick Darío León Bueno de Camargo, Olavo Luppi Silva and Talles Batista Rattis Santos. I sincerely thank them for their advice and assistance. There were many hours spent soldering, testing components, making cables, and the construction of the the ACE1 device would have been very difficult without the efforts of those at CSU and USP.

Much of this doctoral research project was supported by Award Number 1R21EB016869-01 A1 from the National Institute of Biomedical Imaging and Bioengineering. The content is solely my responsibility and does not necessarily represent the official view of the National Institute of Biomedical Imaging and Bioengineering or the National Institutes of Health.

TABLE OF CONTENTS

LIST OF TABLES

LIST OF FIGURES

CHAPTER 1

SPECIFIC AIMS AND RESEARCH SUMMARY

This short chapter addresses the context of this work within the Electrical Impedance Tomography (EIT) field. This dissertation aims to increase understanding in the complexities of constructing a new electrical impedance tomograph, addressed through aim one (Section 1.1). It also looks at the electrode-skin contact impedance, specifically how it relates to ACE1 measured data through aim two (Section 1.2).

1.1. Aim One: The Active Complex Electrode (ACE1) EIT System

In EIT, the resolution and accuracy of conductivity and/or permittivity images are limited by both hardware and software. The clarity of anatomical features within an image is greatly dependent on the precision of the acquired voltage data. Errors and noise in voltage measurements result in errors of conductivity or permittivity values in the reconstructions. To create images of permittivity, accurate phase information must be known about both the injected currents and measured voltages of an EIT system. *The first aim of this work was to design an electrical impedance tomography system in which magnitude and phase of measured voltages and currents can be determined.*

An overview of the design of the ACE1 system, which meets the first objective is presented in Chapter 3. An advantage of this system when compared to existing systems, discussed in Section 2.4, is the design of the active electrode, which provides a way to determine the magnitude and phase of injected current close to the domain. The performance of this system is rigorously addressed in Chapter 4. Results related to testing the ACE1 current source are presented in Section 4.2. The output impedance of the source is often used to determine source performance, but measuring the current on the active electrode allows for

use of a source with less than ideal behavior. Output impedance of the source varies based on frequency and tests are consistent with National Instruments Multisim circuit simulations. The overall frame-to-frame variation of calculated currents at the active electrode is low. During human subject data collection, bipolar currents are injected approximately 0.31% $\pm$ 0.02% out of phase with one another and with a 1.31% $\pm$ 0.09% difference in amplitude.

Chapter 4 also contains results for experiments addressing the resolution, precision, accuracy, and reproducibility of data in Section 4.3. ACE1 is able to precisely measure voltage amplitudes to within 27 μV and voltage phase to within 0.045 radians. For tank phantom data, the voltage amplitude measurements are reproducible from frame-to-frame to 60 μV or less and voltage phase measurements to within 0.05 to 0.1 radians. The sensitivity of the system or its ability to distinguish differences in tank phantom targets is presented in Section 4.4. The difference between a 0.95 cm and 1.3 cm insulator placed in the center of the tank phantom was distinguishable at skips 2, 4 and 6 by several non-injecting electrodes by voltage differences greater than the reproducibility of measured data. Select reconstructed images are also shown in Section 4.5.

Chapter 5 presents results from signal-to-noise ratio (SNR) experiments in Section 5.1. The SNR is highest on injecting electrodes and decays as distance from injection electrodes increases. A mean SNR over all electrodes, current patterns and frames is generally highest for skip patterns 4 to 8 and when data is acquired at the 1024 point acquisition rate. Section 5.3 aims to estimate stray capacitance at different locations within in the EIT system. Results suggest that at 125 kHz, as much as approximately 5% of current is drained by stray capacitance present at the electrode.

1.2. Aim Two: Anatomically Inspired Modeling of Electrode-Skin Contact Impedance

Incorporation of electrode models into reconstruction algorithms is an important part of EIT. This work investigates the role of the forward problem and limitations in modeling the electrode-skin contact impedance. Accurate forward problem simulations must include a model for this contact impedance. When it is not considered, simulated and measured voltages will not agree. *The second aim of this dissertation was to use the EIT forward problem to investigate physiologically inspired models of the skin-electrode interface.*

To better consider the influence of contact impedance on measured data, both electrode-saline (Section 6.1) and electrode-skin (Section 6.2) contact impedance were investigated. Chapter 6 also presents physiological and anatomical information about skin to give context and motivation for using a model describing current flow through pores of the skin [10] in Section 6.5. This model is modified to be appropriate for use in the EIT forward problem modeling the electrode-skin interface in Section 7.4.

In Chapter 7, the EIT forward problem and electrodes models are discussed in detail. The results of the anatomically-inspired model simulations are compared to existing EIT electrode models and to measured human subject data from the ACE1 system in Section 7.4.2. In some situations, use of this model can help create simulated data that is accurate on both injecting and neighboring electrodes.

CHAPTER 2

AN OVERVIEW OF ELECTRICAL IMPEDANCE TOMOGRAPHY

Electrical Impedance Tomography (EIT) is an imaging modality which creates low spatial resolution images that map electrical properties. In medical EIT acquisition, small sinusoidal currents injected on electrodes are passed through a region of the body, and measured voltages are used to solve an inverse problem to recover conductivity and/or permittivity distributions. Due to the electric properties of biological tissues, further discussed in Section 2.1, EIT is a suitable imaging technique for many medical applications [1, 2, 14, 15].

There are several advantages to using EIT as a medical imaging technique. It is radiation-free, non-invasive, low-cost, portable, has a high temporal resolution and could be used for long-term bedside monitoring of patients in many clinical settings. Specific examples of EIT use are further discussed in Section 2.2. Despite its many advantages, EIT has several limitations. It often suffers from low signal-to-noise ratios (SNR) and is sensitive to modeling errors, such as accurate contact impedance and knowledge of electrode placement [14, 15, 2, 16, 11]. The amount of significant clinical information present in EIT images depends greatly upon both the reconstruction algorithm and hardware. In particular, the spatial resolution of reconstructed images of all EIT systems vary because they depend on accuracy and SNR of measured data as well as the algorithm used. System tests for the ACE1, including SNR, are presented in Chapters 4 to 5 .

2.1. Tissue Impedance

In EIT, images are reconstructed to show distributions of conductivity and/or permittivity. Conductivity (σ), the inverse of the resistivity, can be defined as the extent to which

electricity flows in a domain or as the charge concentration. A larger conductivity corresponds to increased ease of charge movement. Permittivity (ϵ), related to capacitance, is a material's resistance to forming an electric field [17]. A greater permittivity in a substance corresponds to an increased ability to store electric charge. Conductivity and permittivity are combined in Equation (2.1) to obtain admittivity (γ), where $\omega = 2\pi f$ is the angular frequency in radians/second.

$$\gamma = \sigma + i\omega\epsilon \tag{2.1}$$

Table 2.1 illustrates the differences in bulk conductivity properties of human tissue. A large range in impedance exists within the body. For example, cerebrospinal fluid is 250 times more conductive than bone [1, 2]. In addition, conductivity and permittivity values change based on the physiological states of organs or tissues and with the orientation of the measurement to existing fibers. The electrical characteristics of muscles vary whether they are measured along the fibers (longitudinally) or across the fibers (transversely). Table 2.1 also shows a decrease in lung conductance and permittivity during inspiration [1, 2]. This change in conductivity and permittivity is created by the increase or decrease of air in the lungs, where the resistance of air is greater than tissue.

Bulk electrical properties are helpful in identifying uses of medical EIT and understanding reconstructed EIT images. The higher conductivity of blood and the change in impedance during respiration support use of EIT images for depicting areas of ventilation and perfusion. Presently, conductivity images are the most widely used. However, conductivity images alone are not necessarily sufficient in a clinical setting. EIT images would benefit from the inclusion

Table 2.1. Accepted values for bulk conductivity and permittivity of human tissues at 100 kHz [1–3].

Tissue	**Conductivity [mS/cm]**	**Permittivity [μF/m]**
Cerebrospinal fluid	15.4	—
Blood	6.7	0.05
Liver	2.8	0.49
Skeletal muscle	8.0 *long.* & 0.6 *trans.*	—
Cardiac muscle	6.3 *long.* & 2.3 *trans.*	0.88 *long.* & 0.36 *trans.*
Neural tissue	1.7	—
Gray matter	3.5	—
White matter	1.5	—
Lung	1.0 *exhale* & 0.4 *inhale*	0.44 *exhale* & 0.22 *inhale*
Fat	0.36	0.18
Bone	0.06	0.0027
Skin	0.0012	0.0144

of permittivity, which may make it easier to visualize differences between tissues that have similar resistivities or healthy tissue from anomalies [2, 15].

The frequency chosen for current injection in EIT data acquisition influences which features within a tissue are emphasized. A lower frequency of injected current is believed to weave around cells in the extracellular matrix, and a higher frequency passes more directly through cells. For example, changes in cellular swelling may be more readily seen with frequencies at approximately 200 Hz [11]. Many EIT systems use a mid-range frequency (30 kHz - 200 kHz) in which information relevant to both low and higher frequencies can be obtained [12, 18].

Since electrodes are used in EIT, the high contact impedance between the epidermis of the skin and the electrode results in large electric potential drops at the interface which can mask changes within. Contact impedance is further discussed in Chapter 6. A reason some EIT groups use frequencies of approximately 100 kHz or greater is that higher frequencies can lessen the effects of contact impedance caused by the capacitance associated with the

skin. The skin's high impedance often creates artifacts along the boundaries of reconstructed images, and improving how it is modeled is one of the challenges in EIT.

2.2. EIT for Medical Imaging

With proper electrode placement, EIT is commonly used to image impedance changes in the brain, breasts, and the chest or thorax to target the lungs and heart [2, 11]. Medical applications of EIT not discussed in detail in this text include use for prostate cancer detection [19, 20] and cervical cancer detection [21, 22]. Developments have led to the creation of commercial systems by Zilico [23] and Impedance Medical Technologies [24], which are marketed for cervical screening. EIT has also been considered as a method for monitoring radio-frequency induced hyperthermia, which is a technique used for ablating tumors [11, 25].

Motivation and promising work in EIT for neural imaging, breast cancer detection and thoracic imaging are discussed in subsequent subsections and associated tomographs are discussed in Section 2.4.

2.2.1. Types of EIT Images. EIT images can be either 2-D or 3-D depending on placement of electrodes and reconstruction algorithms used. Images can show structure as well as function. In the creation of EIT *difference images*, a reference image is chosen and reconstructed images reflect a change in impedance characteristics from the reference. Most EIT data is dynamic or collected over a period of time so that a series of images or a movie can be created. Time-difference dynamic EIT images are particularly useful to image bodily functions or organs and fluids that move within the body, such as blood flow, air flow or stomach s(gastric) emptying. Difference images are commonly created by commercial and research groups because noise from experimental conditions and noise from the electronics or equipment is mostly subtracted out [15, 26]. Sampling and frame rates can be used to

vary the time resolution of images, but there is a direct relationship with the signal-to-noise ratio (SNR) that is discussed in Chapter 5.

There is another type of EIT images that can be obtained. *Absolute images* do not use a reference frame to create images, but often use a model as a reference during image reconstruction. These types of images are difficult to obtain because the noise from the experimental conditions and equipment is not subtracted out, so it either has to be greatly minimized and/or accurately modeled. Obtaining absolute conductivity EIT images is easier to do than absolute permittivity EIT images. Since permittivity information is taken from voltage phase measurements, small errors introduced by parasitic capacitance can make absolute permittivity EIT images very difficult to obtain. Absolute EIT images are the best for imaging anatomy or structure within the body. Absolute images can be time varying or dynamic or may be a single static image. If a sequence of absolute images is created, functional information can be obtained as well.

2.2.2. Brain Imaging. For approximately 7-8% of patients that experience habitual seizures, surgical intervention to destroy neuronal tissue causing these episodes is a necessary treatment [27]. To have the best surgical outcomes, it is essential to identify the area of the brain that is the greatest contributor for causing seizures and destroy only that tissue. While EIT may someday be routinely used to look for impedance changes in the brain caused by the seizures, other imaging techniques and monitoring methods are presently used. Electroencephalograms (EEGs) are often used to test for basic epileptic characteristics in the brain and magnetic resonance imaging (MRI) and positron emission tomography (PET) are often used to localize cortical abnormalities [28].

Researchers have been exploring EIT as a method for imaging brain function since the early 1990s. Brain activity during an artificially induced stroke was first studied in 1992 by Holder [29]. During a stroke, impedance changes caused by cell swelling and changes in the volume of blood can be detected with EIT. Additionally, Holder and coworkers investigated the use of EIT for imaging fast impedance changes in the brain associated with neuronal activity. EIT has also been used to look at depression [30], localize epileptic foci and measure brain activity during seizures [11, 31, 27, 32]. One of the most promising EIT research studies involving localization of epileptic foci was performed on anaesthetized rabbits in 1996 [32]. In this study, 16 electrodes were placed around perimeter of one plane of the exposed superior surface of the brains of rabbits. Reproducible impedance changes were detected in corresponding cortical areas appropriate to induced electrical stimulation.

In 2006, a feasibility study by Fabrizi and coworkers looked at combining EIT using 31 electrodes with EEG on seven human subjects that experienced at least one seizure over the course of several days. However, reconstructed localized conductivity changes did not correlate with regional information from MRI and EEG [27]. Further analysis by Fabrizi revealed that seizures originating deep within the brain are very difficult to detect with EIT because measured signals are of the same order of magnitude as the noise. Finite element simulations were used by the group to try to better predict signals measured during epileptic episodes, but they report that additional signal processing and reduction of noise in the EIT measured voltages is needed for improved future work [33].

One of the largest challenges in imaging the brain is that the impedance of the skull is far greater than white and gray matter brain tissues [11, 27]. Another challenge specific to imaging patients with seizures are the artifacts from the sudden and abrupt body movements

of the subjects [27]. It is unlikely that EIT will someday replace x-ray computed tomography (CT) or MRI as a modality to produce high resolution structural brain images [11]. However, as the hardware and algorithms advance, it is possible that neural EIT imaging studies may become increasing promising for bedside monitoring or imaging in remote places.

2.2.3. Breast Cancer Detection. More than 12% of women in the US will develop breast cancer over the course of a lifetime [11]. Worldwide, there are more than 1.0 million [34] to 1.7 million in 2012 [35] new cases of breast cancer annually. Presently, routine x-ray mammography is the standard of care for screening for tumors in women beginning at age 40 to 45 [34]. However, it is possible for false negatives (failing to detect a tumor) to occur. It is worth noting that false positives can also be damaging to women's health as studies have found that after a false positive diagnosis, women are less likely attend screenings in the future [36]. There are several research groups investigating EIT as an alternative or additional imaging technique to be used during screening.

Since it can be difficult to visualize the difference between benign and malignant cancerous tumors with traditional mammography, biopsies are typically performed on suspected cancerous tissues [11]. However, there is a significant difference between the resistive and capacitive properties of benign and cancerous breast tumors [37–39], so identification with EIT is promising. Changes in electrical properties of cancerous tissue is caused by increased water and salt concentrations within the cell, altered cellular membrane permeability and cell arrangement [40].

There have been several human subject studies using EIT for breast cancer detection. A group using an EIT mammograph with a planar electrode array (patented by Technology Commercialization International Inc., in Albuquerque, NM) found that more than 86% of

their examinations at least partially agreed with diagnoses made by x-ray mammography and biopsy [40, 41]. A group in Moscow, Russia has investigated use of the commerical MEIK EIT mammograph in a study in 2012 containing 117 subjects. The researchers found 12.61% of examinations resulted in a false positive diagnosis with the MEIK system [34].

Most recently, a 2015 study by Halter and colleagues was further able to identify benign from malignant tumors using blood flow. The vasculature near malignant tumors is chaotic and patterns in the pulsations of blow flow is different from the vasculature of benign tumors. To acquire this type of information, researchers synced pulse-oximetry data with EIT results [26].

2.2.4. Thoracic Imaging. EIT can be used to to image the lungs and the heart, since impedance changes are associated with respiratory and cardiac related activity [42]. A recent review by Adler and investigators from other EIT research groups [16] suggest that thoracic EIT may soon be ready for routine clinical applications, including assessment of acute lung injury and monitoring mechanically ventilated patients in intensive care units (ICU). According to study published in 2006 on critical care in the United States, more than 55,000 patients are cared for in ICUs daily. Primary reasons for ICU admission include: respiratory insufficiency/failure, postoperative care and heart failure. Approximately 40% of these patients receive intervention that includes mechanical ventilation [43]. It is possible that thoracic EIT use could improve care and monitoring for some ICU patients.

Recent work at Colorado State University has investigated another clinical application for thoracic EIT. Patients ages 2 to 21 at the Children's Hospital of Colorado with cystic fibrosis were imaged during tidal breathing, breath holding and during pulmonary function tests (PFT) in which spirometry was used to collect information about lung volumes and

air flow rates. (This work was supported by grant award number 1R21EB016869-01 A1 from the National Institute of Biomedical Imaging and Bioengineering. The content is solely the responsibility of the authors and does not necessarily represent the official view of the National Institute of Biomedical Imaging and Bioengineering or the National Institutes of Health.) Preliminary findings show ventilation patterns in reconstructed images that correspond well with the PFT maneuver. Both conductivity and permittivity images have been obtained [44].

In addition, thoracic EIT has been studied for use in determining tidal and intrathoracic volumes and respiratory system mechanics. This further allows for determination of tidal recruitment, detecting overinflation of the lungs and atelectasis (partial or complete lung collapse) [15, 16]. Regional lung perfusion or blood flow can also be seen. Perfusion information can be used to determine cardiac output, access timing or look for heart-related defects [11, 45, 46]. It has also been demonstrated that information about gas exchange can be determined, including: regional ventilation [47], regional ventilation-perfusion ratios [16] or the existence of extra-vascular lung water [48]. After EIT image reconstruction, further filtering is often required to isolate perfusion and ventilation signals or images [11]. The placement of the electrodes during data acquisition should be considered. Most thoracic EIT systems require electrodes to be placed around the full or partial perimeter of the chest, defining the boundary of the cross-section desired for imaging. In 2-dimensional thoracic EIT images, one group reported that a reconstructed image often corresponds to a 7-10 cm slice of the domain with an approximate 1.5-3 cm resolution in the cross-sectional plane [15]. Other EIT systems are described in further detail in Section 2.4.

Since the lungs are large organs located close to the body's surface, lung-associated pathologies are an ideal focus in thoracic EIT imaging [16]. The impedance of the lung changes up to 300% during tidal breathing [49]. It has also been reported that 10 to 40% of patients under mechanical ventilation can experience complications which can be detected with EIT [50]. A paper by Costa and coworkers discusses the usefulness of absolute images in the real-time detection of a pneumothorax (partial or full lung collapse) and demonstrates detection of volumes as small as 20 mL of air in the pleural space [50]. Research by Camargo presents EIT images in pigs which contain clinically significant information about atelectasis (lung collapse), pneumothorax (air in the pleural space), pleural effusion (fluid buildup), and different ventilation pressures caused by mechanical ventilation [51].

2.3. A Brief History of Medical EIT Hardware

Initial use of electricity for medical purposes to image biological tissues and pathologies began as early as the 1970s. Webster and Henderson proposed use of an impedance camera in 1978 with the intent to image pulmonary edema[52]. This was one of the first electrical impedance tomography-like devices [11, 52]. Their device used a large voltage source placed on one side of the chest/thorax and an array of 100 electrodes on the opposing side to measure current passing through the body. From these measurements, they were able to create a 100 pixel image called an admittance contour map of the human chest. They reported acquisition rates as high as 32 frames/second, but with very poor image resolution, the group admitted that their approach would only be helpful in cases involving an exceptionally large pulmonary edema [52].

The first commercially available EIT system was created by Brown and Barber from Sheffield in 1987. The device contained a ring of 16 electrodes and injected 5 $mA_{peak-to-peak}$

(or mA_{pp}) current at 51 kHz on adjacent pairs of electrodes [53]. The original Sheffield system could only image at 10 frames/second and had poor image resolution. Despite these limitations, it helped researchers begin to explore medical EIT applications including imaging: stomach (gastric) emptying, the cardiac cycle, lung ventilation, and the brain. The Sheffield Mark 1 and 2 systems are both 16 electrode single frequency systems developed from this original design [11].

Since the development of the first systems in the 1970s and 1980s, EIT research groups have designed more sophisticated EIT hardware and reconstruction algorithms [11]. Within the past ten years, Mark systems from Sheffield and the adaptation to the Sheffield by the University of College London have evolved into designs with multi-frequency capabilities, often called electrical impedance spectroscopy (EIS) or multi-frequency electrical impedance tomography (MFEIT) [54]. Presently, there are more than 25 research groups investigating electrical impedance tomography reconstruction techniques and/or hardware [55].

2.4. A Review of EIT Systems

Some EIT systems are easily adapted for use on different areas of the body, and some systems have been designed for specific medical applications. In general, there are three kinds of EIT systems. There is one that allows for variable electrode placement, another that restricts placement to rows of electrodes to be placed around the perimeter of the subject and the other contains planar electrode arrays. EIT systems with variable placement or rows of electrodes are often used to image the chest and brain, while EIT systems with planar arrays are more frequently used to image the breasts. Strengths and limitations of these systems are discussed and contrasted with ACE1. If information is available, design features used to combat extra capacitance from multiplexers and/or stray capacitance are described.

2.4.1. EIT Systems with Planar Arrays. Several groups have been using systems using a single nxn planar array (also known as impedance mapping), primarily for breast cancer detection applications. There are several of these tomographs. A 256 planar electrode array patented by Technology Commercialization International Inc., in Albuquerque, NM has been used in breast cancer studies [40, 41]. Researchers at Rensselaer Polytechnic Institute, created the ACT 4 electrical impedance spectrograph with 64 radiolucent electrodes on two parallel plates on which currents or voltages can be applied and collected simultaneously with traditional x-ray mammography [56]. The ACT 4 can detect spherical inhomogeneities with twice the conductivity as the background when they are as small as 3 mm in diameter in a 10 cm cube [57]. The ACT 4 is one of the most sophisticated and advanced EIT systems to date [56].

Other planar array based systems include a group in Moscow, Russia which has investigated use of the MEIK EIT mammograph, commercially produced by Impedance Medical Technologies. This commerical system contains an array of 256 electrodes on a rigid paddle or plate that can be pressed against the breast. Impedance Medical Technologies has recently released a multi-frequency version of the MEIK called the MEM [58]. In 2014, a group at New York University presented an EIT system which is comprised of high-density, flexible micro-electrode arrays with sub-millimeter spacing which allows the system to easily conform to different shapes. Preliminary results demonstrate the ability of the system to detect phantom tumors, but the group is still in the early stages of performing further studies with this device [59].

2.4.2. EIT Systems for Thoracic Imaging. EIT systems discussed in this subsection can be used for imaging the lungs and/or heart. Additionally, several of the following

systems have also been used in many studies imaging the brain. Features of both commercial and academic systems with an emphasis on their thoracic applications are described here.

2.4.2.1. *Common Current Injection Configurations in Thoracic EIT.* Not all current patterns are equivalently easy to implement in hardware when considering the number and current source characteristics each requires. Common EIT current patterns are described and listed from the most to least sophisticated:

- *Adaptive* current patterns are iteratively found and represent the optimal or best current patterns for a given domain. In this type of pattern, optimal current amplitude and phases are injected on all electrodes [60, 61].
- *Trigonometric* current patterns are optimal for finding a circular target in a circular domain and corresponding currents are injected on all electrodes [2].
- *Pairwise* current patterns inject current on two electrodes at a time, but voltages are still measured on all or most of the other electrodes [2, 61].
- *Interlaced* current patterns use separate electrodes to drive or apply current which are alternated with the receiving electrodes that measure the voltages [62].

Pairwise current patterns are the most popular, as seen in Table 2.3. They are also the style of current pattern implemented in ACE1. A motivation for using pairwise current patterns, despite being non-ideal for data reconstructions, is that they are the least expensive and simple to design. Pairwise current injection is more completely described in Chapter 3.

2.4.2.2. *A Review of Existing Commercial Thoracic EIT Systems.* Limited technical information is available about commercial EIT systems. However, information available about commercially available tomographs is compared here. Systems considered in Table 2.2 include: the ENLIGHT® by Timpel [63, 18], PulmoVista® 500 by Dräger [64], Swisstom

BB^2 [65], the Sheffield MK 3.5 by Maltron [66, 62], and the Goe MF II previously produced by CareFusion [16, 67, 68].

Most commercial systems are marketed for use in respiratory or ventilation beside monitoring in critical care situations. In each tomograph, emphasis is placed on the ease of use and placement of the electrode belt.

2.4.2.3. *A Review of Existing Academic Thoracic EIT Systems.* There are various academic research groups in EIT and many have their own versions of an electrical impedance tomograph. Compared in Table 2.3 are: the ACT III by the group at RPI [12], the Sheffield Mk 3a used at the University of Sheffield [16, 62], the High-speed Electrical Impedance Tomography System by the group at Dartmouth (which also has several customized EIT platforms) [69], the Swisstom Prototype by the group from Switzerland [70, 18], and the active complex electrode (ACE1) which is presented in this work and designed for Colorado State University (CSU) assisted by the University of São Paulo (USP).

Though not apparent from the table, the Sheffield system can be readily compared to ACE1. The Sheffield system attempts to directly measure the applied current through a resistor placed in series with the load (or body) [11], which is similar to the ACE1 system. The difference is the proximity of the sensing resistor to the location where current is injected. The Sheffield sensing resistor is placed in series with the load and data acquisition circuit [11], which is far from the location of current injection into the domain. Though this placement is adequate to enhance precision, it is not enough for phase information or the precise and accurate current information needed for absolute images. This design is subject to capacitive interference in two places, in between the source and load as well as the load and sensing resistor. The ACE1 sensing resistor is placed in between the current source and the load and

Table 2.2. A comparison of key features of commercial thoracic EIT Systems is presented.

Features	ENLIGHT ®	PulmoVista®500	Swisstom BB^2	Sheffield MK 3.5	Goe MF II
Company Location	São Paulo, Brazil	Lübeck, Germany	Landquart, Switzerland	Rayleigh, United Kingdom	Höchberg, Germany
Number of Electrodes	32	16	32	8	16
Current Frequency [kHz]	not specified	80 to 130	150	Multi-frequency (30 frequencies within 2 - 1630 kHz)	50
Frame Rate [frames/sec]	50	10, 15, 20, or 30	50 or less	25	13 (typical)
Belt Characteristics	Five reusable belts in different shapes and sizes for various patient chest perimeters	Five reusable belts in different shapes and sizes for various patient chest perimeters	Single use adjustable sensor belt	Not specified on manufacturer website	Cables connected via standard ECG electrodes
Comments and Features	Electrocardiogram and Pneumotachometer	Electrocardiogram	3D accelerometer to track subject body position	Designed for use on neonates	Out of production, but still used by University of Göttingen and others

as close to the load as possible, minimizing the number of locations for capacitive interference to occur. For accurate phase information, the sensing resistor needs to be as close to the domain being imaged as possible.

For experimental and commercial systems, the fastest achievable frame rates are commonly reported. These rates are not always representative of the typical settings used during data acquisition, since there are typically various parameters that can be varied to collect the best data possible. However, they are good metrics for system comparison.

Table 2.3. A comparison of key features of selected academic thoracic EIT Systems is presented.

Features	ACT III	Sheffield Mk 3a	High-speed EIT	Swisstom Prototype	ACE1
Number of Electrodes	32	16	32	32	16-32 (variable)
Current Frequency	30kHz	Multi-frequency (8 frequencies within 9.6 - 1200 kHz)	Continuously selectable frequencies	Discrete frequencies from 80 to 200 kHz	Discrete frequencies up to 200 kHz
Type of Current Patterns	Adaptive (optimal) or Trigonometric	Interlaced	not reported	pairwise (bipolar)	pairwise (bipolar or monopolar)
Frame Rate [frames/sec]	7.5 or 18	33	<100	10 - 30	up to 33.2
Analog to Digital Converter (ADC)	Analog Devices AD678 [71]	not reported	National Instruments PXIe-6341 [72]	Analog Devices AD9433 [73]	GE ICS-1640 [74]
ADC Bits Measured	12	not reported	16	12	24
Complex Voltages Measured	yes	not reported	not reported	not reported	yes
Additional Features	Automatic trimming of components	Electrical impedance spectroscopy	Tetrapolar system which can apply voltages or currents	Active electrodes pre-spaced on a belt	Active electrode cables allow for variable spacing

CHAPTER 3

ANALOG HARDWARE OVERVIEW: THE ACE 1 SYSTEM

The hardware presented in this work is a pairwise current injection design. It incorporates an active electrode for acquisition of complex voltage measurements. The active complex electrode (ACE1) system contains the same basic components as most pairwise EIT systems: a current source, a tomograph box, and a voltage measurement circuit.

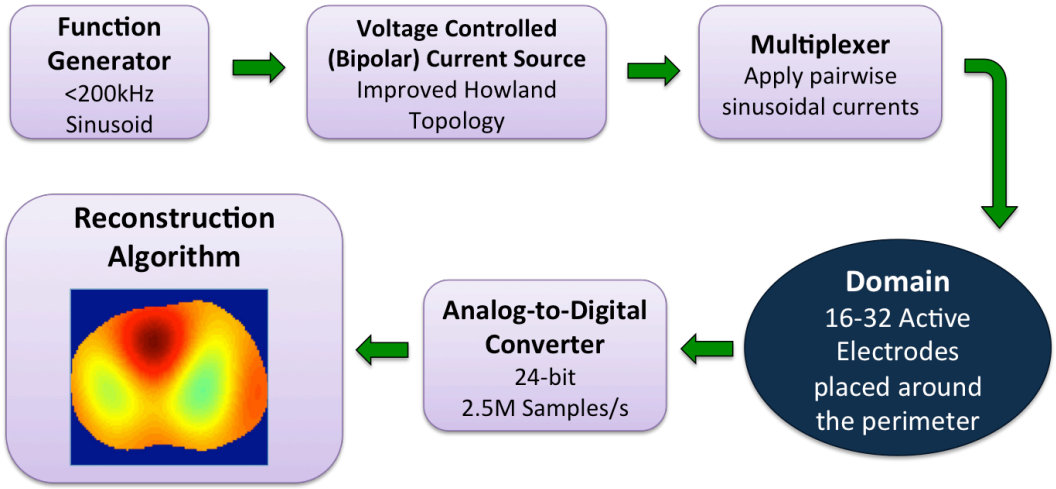

Figure 3.1. The basic design and acquisition of data with the active complex electrode (ACE1) system is described with this block diagram.

The components of the ACE1 system were assembled such that data is acquired in the manner described by the block diagram in Figure 3.1. To attach the system to human subjects, rectangular ECG electrodes are used (Philips 13951C neonatal/pediatric solid gel ECG monitoring snap electrodes). ACE1 is a modular system for use with up to 32 electrodes and injects currents ranging in amplitude from 0.5 mA to 5.0 mA at a discrete user-specified frequency of up to 200 kHz. During acquisition, the parallel port-controlled multiplexers ensure current is sent to the correct electrodes for injection. Electrical current spreads through the body or tank generating corresponding electric potentials on all electrodes.

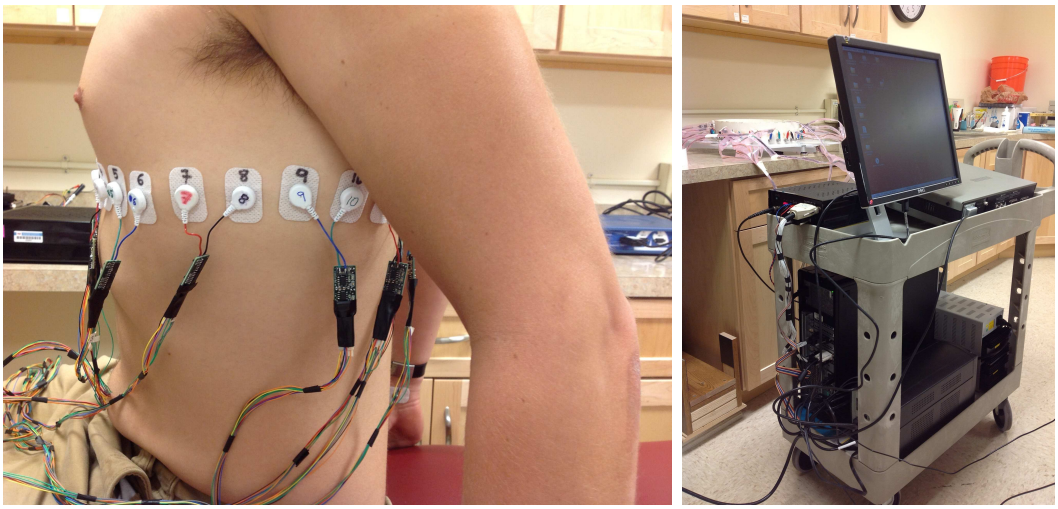

Figure 3.2. The ACE1 tomograph cables connected to a human volunteer (left) and a photo of the portable system (right).

These electric potentials are buffered from noise by the active electrodes and wired to the analog-to-digital converters (ADC) in the computer. Voltages are measured on all electrodes with a 24-bit ADC at 2.5 Msamples/sec. The stored data is then processed for use in image reconstructions [75].

Shown in Figure 3.2 is the ACE1 tomograph used on a human subject and on a portable cart imaging a tank phantom. The main components include:

- the main tomograph box (contains multiplexers, direct current (DC) supply regulators, a logic circuit for active electrode switch control, and the current source)
- cables with active electrodes that connect the tomograph to the subject or tank
- analog to digital converter for 32 channels (2 GE ICS 1640 boards each with 16 channel 24-bit 2.5 Msamples/second)
- function generator (Stanford Research Systems Model DS360 Ultra Low Distortion)
- DC supply for tomograph box (Mastech DC Power Supply HY3005F-3)

The ACE1 EIT system uses pairwise or skip current patterns. In this system, each frame in the dataset is formed by injecting current on two electrodes at a time and rotating the location of injection around the domain until all user-specified electrodes have acted as an injection pair. A single *current pattern* occurs for each instance where current is injected on a pair of electrodes. When all 32 electrodes are in use, 32 different current patterns are applied to form one frame. Potentials on all electrodes are measured during each current pattern of each frame of data acquisition.

The number of electrodes in between each of the injecting electrodes defines the *skip pattern*. For example, as show in Figure 3.3, in skip four, the first current injection pattern occurs between electrode one and six. The third current pattern injects current on electrodes three and eight. After each current pattern, the injection electrodes are rotated about the domain until current has been injected on all possible pairs of electrodes for a given skip pattern.

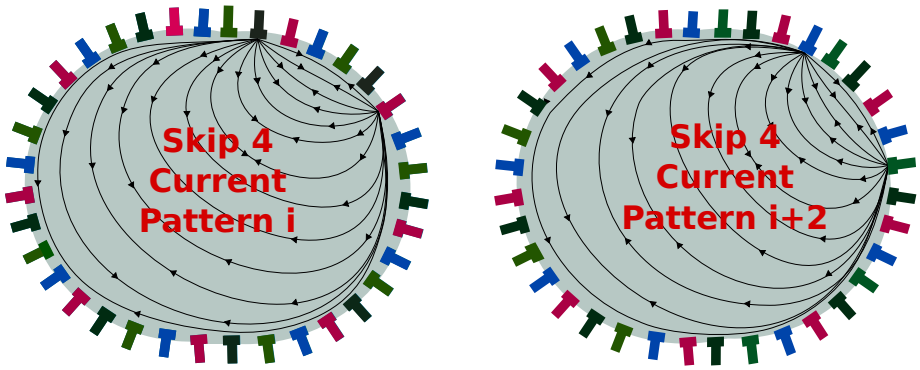

Figure 3.3. This figure illustrates the pairwise injection of current about the domain for a skip four pattern. The direction of bipolar current flow is indicated by the arrows.

In data acquisition, up to 32 electrodes can be used. Based on the number of electrodes (L) placed around the domain, some skip patterns are better for later use in the D-bar algorithm than others. In image reconstruction, it is beneficial to maintain as many linearly

Table 3.1. Frame rates for ACE1 for varying numbers of electrodes and data point acquisition rates.

Number of Channels	256 Point Acquisition Rate [Frames/second]	512 Point Acquisition Rate [Frames/second]	1024 Point Acquisition Rate [Frames/second]
16	66.4	52.6	31.8
17	62.1	46.8	29.7
18	59.0	44.3	28.3
19	56.0	41.8	26.8
20	53.2	39.8	25.6
21	50.9	37.8	24.3
22	48.3	36.2	22.8
23	45.8	34.5	22.1
24	44.3	33.3	21.1
25	42.8	31.7	20.4
26	40.9	30.7	19.6
27	39.2	29.5	18.9
28	37.9	28.5	18.0
29	36.7	27.3	17.4
30	35.5	26.5	16.7
31	33.9	25.6	16.2
32	33.2	24.9	16.0

independent current patterns as possible. For a pairwise injection system of skip α, the number of linearly independent current patterns (N) is represented by Equation (3.1) [76]. Note that L-1 degrees of freedom is the most that can be achieved, resulting in the greatest number of voltage vectors that can be used by the reconstruction algorithm.

$$N = L - gcd(L, \alpha + 1), \text{where gcd is the greatest common divisor} \tag{3.1}$$

Frame rate varies depending on the number of data points or samples taken for each voltage measurement during acquisition. Table 3.1 shows various frame rates that can be achieved with ACE1. To calculate, system time stamps were saved at the beginning and end of a 500 frame data acquisition to determine the average frame rate.

Details of the key components in the ACE1 system are described in the following sections.

3.1. Active Electrodes

Active electrodes are used in both academic and commercial EIT systems [18, 70, 77]. Figure 3.4 clarifies the design and placement of an active electrode in EIT. A simple active electrode design, such as those using an operational amplifier in the follower or buffer configuration, is a good design choice for use in an EIT system. The simplicity of the follower configuration equates to fewer components on the PCB, which results in less component noise and a lower cost of implementation. Active electrodes which incorporate a negative impedance converter (NIC) or general impedance converter (GIC) are also advantageous since they allow for canceling of some or most of stray capacitance present near the electrode-domain interface.

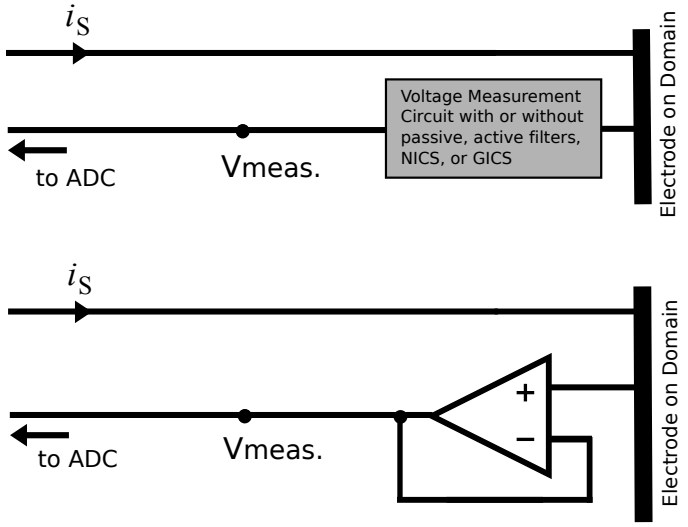

Figure 3.4. This diagram illustrates the basic active electrode implementation design. An operational amplifier used in the follower configuration is simplest of active electrode designs.

3.1.1. Active Complex Electrode Design Used in ACE1.

The active electrode design proposed in Figure 3.4 is not sufficient for complex measurements. It is known that stray capacitance and interference will influence the system by both draining current and

altering the phase. In order to have accurate reconstructions, it is essential to know both the amplitude and phase of the current delivered to the load or domain. Therefore, the active complex electrode design, shown in Figure 3.5A was developed.

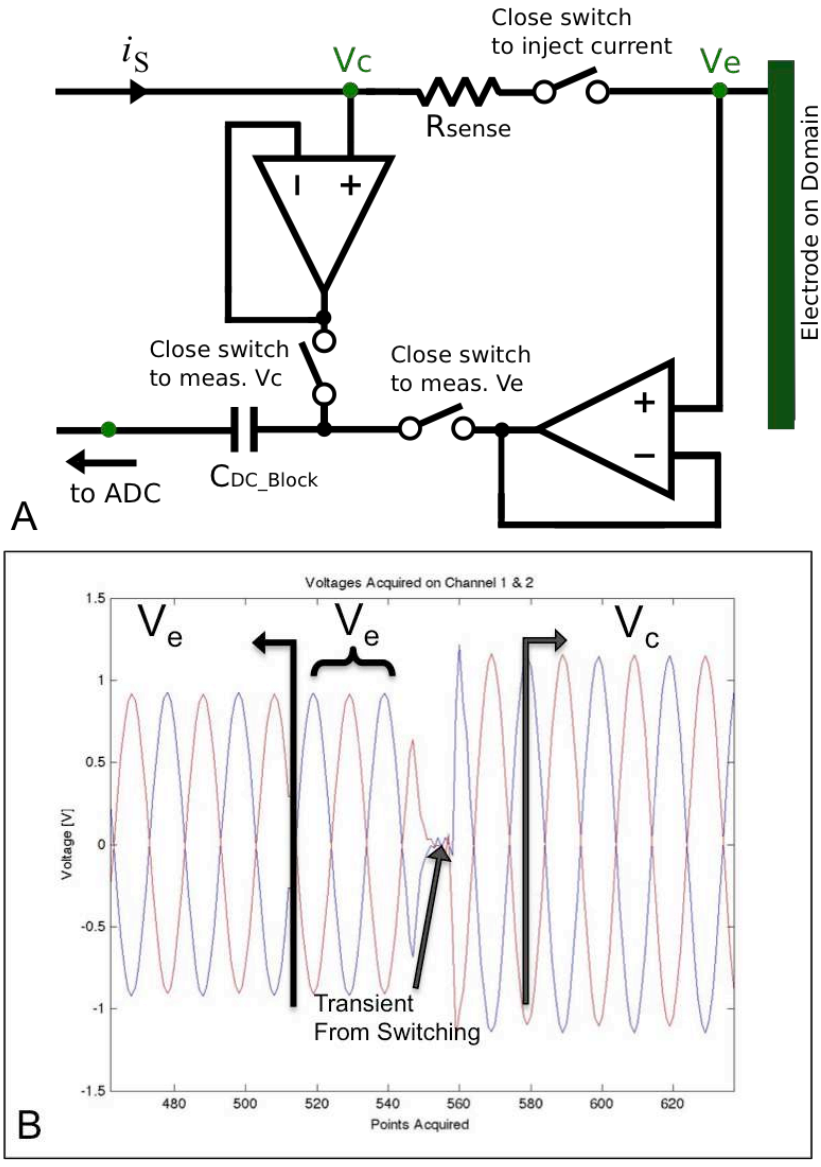

Figure 3.5. Figure A depicts a simplified schematic of the active electrode design. Figure B shows raw data from an injecting electrode pair. During each current pattern, the first samples acquired are of voltages at the electrode (V_e). Using switches allows for acquisition of V_c. Current is determined from V_c, V_e, and R_{sense}.

Voltage measurements associated with nodes in the active complex electrode circuit, shown in Figure 3.5A, are approximately 3 to 4 cm away from the attachment of the electrode to the human subject or tank phantom. The electrode design uses two operational amplifiers in the follower configuration to buffer voltages for measurement on either side of a sensing resistor placed in series with the domain.

By controlling which switches are open and closed, the electrical potential at node V_c or V_e can be measured. With proper calibration of this electrode, accurate phase and amplitude of the current passing through the sensing resistor can be calculated from the potentials using Ohm's Law. Ohm's Law is applicable since the potentials on either side of R_{sense} are measured. When current is not being injected, the switch between the current-sending multiplexer is opened to detach the cable or line from the electrode on the domain. Opening this switch reduces stray capacitance and electromagentic interference introduced by the multiplexer. Regardless of which electrodes are injecting current, both V_c and V_e are measured on each electrode during each current pattern for a specified number of samples or data points determining the acquisition rate.

The operational amplifiers in the follower configuration of Figure 3.5 allow for the measurements of V_c and V_e. Theoretically, the injected current I_{in} is found by:

$$I_{in} = \frac{V_c - V_e}{R_{sense}} \tag{3.2}$$

However, impedance of the switch must be taken into account. Therefore, the injected current can better approximated by:

$$I_{in} = \frac{V_c - V_e}{R_{sense} + Z_{switch}} \tag{3.3}$$

Since the effects of stray capacitance at node V_e cannot be neglected, it is still necessary to calibrate the voltages used in Equation (3.3) to more accurately calculate the current delivered to the load. With one side of the switch connected to node V_e, it was important to select a switch for the ACE1 electrode with a low source and drain capacitance and resistance to reduce effects on the passing signals. It was also necessary for the switch chosen to be robust to routine handling which may subject components to electrostatic discharge (ESD). The ADG442 switch was chosen for use in the active complex electrodes of this tomograph.

An additional benefit of the electrode design presented is that it allows for a less sophisticated and less expensive current source to be used. In most current source designs, ensuring a high output impedance is essential for assuming the applied magnitude of current is close to the theoretical value. Because the current can be measured next to the domain through the electrode, a more accurate calculation of current magnitude and phase can be performed for ACE1. Performance of the source is further discussed in Sections 4.1 to 4.2.

3.1.2. Practical Cable Design Considerations. Careful thought should be given to the design of the cables. An important design constraint to consider is the intended use of the tomograph. In particular, emphasis should be placed on selection of the cable gauge and methods for mounting the cables to the PCB. Through the several iterations of hardware design leading up to ACE1, the cable gauge and mounting changed considerably. Figure 3.6 shows the evolution of the prototype through several iterations. Use of PCBs creates a slimmer profile, which is lighter and less obtrusive to bedridden patients.

In the first iteration of prototype design, active electrodes used a simple buffer configuration and were constructed using DIP components and a custom single layer PCB. For wires, stranded AWG size 20 wire was chosen with locking clips on both sides. Electrodes were

then covered in shrink wrap to assist in securing and maintaining the locking connection between the cables and boards. The first set of tomography cables did not have switches for measuring current and had an electrode board thickness of approximately 1.2 cm, which was too thick for subjects to lay on in a clinical setting.

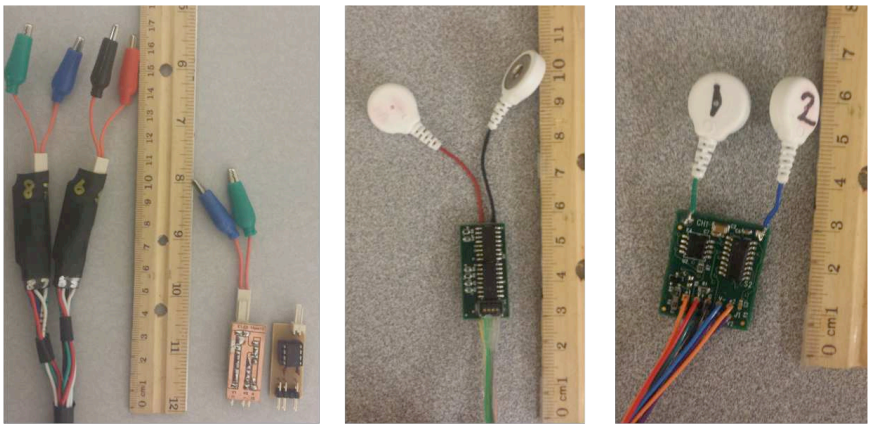

(a) First Iteration (b) Second Iteration (a) Third Iteration

Figure 3.6. The ACE1 electrode iterations became progressively more robust to mechanical forces experienced in certain clinical applications through thicker wire and stronger wire mount connections to the board.

In the second iteration, the cables were made from stranded AWG 30 wire and were too delicate for routine use in certain clinical situations. In this iteration, wire was crimped and placed into low-profile Molex Pico-EZmate connectors, which are also not recommended for use when the robustness of the system is essential. The Molex PCB headers can easily be ripped off the four layer PCB when removing the housings. The headers were fixed with isolation spray and super glue into the housings to prevent crimps from sliding (which results in poor connections). This cable design worked well on tank phantoms and seated or standing subjects. However, the mechanical stress on the wire/active electrode connection while rolling and sliding bed-ridden subjects was too great.

In the final iteration of cable design, stranded AWG 26 wire was soldered directly to PCB through holes. Additional DC blocking capacitors were also added to increase safety. This set of cables is mechanically robust, but the overall design is slightly noisier when compared to the second iteration.

Cables in of a variety of lengths were tested to account for use in a variety of settings. For example, while collecting data on a healthy human subject that is either sitting or standing, a cable length of 1.25 m is sufficient. However, for use on a subject in a hospital bed, a cable length of 1.75 m or greater was desired, but when tested, the additional length introduced extra noise.

3.2. Current Source Design

It is common to use a voltage controlled current source (VCCS) in EIT hardware to apply the current to the domain. The design of a mid to high frequency AC current source that performs well for a variety of loads can be challenging. Most EIT groups use a modification of a Howland or Improved Howland current source design similar to ones presented by Pliquett, *et al* [78] and Bertemes-Filho, *et al* [79]. A negative impedance converter (NIC) or general impedance converter (GIC) can be attached to the output of the Howland VCCS to increase the output impedance, and this approach is used in the ACT III and ACT 4 electrical impedance tomographs [80]. Theory related to the design of the current source used in ACE1 is discussed in Appendix A.

In a pairwise current injection system, there are two types of current sources that can be used: monopolar or bipolar. In the Figure 3.7, the differences between these two current sources as applied to the domain can be seen. Monpolar sources inject current through one electrode and ground through another. Bipolar current sources inject currents that are of

equal magnitude and 180 degrees out of phase with one another. An advantage of the ACE1 system is that it is easy to switch between monopolar and bipolar sources by substituting the current source boards in the tomograph box. However, bipolar current sources are generally preferred since the signal-to-noise ratio is greater on more of the electrodes.

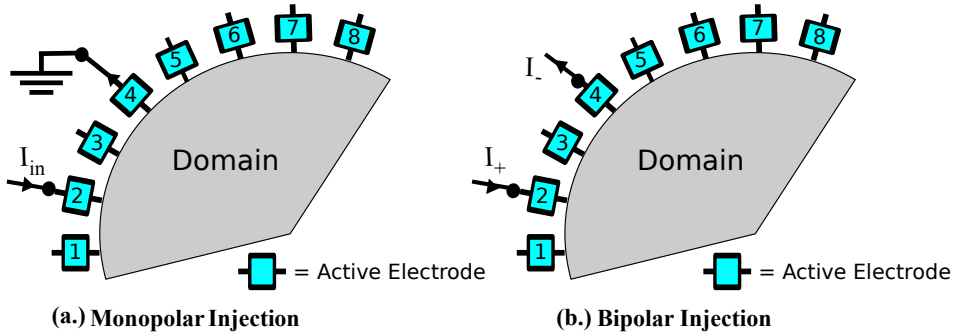

Figure 3.7. The differences between a monopolar current source and a bipolar current source can be seen in this figure. In (a), a Skip 1 pattern is used to inject current into the domain. In (b), a Skip 1 pattern with the bipolar source is shown. For the bipolar, I_- and I_+ are 180 degrees out of phase with one another.

3.2.1. Bipolar Current Source Design. The bipolar current source design used in ACE1 is comprised of two separate monopolar Howland circuits. The monopolar current source follows the the improved Howland design [13]. The Stanford Research Systems Model DS360 Ultra Low Distortion Function Generator has a bipolar sinusoidal voltage output; each output of the voltage source is connected to the input of the Howland source. The ACE1 bipolar current source design is presented in Figure 3.8. It uses an AD8066 operational amplifier and 1% tolerance 47 $k\Omega$ and 1 $k\Omega$ resistors which were carefully measured to ensure that they matched better than 1%. When constructing the source, each group of four of closely matching 47 $k\Omega$ resistors were used for R_{p1}, R_{p2}, R_{p3} and R_{p4} and R_{m1}, R_{m2}, R_{m3} and R_{m4}. 1.0 $k\Omega$ resistors were used for R_{p5} and R_{m5}. C_{p1}, C_{m1} and $C_{DC_{block}}$ are 1.0 μF capacitors. $C_{DC_{block}}$ ensures no DC current is sent to the multiplexer boards to be injected,

and C_{p1} and C_{m1} help remove DC offsets from the feedback loops. A detailed description of design choices and features of the improved Howland are further discussed in Section 4.1 and Appendix Section A.3.

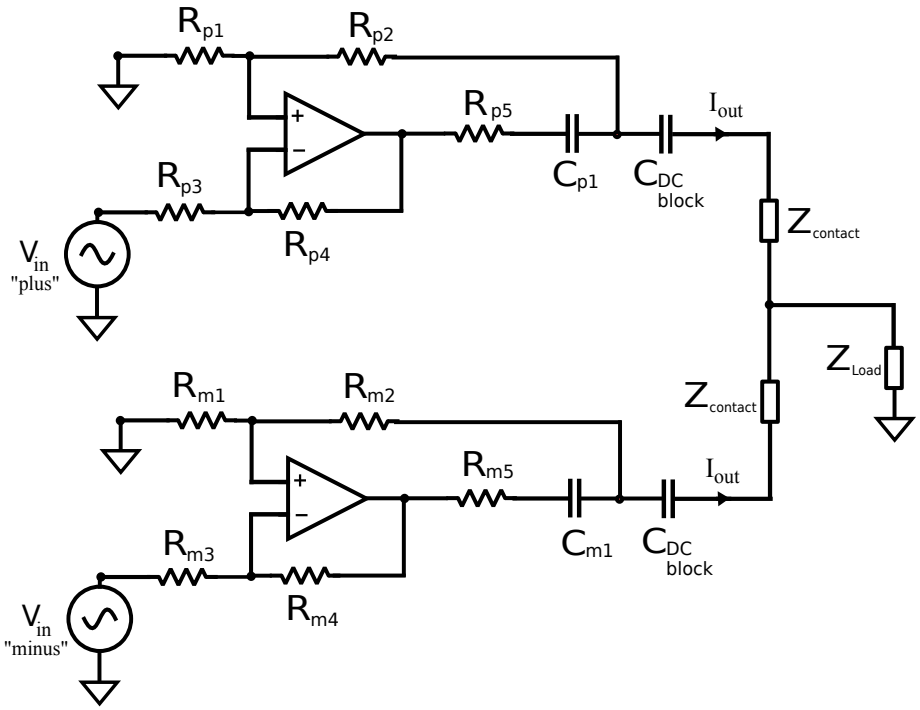

Figure 3.8. The schematic diagram of the bipolar current source.

3.3. Application of Current through Multiplexers and Logic Circuits

The parallel port signals are sent to the logic circuit board and then to two separate printed circuits boards (PCBs) containing ADUM6404-CRWZ isolation chips and ADG406 multiplexers. Interaction of the twelve digital signals from the parallel port sent to circuits inside the tomograph box are illustrated in Figure 3.9. There are four signals that are used to control the enables of the multiplexers. The eight other digital signals are used to control selection of channels of the 16 channel multiplexers A, B, C and D. One set of multiplexers controls the sending of digital signals to control switching on the ACE1 active electrodes for

current injection and the other set of multiplexers sends current to the appropriate electrodes for a given current pattern.

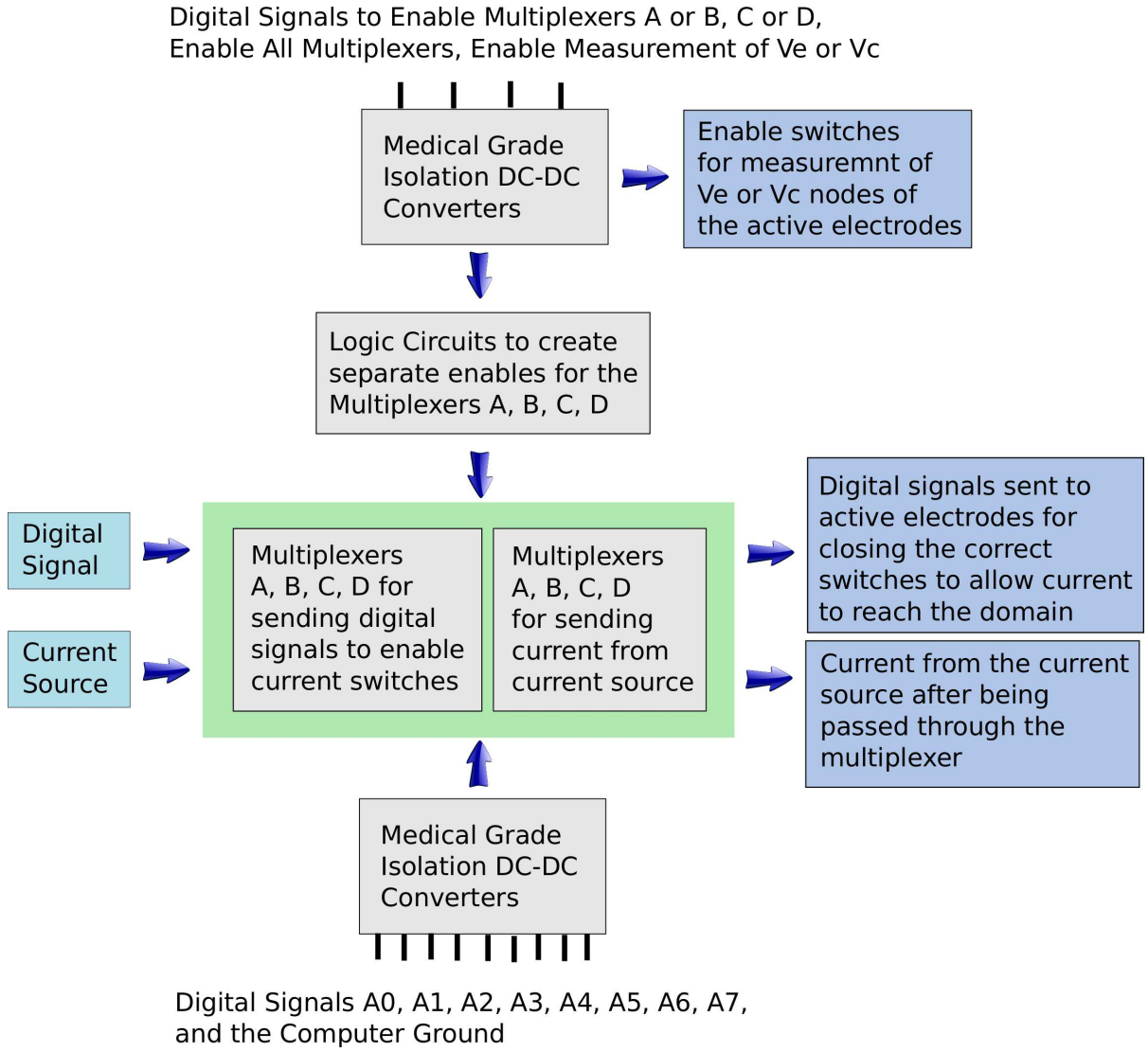

Figure 3.9. The interaction of digital signals from the parallel port, logic circuits and multiplexer to control pairwise current injection and measurement of different nodes in the active electrode is shown.

3.4. Safety Considerations in ACE1 Design

Supporting information about the safety of the system is presented in this section. ACE1 safety features include: subject isolation from earth and computer ground, component selection for minimized risk, and application of current which is consistent with FDA standards.

Proper isolation is achieved through multiplexing board, which contain three ADUM6404-CRWZ isolators [81] with integrated DC-to-DC converters to keep the subject isolated from the computer's ground and signals. The complex active electrode logic board also contains an ADUM6404-CRWZ isolator to ensure that the subject is isolated from the EN_{MS} digital signal, which controls switching between V_e and V_c nodes. The subject is further isolated from earth ground through the use of a medical grade isolation transformer, the Tripp Lite Isolator Series UL60601-1.

To minimize risk to the subject, several steps were taken. Fuses were placed between the DC supply and DC voltage regulation circuits. When data is taken on subjects lying down or in a hospital setting, an anti-static poly tubing, shown in Figure 3.10, is placed around cables to greatly reduce the risk of short circuiting terminals from static electricity, sweat or other bodily fluids. In the active electrodes, normally open ADG442 switches [82] were selected to ensure current can only be applied when commanded to do so by the acquisition code. If the ADG442 switch were to catastrophically fail, it is possible the subject could be briefly exposed to +10V or -10V DC and PCB components may become warm before the DC power regulating fuse would blow. To minimize this risk, the electrode circuit boards are individually tested and monitored for irregular behavior. To protect both the data acquisition boards and the subject, ceramic DC blocking capacitors are placed in series with active electrodes and the ADC.

The current source was designed to be compliant with FDA standards, ANSI/AAMI ES60601-1:2005 8.7.3(e) [83], which state that the maximum current regardless of waveform and frequency that one can inject is 10 mA rms. The 10 mA cutoff is still well below the threshold for perception, and the ACE1 system is approved to apply 6 mA peak-to-peak or

Figure 3.10. ACE1 cables in an anti-static encasing for ease of cleaning and reducing short circuit risks.

less in most ongoing IRB studies. Electric currents of the order of 100 mA at 60 Hz can induce ventricular fibrillation in normal adult humans [84], which is one of the reasons that EIT systems typically operate in the kHz frequency range (for other reasons see Section 2.1). Additionally, the subject is protected from the accidental application of a DC current from the current source through use of DC blocking capacitors placed in series with the current source output.

CHAPTER 4

SYSTEM TESTS RELATING TO PERFORMANCE

Results presented in this chapter provide insight about the performance of the ACE1 system. Test results assessing the presence and influence of noise and stray capacitance are found in Chapter 5. Accurate knowledge of the system is essential to improve calibration, best understand limitations of acquired data and find ACE1 settings that maximize performance. Background information about the current source and relevant simulation results are given in Section 4.1. Tests on the system look at other specifics, including: bipolar source performance (Section 4.2), system characteristics of resolution, precision, accuracy and reproducibility (Section 4.3), distinguishabilty of tank phantoms (Section 4.4) and select reconstructed images (Section 4.5).

4.1. Estimating Improved Howland Source Output Impedance

The performance of the source is tied to the ability to accurately predict current amplitude from function generator voltage settings. An ideal voltage controlled current source (VCCS) has an infinite output impedance, so a well performing current source should have an output impedance that is high compared to the load [8, 11, 12, 80, 85]. A well designed source should also be stable and contain high precision circuit components or be trimmed to increase the source's output impedance [80]. Additionally, the output impedance of the source must remain high near the load even when the source is located physically far from the location of current injection. A non-ideal current source will always output less current than predicted by theory from the voltage input. The ACE1 bipolar current source, shown in Figure 3.8, is comprised of two improved Howland sources. Its performance can be analyzed in several ways. Presented in this section is a derivation of output impedance and

simulations of the current source which relate to performance. Appendix A contains detailed information about the design and additional methods used to increase output impedance.

The ideal current output for the source in Figure 4.1 is achieved when resistors are perfectly trimmed: $R_2 = R_3 + R_4$, and $R_1 = R_3 = R_5$ [86, 87].

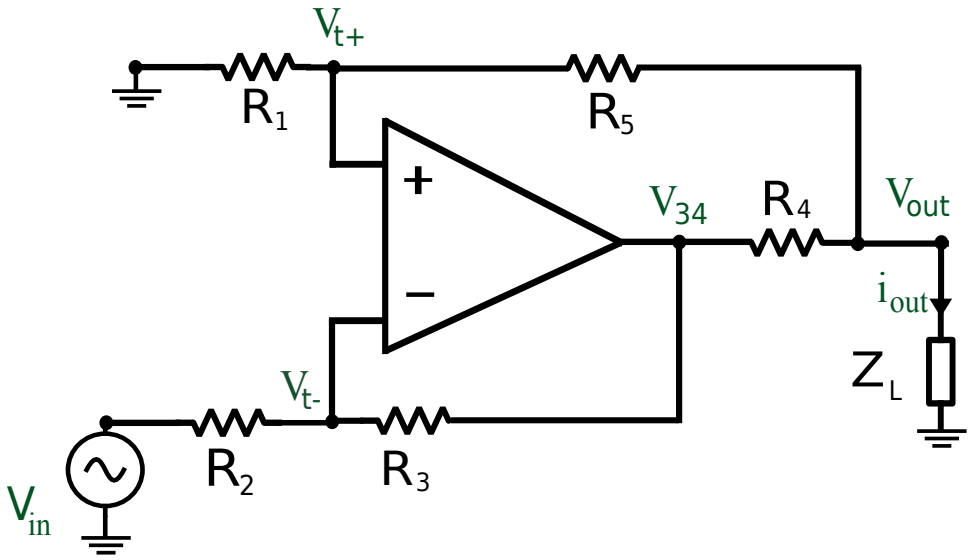

Figure 4.1. Improved Howland circuit model [8], where $V_{t-} = V_{t+} = V_t$ when assuming ideal op amp behavior.

The calculation for this ideal current is given by Equation (4.1).

$$i_{out} = \frac{V_{in}}{R_2 + R_3}\left(1 + \frac{2R_3}{R_4}\right) \tag{4.1}$$

However, the ACE1 current source is non-ideal. The following subsections report information relevant to understanding source behavior.

4.1.1. Ideal Output Impedance. Assuming that the op amp exhibits ideal behaviors, nodal Equations (4.2) - (4.5) corresponding to Figure 4.1 can be solved to find an expression of ideal output impedance [8]. For the ideal op amp assumption to be valid, it is assumed that the specific op amp input impedance (Z_{in}) is sufficiently large and that the positive

and negative input terminals are equal (V_t). The input voltage to the VCCS (V_{in}) is be set to ground because this is consistent with how to measure Z_{out} in a physical circuit. A derivation for the ideal improved Howland output impedance follows.

At the positive input terminal (V_{t+}):

$$\frac{V_t - V_{out}}{R_5} + \frac{V_t}{R_1} = 0 \tag{4.2}$$

At the negative input terminal (V_{t-}):

$$\frac{V_t - V_{in}}{R_2} + \frac{V_t - V_{34}}{R_3} = 0 \tag{4.3}$$

At the output terminal of the op amp (V_{34}):

$$\frac{V_{34} - V_t}{R_3} + \frac{V_{34} - V_{out}}{R_4} = 0 \tag{4.4}$$

Where current is leaving the source (V_{out}, i_{out}):

$$i_{out} = \frac{V_{out}}{Z_L} = \frac{V_{34} - V_{out}}{R_4} + \frac{V_t - V_{out}}{R_5} \tag{4.5}$$

By rearranging Equation (4.2) and Equation (4.3) for V_{out}, and substituting into Equation (4.5), an expression for Z_{out}, or $-V_{out}/i_{out}$ can be obtained. The negative sign in $-V_{out}/i_{out}$ indicates that the direction of current is opposite typical source behavior. Therefore, the output impedance of this Improved Howland design can be calculated by:

$$Z_{out} = \frac{R_2 R_4 (R_1 + R_5)}{R_2 R_4 - R_1 R_3 + R_2 R_5} \tag{4.6}$$

An ideal design choice is to choose $R = R_2 = R_3 = R_5$, $r = R_4$ and $R + r = R_1$. Assuming this design, Equation (4.6) can be simplified, where all resistors (R) and the gain setting resistor (r) match. In practice, error is introduced by the tolerance of components, but ignoring that error gives Equation (4.7) which shows an ideal improved Howland current source has infinite output impedance.

$$Z_{out} = \frac{Rr(2R + r)}{rR - R(r + R) + R^2} \tag{4.7}$$

$$Z_{out} = \lim_{D \to 0} \left(\frac{Rr(2R + r)}{rR - rR - R^2 + R^2} \right) = \infty \tag{4.8}$$

where: (4.9)

$$D = rR - rR - R^2 + R^2 \tag{4.10}$$

For simplicity, it is common when implementing this design to choose $R = R_1 = R_2 = R_3 = R_5$ and $r = R_4$ in Equation (4.6) because r is usually close to two orders of magnitude smaller than R. Although this is not ideal, building the source with high precision components (such as 1% tolerance or less) and measuring resistor values carefully before assembling the source allows resistors in the feedback loops to be closely balanced such that $R_1 = R_4 + R_5$ and $R_2 = R_3$.

4.1.2. Simulated Effects of Op Amp Selection on Source Performance. A non-ideal VCCS has a finite output impedance, and as the output impedance decreases, the source will exhibit more non-ideal behavior. Simulations were performed in National Instruments Multisim 11.0 software to compare the performance of various different op amps, including: AD8066, LF412, ADA4817, OPA656, AD713, and the AD746. A sample simulation circuit is shown in Figure 4.2.

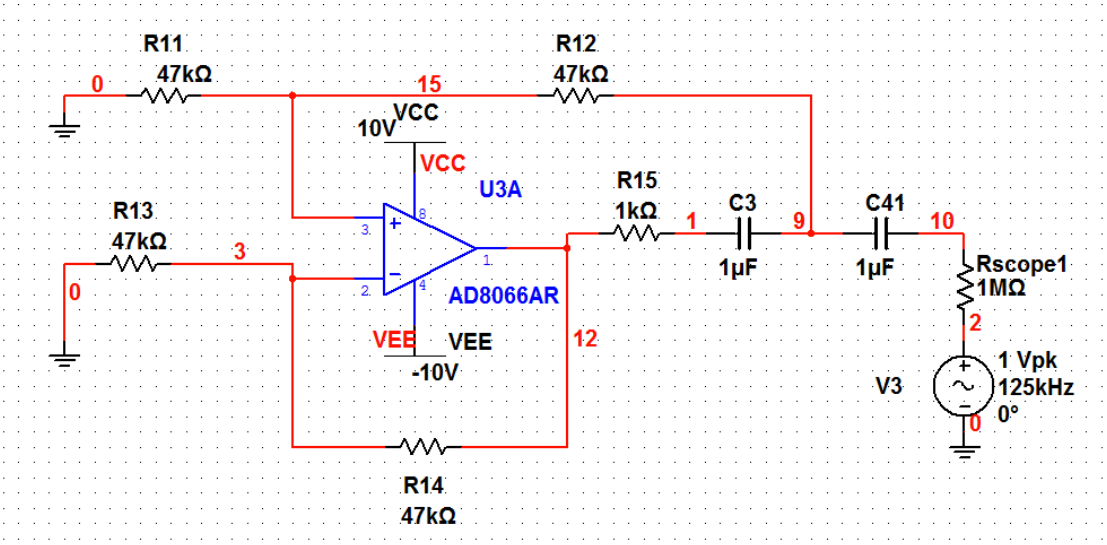

Figure 4.2. Multisim circuit showing the test configuration for Zout. Inputs are grounded to the source and a voltage source is placed at the output. C_3 and C_{41} are DC-blocking capacitors that were added to the improved Howland design to block any DC offsets.

The performance of the source is influenced by the common mode rejection ratio (CMMR) of the op amp. Op amps with CMMR less than 80 dB are generally not a good choice for EIT applications. Recent work by Bertemes [79] presents specific op amp specifications that directly effect output impedance of the source. These op amp parameters include: input impedance, output impedance and open loop gain. Op amp selection greatly influences source behavior around 100 kHz - 200 kHz. The op amp with the most consistent output impedance up to 200 kHz of those tested is the AD8066, as shown in Figure 4.3.

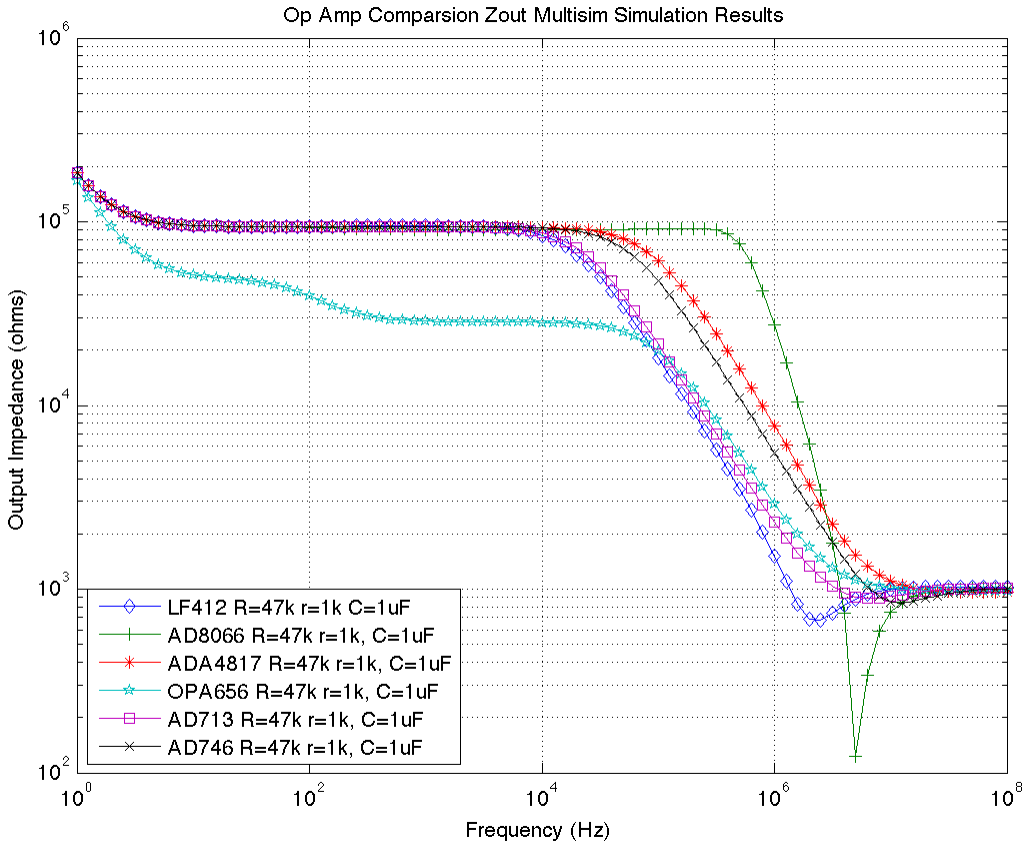

Figure 4.3. Multisim was used to test several different op amps to see which yielded the highest output impedance for frequencies larger than 100 kHz. The test setup from Figure 4.2 was used. R designates the resistor values for R_{11}, R_{12}, R_{13}, R_{14}, and r is R_{15}. C is the value of the DC blocking capacitors.

4.2. ACE1 Source Output Impedance

The output impedance of a voltage controlled current source (VCCS) is an important metric for understanding how ideally the source performs. It is common to report the source characteristics while it is isolated from the EIT system, and these tested results are consistent with the Multisim circuit simulations shown in Figures 4.2-4.3.

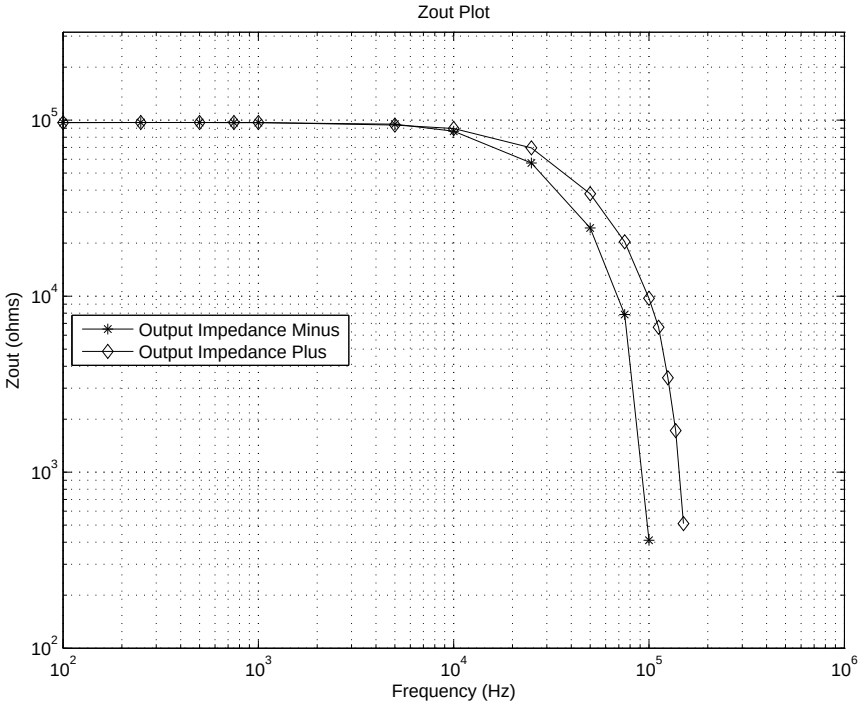

Figure 4.4. The output impedance of the ACE1 current source from isolated testing.

As a result of analyzing the isolated source, it was determined that frequencies less than 100 kHz have an higher output impedance, and for such frequencies, both halves of the bipolar are more closely matched. For these reasons, frequencies less than 100 kHz may be a better choice in some instances for maximizing performance of the VCCS. However, these results may be slightly misleading because when the source is connected in the system, the source output impedance is influenced by the stray capacitance and other components in the system.

4.2.1. Effective Source Output Impedance. To best understand a source's performance as part of the ACE1 system, the concept of "effective output impedance" was developed. This output impedance value is a measure of Z_{out} as seen from the active electrode board, and is calculated using a voltage divider in Equation (4.11). Figure 4.5 illustrates

how the effective output impedance defined. To test for effective output impedance, the inputs to the source are grounded and a voltage source is placed at V_e.

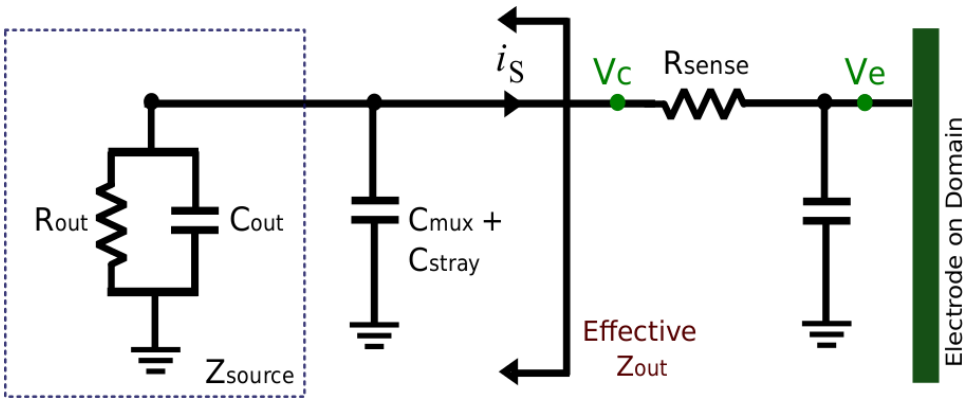

Figure 4.5. The effective output resistance of the ACE1 current source, where R_{out}, C_{out} and $C_{mux+stray}$ describe Z_{out}.

$$Z_{out} = \frac{R_{sense}V_c}{V_e - V_c} \tag{4.11}$$

When using only demodulated voltage amplitudes in effective output impedance calculations, the output impedance of the source is 50-100 times larger than the typical load of 1 kΩ, as shown in Figure 4.6. This figure shows the maximum effective output impedance that could be expected from the source, which is approximately equal to the output impedance found from isolated testing, shown in Figure 4.4. The closer the effective output impedance is to values obtained in isolated testing, the less influenced the source is from interference occurring between the source and point where current leaves the active electrode. The effective output impedance decreases as frequency increases, although even at 125 kHz, calculated values for each current pattern are all greater than 43 kΩ.

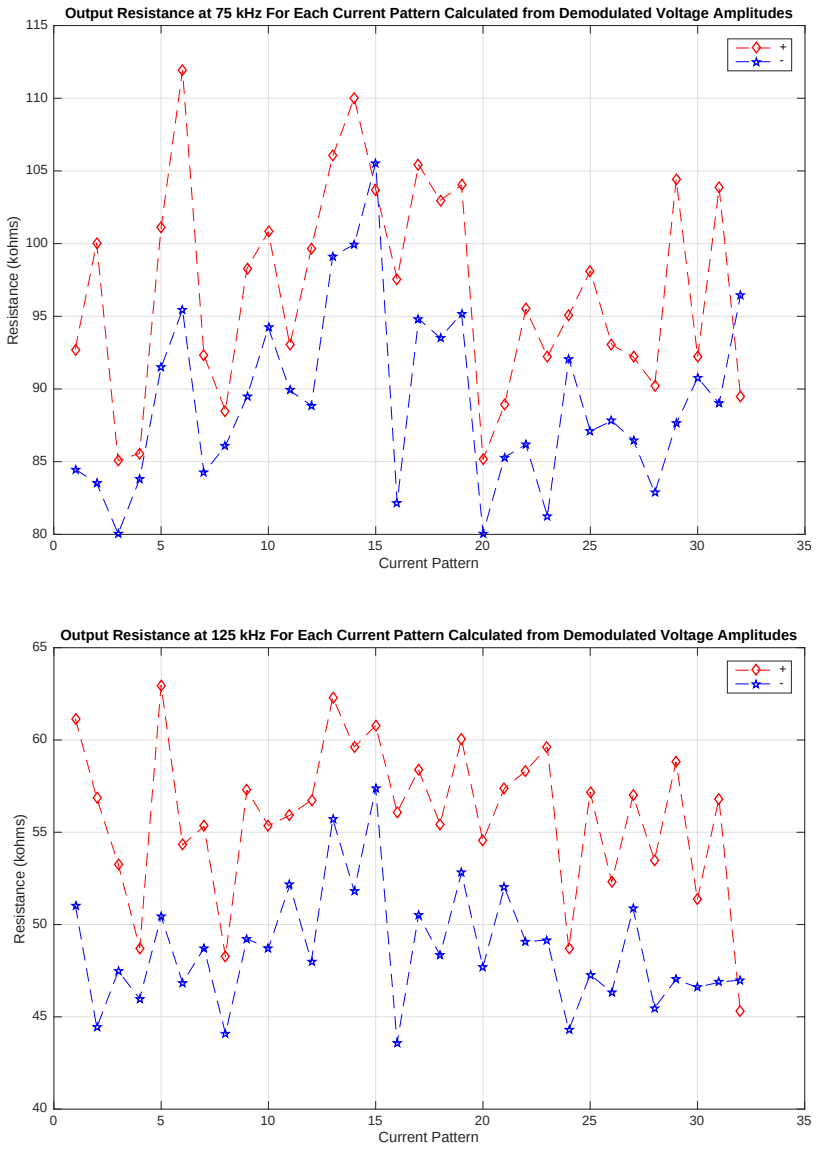

Figure 4.6. The effective output impedance of the ACE1 current source for each current pattern at 75 kHz (top) and 125 kHz (bottom).

When considering both magnitude and phase, the current source output impedance (Z_{out}) can be modeled as a resistor (R_{out}) and capacitor (C_{out}) in parallel, shown by Equation (4.12). The model R_{out} and C_{out} can be calculated using Equations (4.13) - (4.14) if the

output impedance as determined by Equation (4.11) is found at two different frequencies.

$$Z_{out} = \frac{R_{out} X_{c_{out}}}{R_{out} + X_{c_{out}}} \tag{4.12}$$

$$C_{out} = \frac{Z_{out2} - Z_{out1}}{j2\pi Z_{out1} Z_{out2}(f_1 - f_2)} \tag{4.13}$$

$$R_{out} = \frac{Z_{out1}}{1 - j2\pi f_1 C_{out} Z_{out1}} \tag{4.14}$$

Model R_{out} and C_{out} for each current pattern for both halves of the bipolar source are shown in Figure 4.7. The large capacitance is caused by the addition of stray capacitance along the cables and ADG406 multiplexer. This multiplexer has fairly large capacitances associated with its channels which can sink current. From the ADG406 datasheet, the capacitances and resistance associated with typical channels are: $C_{source_{(\text{off})}} = 5\text{pF}$, $C_{drain_{(\text{off})}} = 50\text{pF}$, $C_{source_{(\text{on})}} = C_{drain_{(\text{on})}} = 60\text{pF}$ and $R_{on} = 50\Omega$. These larger capacitance values contribute to the lower effective output impedance. The average output capacitance of approximately 56 pF across all channels suggests that incorporating capacitance canceling elements into the design would improve the current source performance. Capacitance canceling design techniques are discussed in Appendix A. The average output resistance was approximately 2 kΩ. The mean output resistance and capacitance were used in the model.

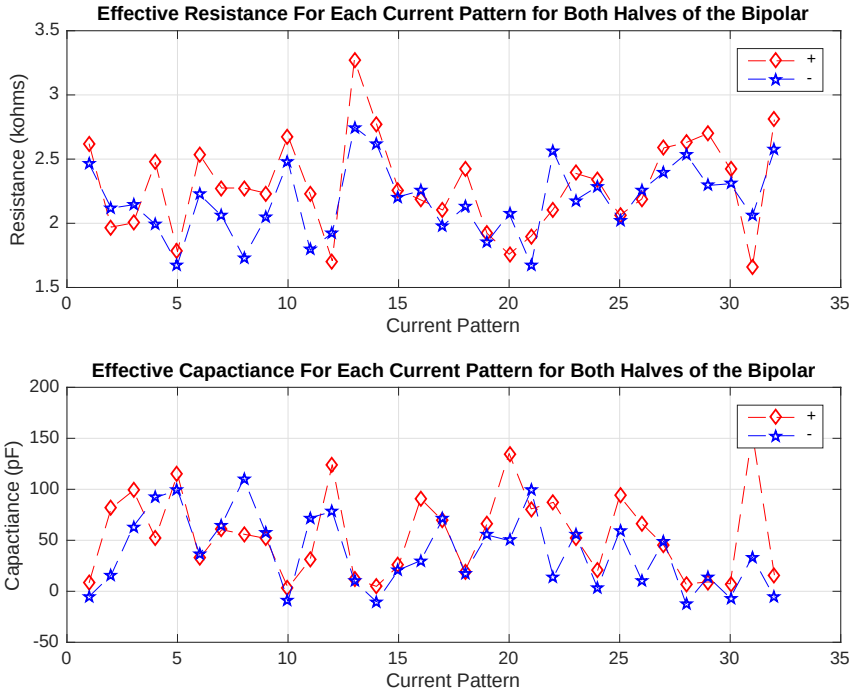

Figure 4.7. The current source output impedance (Z_{out}) as modeled by a resistor (R_{out}) and capacitor (C_{out}) in parallel.

To test the model, Equation (4.12) was calculated for a range of frequencies. The effective output resistance ($R_{out_{\text{effective}}}$) is found by taking the real component of Z_{out} and the effective output capacitance ($C_{out_{\text{effective}}}$) is found from the imaginary component of Z_{out}. Results of of this test are shown in Figure 4.8

$$Z_{out} = R_{out_{\text{effective}}} - jX_{out_{\text{effective}}} \tag{4.15}$$

$$C_{out_{\text{effective}}} = \frac{1}{j2\pi X_{c_{out_{\text{effective}}}}} \tag{4.16}$$

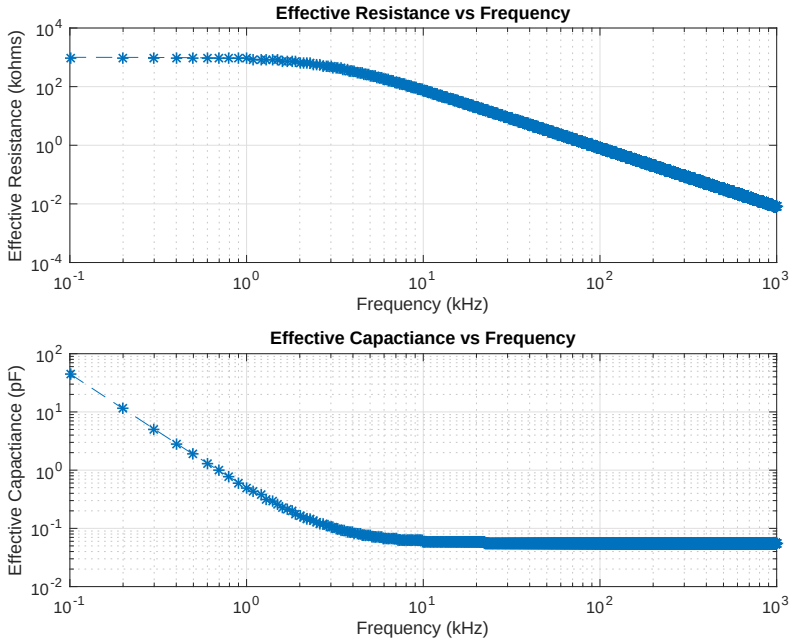

Figure 4.8. The effective output impedance of the ACE1 current source.

4.2.2. Mismatch of the Source. Performance of the current source would additionally improve if each channel were injecting current on identical purely resistive loads. However, this situation is never practically encountered. Thus, performance of the current source for use on a tank phantom (a primarily resistive load) and a human subject volunteer (a complex load) is compared. It is expected that differences in the the contact impedance between the stainless steel tank electrodes and saline or the ECG electrodes and human skin would influence source behavior in addition to differences in the interior of the domain.

Figure 4.9 shows calculated current amplitudes for injected current on a human subject. Due to non-uniform contact impedance for all electrodes on a domain, it would be misleading to compare only V_e voltage values. Equation (3.3) is used to calculate current, assuming a combined sensing resistor and switch impedance of 240 ohms to calculate current. Amplitude mismatch, or the sum of bipolar current amplitudes is plotted in Figure 4.9.

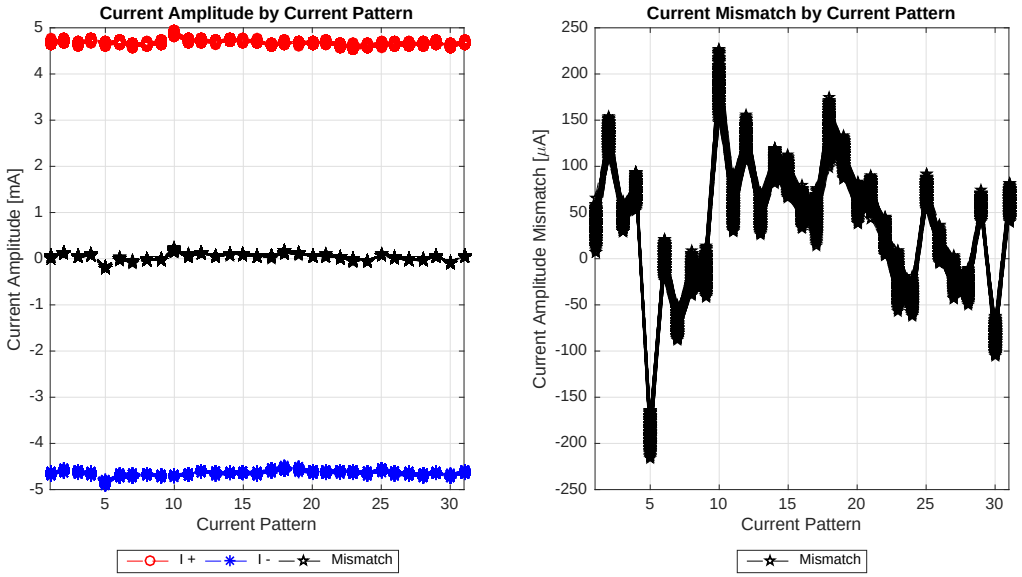

Figure 4.9. Calculated current amplitude for both parts of the bipolar source as well as their sum (or mismatch) is plotted for each of the 500 frames (or about 20 seconds) data collected on a healthy human subject during breath holding at 15.8 frames/second with a skip 4 current pattern. 31 electrodes were used.

Figure 4.9 is a representative plot that reveals the consistency of the amplitude of injected current on electrodes for all frames, even during use of ACE1 on a human subject. For different representative breath holding human subject dataset, the mismatch of the source was calculated. Parameters used were: skip 8, 31 electrodes, 600 frames, the 512 point sample rate and an average current amplitude of 4.75 mA. For this set, the average amplitude mismatch was 18.7 μV or 0.42% and 0.0593 radians or 3.40 degrees. These mismatch values are approximately within the range of measurements that can reproducibly obtained. Reproducibility is further discussed in Section 4.3.4.

Figure 4.11 displays the average percent of current amplitude and phase mismatch for 30 frames of data for various levels of current injection and skip patterns on a homogeneous tank phantom filled with 1 liter of approximately 0.9 mS/cm saline, shown in Figure 4.10.

Mismatch is defined as extent to which the magnitude and phase of the bipolar source is non-ideal. For an ideal source, the mismatch would be zero. In a poorly matched bipolar source, the magnitude would not be identical and the two currents are not 180 degrees out of phase with one another.

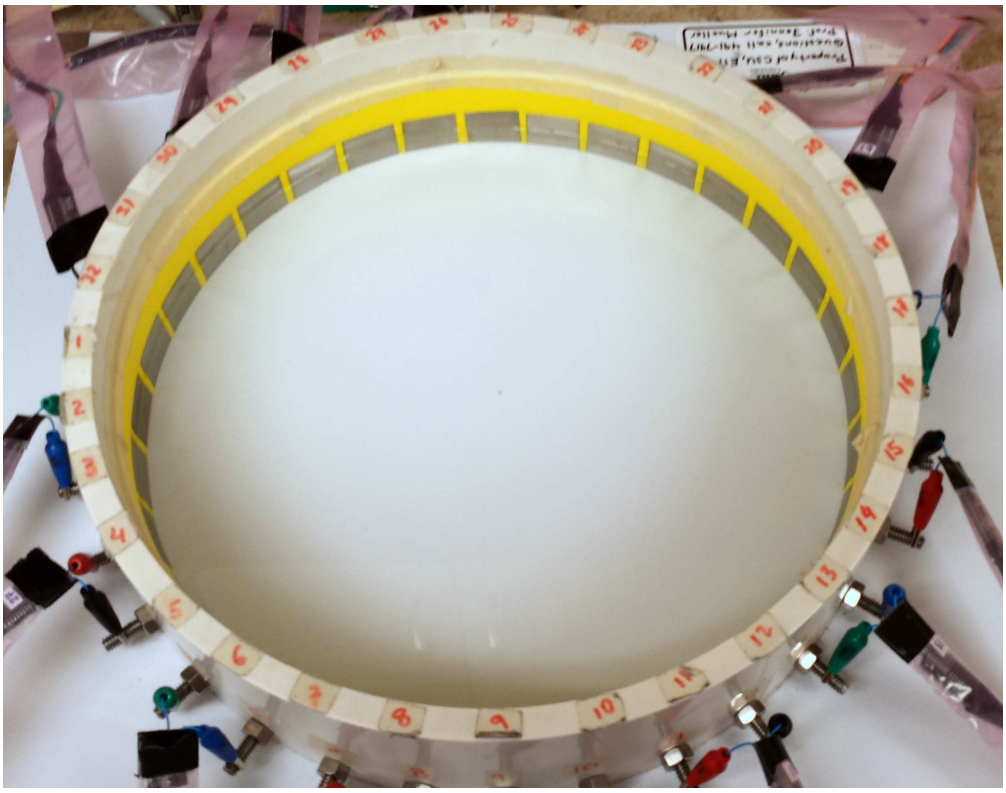

Figure 4.10. An image of the plastic tank phantom, which has an inner diameter of 30 cm and contains 32 square stainless steel electrodes (2.54 cm by 2.54 cm) placed 4 mm apart. When 1 liter of saline solution is added, the tank fills to a height of 1.4 cm.

The overall frame-to-frame variation is excellent since the data presented in Figure 4.11 shows small standard deviations for both measures of mismatch in the source. Figure 4.11(A) shows 1.31% amplitude mismatch with a overall standard deviation of 0.09%. Overall phase mismatch is 0.31% with a standard deviation of 0.02%.

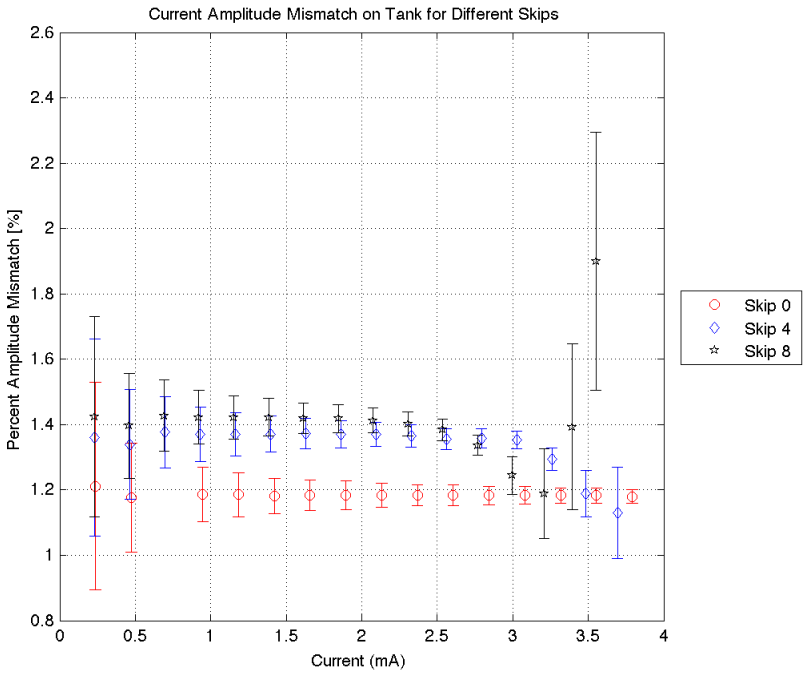

(a) Percent mismatch between bipolar current amplitudes.

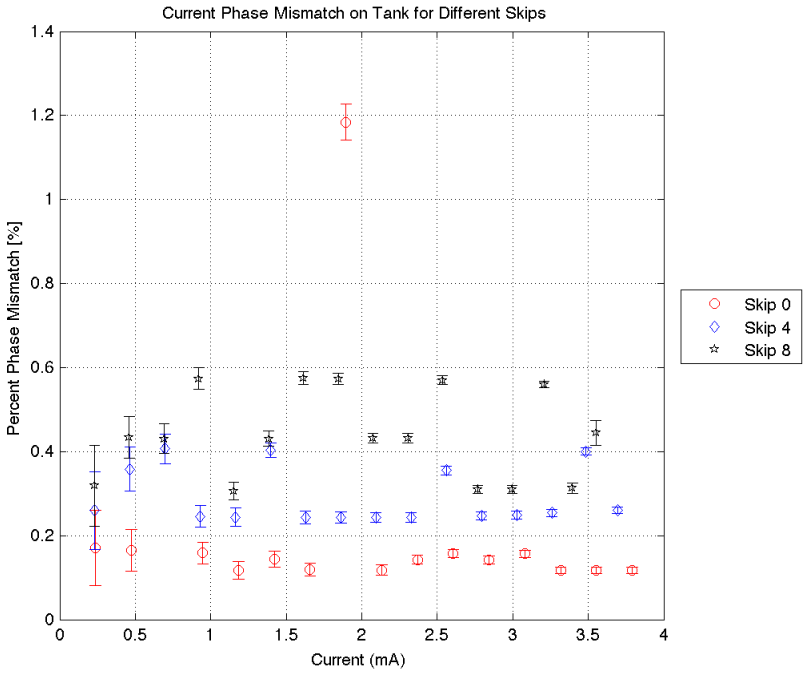

(b) Percent mismatch between bipolar current phases, where 180 degrees is 0%.

Figure 4.11. Source mismatch from 30 frames of data taken on a homogeneous tank for different skip patterns and varying injected currents.

4.3. System Characteristics

This section addresses the resolution, precision, accuracy and reproducibility of data. Given that the results presented here are limited by the performance of the function generator, some of the Stanford Research System DS360 ultra low distortion function generator specifications are given. This calibration of the DS360 is NIST traceable with an accuracy of 0.0025%. The total harmonic distortion (THD) of frequencies between 40 kHz to 100 kHz is typically less than -90 dB and typically less than -76 dB for 100 kHz to 200 kHz [88]. It was used in this section as the AC voltage supply for the accuracy and precision tests and as input to the VCCS when acquiring tank data.

Experiments on precision and accuracy share the same the set-up, shown in Figure 4.12. The similarity of the covariance of datasets used to determine accuracy and precision were compared with the Bartlett test. It was found that datasets for all tested skips contained statistically equal variances ($p < 0.01$).

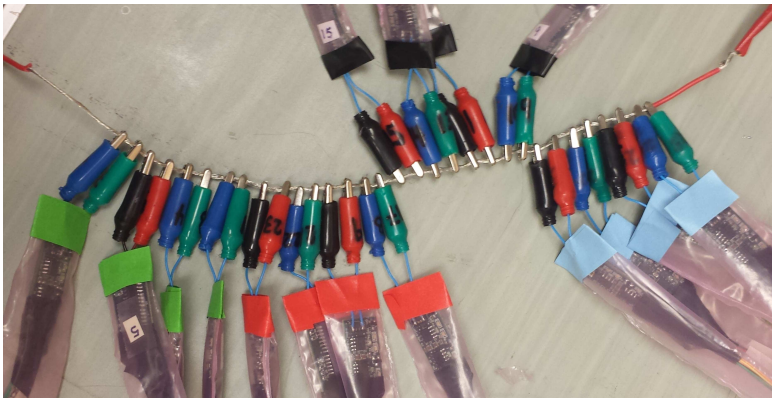

Figure 4.12. Test set-up where all of the ACE1 cables were connected to the same voltage source and 100 frames of data was collected. Inputs to the ACE1 current source were grounded.

For the convenience of the reader, select results are briefly described here. For example, at 125 kHz, ACE1 was able to precisely measure voltage amplitudes to within 27 μV and

with an accuracy of $\pm$ 0.237 μV. Precision during a single current pattern is shown in Figure 4.13 in Section 4.3.2. Accuracy during a single current pattern is shown in Figure 4.18 in Section 4.3.3. The mean (over skips 0, 2, 4, 6 and 8) of relative precision and relative accuracy for amplitude measurements is reported in Table 4.1 and phase measurements in Table 4.2. The voltage phase was found to be precise to within 0.045 radians at 125 kHz as shown in Figure 4.14 in Section 4.3.2.

Table 4.1. Percent accuracy $(\%A_{pk})_{mean}$ and percent precision $(\%P_{pk})_{mean}$ of voltage amplitudes at the 512 and 1024 point acquisition rates as calculated by Equations (4.37) and (4.26) respectively for 0.25 V_{pk} applied.

Frequency [kHz]	Accuracy [%] 512 point acq.	Precision [%] 512 point acq.	Accuracy [%] 1024 point acq.	Precision [%] 1024 point acq.
175	96.639	0.0055	96.631	0.0039
150	96.578	0.0065	96.573	0.0048
125	97.912	0.0098	96.913	0.0076
100	97.151	0.1106	97.005	0.1092
75	96.421	0.0391	96.309	0.0277
25	94.832	0.0140	94.747	0.0102

Table 4.2. Percent precision $(\%P_{\theta})_{mean}$ of voltage phase at the 512 and 1024 point acquisition rates as calculated by Equation (4.30) for 0.25 V_{pk} applied.

Frequency [kHz]	Precision [%] for 512 point acq.	Precision [%] for 1024 point acq.
175	0.899	0.557
150	0.698	0.816
125	0.782	0.658
100	0.461	0.539
75	0.614	0.398
25	1.217	1.240

Reproducibility experiments described in Subsection 4.3.4 used 100 frames of data collected on a homogeneous tank phantom. At 125 kHz, voltage amplitudes were reproducible to within 60 μV and voltage phase measurements to within 0.05 to 0.1 radians.

4.3.1. Resolution. The resolution of a measurement system is the smallest increment that can be measured with certainty [89]. Information related to the resolution of GE ICS-1640 analog-to-digital converter (ADC) was obtained from the datasheet. The resolution of the ICS-1640 ADC is given by Equation (4.17) and depends on the number of bits (ν) [12]. The 24-bit ICS-1640 has a non-adjustable full scale range of 20 V (from -10 V to $+10$ V), which gives a resolution of 1.2 μV. However the resolution of the ADC boards is not equivalent to the precision of the ACE1 system.

$$\text{resolution} = \frac{\text{ADC}_{full-scale}}{2^{\nu}} \tag{4.17}$$

4.3.2. Precision. In practice, the precision of ACE1 is worse than the resolution of its ADC boards. For the precision of the system to be quantified, then the sensitivity or the smallest detectable change in voltage measurements (V_l^k) must be determined [89]. Precision is a particularly important metric in EIT since the precision of the system limits the spatial resolution of reconstructed absolute and difference images.

One standard deviation (std) is used define precision (P) in this section for both amplitude (V_{pk}) and phase (V_θ) measurements from ACE1. The experimental set-up, shown in Figure 4.12, was used to acquire 100 total frames (F) of data, where 32 electrodes (L) were used and the total number of current patterns (K) is the same as the total number of electrodes ($L = K$).

The precision of the ACE1 system was considered in a variety of ways. Equation (4.18) shows a single standard deviation of amplitude measurements (${P_{pk}}_l^k$) for each electrode (l) during each current pattern (k) over all frames. The mean amplitude precision for each

electrode over all current patterns (${P_{pk_l}}^{mean}$) and the overall mean amplitude precision over all electrodes and current patterns ($(P_{pk})_{mean}$) were also considered, detailed by Equation (4.19) and Equation (4.20), respectively.

$$(4.18) \qquad {P_{pk_l}}^{k} = \text{std}({V_{pk_l}}^{k}(f)), \text{ for } l, k = 1, 2, ...L \text{ and std is computed over } f$$

$$(4.19) \qquad {P_{pk_l}}^{mean} = \frac{\sum_{k=1}^{L} {P_{pk_l}}^{k}}{L}$$

$$(4.20) \qquad (P_{pk})_{mean} = \frac{\sum_{l=1}^{L} {P_{pk_l}}^{mean}}{L}$$

Figure 4.13 shows that the precision of ACE1 amplitude measurements (${P_{pk_l}}^{k}$), as calculated by Equation (4.18), varies based on the frequency and not on the skip pattern. Each plot within Figure 4.13 shows a representative current pattern ($k = 18$) at a different frequency for skips 0, 2, 4, 6 and 8. Scatter plots are used to emphasize that the precision values associated with each electrode are not influenced by the skip pattern. Appendix Figures B.1 - B.3 in Section B.1 show similar results, despite using a faster frame rate (or the 512 point acquisition rate) and a range of applied voltages.

Figure 4.13 additionally shows that increasing frequency can generally increase precision. 175 kHz is most precise for voltage amplitude measurements with a precision less than 16 μV. However, 100 kHz is the poorest performing of tested frequencies with measurement precision less than 340 μV. Fast Fourier Transforms (FFTs) suggest that demodulated 75 kHz and 100 kHz datasets could be influenced by 600 kHz system noise, which is shown in more detail in Appendix C.

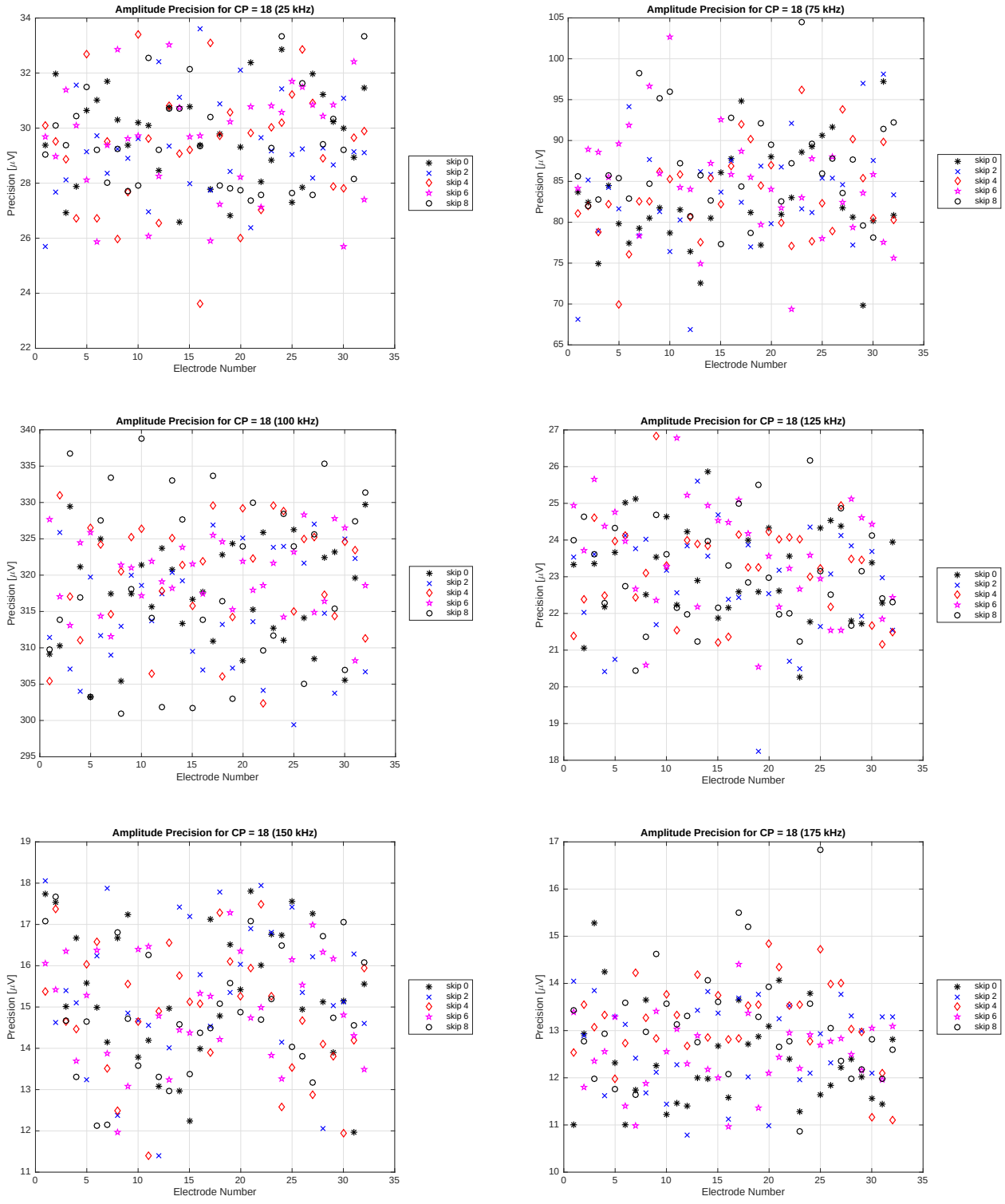

Figure 4.13. The precision (P_{pkl}^{k}) of measured voltage amplitudes in μV for each electrode for a single current pattern ($k = 18$) for a 0.25 V_{pk} applied voltage at various frequencies for 100 frames of data acquired at the 1024 point acquisition rate.

Phase precision can be obtained, but slightly different equations are needed because in this test electrodes only measure the same phase during a single current pattern in a single frame. To calculate phase precision for each current pattern in each frame (${P_\theta}^k(f)$), Equation (4.21) can be used. However, the mean phase precision (($({P_\theta}^k)_{mean}$) in Equation (4.22) refers to the mean precision for each current pattern over all frames and is practically more meaningful. The overall mean phase precision is ($(P_\theta)_{mean}$) from Equation (4.23) is used when comparing different acquisition rates and frequencies.

$$(4.21) \qquad {P_\theta}^k(f) = \text{std}(V^k_{\theta 1:L}(f)), \text{ for } k = 1, 2, ...L \text{ and std is computed over } f \text{ and } l$$

$$(4.22) \qquad ({P_\theta}^k)_{mean} = \frac{\sum_{f=1}^{F} {P_\theta}^k(f)}{F}, \text{ for } k = 1, 2, ...L$$

$$(4.23) \qquad (P_\theta)_{mean} = \frac{\sum_{k=1}^{L} ({P_\theta}^k)_{mean}}{L}$$

Figure 4.14 plots the mean precision of ACE1 phase measurements in radians for each current pattern (k) in ($({P_\theta}^k)_{mean}$), as calculated by Equation (4.22). The precision of voltage phase measurements varies slightly based on frequency. The largest difference between frequencies is the number of precision values larger than 0.01 radians or 0.6 degrees. 25 kHz was the least precise frequency, containing a few mean phase precision values as large as 0.15 radians or 8.6 degrees for some current patterns. All other frequencies were precise to within 0.085 radians or 4.9 degrees. For most current patterns, the mean precision is less than 0.01 radians.

Overall mean amplitude precision ($(P_{pk})_{mean}$) and overall mean phase precision ($(P_\theta)_{mean}$) were calculated for skip patterns 0, 2, 4, 6 and 8 at a variety of frequencies. In general, both

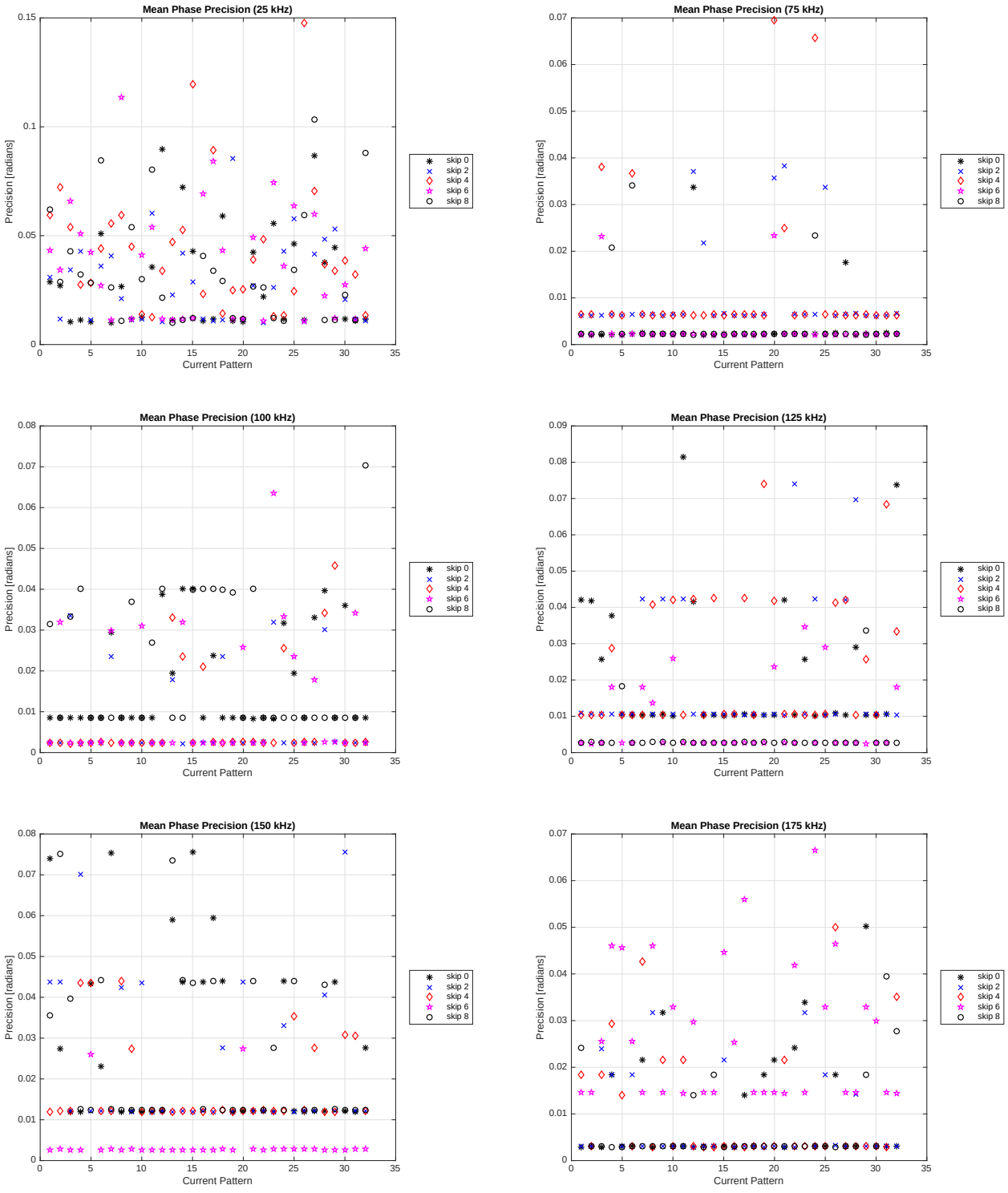

Figure 4.14. Mean phase precision in radians for each current pattern ($(P_\theta{}^k)_{mean}$) for measured voltage phases corresponding to a 0.25 V_{pk} applied voltage at various frequencies for 100 frames of data acquired at the 1024 point acquisition rate.

amplitude precision and phase precision, which are shown in Figure 4.15, are not influenced by acquisition rate. $(P_{pk})_{mean}$ is influenced by frequency, where 75 kHz and 100 kHz voltage amplitude measurements are approximately a factor of 2 to 6 times and 2 to 20 times, respectively, less precise than other tested frequencies. 100 kHz was only precise to 340 μV. 125 kHz, 150 kHz and 175 kHz are precise to approximately 11-27 μV. $(P_{\theta})_{mean}$ is not greatly influenced by frequency, but for many skip patterns 25 kHz is the least precise. All frequencies were precise to within 0.045 radians or 2.6 degrees.

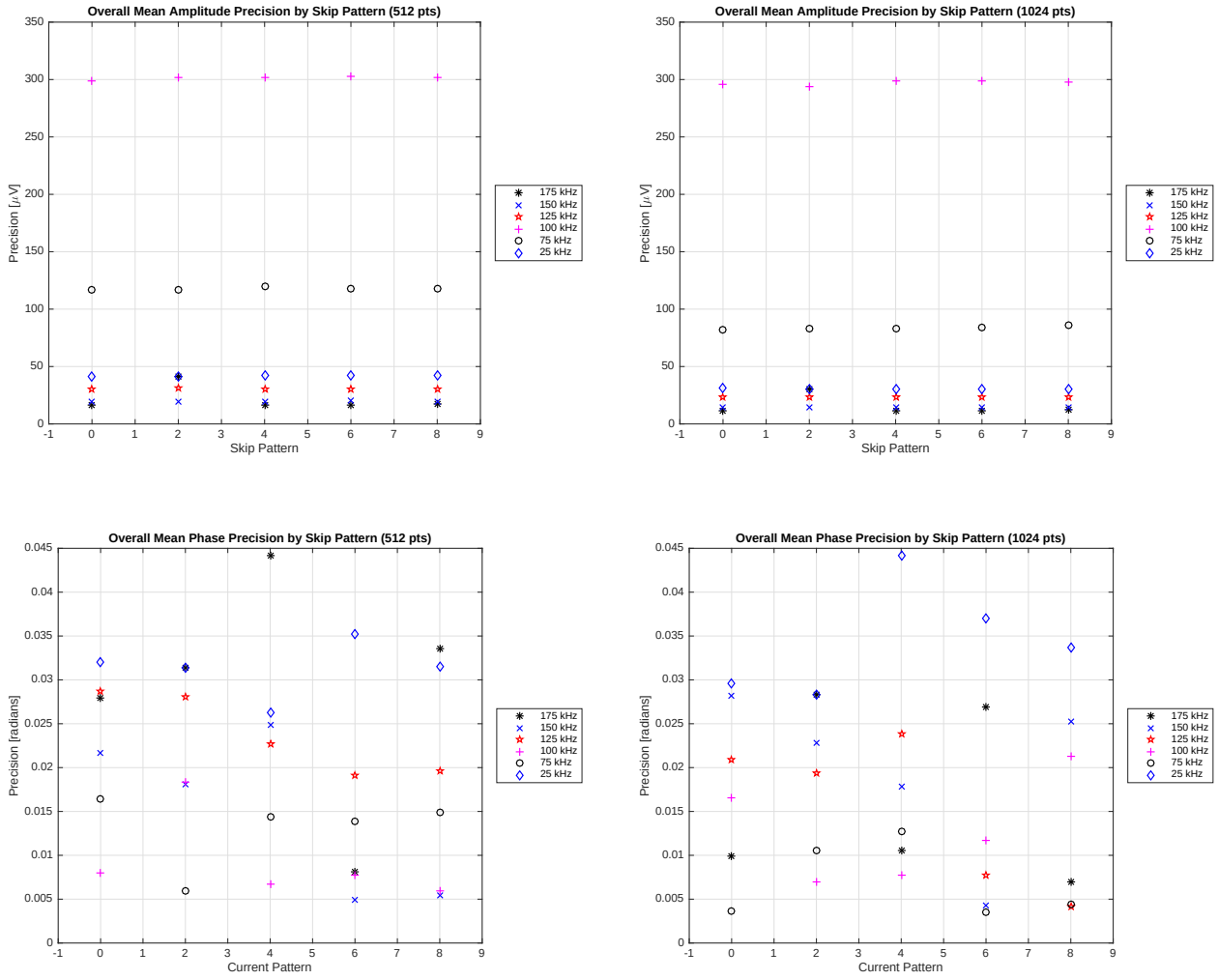

Figure 4.15. Overall mean precision for amplitude $(P_{pk})_{mean}$ (top row) and phase $(P_{\theta})_{mean}$ (bottom row) for different skip patterns and frequencies taken at the 512 acqusition rate (left) and 1024 acquisition rate (right).

4.3.2.1. *Relative Precision.* It is common to report the relative or percent precision, so relative amplitude and relative phase precision were calculated for V_{pk} and V_{θ} measurements. Equations (4.24) to (4.26) were used to calculate relative amplitude precision, which are relative measures of system precision. Similarly, Equations (4.27) to (4.30) were used to calculate relative phase precision. Smaller calculated percentages indicate better system performance. ${}^{k}_{l}\%P_{pk}$ and ${}^{k}_{l}\%P_{\theta}$ results are given in Appendix B. Overall mean relative amplitude precision ($\%(P_{pk})_{mean}$) and overall mean phase precision ($\%(P_{\theta})_{mean}$) results follow in this section.

$$ {}^{k}_{l}\%P_{pk} = \frac{{}^{k}_{l}V_{pk}(f) - {}^{k}_{l}V_{pk}}{{}^{k}_{l}V_{pk}} \text{ for } \begin{cases} l,k = 1,2,...L \\ f = 1,2,...F \end{cases} \tag{4.24} $$

where:

$$ {}^{k}_{l}V_{pk} = \frac{\sum_{f=1}^{F} {}^{k}_{l}V_{pk}(f)}{F} $$

$$ {}^{mean}_{l}\%P_{pk} = \frac{\sum_{k=1}^{L} {}^{k}_{l}\%P_{pk}}{L} \text{ for } l = 1,2,...L \tag{4.25} $$

$$ \%(P_{pk})_{mean} = \frac{\sum_{l=1}^{L} {}^{mean}_{l}\%P_{pk}}{L} \tag{4.26} $$

$$ {}^{k}_{l}\%P_{\theta}(f) = \frac{{}^{k}_{l}V_{\theta}(f) - {}^{k}_{mean}V_{\theta}(f)}{{}^{k}_{mean}V_{\theta}(f)} \text{ for } \begin{cases} l,k = 1,2,...L \\ f = 1,2,...F \end{cases} \tag{4.27} $$

where:

$$V_{\theta}{}^{k}_{mean}(f) = \frac{\sum_{l=1}^{L} V_{\theta}{}^{k}_{l}(f)}{L}$$

$$\%P_{\theta}{}^{k}_{l} = \frac{\sum_{f=1}^{F} \%P_{\theta}{}^{k}_{l}(f)}{F} \text{ for } l, k = 1, 2, ...L \tag{4.28}$$

$$\%P_{\theta}{}^{mean}_{l} = \frac{\sum_{k=1}^{L} \%P_{\theta}{}^{k}_{l}}{L} \text{ for } l = 1, 2, ...L \tag{4.29}$$

$$\%(P_{\theta})_{mean} = \frac{\sum_{l=1}^{L} \%P_{\theta}{}^{mean}_{l}}{L} \tag{4.30}$$

Overall percent or relative amplitude and phase precision are given in Figure 4.16. In general, both the percent or relative amplitude and phase precision values were not influenced by changing between the 512 point and 1024 point acquisition rates.

Overall mean amplitude precision was influenced by frequency. 100 kHz was the poorest performing and was only precise to approximately 1.1% (340 μV). 125 kHz, 150 kHz and 175 kHz are precise to less than 0.02 % (27 μV). Overall mean amplitude precision in Figure 4.16 was also reported in Table 4.1. Section 5.2 presents fast Fourier transform (FFT) results and better explains differences between chosen frequencies.

Overall mean phase precision was not greatly influenced by frequency, but for many skip patterns, 25 kHz was the least precise. All frequencies were precise with respect to phase to less than 1.6 % (2.6 degrees) many skip patterns were further precise to less than 1.0 % (1.5 degrees). These results suggest that 125 kHz to 175 kHz are the best choices of tested

frequencies to ensure that precision of voltage measurements is the highest. Relative phase precision is also reported in Table 4.2.

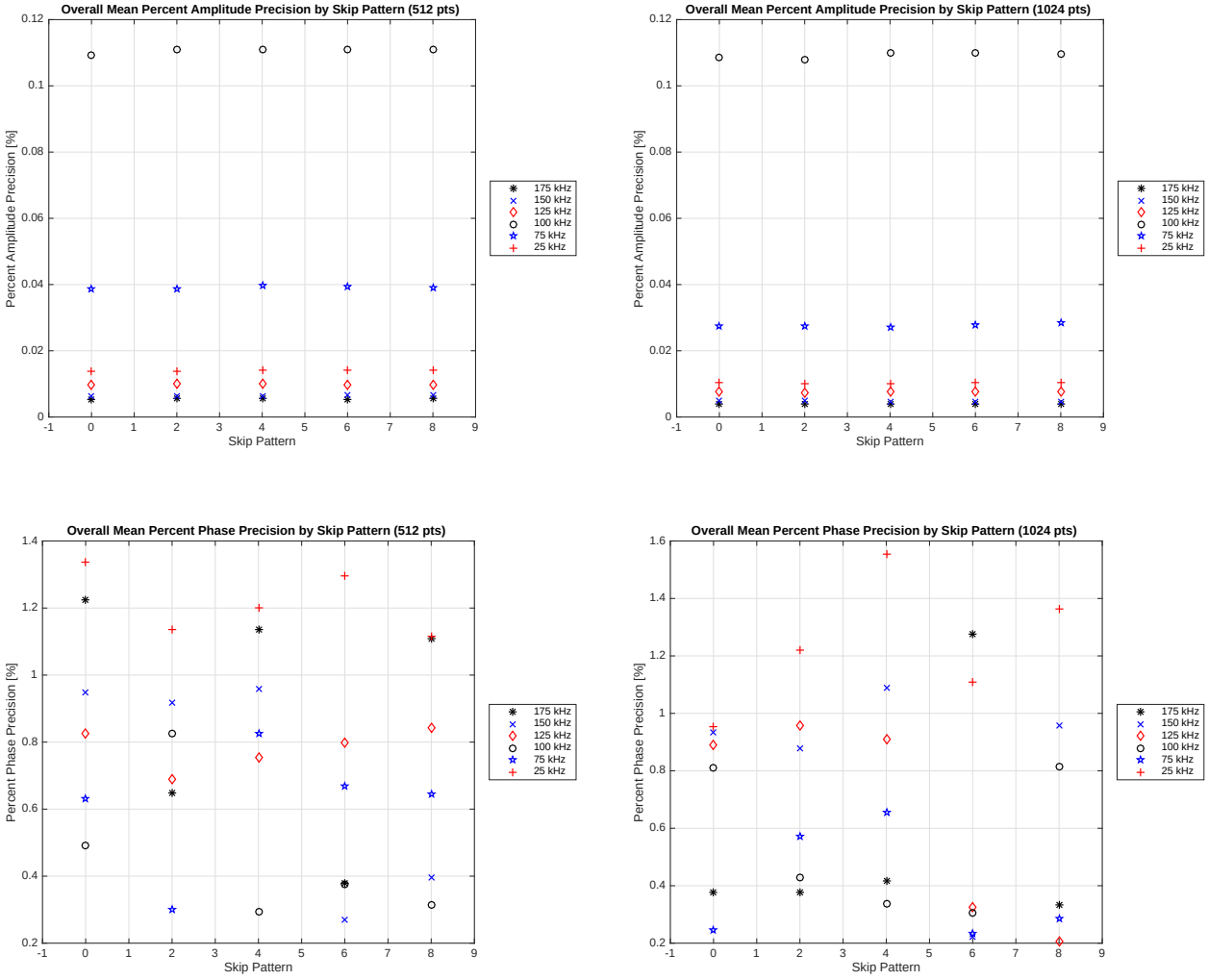

Figure 4.16. Overall percent mean precision for amplitude $\%(P_{pk})_{mean}$ (top row) and phase Percent $\%(P_{\theta})_{mean}$ (bottom row) for different skip patterns and frequencies taken at the 512 acqusition rate (left) and 1024 acquisition rate (right).

4.3.3. Accuracy. The accuracy of a measurement is determined by the difference between the measured quantity and the true value [89]. The true value in these experiments is accepted to be the Stanford Research System DS360 ultra low distortion function generator settings since the device is NIST traceable. In EIT, the accuracy (A) of measured

values is not essential for creating difference images, but it is important for absolute image reconstruction.

Accuracy of voltage amplitude measurements (${A_{pk}}_l^k$) can be calculated, since the in the test shown in Figure 4.12, the applied voltage amplitude was known. 0.125 V_{pk}, 0.25 V_{pk} and 0.375 V_{pk} applied voltages were taken to be the true value. Data for the different voltages was acquired at the 512 point acquisition rate, and 0.25 V_{pk} was additionally acquired at the 1024 point acquisition rate. Since the phase of the applied voltages was not controlled, phase accuracy cannot be calculated.

${A_{pk}}_l^k$ for each electrode (l) during each current pattern (k) is taken as the mean over all frames (F), described by Equation (4.31). The mean amplitude accuracy for each electrode over all current patterns (${A_{pk}}_l^{mean}$) and the overall mean amplitude accuracy ($(A_{pk})_{mean}$), are given by Equation (4.32) and Equation (4.33), respectively.

$$ {A_{pk}}_l^k = \text{mean}({V_{pk}}_l^k(f)), \text{ for } l,k = 1,2,...L \tag{4.31} $$

$$ {A_{pk}}_l^{mean} = \frac{\sum_{k=1}^{L} {A_{pk}}_l^k}{L}, \text{ for } l = 1,2,...L \tag{4.32} $$

$$ (A_{pk})_{mean} = \frac{\sum_{l=1}^{L} {A_{pk}}_l^{mean}}{L} \tag{4.33} $$

Figures 4.17 to 4.18 plot both accuracy (${A_{pk}}_l^k$) and precision (${P_{pk}}_l^k$) of voltage amplitude measurements at the 512 point and 1024 point acquisition rates, respectively. The amplitude accuracy is dependent on frequency and current pattern. 100 kHz measurements are the most accurate, despite having the largest corresponding standard deviation or precision. For 125 kHz, 150 kHz and 175 kHz, the accuracy increases slightly on injecting electrodes.

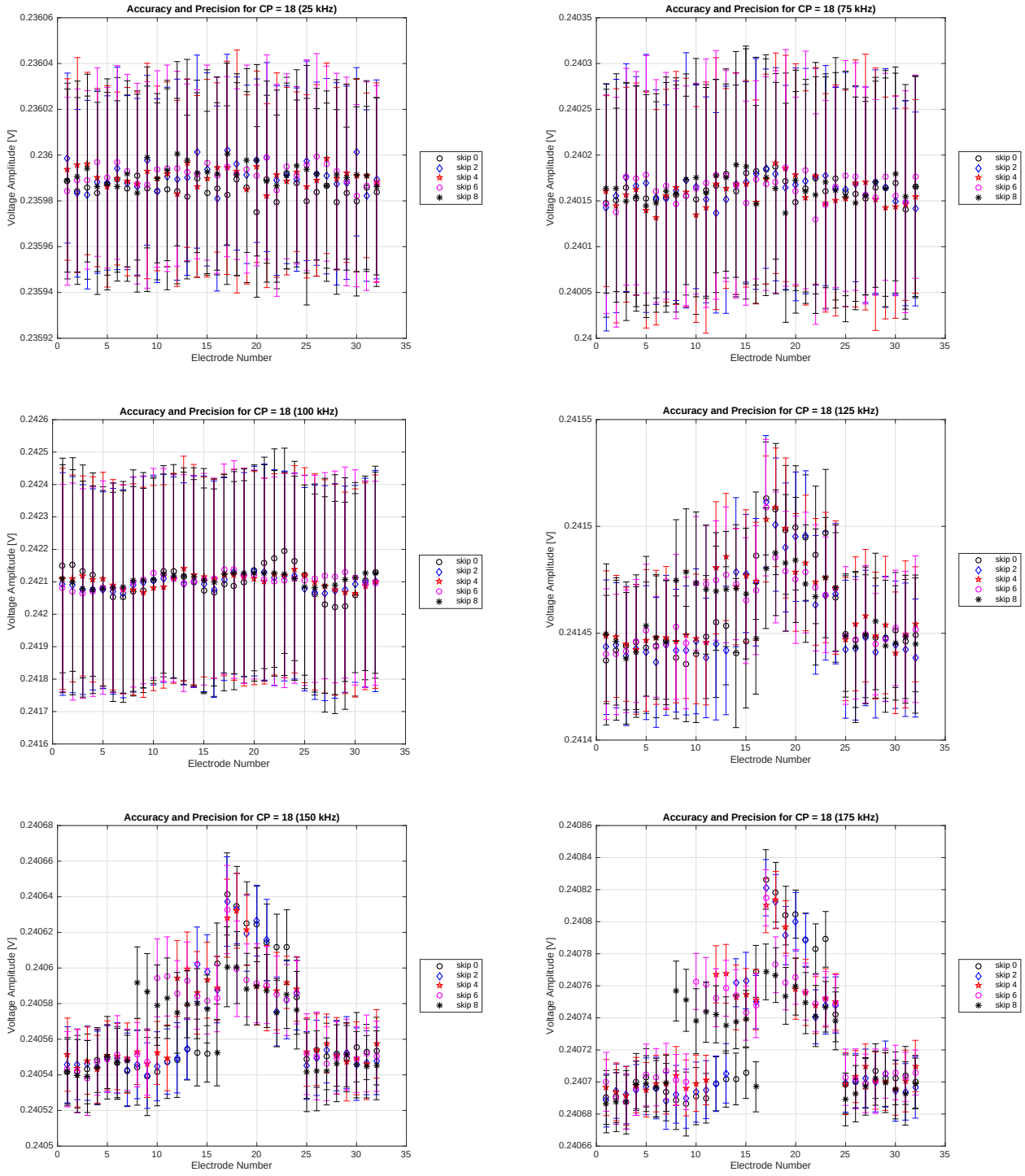

Figure 4.17. Accuracy and precision of voltage amplitude measurements for a representative current pattern ($k = 18$) for a dataset taken at the 512 acquisition rate for a 0.25 V_{peak} applied voltage.

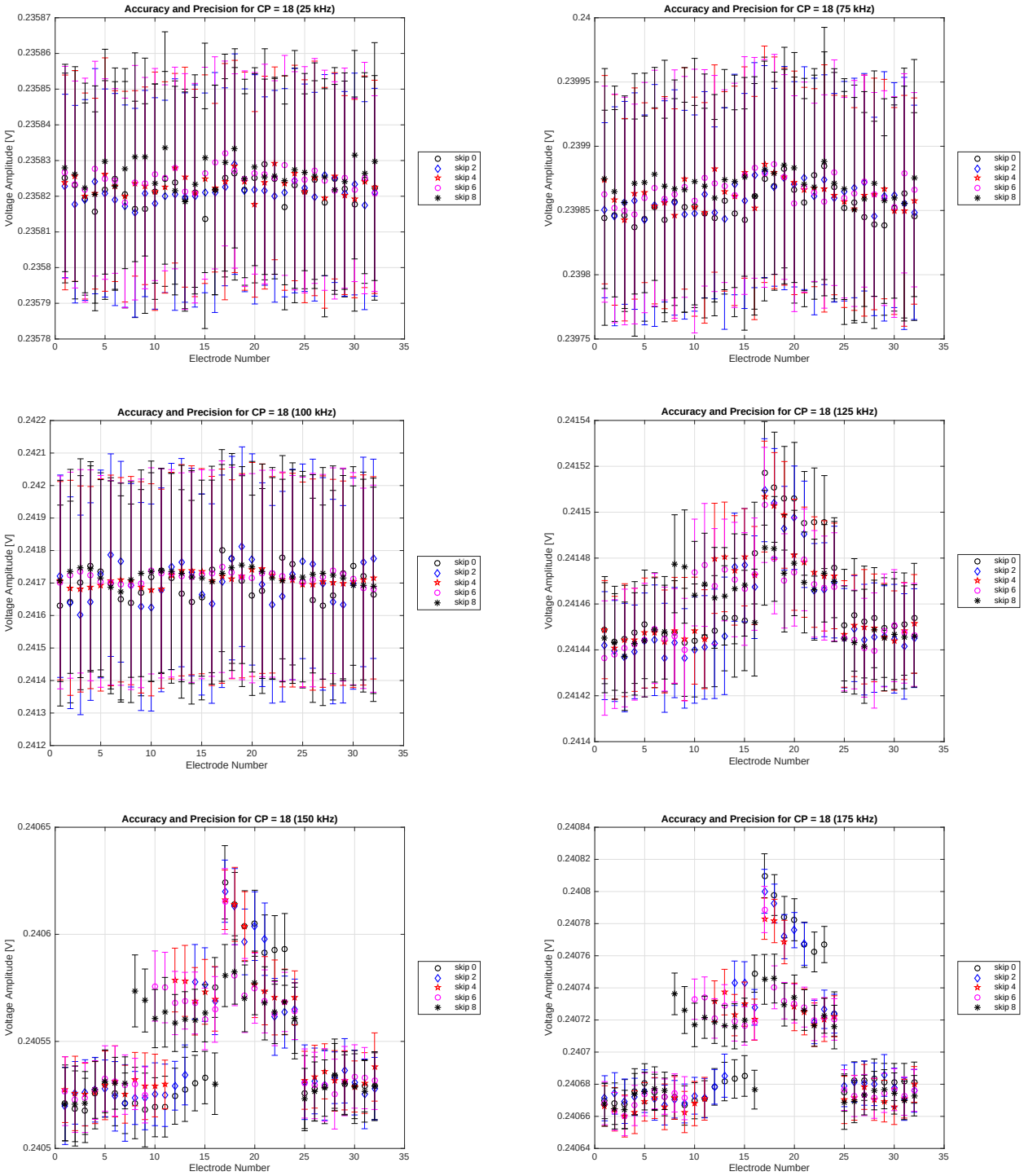

Figure 4.18. Accuracy and precision of voltage amplitude measurements for a representative current pattern ($k = 18$) for a dataset taken at the 1024 acquisition rate for a 0.25 V_{peak} applied voltage.

4.3.3.1. *Relative Accuracy.* Relative or percent accuracy is often preferred to report how close measurements are to the true value. Relative amplitude accuracy is given by Equations (4.34) - (4.37). It can be calculated for each measurement (${\%A_{pk_l}}^k(f)$) using Equation (4.34). Overall mean amplitude accuracy (${\%(A_{pk})}_{mean}$) is given by Equation (4.37) and results are shown in Figures 4.19 to 4.20.

$$(4.34) \qquad {\%A_{pk_l}}^k(f) = 1 - \frac{|{V_{pk_l}}^k(f) - V_{pk_{applied}}|}{V_{pk_{applied}}} \text{ x } 100 \text{ for } \begin{cases} l,k = 1,2,...L \\ \\ f = 1,2,...F \end{cases}$$

$$(4.35) \qquad {\%A_{pk_l}}^k = \frac{\sum_{f=1}^{F} {\%A_{pk_l}}^k(f)}{F}, \text{ for } l,k = 1,2,...L$$

$$(4.36) \qquad {\%A_{pk_l}}^{mean} = \frac{\sum_{k=1}^{L} {\%A_{pk_l}}^k}{L}, \text{ for } l = 1,2,...L$$

$$(4.37) \qquad {\%(A_{pk})}_{mean} = \frac{\sum_{l=1}^{L} {\%A_{pk_l}}^{mean}}{L}$$

Overall mean percent amplitude accuracy (${\%(A_{pk})}_{mean}$) in Figure 4.19 and Figure 4.20 reveal similar results to Figure 4.18. 100 kHz measurements are the most accurate, despite having the largest corresponding standard deviation or precision. 125 kHz is approximately 0.3% less accurate than 100 kHz, but it has much better precision. Therefore, 125 kHz is recommended to achieve both high accuracy and precision. Additionally, ${\%(A_{pk})}_{mean}$ is mostly independent of acquisition rate and skip pattern, as shown in Figure 4.20. 75 kHz and 100 kHz overall mean percent amplitude accuracy values increase by approximately 0.1%, but other tested frequencies are unchanged. Similar results were achieved for the different

applied voltages. Figure 4.19 shows changes less than 0.1% between each test for the tested frequencies.

4.3.4. Reproducibility. The reproducibility of data is a better threshold for determining the consistency with which output voltages can be measured for a given input. Webster defines the reproducibility or repeatability of a system as the ability to measure the same output for the same input over a period of time [89]. Results from the previous subsections reveal that accuracy and precision are largely influenced by frequency and slightly influenced by channel number, current pattern and skip pattern. Measures of reproducibility would take into account the geometry and layout of the ACE1 system, variations in contact impedance for each channel, source performance and precision of measurements. Reproducibility experiments were performed on a homogeneous tank phantom, shown in Figure 4.10. 250 frames of data was collected for a variety of acquisition rates.

Figure 4.21 shows plots of a single standard deviation of voltage measurements on each electrode during a single current pattern averaged over all frames. The precision with which voltage amplitudes are reproducible was calculated with Equation (4.18). Reproducibility in this sense varies based on frequency. At 75 kHz, the reproducibility of voltage amplitude measurements (R_{pk}) is approximately twice as large (or two times less reproducible) when compared to 125 kHz. At the 1024 point acquisition rate, the mean reproducibility over all electrodes and all current patterns is 126 μV at 75 kHz and 55 μV at 125 kHz. This is consistent with results found in Section 4.3.2. Additionally, Figure 4.21 shows that the reproducibility improves as acquisition rate increases. Increasing the acquisition rate from 256 points to 1024 points approximately doubles the reproduciblity for both frequencies.

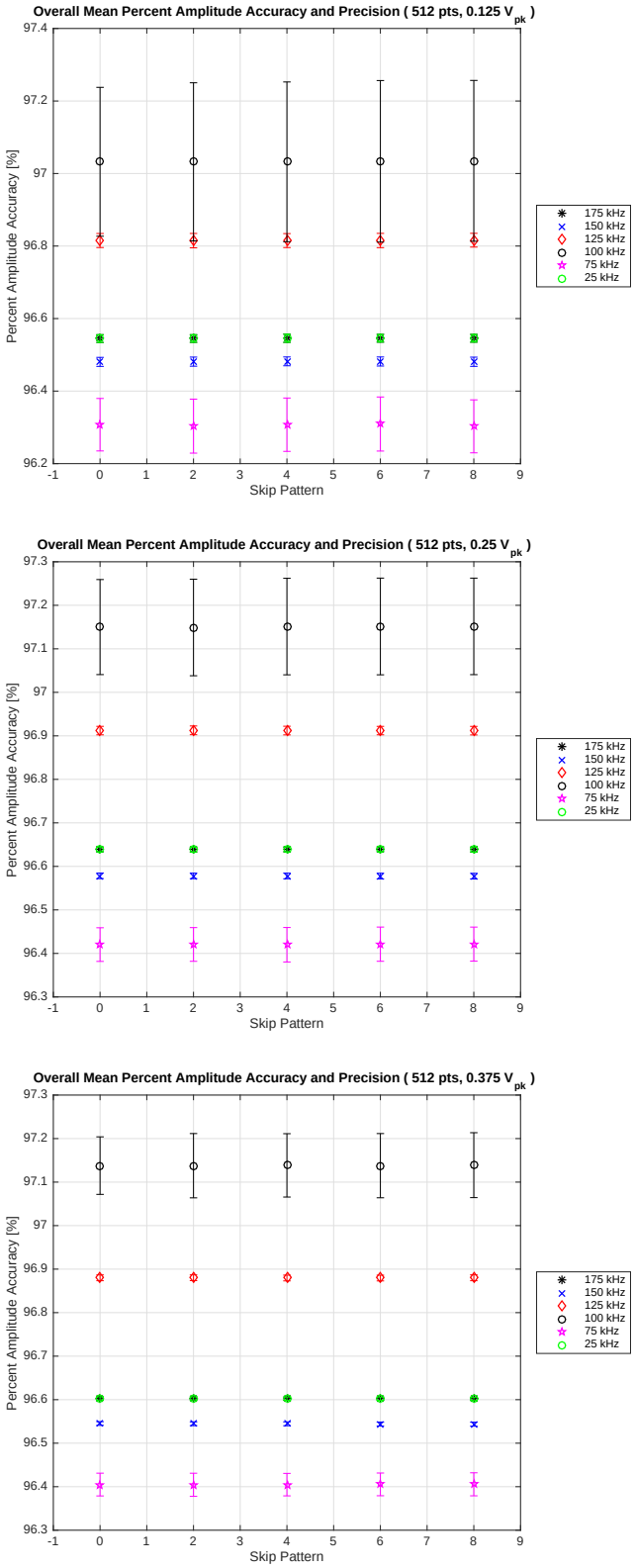

Figure 4.19. Overall mean percent amplitude accuracy and precision for the 512 point acquisition from 100 frames of data measuring a 0.125 V_{pk}, 0.25 V_{pk} and 0.375 V_{pk} applied voltage.

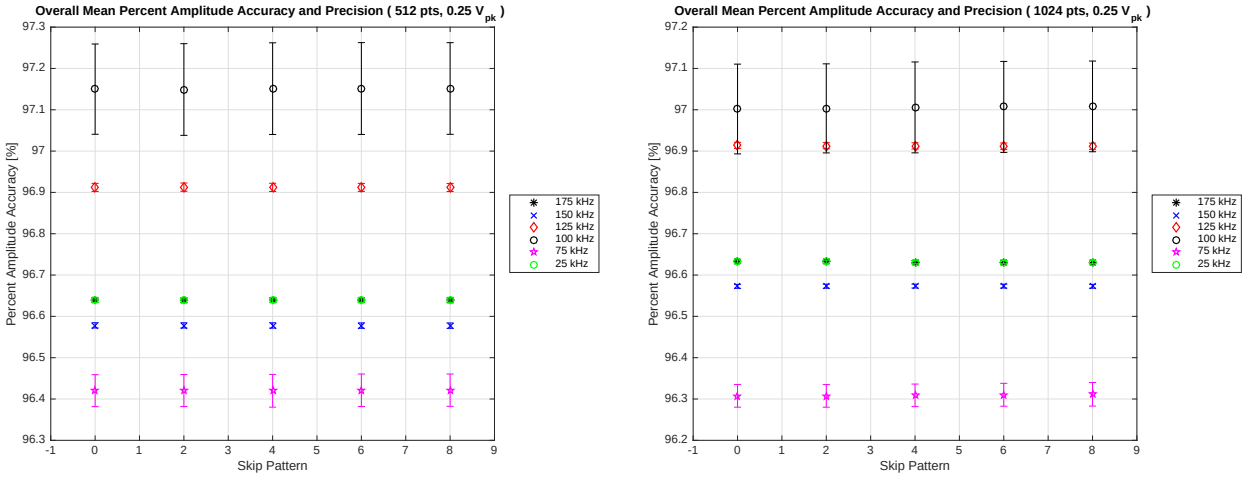

Figure 4.20. Overall mean percent amplitude accuracy and precision for the 512 point (left) and 1024 point acquisition rate (right) from 100 frames of data measuring a 0.25 V_{pk} applied voltage.

Overall mean amplitude reproducibility and mean percent amplitude reproducibility, shown in Figure 4.22, were calculated using Equation (4.20) and Equation (4.26), respectively. Results shown in this figure are used to determine a threshold for distinguishability experiments in Section 4.4. If time resolution is not a concern, Figure 4.22 would suggest that the 1024 point acquisition rate is the best choice.

Since the phase of voltage measurements on each electrode differs during each current pattern and each frame, to determine phase reproducibility (R_θ), a reference phase was needed. The shifting of phases is described by Equation (4.39), which sets the leading injection electrode ($l = k$) to $\pi/2$ for each current pattern (k) in each frame (f) and shifts the measurement on each electrode (l) accordingly. Phase reproducibility can be calculated similarly to P_{pk} which was used to calculate R_{pk}. Phase reproducibility is described by Equations (4.38) - (4.41). Percent phase reproducibility is given by Equations (4.42) - (4.45).

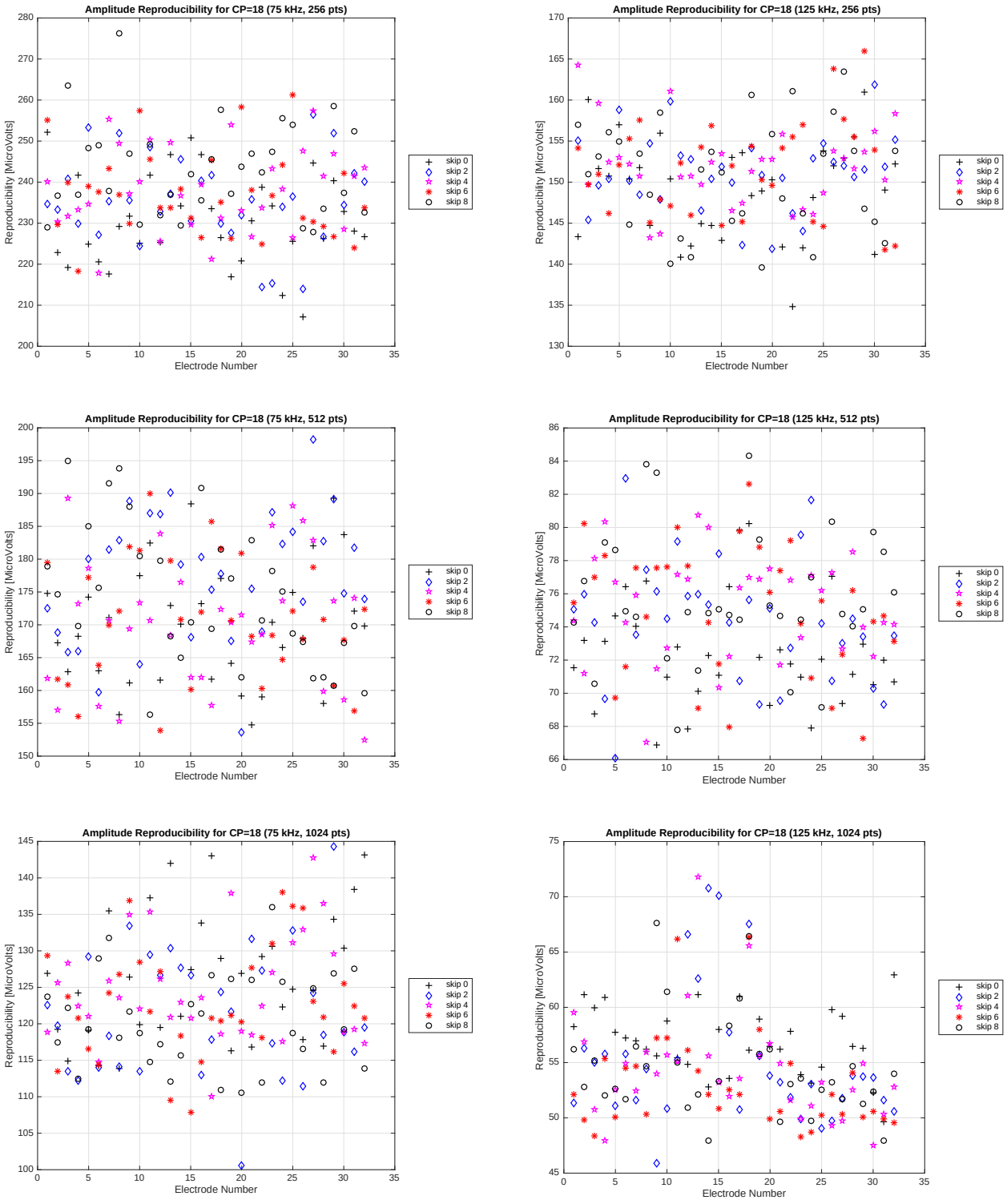

Figure 4.21. Reproducibility of homogeneous tank data voltage amplitude measurements at different frame rates is shown for 75 kHz (left) and 125 kHz (right). Data was also taken at a different acquisition rates: 256 points (row 1), 512 points (row 2) and 1024 points (row 3).

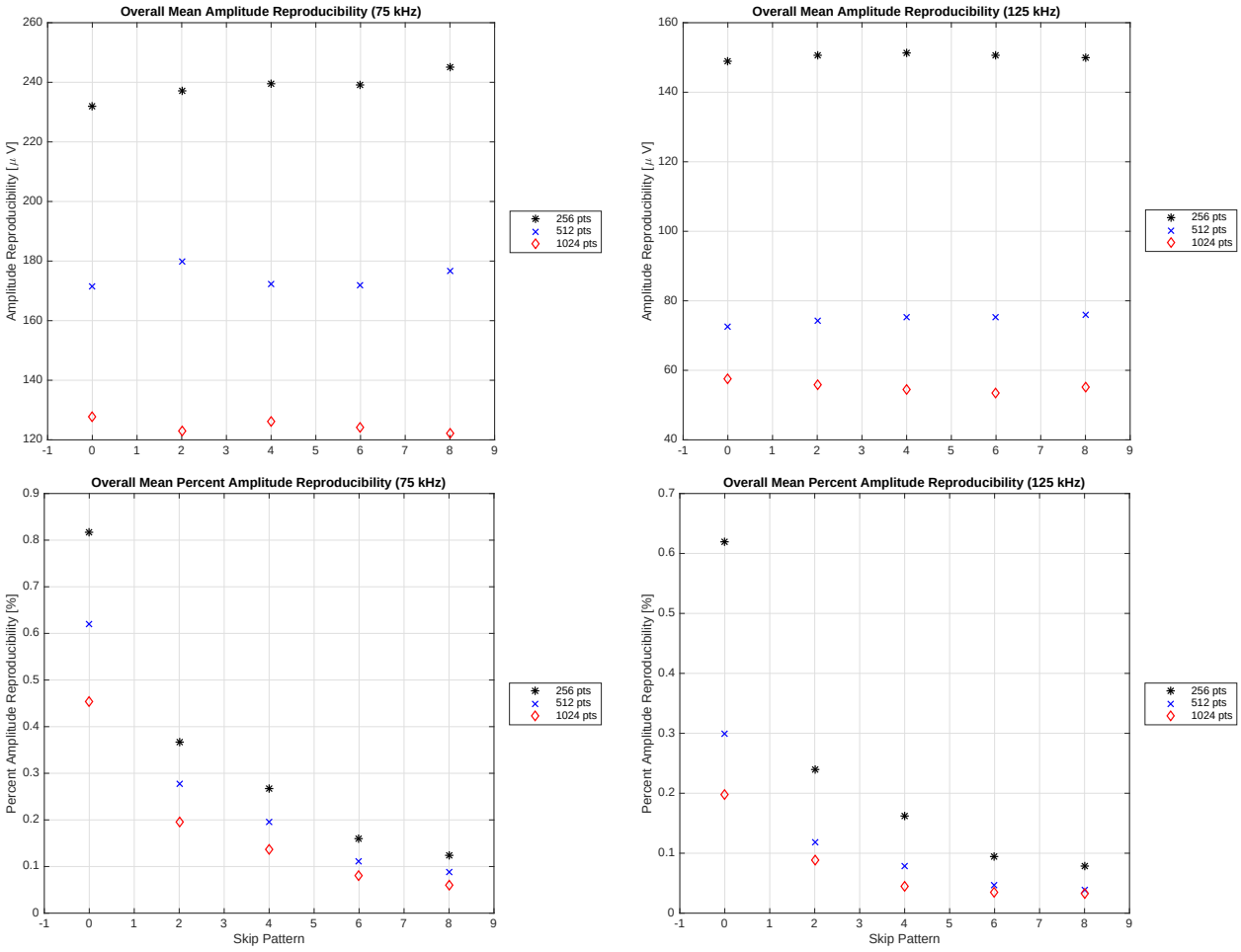

Figure 4.22. Overall mean amplitude reproducibility (top row) and overall mean percent amplitude reproducibility (bottom row) of different skip patterns for 75 kHz (left) and 125 kHz (right) for the 256 point, 512 point and 1024 point acquisition rates.

$$R_{\theta_l}^{k} = \text{std}(V_{\theta' l}^{k}(f)), \text{ for } l, k = 1, 2, ...L \tag{4.38}$$

where:

$$V_{\theta' l}^{k}(f) = V_{\theta l}^{k}(f) - V_{\theta k}^{k}(f) + \pi/2 \tag{4.39}$$

$$R_{\theta_l}^{mean} = \frac{\sum_{k=1}^{L} {P_{pk}}_l^k}{L} \tag{4.40}$$

$$(R_\theta)_{mean} = \frac{\sum_{l=1}^{L} {P_{pk}}_l^{mean}}{L} \tag{4.41}$$

$$\%R_{\theta_l}^k = \frac{{V_{\theta'}}_l^k(f) - {V_{\theta'}}_l^k}{{V_{\theta'}}_l^k} \text{ for } \begin{cases} l, k = 1, 2, ...L \\ \\ f = 1, 2, ...F \end{cases} \tag{4.42}$$

where:

$${V_{\theta'}}_l^k = \frac{\sum_{f=1}^{F} {V_{\theta'}}_l^k(f)}{F} \tag{4.43}$$

$$\%R_{\theta_l}^{mean} = \frac{\sum_{k=1}^{L} \%R_{\theta_l}^k}{L} \text{ for } l = 1, 2, ...L \tag{4.44}$$

$$\%(R_\theta)_{mean} = \frac{\sum_{l=1}^{L} \%R_{\theta_l}^{mean}}{L} \tag{4.45}$$

Figure 4.23 plots phase reproducibility in radians. Reproducibility of phase measurements is highly dependent upon current pattern. Figure 4.24 plots percent phase reproducibility for different current patterns. Reproducibilty is high near injection electrodes. One standard deviation, used to define phase reproducibility, can be as great as 1 one radian or 45 to 55% when approximately 10 to 16 electrodes away from injecting electrodes. Reproducibility of phase is slightly better at 75 kHz compared to 125 kHz and is not greatly influenced by acquisition rate.

Figure 4.25 and Figure 4.26 plot phase reproducibility for each skip pattern at the three different acquisition rates (256 points, 512 points and 1024 points). Skip 0 and skip 2 have worse phase reproducibilty overall when compared to skip patterns 6 and 8. This likely related to the poor signal-to-noise ratio as one moves further from the injection electrodes, which if further discussed in Section 5.1.

Plots of overall mean and overall mean percent phase reproducibility, shown in Figure 4.27, are slightly misleading since reproducibility of phase measurements depends on proximity to injecting electrodes. Plotted values and percentages represent the minimum mean phase shift that is required to reproducibily measure a change associated with the domain. However, Figure 4.24 might suggest that changes less than 2.5% or 0.05 to 0.1 radians could reliably be reproduced, but not on all electrodes during all current patterns. It is likely that phase reproducilibity is influenced by stray capacitance present at the active electrodes, which is supported by better results at 75 kHz when compared to 125 kHz.

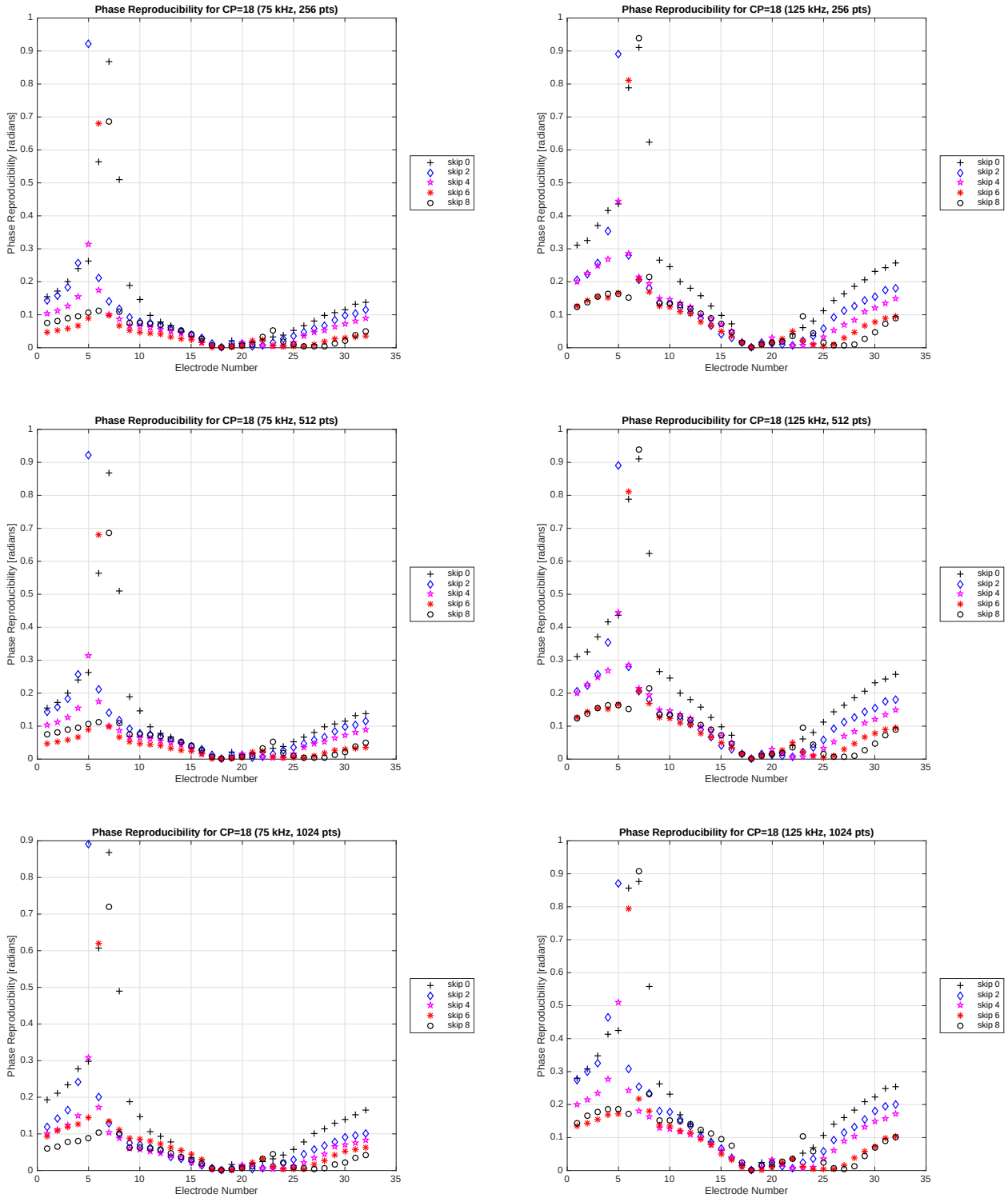

Figure 4.23. Reproducibility of homogeneous tank data voltage phase measurements is shown for 75 kHz (left) and 125 kHz (right). Data was also taken at a different acquisition rates: 256 points (row 1), 512 points (row 2) and 1024 points (row 3).

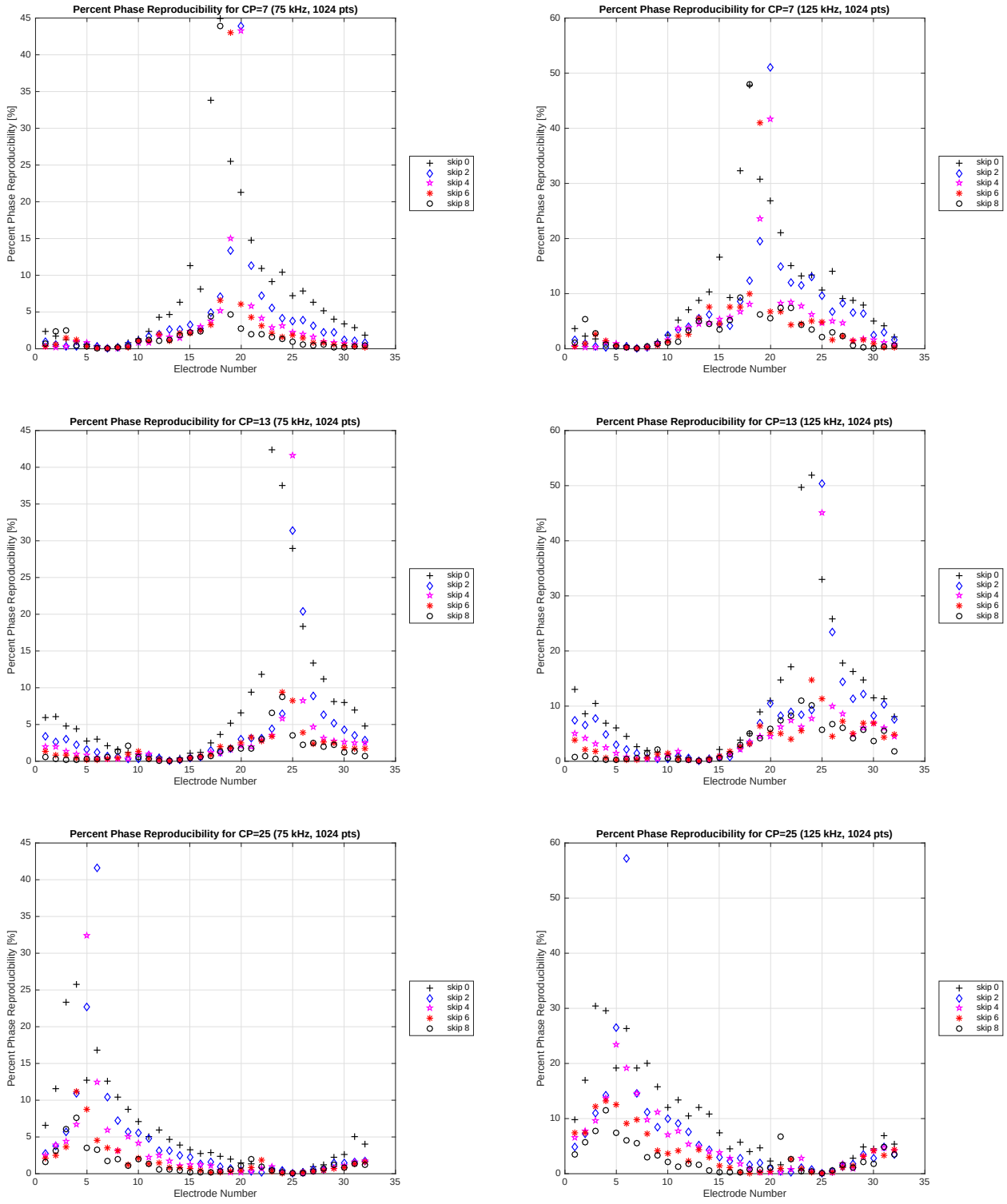

Figure 4.24. Percent phase reproducibility for homogeneous tank data taken at the at the 1024 point acquisition rate is shown for 75 kHz (left) and 125 kHz (right) for three different current patterns: 7 (row 1), 13 (row 2), 25 (row 3).

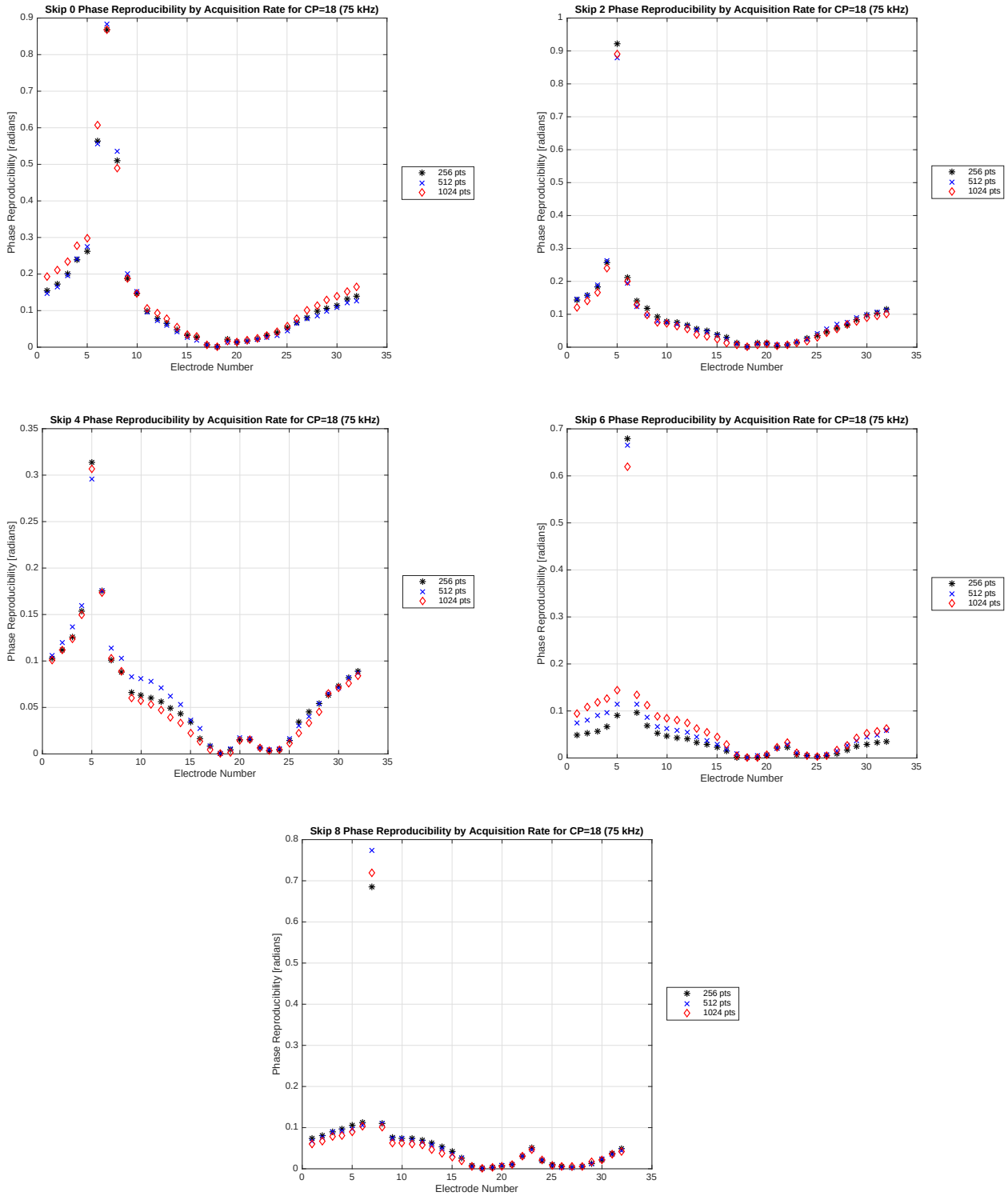

Figure 4.25. Phase reproducibility is radians at 75 kHz is shown for the different acquisition rates for skip patterns: 0, 2, 4, 6, and 8.

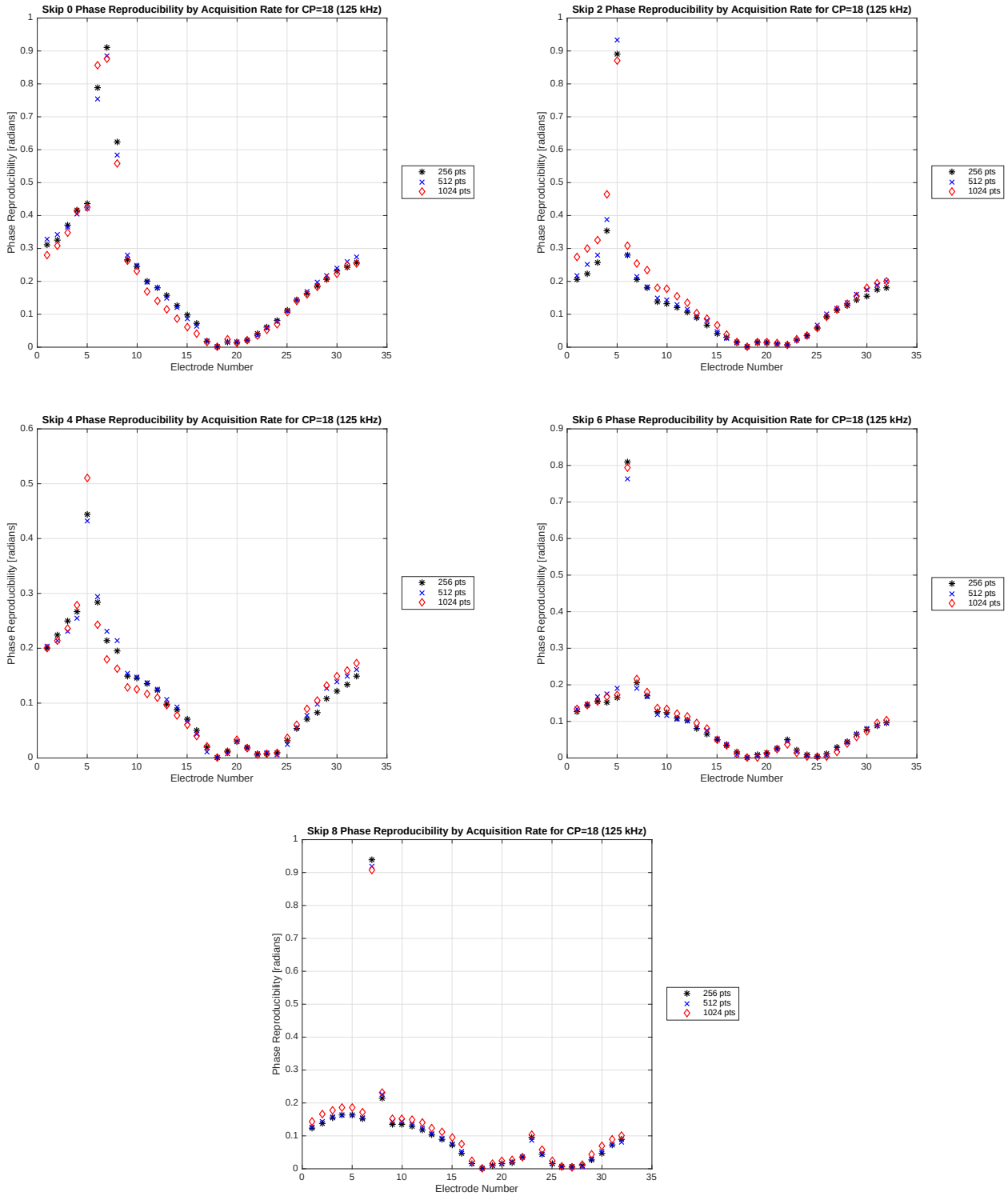

Figure 4.26. Phase reproducibility is radians at 125 kHz is shown for the different acquisition rates for skip patterns: 0, 2, 4, 6, and 8.

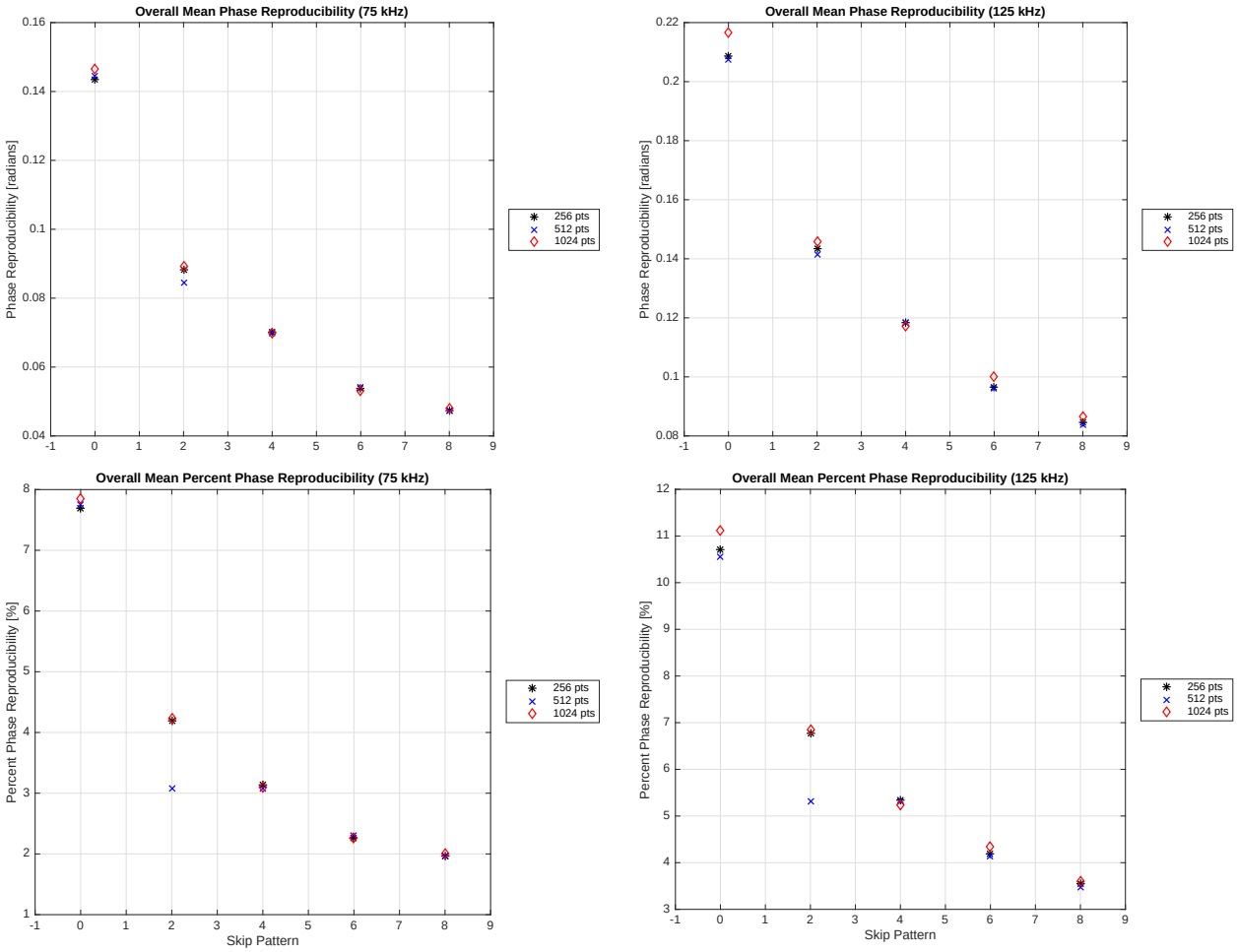

Figure 4.27. Overall mean phase reproducibility (top row) and overall mean percent phase reproducibility (bottom row) of different skip patterns for 75 kHz (left) and 125 kHz (right) for the 256 point, 512 point and 1024 point acquisition rates.

4.4. Distinguishability Experiments

The distinguishability of inhomogeneous test phantoms of various sizes can be used to demonstrate the ability of an electrical impedance tomograph to measure voltage differences when compared to a homogenous tank [12, 90, 91]. In this test of the ACE1 system, copper and plastic cylindrical targets, shown in Figure 4.28, were placed in the center the tank phantom, described in Figure 4.10. Approximately 2.4 mA of current was applied during the collection of each dataset. Each dataset was further comprised of the 51 frames taken at the 1024 point sample rate. Experiment targets were made from 1/4 in, 3/8 in, 1/2 in, and 3/4 in plastic and copper pipe. The corresponding outer diameters for the plastic targets (P1, P2, P3, P4) are: 0.95 cm, 1.3 cm, 2.2 cm, and 2.88 cm. Outer diameters for the copper targets (C1, C2, C3, C4) are: 1.1 cm, 1.45 cm, 1.8 cm and 2.45 cm.

Figure 4.28. Distinguishability experiment targets are made from 1/4 in, 3/8 in, 1/2 in, and 3/4 in plastic and copper pipe. The corresponding outer diameters for the plastic targets (P1, P2, P3, P4) are: 0.95 cm, 1.3 cm, 2.2 cm, and 2.88 cm. Outer diameters for the copper targets (C1, C2, C3, C4) are: 1.1 cm, 1.45 cm, 1.8 cm and 2.45 cm.

Distinguishability (δ) from measured voltages is given by Equation (4.46) and is defined as the difference of the mean demodulated voltage amplitudes (V_l^k) for each electrode (l) for each current pattern (k) for the homogeneous tank compared to the target [90]. The

overall mean distinguishability ($\delta V_{overall}$) in Equation (4.47) uses mean demodulated voltage amplitudes $(V)_{mean}$ which are calculated as described by Equation (4.37).

$$\delta V_l^k = V_l^k(\sigma_{target}) - V_l^k(\sigma_{hom.}) \tag{4.46}$$

$$\delta V_{overall} = (V)_{mean}(\sigma_{target}) - (V)_{mean}(\sigma_{hom.}) \tag{4.47}$$

The target is distinguishable if δV_l^k or $\delta V_{overall}$ is greater than the smallest voltage ACE1 can measure, which from Section 4.3.4, should be approximately greater than the mean reproducibility calculations. Since distinguishability experiments were performed at a variety of frequencies, two thresholds were used. For 25 to 100 kHz, approximately 150 μV was used as a threshold and approximately 70 μV for 125 to 175 kHz.

From Figures 4.29 to 4.30, a clear trend in the increased $\delta V_{overall}$ of tank phantoms is shown as skip pattern increases. Plots in these figures also show that P1 and P2 are the two phantoms which are the most difficult to distinguish from one another. Using the thresholds determined by reproduciblity, P1 and P2 can only be distinguished from one another at skip 8 for 100 kHz, at skip 6 and 8 for 125 kHz and at skip 4, 6, and 8 for 175 kHz.

Figures 4.29 to 4.30 further show that skip 0 is the worst for distinguishing differences between targets in the center. At 25 kHz, the difference between the smallest copper and plastic pipe tank phantoms is difficult to detect. For example the difference between the overall mean voltages between C1 and C2 is 0.54 mV and C1 and C3 is 0.137 mV. The differences between plastic pipe targets is less. As an example, the difference between P1 and P2 is 0.05 mV. At 25 kHz, the worst results were achieved and results would suggest it would be difficult to distinguish P1, P2, P3, C1 and C2 from one another. These results suggest

that higher skip patterns and/or increasing frequency can increase the distinguishability between conductive and insulative anomalies in the center.

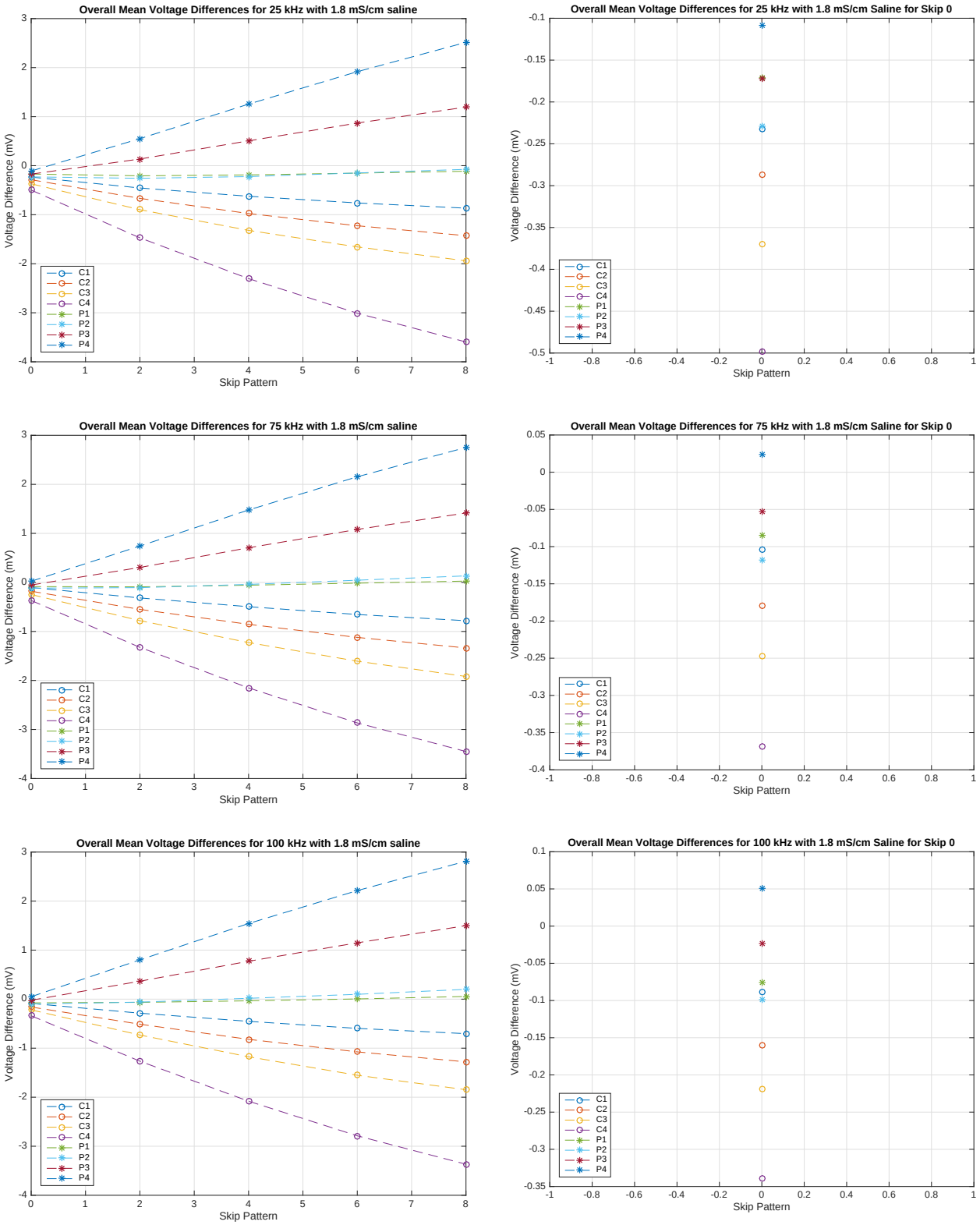

Figure 4.29. Distinguishability plots for all targets and skip patterns for frequencies (25 kHz to 100 kHz) where the overall mean calculation uses mean measured voltage over all electrodes and current patterns.

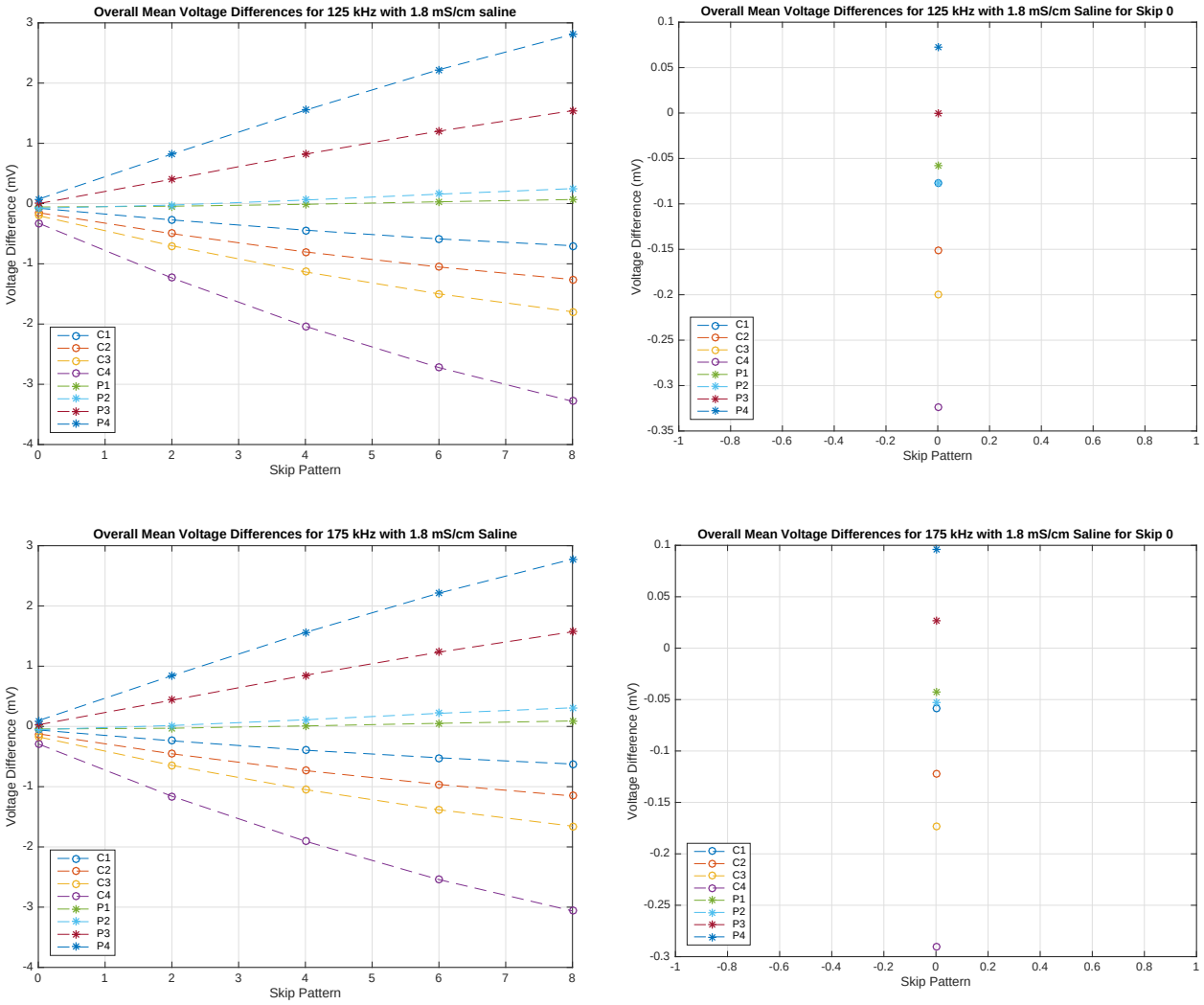

Figure 4.30. Distinguishability plots for all targets and skip patterns for frequencies (125 kHz to 175 kHz) where the overall mean calculation uses mean measured voltage over all electrodes and current patterns.

The ability to distinguish tank phantom targets from one another is not always clear by comparing the mean voltage differences or voltage differences of injection electrodes. Figure 4.31 and Figure 4.32 contain plots of mean distinguishability of a single current pattern at 125 kHz for copper pipe and plastic pipe targets, respectively. Each plot with each figure is of a different skip pattern. Both figures show that the maximum difference between targets is found on non-injection electrodes. They also show that this voltage difference associated

increases as skip pattern increases. In Appendix B Section B.2, there are additional figures of mean distinguishability of a single current pattern at shown for 25 kHz, 75 kHz, 100 kHz and 175 kHz.

From these figures, Equation (4.48) can used to describe the maximum distinguishability ($\max \delta V_l^k{}_{targets}$) between two tank phantom targets on a single electrode (l) in a single current pattern (k):

$$\max \delta V_l^k{}_{targets} = \sup \left| \left(V_l^k(\sigma_{target1}) - V_l^k(\sigma_{hom.})\right) - \left(V_l^k(\sigma_{target2}) - V_l^k(\sigma_{hom.})\right) \right| \tag{4.48}$$

The maximum difference between voltages of non-injection electrodes for a single current pattern, suggests that nearly all targets are distinguishable from one another by more than 0.15 mV. The exception is the difference between plastic target P1 and P2 at 25 kHz and skip 0, where the maximum difference is 0.1375 mV.

It is important to note that distinguishability on one or several electrodes in the system does not necessarily mean that the target will be seen in reconstructed images. In particular, many results in this dissertation suggest that larger skip patterns might be better. However, the Colorado State University EIT lab has had great success reconstructing images from datasets taken with the skip 0 current pattern. This is likely due to the fact that the areas of interest, such as the lungs and heart, are close to the exterior of the chest. Though the system is capable of resolving measurements related to changes in target diameter as small as 3.5 mm for some skip patterns, these differences would difficult to see in images due to the smoothing nature of EIT image reconstruction algorithms.

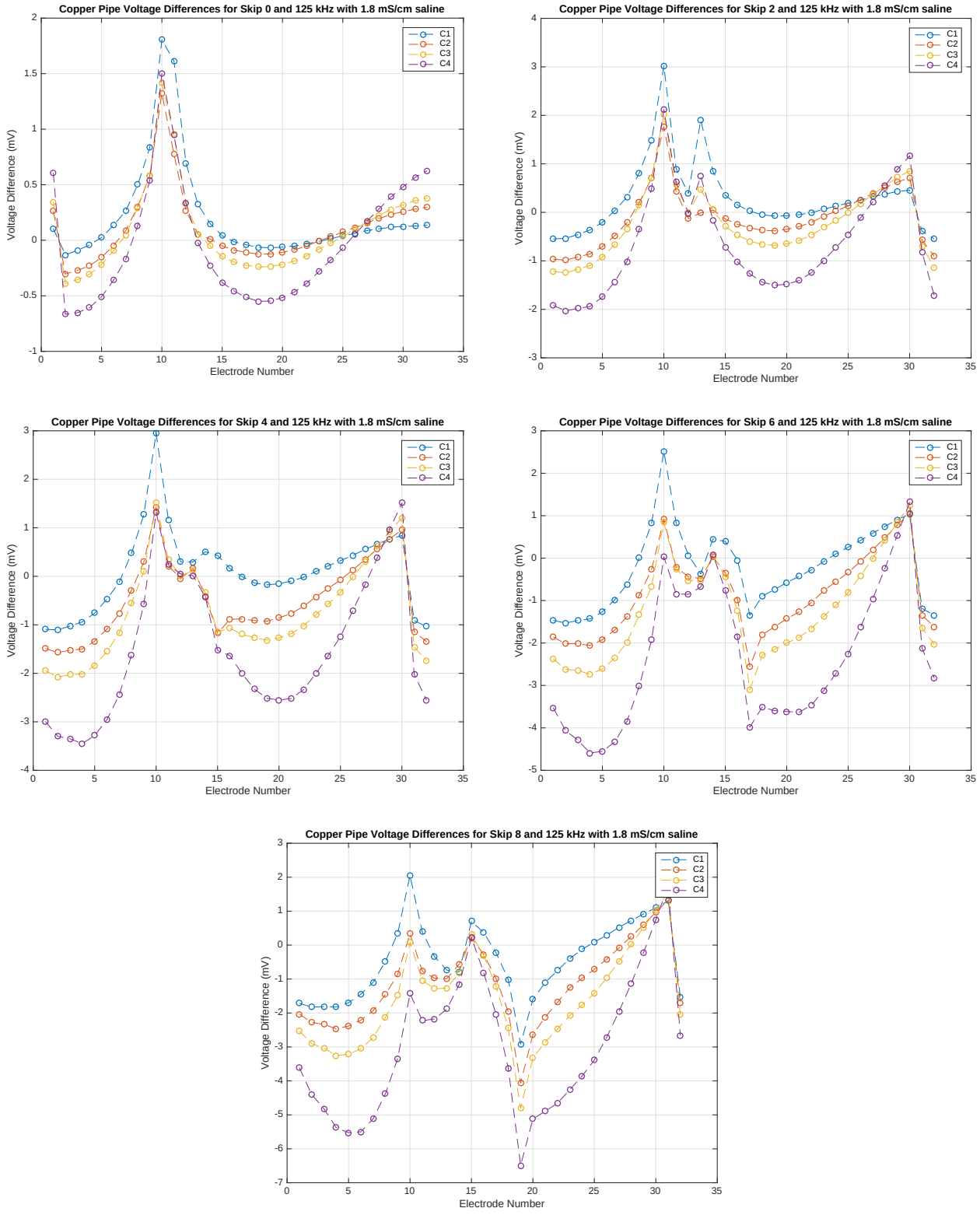

Figure 4.31. Mean distinguishability plots for data collected at 125 kHz for current pattern (k) number 10 for various skip patterns 0, 2, 4, 6, and 8 (which are the best for 32 electrodes by Equation 3.1 where C1, C2, C3 and C4 are the copper pipe tank phantom targets.

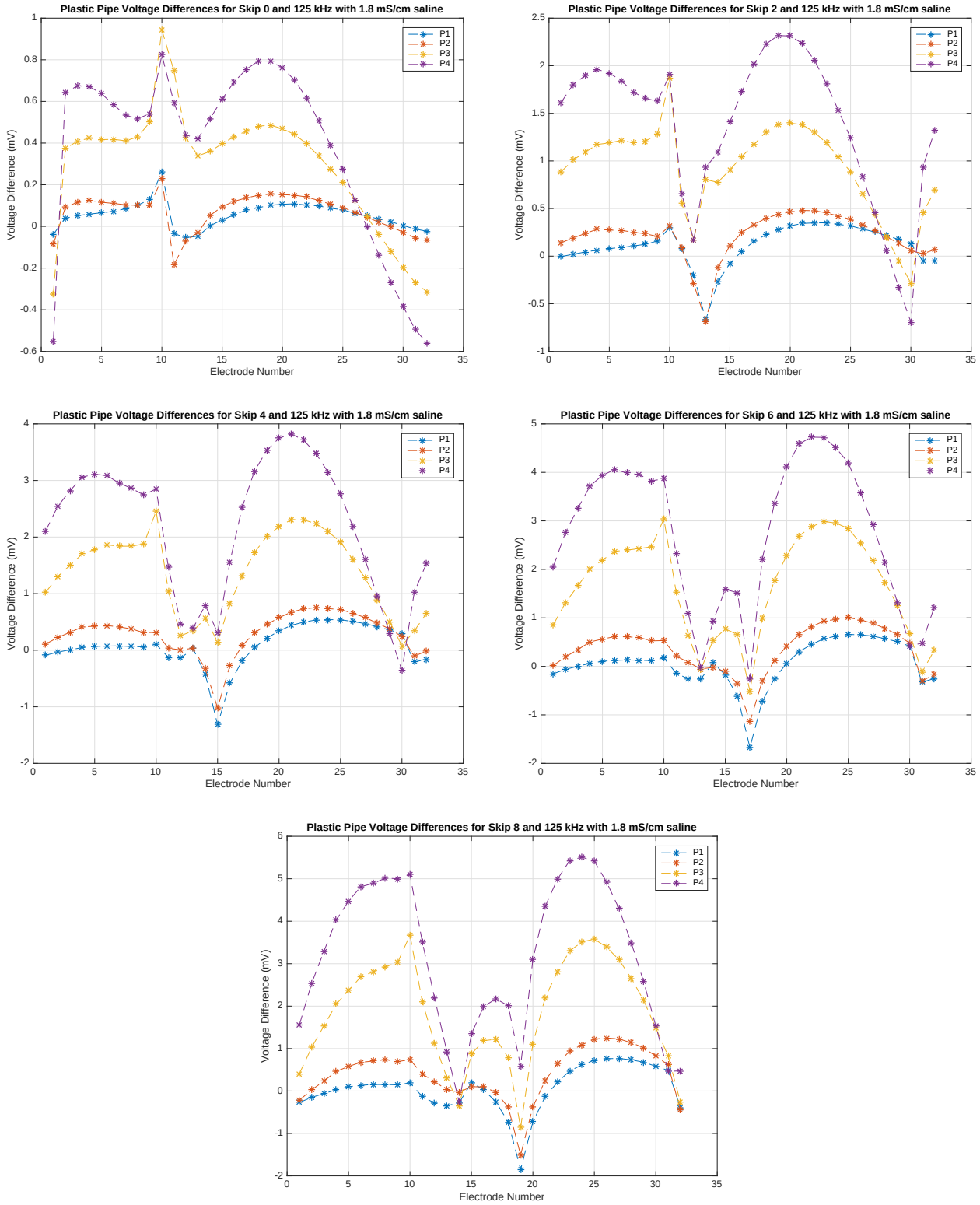

Figure 4.32. Mean distinguishability plots for data collected at 125 kHz for current pattern (k) number 10 for various skip patterns 0, 2, 4, 6, and 8 (which are the best for 32 electrodes by Equation 3.1 where P1, P2, P3 and P4 are the plastic pipe tank phantom targets.

4.5. Select Reconstructed Images from ACE1

Although not a formal test of system performance, use of the data for creating image reconstructions is informative about the usability of measured data. The data obtained from ACE1 on tank phantoms (Section 4.5.1) and human subjects (Section 4.5.2) has be used to create quality image reconstructions of conductivity and permittivity using the D-bar method.

4.5.1. Tank Phantom Images. To accurately reconstruct both conductivty and permittivty images, real and imaginary components of measured data are used. In Figure 4.33 conductivty and permittivty difference images are shown for cucumber targets in a saline filled tank. In the experiment, adjacent skip patterns were used and 50 frames of data was averaged together. Saline has no permittivity and was used as the reference image.

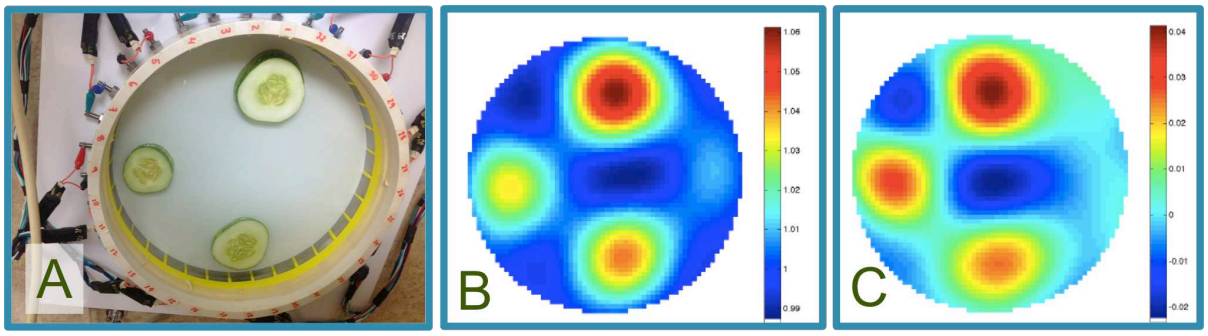

Figure 4.33. Picture A shows the experimental setup of the tank filled with saline and three cucumber phantoms. Reconstructions by Jennifer Mueller show conductivity (B) and permittivity (C).

4.5.2. Images of Healthy Human Subjects. Initial use of ACE1 in CSU Institutional Review Board (IRB) approved studies (protocol number 10-1755H) demonstrates the success of data for use in creating differences images. Data was collected with 32 electrodes and adjacent pairwise current injection (or skip 0). Reconstructions were computed using 2-D D-bar methods. Human subject images in Figure 4.34 and Figure 4.35 were computed

using the D-bar method [76]. In both figures, blue regions show areas of low conductivity (or high resistivity) and red indicates areas of high conductivity.

In Figure 4.34, perfusion or blood flow is seen in the sequential images that show regional changes in conductivity. To obtain these images, each human subject is asked to hold his/her breath for a few seconds. In the first image (located in the first column on the top row), the heart is in its contracted state (systole) and does not contain much blood. The heart fills with blood as one moves right across the top column and across the bottom row until it is full (diastole). Due to the high conductivity of blood with respect to other tissues, the filling of the heart is shown by the darkening red color located in the upper center circle (or heart) of each image. Oxygenated blood from the lungs also fills the heart and as the blood leaves the lung tissue becomes less conductive or more blue in color.

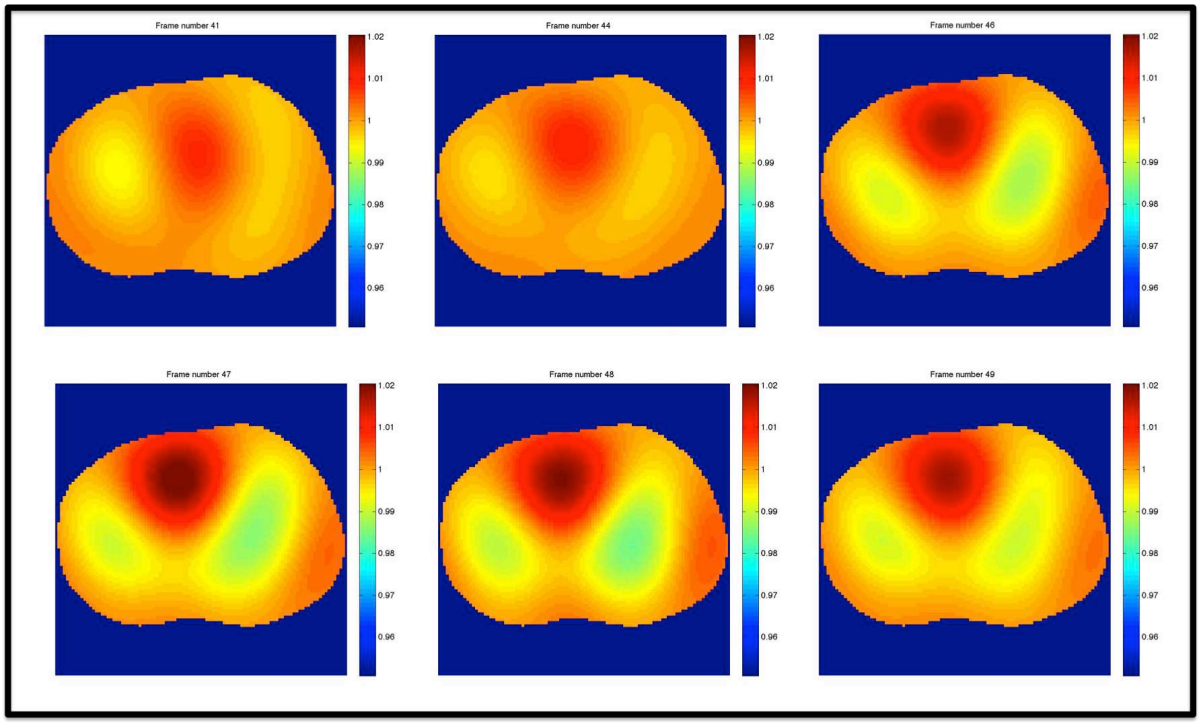

Figure 4.34. Shown are reconstructed conductivity images of the cardiac cycle in a healthy human subject by Melody Alsaker. The six sequential images show the heart moving from systole (contraction) to diastole (relaxation and filling) at 15.8 frames/sec.

In Figure 4.35, ventilation of the lungs is shown. During data acquisition for ventilation images, human subjects are asked to breath normally. Blue regions in the images indicate the presence of air in the lungs. The series of images starts with expiration in the first column in the top row. As the subject inspires, the lung conducitivity decreases which causes the lungs to appear more blue in color. As the subject exhales, the lung conducitivity increases which causes the lungs to return to the background color.

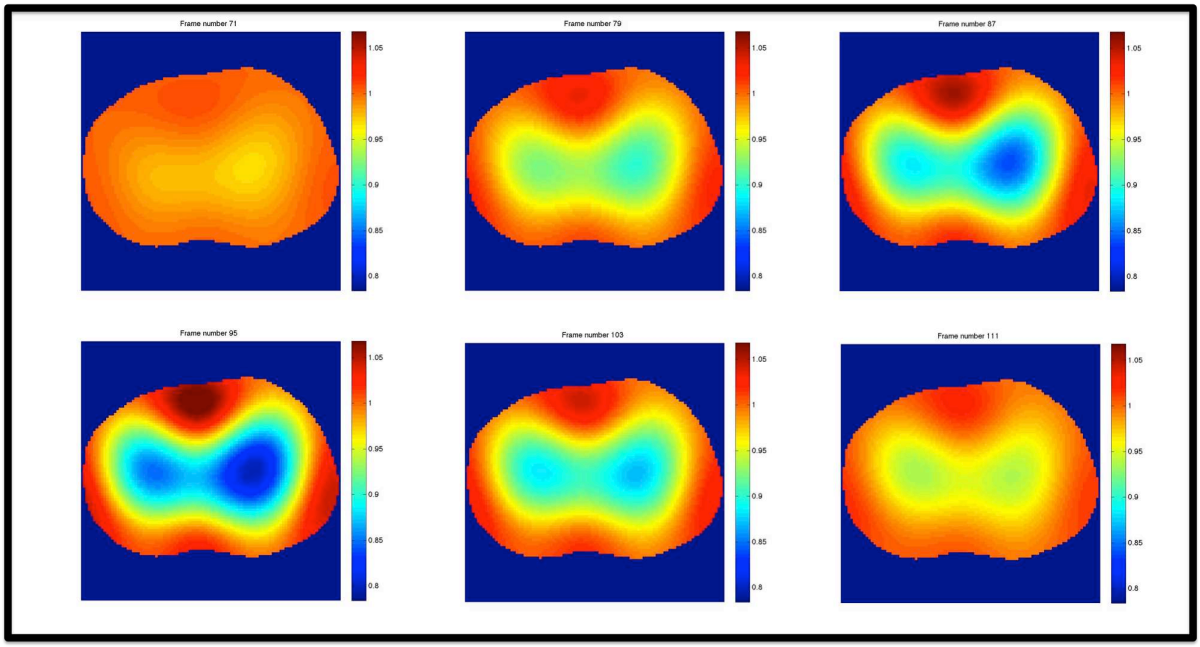

Figure 4.35. Shown are reconstructed conductivity images of tidal breathing in a healthy human subject by Melody Alsaker. The six frames show inflation from the lungs from expiration to inspiration to expiration at a frame rate of 15.8 frames/sec.

CHAPTER 5

SYSTEM TESTS RELATING TO NOISE

Results presented in this chapter provide insight about the influence of noise on the ACE1 system. Calibration of raw data (shifting of phase and scaling of gain) is important to account for differences between ACE1 channels due to tolerances of components and variations in electrical interference caused by the physical placement of parts or connections. To accurately calculate current, stray capacitance at the electrode must be determined. System tests looked at the signal-noise-ratio (Section 5.1), fast Fourier transforms (FFTs) of data (Section 5.2) and stray capacitance at different locations within in the EIT system (Section 5.3).

5.1. Signal-to-Noise Ratio (SNR)

In the context of the ACE1 EIT device, electrical interference or noise is defined as the unwanted interaction of the circuits and/or wires with one another or interaction of circuits and/or wires with the outside environment. Interference can be either magnetic or electromagnetic [13]. Internal electrical interference within the ACE1 system tomograph box is a result of the many electrical connections linking cables and wires to the different circuit boards. Another source of internal ACE1 interference could be caused by traces on the circuit boards, which can act like an antenna and pick up electrical interference. An important metric of quantifying electrical interference or noise in the system is the signal-to-noise ratio.

The main motivation for assessing the SNR of the ACE1 system is that EIT reconstructed images require solving an ill-posed inverse problem. When inverse problems are ill-posed, small errors in measured data can lead to large errors in image reconstructions [2]. It is

difficult to quantify the accuracy of reconstructions to their relationship with the SNR of ACE1 data because image accuracy depends highly on the exact algorithm used, algorithm parameters and dataset. The specific impact of SNR on images produced with ACE1 data is not discussed in this work. However, it is important to note that acquiring data with increased SNR should lead to improved spatial resolution in reconstructed images.

Various considerations were made in the design of the ACE1 system to maximize the signal-to-noise ratio (SNR). SNR can be defined as a measure of the quality of an acquired signal in the presence of noise or electrical interference. The active electrode protects the signal from interference and noise by increasing the current associated with the measured signal. In addition, sampling at a rate higher then specified by the Nyquist criterion, or oversampling, helps improve SNR of measured voltages. The Nyquist criterion states that one must sample at least twice the rate of the highest frequency signal one desires to capture [13]. In ACE1, each sample is acquired at 2.5M samples/sec by the 24 bit ICS-1640 ADC, improving the SNR of measured voltages.

There are several factors that can influence SNR. These factors include: (1) quantization noise (from the finite precision of the 20 Vpp ICS-1640 analog-to-digital converter), (2) noise and interference inherent to the ACE1 system, (3) noise and interference from the environment, such as those caused by person-to-person differences, lights, nearby electronic equipment and/or other medical devices attached to the patient and (4) shot noise and random noise due to thermal agitation of electrons in resistors and/or tiny fluctuations in voltages and currents of integrated circuits and components in the system [13].

The SNR of each channel in the ACE1 the system can be computed. Prior to computing SNR, the raw data is demodulated or processed by a matched filter in which least mean

squares is used to determine the the magnitude and phase of the signal for the frequency of applied current. Mathematically, SNR is defined as the ratio of the mean squared value of the signal to the mean squared value of the noise. In Equation (5.1), ${V_{pk}}_l^k(f)$ represents the demodulated voltage amplitude during a single frame (f), ${V_{pk}}_l^k$ is the average demodulated voltage over F number of frames. Thus, SNR for each electrode was calculated by:

$$SNR = 10 \log \frac{\left(\sum_{i=1}^{F} {V_{pk}}_l^k(f) \right)^2}{\left(\sum_{i=1}^{F} {V_{pk}}_l^k(f) - {V_{pk}}_l^k \right)^2} \tag{5.1}$$

To determine the best SNR achievable by the ACE1 system, 250 frames (F) of data were collected on a homogeneous saline filled tank with an approximate conductivity of 0.8 mS/cm. Measured voltages of V_e, defined in 3.1.1, were demodulated and used in the SNR calculations. Results of this experiment are presented in Sections 5.1.1 to 5.1.2 and compared to human subject breath holding data, found in Section 5.1.3.

5.1.1. Variations in SNR in Comparison to Electrode Position. A disadvantage of pairwise current injection EIT systems when compared to EIT systems that inject current on all electrodes is that the SNR is not the same on all electrodes when data is collected. In future systems, additional sources would improve SNR of non-injection electrodes. The SNR of each electrode during a single current pattern for a homogeneous tank dataset with no ground placed in the center of the phantom is shown in Figure 5.1 at 25 kHz, 50 kHz and 75 kHz for skip patterns 0 to 15. Figure 5.2 and Figure 5.3 also plot SNR for each electrode during a single current pattern for tank data at 100 kHz and 125 kHz and 150 kHz and 175 kHz, respectively. As seen in Figures 5.1 to 5.3, SNR is highest on injection

electrodes. Additionally, SNR decreases as distance from the injection electrodes increases because measured voltage amplitudes are smaller.

As skip pattern increases, the SNR of electrodes furthest from the injection electrodes also increase. Current pattern 7 as labeled in Figures 5.1 - 5.3, denotes the placement of the leading injection electrode. For skip 2, injection electrodes are 7 and 10 (skipping electrodes 8 and 9). Similarly, for skip 8, injection electrodes are 7 and 16 (skipping electrodes 8, 9, 10, 11, 12, 13, 14, and 15).

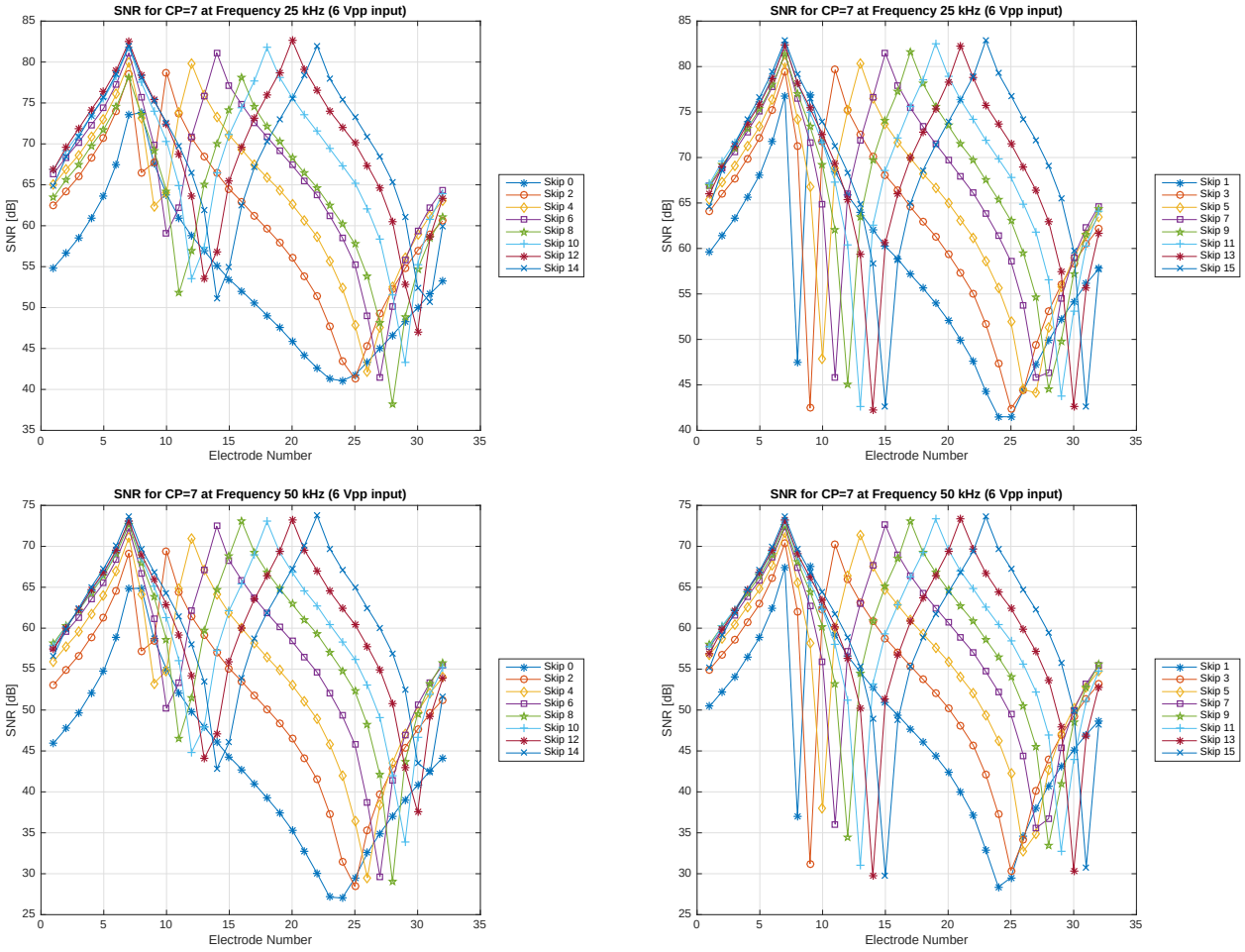

Figure 5.1. Single current pattern SNR over 250 frames at the 512 point acquisition rate for a 6 V_{pp} input and odd skip patterns are shown in the left column and even on the right. (Row 1) 25 kHz. (Row 2) 50 kHz.

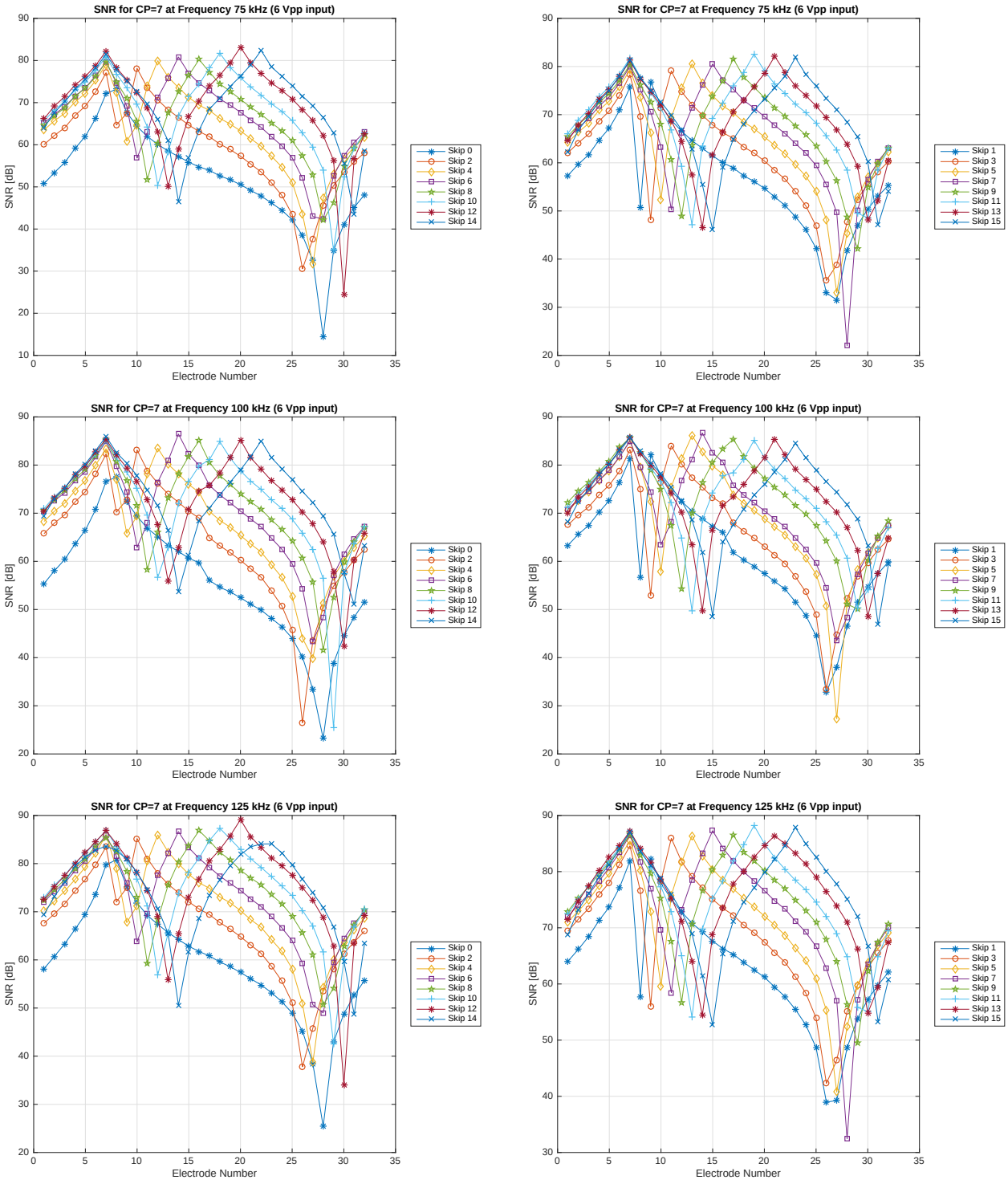

Figure 5.2. Single current pattern SNR over 250 frames at the 512 point acquisition rate for a 6 V_{pp} input and odd skip patterns are shown in the left column and even on the right. (Row 1) 75 kHz. (Row 2) 100 kHz. (Row 3) 125 kHz.

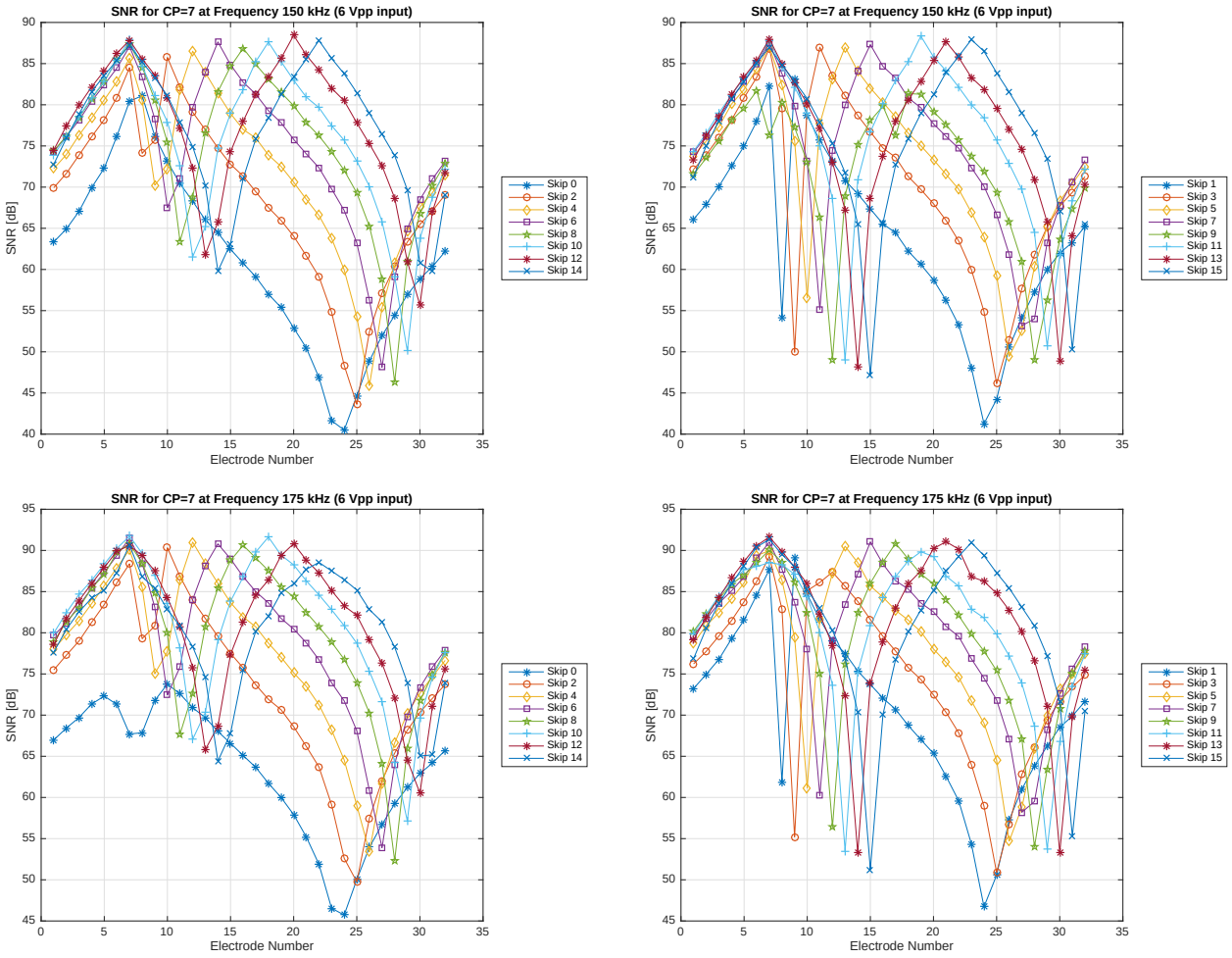

Figure 5.3. Single current pattern SNR over 250 frames at the 512 point acquisition rate for a 6 V_{pp} input and odd skip patterns are shown in the left column and even on the right. (Row 1) 150kHz. (Row 2) 175 kHz.

Figures 5.1 - 5.3 also illustrate changes of individual electrodes for a single current pattern in SNR with respect to frequency. Frequencies of 25 kHz and 175 kHz were tested at the 512 point acquisition rate. Additional plots of current patterns at different acquisition rates (256 and 1024 points) at various frequencies are shown in Appendix C. For odd numbered skip patterns, both halves of the bipolar create lower SNR for the middle skipped electrode.

5.1.2. Variations in SNR of Injection Electrodes Compared to Skip Pattern and Acquisition Rate. For all ACE1 skip patterns, the largest potentials are measured on the injection electrodes. Therefore, the most significant information about the

interior of the domain can be gained from them. In Figure 5.4, the SNR of all injecting electrodes are averaged together for each skip pattern when 250 frames of data was acquired on a homogenous tank phantom with a small ground placed in the center.

The data presented in Figure 5.4 is shown in Table 5.1, where SNR greater than 80 dB is boldfaced. When a small ground is placed in the center of the tank phantom SNR generally decreases when skip patterns larger than 8 are used. However, the advantage of using a ground in the center is that mismatch in the source can be drained. When no ground is used, such as the SNR data presented in Table 5.2, mismatch in the source leaks through stray capacitance in the tank phantom. By comparing Table 5.1 to Table 5.2, it can be observed that larger input voltages to the VCCS, or larger currents, can be used with a small ground.

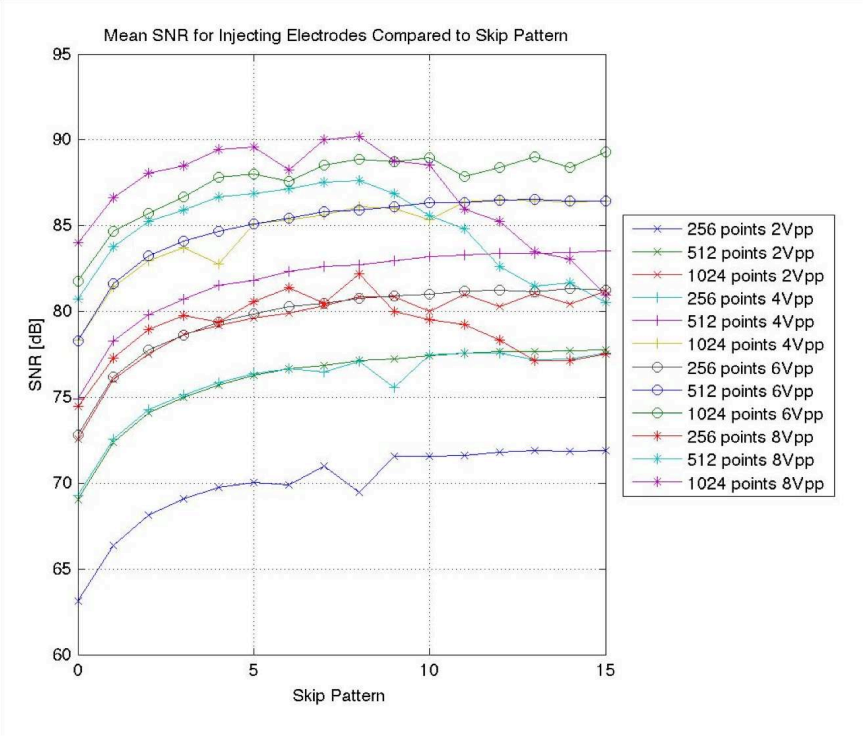

Figure 5.4. SNR on a homogeneous tank phantom data (with a small ground in the center) at 125 kHz for the injection electrodes for different voltage inputs to the VCCS, skip patterns and acquisition rates.

Table 5.1. A comparison of the average SNR of V_e measurements for injecting electrodes is presented. 251 frames of data was taken on a tank phantom filled with a saline solution *a small ground* was placed in the center. Current was injected at 125 kHz. The peak-to-peak voltages correspond to function generator settings of the VCCS. 256, 512, or 1024 indicated the number of samples acquired.

Skip	2Vpp 256	2Vpp 512	2Vpp 1024	4Vpp 256	4Vpp 512	4Vpp 1024	6Vpp 256	6Vpp 512	6Vpp 1024	8Vpp 256	8Vpp 512	8Vpp 1024
0	63.1	69.0	72.6	69.3	74.9	78.3	72.8	78.3	**81.8**	74.5	**80.7**	**84.0**
1	66.4	72.4	76.1	72.6	78.3	**81.5**	76.2	**81.6**	**84.7**	77.3	**83.8**	**86.7**
2	68.1	74.1	77.5	74.3	79.8	**82.9**	77.8	**83.3**	**85.7**	79.0	**85.2**	**88.1**
3	69.1	75.0	78.7	75.1	**80.7**	**83.7**	78.6	**84.1**	**86.7**	79.8	**85.9**	**88.5**
4	69.7	75.7	79.2	75.9	**81.5**	**82.8**	79.4	**84.7**	**87.8**	79.4	**86.7**	**89.4**
5	70.0	76.3	79.6	76.3	**81.8**	**85.1**	79.9	**85.1**	**88.0**	**80.6**	**86.9**	**89.6**
6	69.9	76.7	79.9	76.7	**82.3**	**85.3**	**80.3**	**85.5**	**87.6**	81.4	**87.2**	**88.2**
7	71.0	76.9	**80.3**	76.5	**82.6**	**85.6**	**80.5**	**85.8**	**88.5**	80.5	**87.5**	**90.0**
8	69.5	77.1	**80.8**	77.1	**82.7**	**86.1**	**80.8**	**85.9**	**88.9**	82.2	**87.7**	**90.2**
9	71.6	77.2	**80.9**	75.6	**83.0**	**86.0**	**80.9**	**86.1**	**88.7**	80.0	**86.9**	**88.8**
10	71.6	77.4	**80.0**	77.5	**83.2**	**85.3**	**81.0**	**86.3**	**89.0**	79.5	**85.6**	**88.5**
11	71.6	77.6	**81.0**	77.6	**83.3**	**86.4**	**81.2**	**86.3**	**87.9**	79.2	**84.8**	**86.0**
12	71.8	77.6	**80.3**	77.6	**83.4**	**86.5**	**81.2**	**86.5**	**88.4**	78.3	**82.6**	**85.2**
13	71.9	77.7	**81.1**	77.2	**83.4**	**86.5**	**81.2**	**86.5**	**89.0**	77.1	**81.5**	**83.5**
14	71.8	77.7	**80.4**	77.2	**83.4**	**86.4**	**81.3**	**86.4**	**88.4**	77.2	**81.6**	**83.1**
15	71.9	77.8	**81.2**	77.6	**83.5**	**86.4**	**81.2**	**86.4**	**89.3**	77.5	**80.5**	**81.0**

Table 5.2. A comparison of the average SNR of V_e measurements for injecting electrodes is presented. 251 frames of data was taken on a tank phantom filled with a saline solution with *no ground* in the center. Current was injected at 125 kHz. The peak-to-peak voltages correspond to function generator settings of the VCCS. 256, 512, or 1024 indicated the number of samples acquired.

Skip	2Vpp 256	2Vpp 512	2Vpp 1024	4Vpp 256	4Vpp 512	4Vpp 1024	6Vpp 256	6Vpp 512	6Vpp 1024	8Vpp 256	8Vpp 512	8Vpp 1024
0	64.8	71.1	73.2	70.6	76.5	74.6	74.2	**80.0**	**81.2**	76.7	**82.3**	74.1
1	68.1	74.5	76.1	74.0	79.5	**82.0**	77.5	**83.2**	**85.3**	**80.0**	71.9	**85.9**
2	69.7	75.6	77.4	75.8	**81.2**	**84.4**	**84.8**	79.1	**85.1**	**81.0**	**85.1**	**88.3**
3	70.7	76.7	78.2	76.6	**81.7**	**84.8**	**85.6**	**80.1**	**86.0**	**81.0**	**83.0**	79.1
4	71.5	77.4	78.7	77.4	**82.6**	**85.4**	**86.1**	**80.6**	**87.9**	65.7	73.5	79.8
5	71.9	77.9	78.8	77.9	**82.8**	**86.0**	**86.5**	**81.3**	**89.2**	65.6	75.3	73.6
6	72.3	78.3	79.2	78.2	**84.0**	**86.4**	**86.9**	**81.6**	**89.4**	65.4	70.4	76.1
7	72.6	78.5	79.4	78.5	**83.9**	**86.8**	**87.0**	**81.8**	**89.3**	76.0	72.9	67.5
8	72.8	78.8	79.5	78.7	**84.0**	**87.0**	**87.1**	**82.1**	**89.4**	74.5	68.2	71.3
9	72.9	78.9	79.7	78.9	**84.5**	**87.2**	**87.0**	**82.1**	**77.8**	68.8	67.1	50.8
10	73.1	79.1	79.6	79.0	**84.6**	**87.1**	**87.4**	**82.3**	**53.9**	54.0	50.5	50.1
11	73.1	79.5	78.4	79.2	**84.6**	**87.0**	**87.6**	**82.0**	**79.5**	60.7	62.8	48.9
12	73.1	79.4	78.8	79.1	**84.8**	**87.0**	**87.7**	**82.4**	**88.4**	62.9	48.7	57.6
13	73.2	79.2	79.1	79.4	**84.8**	**87.2**	**87.0**	**82.0**	**85.7**	61.7	47.8	55.2
14	73.3	79.2	78.4	79.2	**84.8**	**87.2**	**83.1**	**82.6**	**88.4**	54.0	54.3	50.7
15	73.3	79.3	79.0	79.3	**84.9**	**87.3**	**84.9**	**82.4**	**85.7**	56.5	51.7	54.7

In EIT, there exists a trade-off between the frame-rate and SNR. Table 5.3 and Table 5.4 compare SNR for a variety of acquisition rates and frequencies for a 6 V_{pp} input to the VCCS. For this test, a homogeneous tank is used and a range of currents, or input voltages to the VCCS, were also considered. The tables suggest that to increase frame rate, by using acquisition of 256 points (or 33 frames/second for 32 electrodes), 100 kHz to 175 kHz are best.

For the tank phantom, 175 kHz is gives the best SNR for the fastest frame rate. The improved performance with increase in frequency is not intuitive when considering the effects of stray capacitance. As frequency increases, one might suspect that the effects of stray capacitance might influence SNR, since they would decrease the effectiveness of the source. For example, assuming a 30 pF stray capacitance at a given electrode, the capacitive reactance (X_c) at: 25 kHz is approximately $212k\Omega$, 75 kHz is approximately $71k\Omega$ and 125 kHz is approximately $42k\Omega$.

Due to the high SNR on injecting electrodes, one can reasonably conjecture that the capacitance remains stable over the duration of an acquired dataset, despite sinking current away from the intended load. The increase in SNR is likely due to greater oversampling for the higher frequencies. Therefore, SNR results must be balanced with the other metrics for system performance.

5.1.3. Psuedo-SNR of Human Subject Data. A psuedo-SNR was calculated using human subject breath holding data. It is not a true SNR calculation since during breath holding the human body is not static like a tank phantom. Equation (5.1) is used to calculate psuedo-SNR, but because this equation uses a mean voltage collected over many frames, temporal differences in measurements that reflect changes in perfusion (blood flow in the

Table 5.3. A comparison of the average SNR of V_e measurements for injecting electrodes for different frequencies for 256 point acquisition rate.

Skip	25 kHz	50 kHz	75 kHz	100 kHz	125 kHz	150 kHz	175 kHz
0	68.0	61.2	70.3	75.1	74.2	**80.6**	**80.2**
1	74.3	64.7	73.7	78.4	77.5	**83.5**	**83.2**
2	76.0	66.3	75.3	74.9	79.1	**85.0**	**84.7**
3	76.8	67.3	76.3	70.1	**80.1**	**86.0**	**85.4**
4	77.6	68.1	76.9	**81.7**	**80.6**	**86.5**	**85.9**
5	78.0	68.5	77.4	**82.4**	**81.3**	**86.8**	**86.3**
6	78.4	68.9	77.9	**82.8**	**81.6**	**87.1**	**86.5**
7	78.7	69.1	78.1	**83.0**	**81.8**	**87.4**	**86.6**
8	78.7	66.6	78.2	**83.1**	**82.1**	**87.1**	**86.9**
9	78.7	69.8	78.3	**83.5**	**82.1**	77.1	**83.4**
10	78.9	69.9	78.5	**83.6**	**82.3**	**88.0**	**87.2**
11	78.7	69.9	78.6	**83.2**	**82.0**	**88.1**	**87.2**
12	78.8	70.1	78.7	**83.7**	**82.4**	**88.2**	**87.2**
13	78.6	70.1	78.8	**83.3**	**82.0**	**86.8**	**85.0**
14	78.6	69.8	78.8	**83.8**	**82.6**	**88.1**	**86.8**
15	78.2	70.1	79.0	**82.5**	**82.4**	**88.0**	**87.3**

Table 5.4. A comparison of the average SNR of V_e measurements for injecting electrodes for different frequencies for 512 point acquisition rate.

Skip	25 kHz	50 kHz	75 kHz	100 kHz	125 kHz	150 kHz	175 kHz
0	73.2	64.6	73.0	77.1	**80.0**	71.9	67.0
1	76.7	67.9	76.2	**80.7**	**83.2**	**85.7**	**87.8**
2	78.6	69.5	77.7	**82.1**	**84.8**	**86.6**	**89.6**
3	79.4	70.4	78.9	**83.2**	**85.6**	**87.8**	**89.5**
4	80.0	71.3	79.7	**83.7**	**86.2**	**87.4**	**90.6**
5	80.6	71.7	**80.0**	**84.4**	**86.5**	**87.9**	**90.9**
6	81.1	72.2	**80.5**	**84.8**	**86.9**	**87.9**	**90.6**
7	81.4	72.5	**80.8**	**82.8**	**87.0**	**88.0**	**90.4**
8	78.0	72.7	**80.9**	**85.1**	**87.1**	**88.8**	**91.1**
9	81.6	73.1	**81.5**	**85.3**	**87.0**	**88.1**	**90.8**
10	82.0	73.1	**81.7**	**84.7**	**87.4**	**88.4**	**91.4**
11	82.0	73.3	**81.8**	**85.4**	**87.6**	**88.1**	**90.5**
12	81.9	73.2	**81.8**	**85.6**	**87.7**	**88.3**	**91.6**
13	82.0	73.4	**81.5**	**85.9**	**87.0**	**86.7**	**90.2**
14	82.0	73.6	**81.8**	**85.1**	**83.1**	**88.4**	**87.1**
15	82.1	73.5	**81.8**	**85.1**	**86.9**	**88.1**	**90.7**

heart and lungs) are included in the mean. Figure 5.5 can be used as a metric of data quality. It has been observed from reconstructions that generally better images can be achieved from subjects with a higher psuedo-SNR on the injection electrodes.

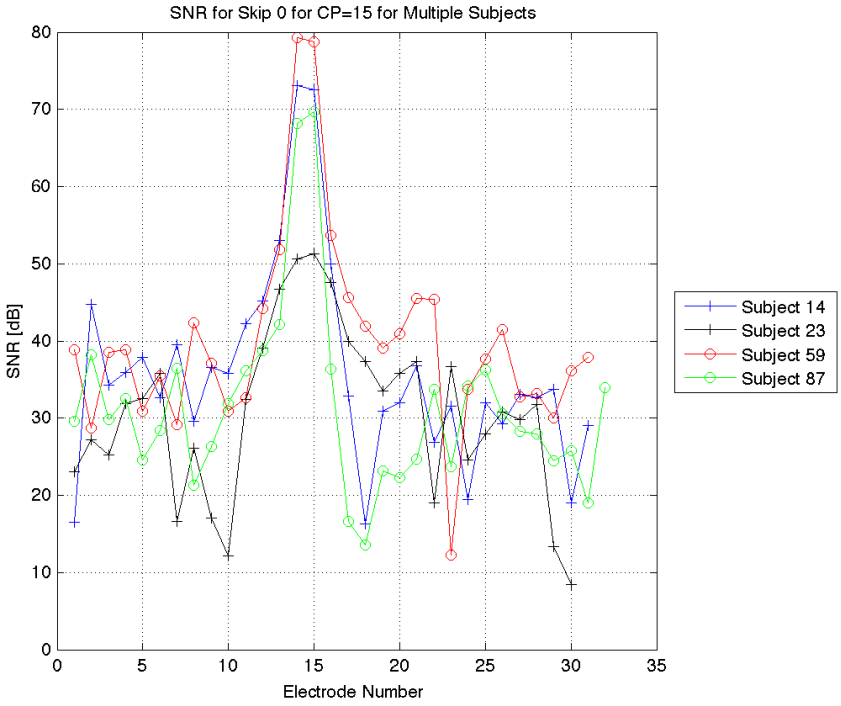

Figure 5.5. Four different human subjects were asked to hold their breath for approximately 20 seconds (or 500 frames). Data was collected at 1024 point acquisition rate with a skip 0 configuration.

Not all subjects were imaged with the same skip patterns due to differences in numbers of electrodes placed around the perimeter of their chests. However, all subjects were imaged at skip 0, so a subject-to-subject comparison is shown in Figure 5.5. SNR of injection electrodes varies greatly between subjects. Subject 59 has an SNR of approximately 30 dB greater than Subject 14, which may partially explained by slight differences in the level of injected current, the ability each each subject to remain still during breath holding and variations in contact impedance. A high contact impedance between the electrodes and skin

likely indicates secure ECG electrode adhesion to the subject. Contact impedance is further discussed in Chapter 6.

For data acquired on human subjects, it is expected that SNR of injection electrodes would be lower when compared to a tank phantom. Figure 5.6, contains average SNR of injection electrode data for healthy human subjects imaged with ACE1.

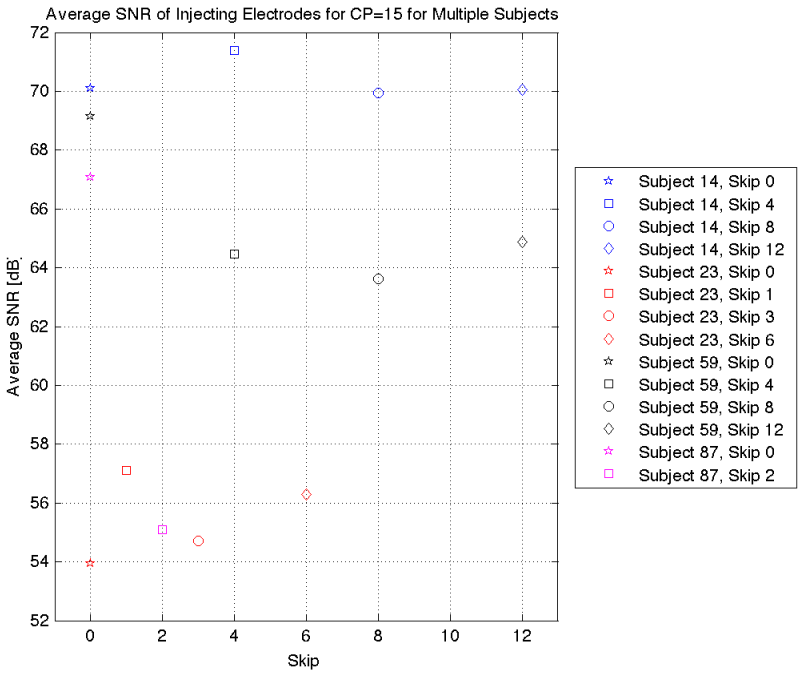

Figure 5.6. Average SNR of injection electrodes of several human subjects during breath holding.

5.2. Frequency Components in ACE1 Data

In terms of precision and repeatability, which are two of the most important metrics of an EIT system due to their ability to influence resolution and accuracy of reconstructed images, 75 kHz and 100 kHz are two of less desirable choices. A discussion of precision and resolution results is presented in Sections 4.3.2 to 4.3.4. A possible explaination why 100

kHz performance be obtained by carefully looking at Figure 5.7 which shows fast Fourier transforms (FFTs) of data taken when the input to the VCCS is off and again when it is on.

The bottom plot in Figure 5.7 shows a decrease in the magnitude of the 100 kHz frequency content of measured signals as distance from the injection electrodes (channels 1 and 2) increases. This is consistent with SNR plots discussed in Section 5.1.1. However, the FFTs shown in this figure contain additional information. The frequency of fluorescent lighting in the room shows up in the frequency spectrums of both plots in Figure 5.7 from approximately 41 to 43 kHz. A 600 kHz frequency also appears in the plots. 600 kHz is a harmonic of both 75 kHz and 100 kHz, and therefore its presence could explain why the amplitude precision and repeatability were not as good.

To investigate the effects of a possible harmonic, total harmonic distortion (THD) was calculated with Matlab. Harmonics are given by frequencies that are whole number multiples of the fundamental frequency of the measured signal. THD is used to calculated the distortion present in the voltage measurements caused by harmonics [92]. In this case, a more negative number in dB indicates less harmonic distortion or better data. The THD of 100 kHz data was -30 dB, which is about 19 dB greater than the THD for the 125 kHz data (-49 dB).

The result of this test indicates that careful consideration must be given to the frequencies chosen if an input waveform containing multiple frequencies is used for the VCCS. One should not use any physiologically relevant frequencies, 41 to 43 kHz or those which contain harmonics at 600 kHz. It is possible that the precision at 100 kHz could be improved by filtering higher frequencies prior to demodulation with the matched filter. Since the sensitivity of the demodulation routine to harmonics is unknown, this should be investigated if a presently "undesirable" frequency is needed or used in the future.

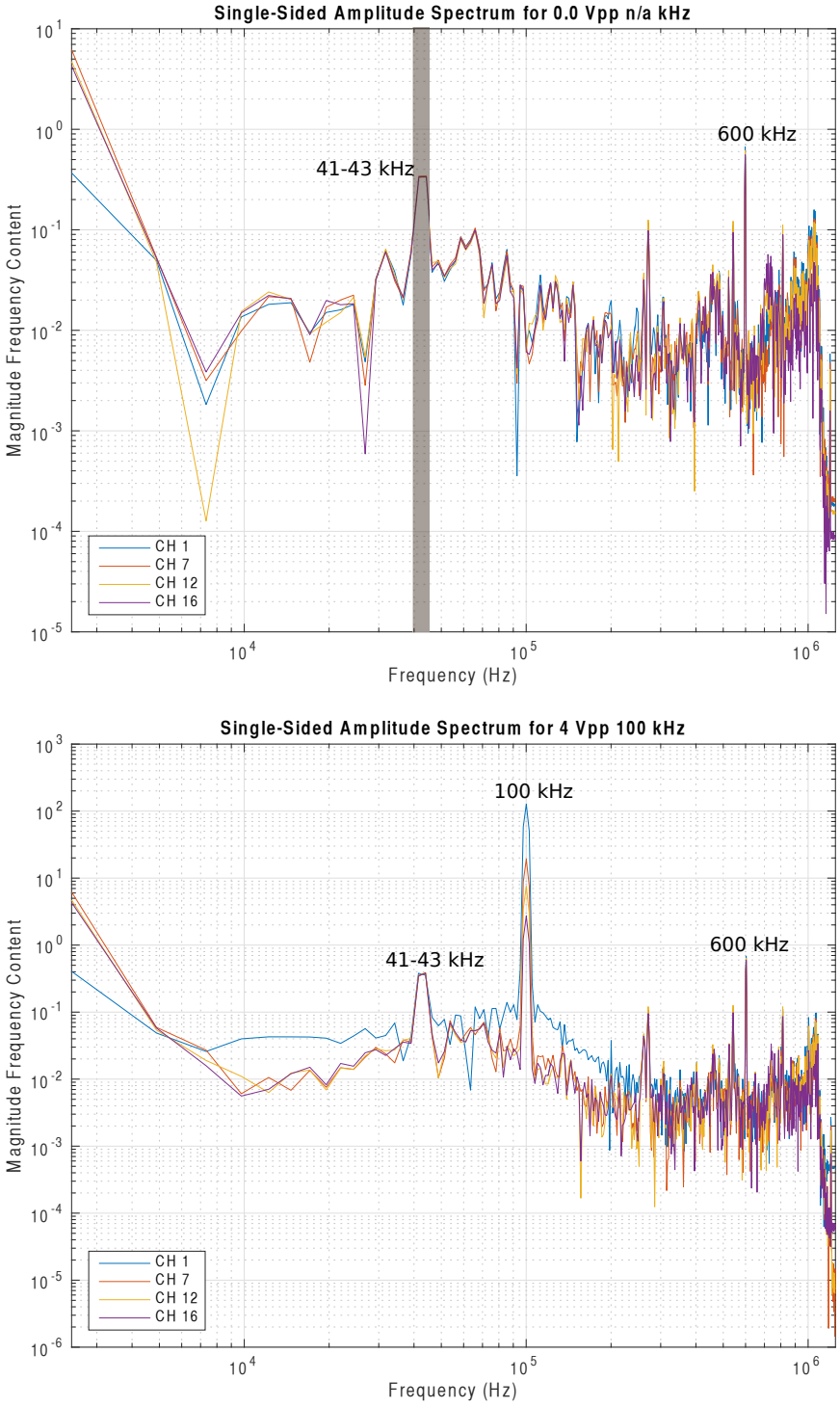

Figure 5.7. FFTs for current pattern 1 and skip 0 for data on different channels of homogeneous tank when the VCCS input is turned off (top) and when the VCCS input is set to 4.0 V_{pp} at 100 kHz.

5.3. Stray Capacitance Influencing ACE1

Stray capacitance existing between the current source and the load or domain can lead to errors in calibration and current measurement through use of the active electrode. Depending on the magnitude of stray capacitance interacting with the ACE1 system, current can be lost to stray capacitance on the cables connecting the active electrodes to the tomograph box. In addition, current can be lost to capacitance of the mulitplexer and switch channels.

5.3.1. Stray Capacitance and Injected Current. When the current source is located physically far from the load, accessing the influence of stray capacitance is essential to understanding the performance of ACE1. Current can be lost many places in between the source and the load, as shown in Figure 5.8. When the output impedance of the current source is not several orders of magnitude higher than the load, then current can be lost due to non-ideal source behavior (I_1). Stray capacitances and electric interference will also direct current away from the load (I_2). Current is also sunk by capacitance from components existing in the system (I_3), and remaining current is delivered to the load (I_4).

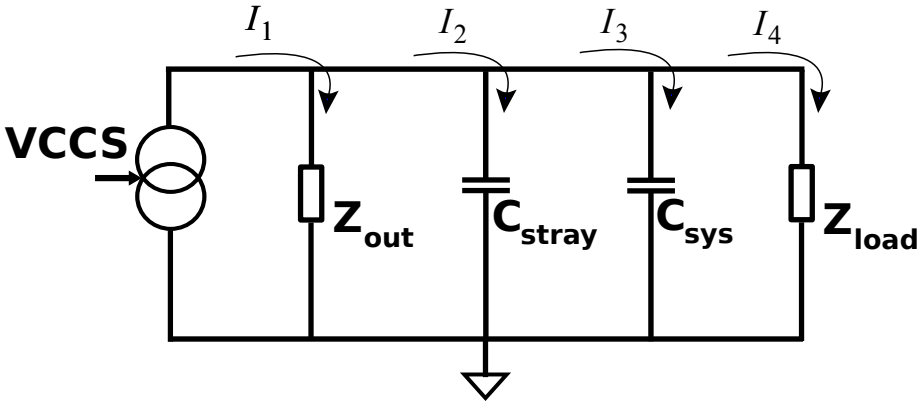

Figure 5.8. This schematic represents the loss of current in between the voltage controlled current source (VCCS) and the load.

Mathematically, we can express the current lost from the VCCS theoretical output through Kirchoff's Current Law in Equation 5.2. For analysis purposes, I_3 and I_4 can be lumped together.

$$I_{theory} = I_1 + I_2 + I_3 + I_4 \tag{5.2}$$

5.3.2. Stray Capacitance at the Electrode. Parts of the ACE1 system can be modeled and stray capacitance estimated, when tested by the method proposed in Figure 5.9. To perform this test, the current source was disconnected from the multiplexer board inputs and a voltage source was connected. A 1 kΩ resistor with 0.01% tolerance was connected as the load, or at node V_e and voltage measurements were collected with the system. This test was modeled as Figure 5.9B, where V_e and V_c are nodes in a voltage divider.

Using Kirchoff's laws, nodal equations can be written for Figure 5.9B. Equation (5.3) is at node V_c. Equations (5.4) to (5.5) are at node V_{ce}. Equation (5.6) is at node V_e. In the equations, the value for R_{sense} is 200 Ω, the typical resistance from the datasheet for the switch (R_{switch}) is 40 Ω. The typical value for $C_{switch-open}$ is 4 pF and closed is 16 pF. Z_L is the combined impedance of R_{Load} and $X_{C_{Stray}+C_{Switch}}$.

$$i = \frac{V_c - V_{ce}}{200} \tag{5.3}$$

$$\frac{V_c - V_{ce}}{200} = \frac{V_{ce} - V_E}{40} + \frac{V_{ce}}{X_{C_{Stray}+C_{Switch}}} \tag{5.4}$$

$$V_{ce} = \left(\frac{V_c}{200} + \frac{V_e}{40}\right) \Big/ \left(\frac{1}{40} + \frac{1}{200} + \frac{1}{X_{\,c_{Stray}+c_{Switch}}}\right) \tag{5.5}$$

$$\frac{V_{ce} - V_e}{40} = \frac{V_e}{Z_L} \tag{5.6}$$

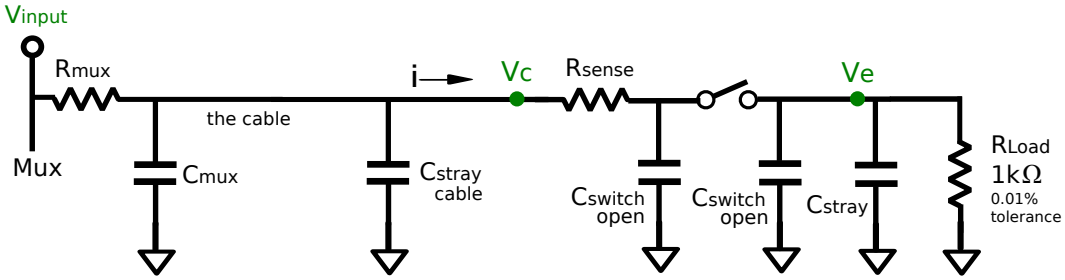

(a) Model of one active electrode channel when not injecting current.

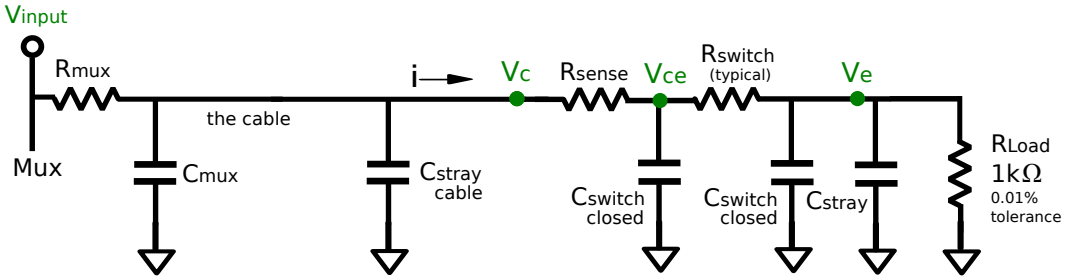

(b) Model of one active electrode channel when current is being injected.

Figure 5.9. Circuit model and testing set-up using a precise 1.0 kΩ resistor to determine the effects of stray capacitance at the electrode.

Using a selected frequency, $X_{C_{Stray}+C_{Switch}}$ in Equation (5.7) can be used to calculate the capacitance at node V_e.

$$X_{C_{Stray}+C_{Switch}} = \frac{Z_L R_{Load}}{R_{Load} - Z_L} \tag{5.7}$$

Figure 5.10 shows the capacitance while electrodes are injecting. 96 current patterns worth of data were collected, the mean across all electrodes during injection is 8.1 ± 59.5 pF and 8.6 ± 60.2 pF for both halves of the bipolar. At approximately 8 pF, the capacitive reactance ranges from 265 kΩ to 160 kΩ for frequencies of 75 kHz to 125 kHz. Increasing the capacitance to 68 pF, the capacitive reactance ranges from 31.2 kΩ to 18.7 kΩ for frequencies of 75 kHz to 125 kHz.

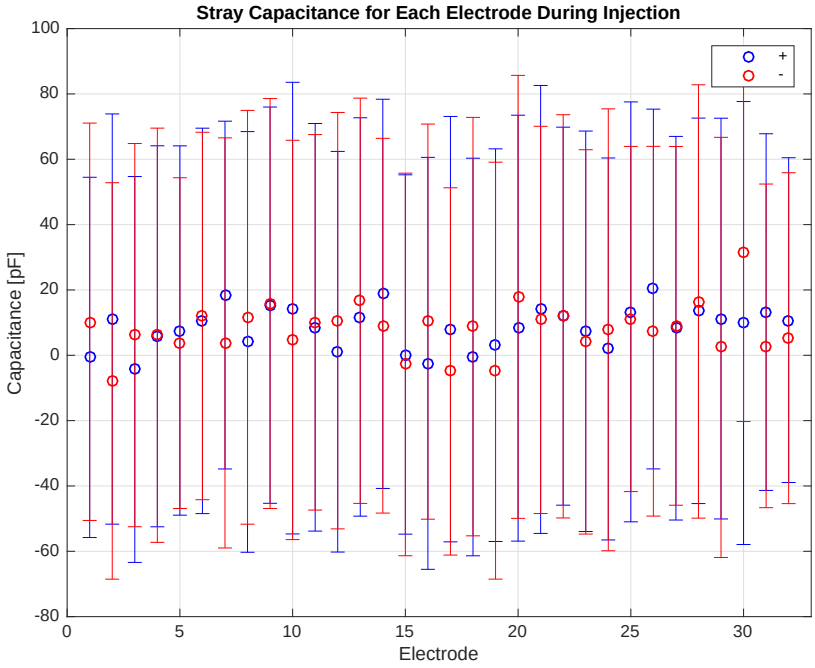

Figure 5.10. C_{stray} capacitance with standard deviation for each electrode for 96 current patterns of data. This includes the capacitance from the switch.

For normal ACE1 operation (bipolar current source connected), a current divider exists at node V_e and is shown in Equation .

$$I_{RL} = \frac{X_{C_{Stray}+C_{Switch}} I_e}{R_L + X_{C_{Stray}+C_{Switch}}} \tag{5.8}$$

Equation (5.8) can be used to precisely calculate the current being delivered to the load. However, a limitation of this calculation is that I_{RL} can only be determined the same level of certainty to which R_L is known. Approximating the impedance of the human body as 1.0 -1.5 kΩ, then the lost current at the electrode would be approximately 5-7.5% at 125 kHz.

5.3.3. In Between the Source and Node V_e. In addition to capacitance at the electrode board, capacitance is introduced to each of the 32 channels by the multiplexer and 1.25 - 1.5 m cable connecting the tomograph box to the active electrode. Figure 5.11 shows

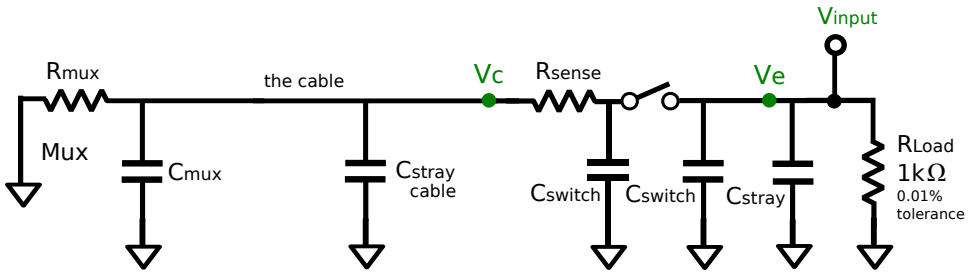

(a) Set-up

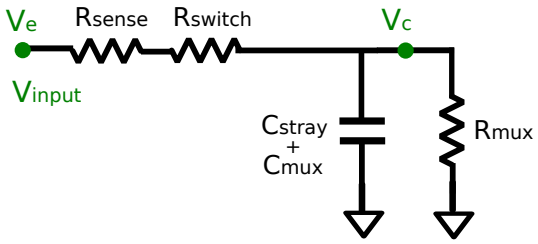

(b) Voltage Divider Assumption

Figure 5.11. Experiment to determine stray capacitance in between the multiplexer (mux) and active electrode, where the combined impedance of the stray and mux capacitance and line and mux resistance is considered Z_{cable}.

that when tested by the proposed method, stray capacitance on the connecting cable can be determined for each channel. In this test, the multiplexer inputs are grounded and a 125 kHz AC voltage source and high precision resistor load are connected at node V_e. In this experiment, data was collected for 30 frames at the 1024 point acquisition rate for both V_e and V_c. This test set-up can also be reduced to a voltage divider, shown in Figure 5.11B.

Equation (5.9) can be used to determine the impedance Z_{cable}, which is the combination of C_{stray}, C_{mux} and R_{mux}, between the tomograph box and active electrode shown in Figure 5.11. Specifically, from this calculation the capacitive component can be determined. Equation (5.10) is the equation from which capacitive reactance for stray and multiplexer

components can be calculated.

$$Z_{cable} = \frac{R_{sense+switch} V_c}{V_e - V_c} \tag{5.9}$$

$$X_{Cstray+Cmux} = \frac{Z_{cable} R_{mux}}{R_{mux} - Z_{cable}} \tag{5.10}$$

Using the proposed test, stray capacitance influencing an injecting channel was estimated. Figure 5.12 shows individual estimates of stray capacitance. The mean of stray capacitance influencing one channel is 12.7 nF with a mean standard deviation of 16.7 pF. However, there appears to be a relationship between stray capacitance effecting a channel and the design or configuration of channels in each cable. There are four cables of eight channels each in ACE1. Placement of wires is identical in each cable. Stray capacitance for a channel within each set of eight increases as channel number increases.

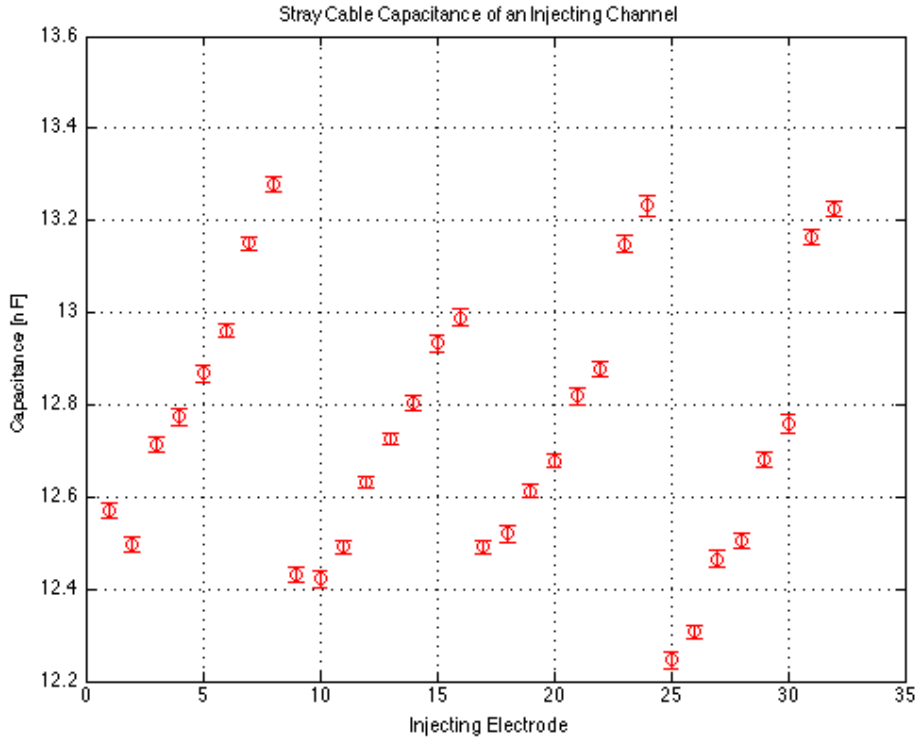

Figure 5.12. The stray capacitance affecting each channel during injection.

Capacitance at this location in the ACE1 system greatly impacts the efficiency of the current source, but does not influence the accuracy of current calculations. The higher the capacitance located between the source and node V_c, the greater the percentage of current that is lost compared to what should theoretically be delivered using the improved Howland VCCS equations. The stray capacitance values in Figure 5.12 could be used as a starting point for future ACE1 current source designs incorporating a NIC or GIC.

CHAPTER 6

THE EFFECTS OF CONTACT IMPEDANCE IN EIT

Contact impedance occurs in EIT in experiments using tank phantoms and when collecting data on human subjects. When electrical potentials are measured at a surface, a difference between conductivity between the electrode and skin or saline in the tank creates a contact impedance. This high impedance creates a non-uniform current distribution that is difficult to model [2, 93, 94]. This chapter discusses: contact impedance in the context of the tank (Section 6.1), ECG electrode - skin contact impedance (Section 6.2), anatomy and properties of human skin (Sections 6.3 - 6.4) and a proposed adaptation of a model describing current penetration through the skin (Section 6.5).

6.1. Metal Electrode - Saline Contact Impedance

A simple experiment was proposed to approximate the contact impedance ($Z_{electrode}$) experienced in tank phantom experiments. A small test cell was filled with a saline of known conductivity, and contact impedance was calculated assuming $Z_{electrode}$ exists in series and on both sides of the saline media. Electrodes one and two are connected to one side of the test cell and electrodes three and four to the other. Current is injected on electrode one and ground on electrode three. Electrodes two and four are passive. Figure 6.1 shows the test set-up. 15.0 mL of saline solution was added to fill the test cell to a height of approximately 1.72 cm. Contact impedance varies based on the area of the electrode touching the solution, so the test cell was filled to a similar height used in tank phantom experiments using approximately 1 liter of saline.

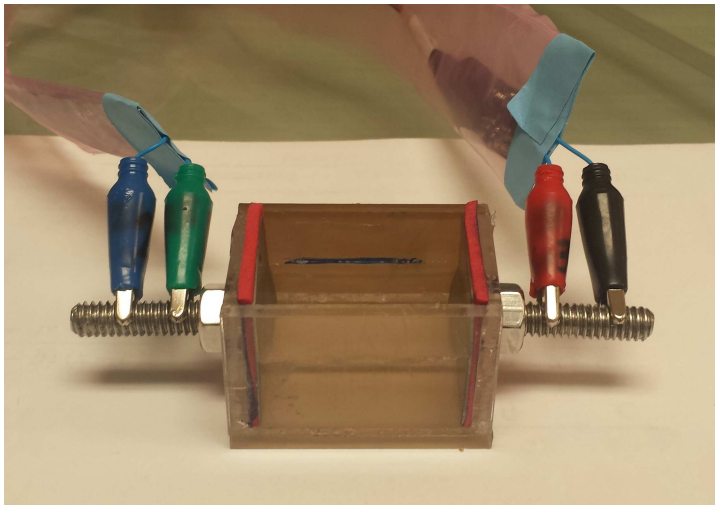

Figure 6.1. Saline was added to fill the test cell to a height of 1.72 cm.

Using a voltage divider, the total impedance (Z_{total}) can be calculated in Equation (6.1). Equation (6.2) is consistent with other experiments performed by other groups [95, 96]. It should be noted that these equations are only valid for the two electrode test cell configuration [95]. The resistance of the saline is found in Equation (6.3) using the measured conductivity (σ_{saline}) and dimensions of the test cell, where L is the distance (3.6 cm) between electrodes and A_e is the area of electrode interfacing with the saline.

$$Z_{total} = \left(R_{sense} + R_{switch}\right)\left(\frac{V_{e1}}{V_{e2} - V_{c2}} - 1\right) \tag{6.1}$$

$$Z_{total} = 2Z_{electrode} + R_{saline} \tag{6.2}$$

$$R_{saline} = \frac{L}{\sigma_{saline} A_e} \tag{6.3}$$

Using the test described, $Z_{electrode}$ was found to be approximately 100.8 ± 27.4 Ω for a saline solution with conductivity of 1.90 mS/cm (which is the same saline concentration used in tests of distinguishability in Section 4.4). For a saline solution with conductivity of 0.901 mS/cm, $Z_{electrode}$ is approximately 147.1 ± 52.5 Ω.

6.1.1. Contact Impedance and ACE1 Tank Phantom Data. Contact impedance created by the electrode-electrolyte interface on injecting electrodes [95] may partially explain why changes inside the domain may be masked on these electrodes. This effect can be seen in Figure 6.2 which shows a representative current pattern from a skip 2 dataset from the distinguishability tests in Section 4.4. All skip patterns are shown in Figure 4.31 and Figure 4.32. The difference in disinguishability between different sizes of conductive and insulative targets relative to each other is less on injecting electrodes compared to non-injecting electrodes. Injecting electrodes in Figure 6.2 are electrodes 10 and 13. While these electrodes are sensitive to the presence of a target in the center of the tank, it would be difficult to determine which target is larger using only the voltage measurements on the injecting electrodes.

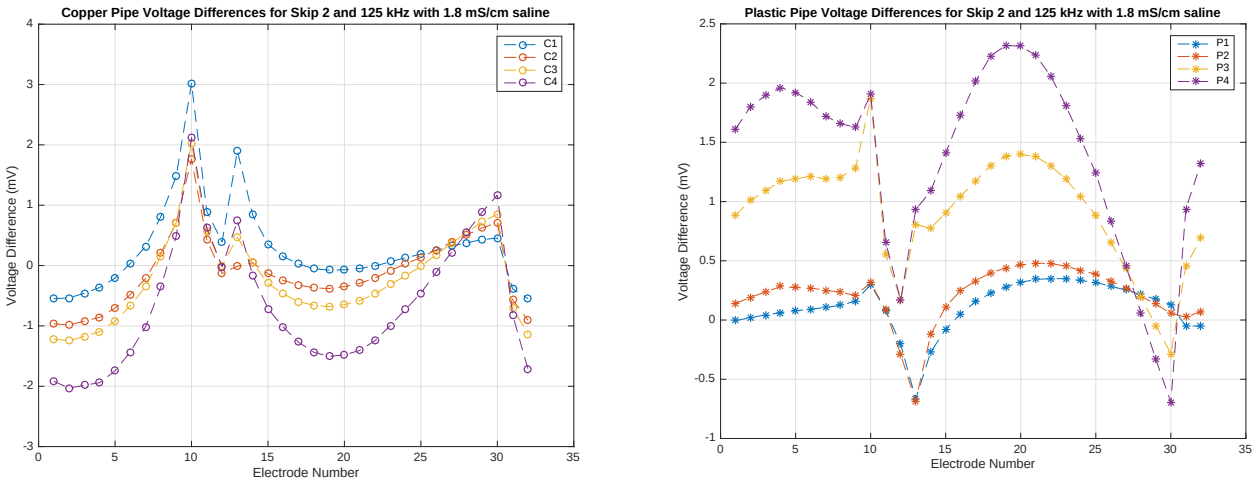

Figure 6.2. Mean distinguishability for skip 2 data collected at 125 kHz for current pattern 10 where C1, C2, C3 and C4 are the copper pipe targets (left) and P1, P2, P3 and P4 are the plastic pipe targets (right).

A trend in voltage differences relative to size is clearly visible on non-injecting electrodes 15 to 25 of Figure 6.2. The greater the diameter of copper pipe, the greater the voltage

decrease from a homogeneous tank reference. For the plastic pipe phantoms, the voltage increase from the homogeneous tank reference was also proportional to the size of the target.

The effects of contact impedance, which can mask details about the domain, should be considered in future versions of ACE1. Increasing the number of sources would improve SNR and reproducibility on electrodes, but there is value in having some non-injecting electrodes, since they may be more sensitive to details within the domain. There are groups with skip pattern injection style EIT systems that do not use voltages measured on injection electrodes. However, at this point, the group at CSU includes the high SNR measured data from these electrodes in reconstruction algorithms.

6.2. Electrode - Skin Contact Impedance

The high contact impedance between the skin and the electrode results in large measured electrical potentials. When discussing contact impedance, this value usually takes into account two physical phenomena: (1) impedance caused by an electrochemical effect transforming applied current ionic current and (2) the high impedance of the skin [97]. When current flows into the skin, higher currents are applied through the edges of the electrodes [11, 93]. Additionally, a shunting or "skinning" effect often occurs. A portion of the injected current will flow near the surface of the skin to the nearest electrodes instead of flowing into the interior of the body [93, 95]. Contact impedance is difficult to correctly model, but failing to do so would result in large errors when reconstructing absolute images [97].

One of the most commonly used methods to model contact impedance is the Complete Electrode Model (CEM) which considers the shunting and edge effects of large electrodes to reduce image artifacts [98]. Other commonly considered models that do not incorporate contact impedance are the gap and shunt models. While the CEM has helped to improve

reconstructions in some situations, including more accurate models of the skin may be beneficial. The CEM model is discussed further in Section 7.3.3.

6.2.1. Contact Impedance and ACE1 Human Subject Data. A CSU institutional review board (IRB) approved pilot study (11-2717H) was used to best understand the sensitivity of ACE1 to changes in skin impedance of human subjects. The skin is one of the the least conductive tissues in the body, and its electrical properties vary based on many factors, discussed in Section 6.4. It is well known that the impedance properties of the skin vary based on temperature [4], so this pilot study investigated the influence of skin temperature on ACE1 data.

Three different skin temperatures were investigated: cool, normal and warm. Cool data was collected first. To cool the subject's skin, a cold pack was applied for approximately 5 minutes, and a fan was used to help him remain feeling cool during data collection. Placement of the electrodes was carefully noted, so that fresh electrodes could be placed in the same locations on the subject for each of the next two skin temperature tests. The second set of data was collected under normal conditions, without a fan and at room temperature.

To induce a slightly sweaty skin condition, subjects were asked to exercise just until they felt warm enough to feel somewhat uncomfortable. In the hospital this translates to two scenarios. Firstly, feeling sweaty and warm could occur on the patients' backsides while lying in the hospital bed and waiting for their physician. Secondly, fever and illness could contribute to a patient feeling warm and sweaty. Both cases would lead to an increased pore diameter and the presence of perspiration, so exercise was used to help mimic these skin conditions. These two scenarios mainly consider hospital conditions in the United States. However, in developing countries, it is uncommon for hospitals to have air conditioning. In

the summer months, in such places, many patients would be warm and uncomfortable due to poor climate control in the hospital building.

Figure 6.3 contains the unfiltered ventilation signals for a subject used in this pilot study. The clearest ventilation signal is often obtained by plotting the voltage of an injecting electrode from the same current pattern for all frames. In this test, 31 electrodes were placed around the perimeter of the subject and 150 frames of data was acquired at the 1024 point acquisition rate. In a ventilation signal, voltage measurements increase during an inhale and decrease during an exhale. Signals in Figure 6.3 are at least 5 mV_{pp} when the subject was cool. Ventilation signals corresponding to data taken when the subject was feeling comfortable are approximately 4 mV_{pp} and decrease to 2 mV_{pp} for skip 0 and 2.5 mV_{pp} for skip 2 when the subject was warm and sweaty.

The results of this test suggest that warm and sweaty skin may diminish the quality of data acquired. It is also reasonable to conjecture, from qualitative data noted during the study, the decrease in clarity of the ventilation signal may be related to sweat causing the electrodes to be "less sticky."

6.2.2. Determining the Conductivity of the ECG Electrodes. Conductivity is not typically reported for the hydrogel backing of (electrocardiogram) ECG electrodes. To determine the conductivity of Philips 13951C rectangular neonatal/pediatric solid gel electrodes, the test shown in Figure 6.4 was conducted. ECG electrodes were stuck together and monopolar current was injected.

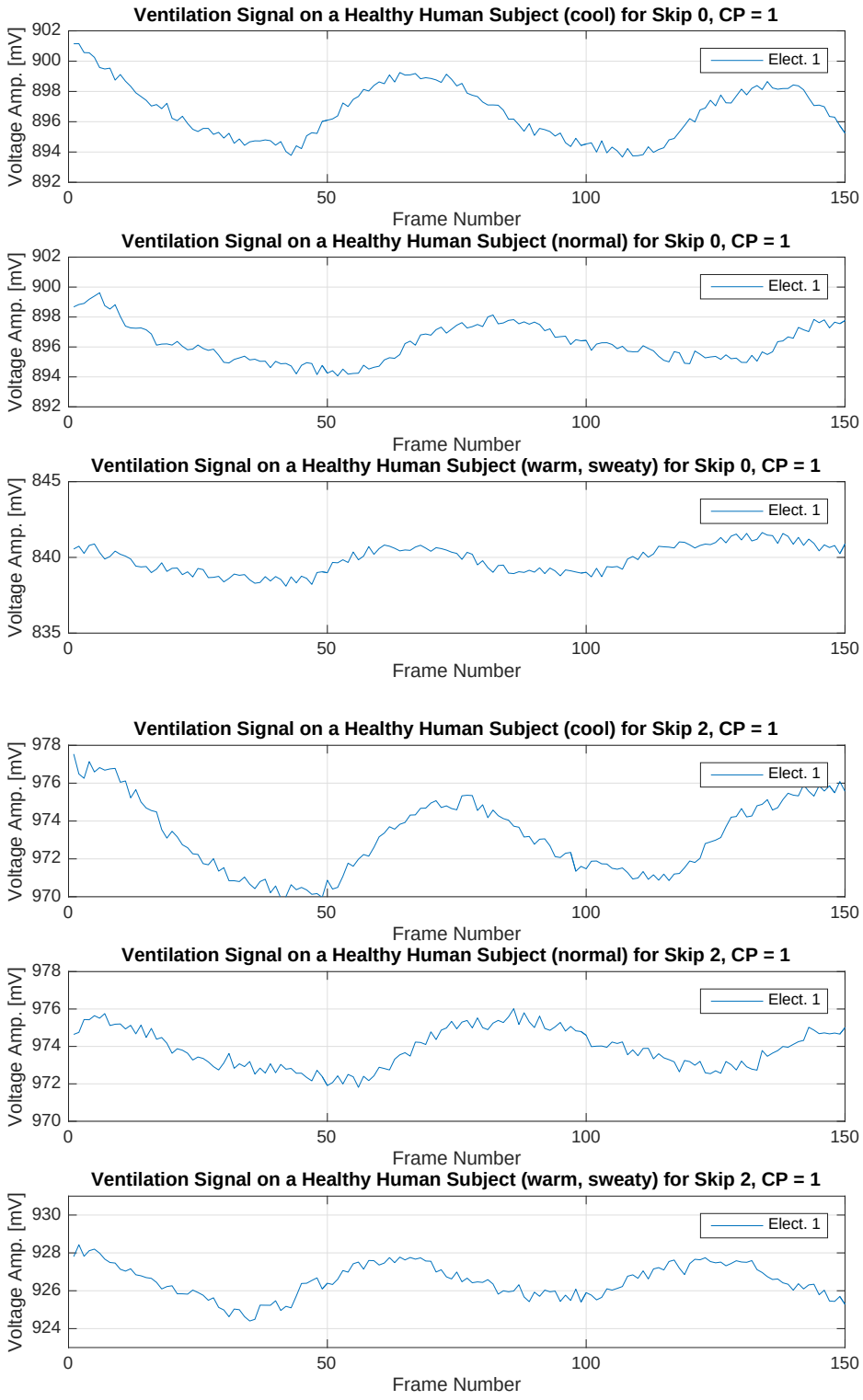

Figure 6.3. Ventilation signals from electrode one on a healthy human subject feeling cool, normal and warm, where the top set of plots is for data taken with skip 0 pattern and the bottom is skip 2.

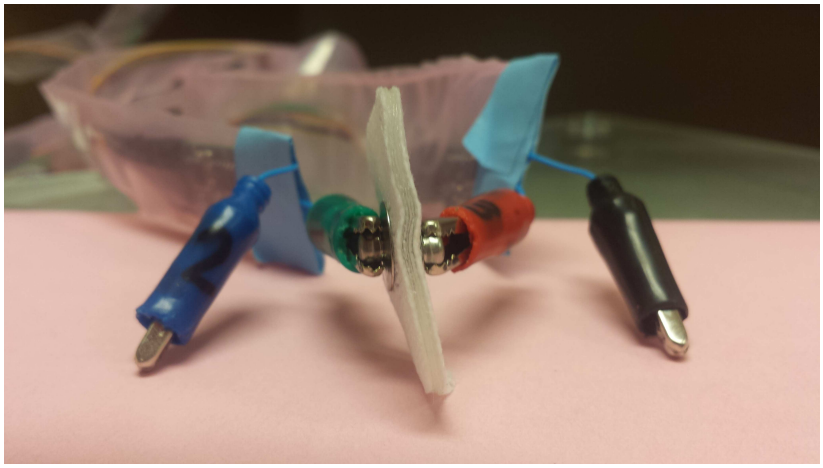

Figure 6.4. Experimental set-up to determine conductivity of ECG electrode gel.

Equations (6.4) - (6.6) were used to approximate the conductivity of the gel (σ_{gel}), where (V_{meas}) is the difference between V_e measurements on either side of the ECG electrodes and $I_{applied}$ is the current injected by the monopolar source. Using Ohm's law, a total impedance (Z_t) for the two electrode gels (Z_{el}) was approximated. The physical dimensions for the electrode area (A_e) of 2.2 cm by 3.3 cm and thickness (t) of 0.1 cm were used to calculate σ_{gel}. For an unused ECG electrode, σ_{gel} was approximately 0.2 mS/cm.

$$Z_t = V_{meas}/I_{applied} \tag{6.4}$$

$$Z_t = 2Z_{el} \tag{6.5}$$

$$\sigma_{gel} = \frac{t}{Z_{el}A_e} \tag{6.6}$$

The same calculations were performed on electrodes saved from the study in Section 6.2.1. It was hypothesized that ECG gel would absorb some sweat, so electrode gel conductivities were approximated from electrodes used on the subject from the normal and warm conditions. Pairs of electrodes adjacent to one another around the perimeter of the chest were used to

determine how the conductivity of the electrode gel changed over the approximate 15 minutes needed to complete data acquisition for each temperature test.

Figure 6.5 shows mean electrode gel conductivity with one standard deviation from worn electrodes. Approximate conductivity values generally seemed to vary depending on whether the subject was sweaty or not and where the electrodes were placed on the perimeter of the subject's chest. Calculated values ranged from approximately 0.25 to 0.65 mS/cm. Electrode gel conductivities from ECG electrodes worn when the subject was warm were found to be generally more conductive compared to when the subject was comfortable. It should be noted that there was no significant change in electrode gel conductivity from electrodes from the right arm pit area of this subject. However, it is possible that results from the arm pit area may have been influenced by antiperspirant.

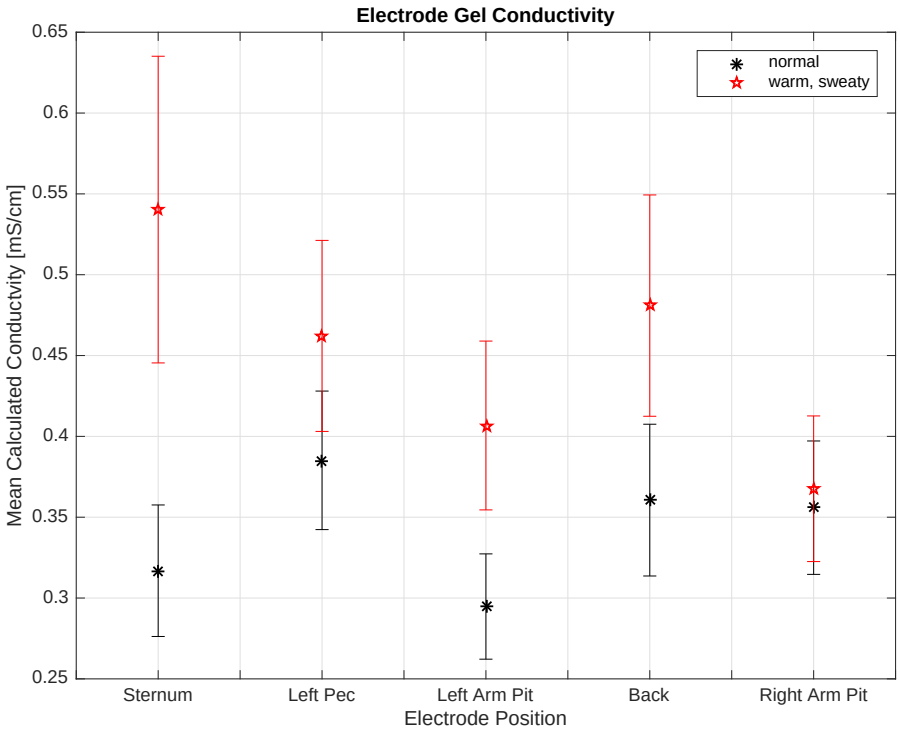

Figure 6.5. Gel absorbence of sweat based on anatomical location.

6.3. Anatomy of the Human Skin

The skin is the largest organ in the human body and plays an important role in protecting the body from the outside environment. The skin is composed for three main layers: the epidermis, dermis and subcutaneous tissue [5], shown in Figure 6.6.

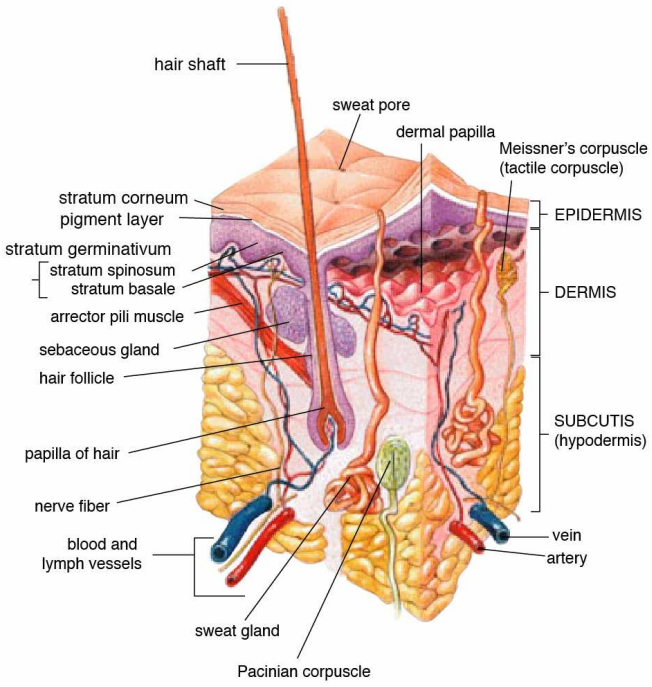

Figure 6.6. The anatomy of the human skin [9].

There are several layers unique to the epidermis. The outermost layer is in the stratum corneum. This layer is comprised of dead cells, called corneocytes. The 10 to 15 layers of corneocytes are filled with the fibrous structural protein keratin and other waxy fats and are approximately 0.05 to 0.15 mm thick. Underneath the stratum corneum are the stratum granulosum, stratum spinosum, and the stratum basale. The lower layers are responsible for the proliferation of keratinocytes and preparing them to become the dead corneocytes found in the outermost layer of skin [5].

The dermis is the skin layer that is found between the epidermis and subcutaneous layers. It is primarily made of connective tissue, such as collagen and other fibers. In addition to containing hair follicles and glands, it also can contain blood and lymphatic vessels. This layer helps provide mechanical support to the epidermis. The dermis ranges in thickness from 1.5 to 4 mm [5].

The nearby subcutaneous tissue is often referred to as the third layer of skin. It primarily contains fat (or adipose) and other fibrous bands and cells which help anchor the skin to deeper tissues. Hair follicle roots also penetrate into this layer. It may also contain nerve endings and typically contains blood and lymphatic vessels that supply the dermis [5].

6.4. Properties of the Human Skin

The changing physical properties of the epidermis cause variations in the electrode-skin contact impedance from person-to-person [89]. Unlike other biological tissues, there is not one routinely cited value for the conductivity and permittivity of the skin because the impedance of the skin is influenced by many things. McAdams and coworkers [4] have investigated factors affecting electrode-gel-skin interface and found that temperature, humidity, and thickness of the stratum corneum (outermost layer of skin) are significant. They also report that as temperature increases, the skin resistance decreases and conjecture that this is due to dilating pores which allow current to pass more easily though the skin. The distribution of sweat ducts, hair follicles, thickness and composition of the stratum corneum are also given in [4]. Relevant features of the human skin are found in Table 6.1.

When measuring the electrical properties of skin, the values will depend secreted amounts of sweat, dilation of nearby blood vessels and moisture content in each of the skin layers [7].

Table 6.1. Anatomical and physiologyical properties of human skin [4–7].

Feature	**Value**
Composition of Stratum Corneum	40 % water 40% protein 20% lipid
Thickness of the Stratum Corneum	10 - 15 μm 12-30 cell layers
Thickness of the Dermis	1.5 - 4 mm
Distribution of Hair Follicles	40 - 70 per cm^2
Distribution of Sweat Ducts	200 - 250 per cm^2
Diameter of Sweat Ducts	5-20 μm
Salt Concentrations of Sweat	0.1 - 0.4% NaCl
Conductivity of 0.5% NaCl (Concentration by Mass)	8.2 mS/cm
Capacitance of Skin (typical)	0.02 - 0.06 μF per cm^2
Isoelectric point of the skin	3 - 4

There are additional miscellaneous factors that are known to cause person-to-person variation in the electrical properties of the skin. Skin impedance is higher for darker-skinned subjects due to a stratum corneum that contains more layers and is more dense. Additionally, abrading the skin (ie, by rubbing) increases capacitance but decreases the resistance. However, rubbing the skin with alcohol will increase resistance since it dries out the skin [4]. It is also reported that the skin is thinner in children than adults. Male skin is also generally thicker than female skin [99] and properties can further vary in the presence of skin pathologies [7].

Some studies suggest that under the application of small currents or voltages, that current passes through the stratum corneum layer through appendageal macropores, or hair follicles and sweat ducts, to reach underlying tissues. Only under the application of a large voltage or current would current pass directly through corneocyte cells instead of shunting around them through pores [10, 100]. Electrode models in EIT, reviewed in Chapter 7, consider the bulk properties of tissue and "skinning effect" of current when it passes between materials

of differing conductivities. The influence of the stratum corneum decreases with increasing frequency [101]. However, a contact impedance remains and is a challenge present in all medical applications of EIT.

At low frequencies (less than 1 Hz), the electrode-electrolyte impedance dominates. At mid range frequencies (between 1 Hz and 10 kHz) the impedance of the skin dominates that of underlying tissue. At frequencies greater than 10 kHz the overall impedance of underlying tissue may be greater [4]. The skin behaves like a capacitor because it is a mostly insulative layer placed between two conductive layers (the electrode and other tissues). The capacitance of human skin ranges from 0.02 to 0.06 μF/cm^2 [4, 7]. Specifically, one group reported 0.0398 μF/cm^2 as the average effective skin capacitance from 145 cadaver skin samples for a measurement setup that included use of two Ag/AgCl electrodes [102]. The capacitive reactance of the skin at 0.025 μF/cm^2 is given in Table 6.2.

Table 6.2. Capacitive reactance of a 1 cm^2 skin section of human skin [7].

Frequency	**Capacitive Reactance**
1 Hz	6.3 MΩ
10 Hz	630 kΩ
100 Hz	63 kΩ
1 kHz	6.3 kΩ
10 kHz	630 Ω
100 kHz	63 Ω

The following calculations suggest that Table 6.2 underestimates the capacitive reactance of the skin. As an example, consider the skin covered by an ECG Ag-AgCl electrode used in EIT data collections with dimensions of 2.2 cm by 3.3 cm comprising the area (A_{elect}). Also consider the thickness (t) of human skin to range from 0.15 cm to 0.40 cm for the epidermis and dermis. Let the skin permittivity (ϵ) value used be 0.02 $\mu F/m$ which is slightly higher than the value given in Table 2.1. Then, one can calculate the capacitive reactance of the

skin at a frequency (f) of 100 kHz using Equation (6.7), which is a modification of Equation (6.6).

$$X_{c\text{skin}} = \frac{t\tilde{\epsilon}}{A_{elect}} \tag{6.7}$$

$$\text{where: } \tilde{\epsilon} = \frac{1}{2\pi f \epsilon} \tag{6.8}$$

In this case, $X_{c\text{skin}}$ is 1.19 kΩ for a 0.15 cm thickness and 3.18 kΩ for 0.40 cm thickness. 1.19 kΩ is near the range of values reported for electrode-skin contact impedance [98] and within the range of load values used to test current sources [103]. Per unit of area, this impedance is larger than the impedance of the solution filling the pores of human skin (tested conductivity values shown in Table 7.2).

6.5. Modeling Current Penetration Through the Skin

The properties of skin can vary, and while EIT generally considers bulk properties of tissues, models of may benefit from considering sub-macroscopic skin anatomy. Presently, models of the skin exist in other fields, but no anatomical or physiologically inspired models have been considered for use in EIT. If such a model would prove feasible, it should also consider the electrode, since skin resistance also varies greatly depending on the type of electrode gel and whether or not one is used [4]. There are several circuit models that have been used to describe the impedance of human skin [104]. However, recent evidence has been found that pores are the primary pathway for current to flow through the skin into the body [105].

Chizmadzhev [10] proposed a model relating to drug delivery through the skin via iontophoresis in which skin appendageal macropores are the pathways for electric current. To

consider this model from the point of EIT, the boundary conditions were modified. An image of the pore model is shown in Figure 6.7. The purpose of testing this model was to consider incorporating skin anatomy and physiology at a sub-macroscopic level to better represent the bulk electrical properties of skin in an EIT forward problem, discussed in Section 7.4.

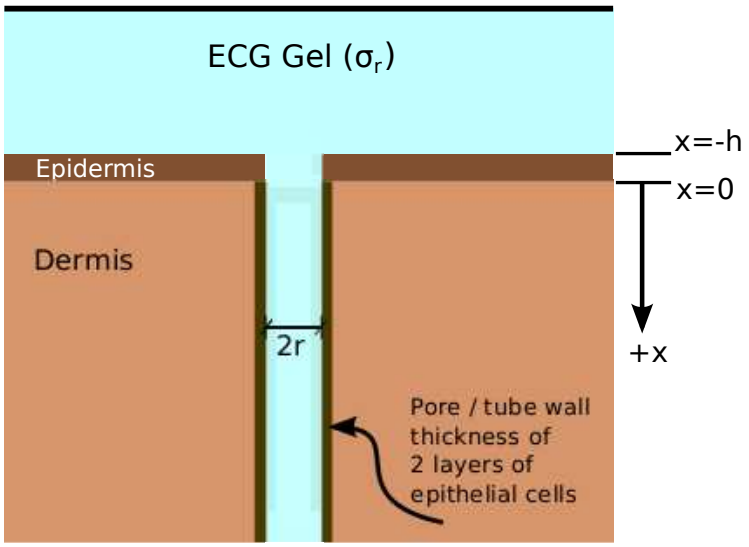

Figure 6.7. The anatomically inspired skin model, modified from the model proposed by Chizmadzhev [10] for use in EIT.

The proposed model [10] was modified for EIT applications to use the applied current (J) touching an individual pore. Assumptions for the model are as follows: (1) The epidermis layer behaves like a perfect insulator of thickness (h) which only allows current to pass through the pores with a mean radius (r), and (2) the pores in the skin are modeled as a semi-infinite tube. Parameters in the model include: voltages (ϕ) associated with each pore, specific capacitance of the pore wall (C_w), conductance of the pore wall (G_w), conductivity of solution filling the pore (σ_r), the cross-sectional area of a single pore (A_{cs}), and a known density of the pores (n). In this model, given in Equations (6.9) - (6.11), σ_r is assumed to

be the electrode gel conductivity.

$$C_w \frac{\partial \phi}{\partial t} = \frac{\sigma_r}{2} \frac{\partial^2 \phi}{\partial x^2} - G_w \phi, \text{ where } x > -h,\ t > 0 \tag{6.9}$$

$$\phi(\infty, t) = 0, \text{ where } t > 0 \tag{6.10}$$

$$-A_{cs}\sigma_r \left.\frac{\partial \phi}{\partial x}\right|_{x=-h} = J \tag{6.11}$$

The application of AC current results in harmonic voltages ($\phi = \widetilde{\phi} e^{i\omega t}$) and currents ($J = \widetilde{J} e^{i\omega t}$) inside the pores, and the partial differential equation described in Equation (6.9) can be reduced to the ordinary differential equation in Equation (6.12) [10]. The upper layer of the skin is assumed to behave like a perfect insulator, forcing current to remain in the pore through the stratum corneum skin layer. This boundary condition is given in Equation (6.13). The semi-infinite tube assumption remains in Equation (6.14).

$$\frac{d^2\widetilde{\phi}}{dx^2} = \underbrace{\frac{2G_w}{\sigma_r}\left(\frac{C_w}{G_w} i\omega + 1\right)}_{\widetilde{b}} \widetilde{\phi} \tag{6.12}$$

$$-A_{cs}\sigma_r \left.\frac{\partial \widetilde{\phi}}{\partial x}\right|_{x=0} = -A_{cs}\sigma_r \left.\frac{\partial \widetilde{\phi}}{\partial x}\right|_{x=-h} = \widetilde{J} \tag{6.13}$$

$$\widetilde{\phi}(\infty) = 0 \tag{6.14}$$

The solution to the ODE is presented in Equation (6.15).

$$\widetilde{\phi}(x) = \frac{\widetilde{J} e^{-\sqrt{\widetilde{b}}x}}{\sqrt{\widetilde{b}} A_{cs} \sigma_r} \tag{6.15}$$

The current ($\widetilde{J}$) used when testing this model is given by Equation (6.16), where $I_{applied}$ is the current applied a an electrode and is relative to the cross-sectional area of a pore (A_{cs})

and electrode area (A_{elect}).

$$\widetilde{J} = I_{applied}\frac{A_{cs}}{A_{elect}} \tag{6.16}$$

Determining an appropriate electrode gel conductivity (σ_r) is difficult. Results from Section 6.2.2 indicate that the hydrogel backing of the ECG electrodes does absorb sweat from the pores of the skin. Although the model illustrated in Figure 6.7 shows only shows gel filling the pore, the gel conductivity could be much greater than the 0.25 to 0.65 mS/cm values obtained from experiments since the conductivity of sweat in the pore may be as high as 8 mS/cm [6].

To best understand the limitations of this model, it was considered in two scenarios. The first scenario assumes that there is little sweat in the pore and that the conductivity of the gel is approximately equal to values found in Section 6.2.2. This scenario will be referred to as the *gel-filled pore* model. The other option to consider is that the pores are sweaty when the gel is applied and/or the subject is secreting sweat during the data collection. In this second scenario, referred to as the *sweaty pore* model, the conductivity value for σ_r in the pore is assumed to be at least the average conductivity value of sweat and the gel. Model parameters used are given in Table 6.3.

Table 6.3. Parameters used in the proposed anatomically inspired skin model.

Model Parameter	**Sweaty Pore**	**Gel-Filled Pore**
Pore Wall Specific Capacitance (C_w)	0.03 μF/cm	0.03 μF/cm
Conductance of Pore (G_w)	0.01 mS/cm	0.01 mS/cm
Conductivity Inside Pore (σ_r)	4 - 8 mS/cm	0.25 - 0.65 mS/cm
Radius of the Pore (r)	20 μm	20 μm
Thickness of the Epidermis (h)	10 μm	10 μm

Another important parameter to consider is the thickness of the skin around the human torso. Though this value is not directly used in the model, it will be considered when integrating this anatomically inspired skin model into the EIT forward problem, discussed in Section 7.4. Considering voltages produced at the 2 to 3 mm distance (or the distance at which the dermis would interface with fat and other subcutaneous tissues) is important for determining the appropriateness of this model in the context of thoracic EIT.

The predicted voltage over a whole electrode ($V_{whole-elect}$), shown in the bottom rows of Figures 6.8 - 6.9, can be calculated with Equation (6.17). In this equation, the number of pores in a single horizontal row ($\widetilde{m}$) across a 2.2 cm wide ECG electrode is used.

$$V_{whole-elect} = \widetilde{m}\widetilde{\phi}(x) \tag{6.17}$$

Voltage amplitude and phase as well as real and imaginary components are shown for the *gel-filled pore* version of the model in Figure 6.8. The *sweaty pore* model plots are given in Figure 6.9. By comparing the two figures, it can be seen that there is a greater decay of voltages along the pore with a σ_r closer to the conductivity of ECG gel for the same C_w. The change in phase is also greater for lower conductivities. In Section 7.4, values consistent with the *sweaty pore* model were not needed. This may be due to use of human subject data for a reference that was from a subject that was not sweaty. However, in future work comparing this model to human subject data, these parameters may be useful.

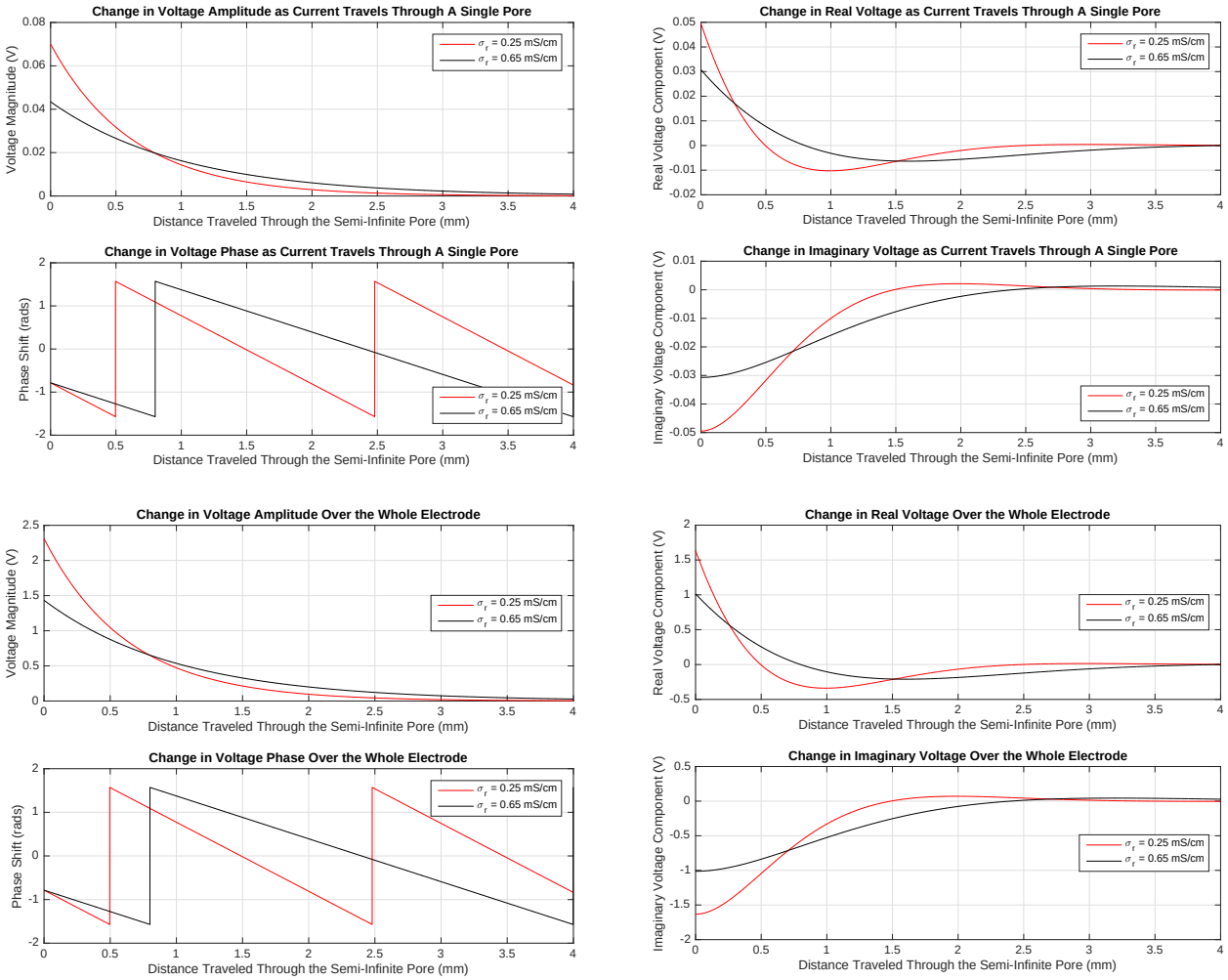

Figure 6.8. Voltages calculated using parameters for the *gel-filled pore* model are given for a single pore (top row) from Equation (6.15) and the whole electrode (bottom row) from Equation (6.17).

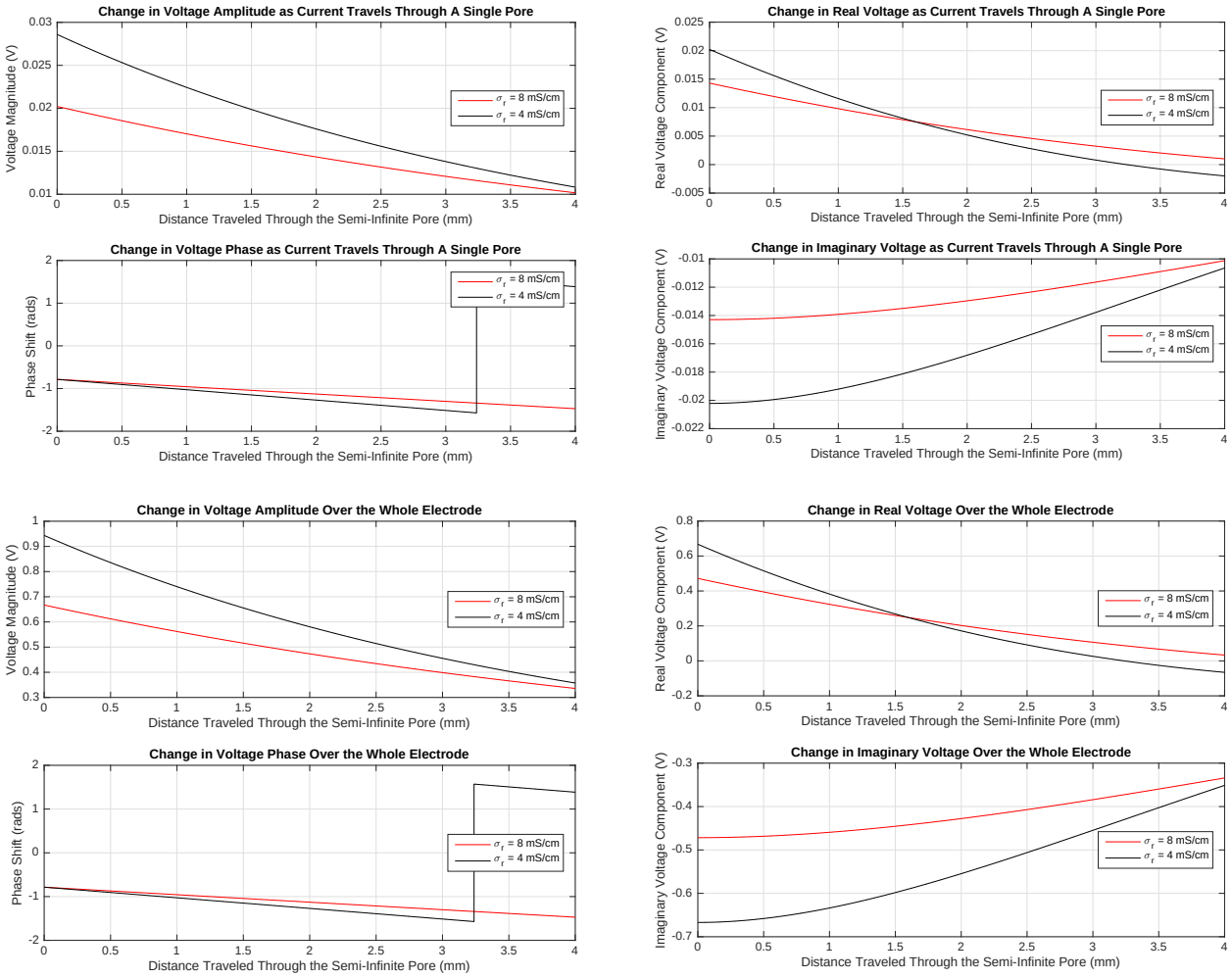

Figure 6.9. Voltages calculated using parameters for the *sweaty pore* model are given for a single pore (top row) from Equation (6.15) and the whole electrode (bottom row) from Equation (6.17).

CHAPTER 7

THE EIT FORWARD PROBLEM

The EIT forward problem is often used to simulate measured voltages on the boundary of a tank phantom or model human cross section. For these models, conductivity with or without permittivity is defined for the interior of the domain as is amplitude and phase of current injected at modeled electrodes around the boundary. By using finite elements, voltages (u) are solved for at discrete points in the interior and at the electrodes around the perimeter of the domain or model.

In this work, the solutions of the 2-D EIT forward problem are compared to data collected with ACE1. Sections 7.2 to 7.3 discuss the background and theory related to finite element formulation and the electrode models used in the forward problem. Initial testing of the forward problem code involved comparing the results to tank phantom data (Section E.1). The forward problem on a human subject mesh is considered in Section E.2. Incorporating an anatomically-inspired model for current flow through the pores of the skin into the finite element code is discussed in Section 7.4, and the results are compared to existing methods.

7.1. The Conductivity Equation

To solve the EIT Forward Problem, the generalized Laplace equation or the conductivity equation as defined by Equation 7.1 is solved for u. The way in which the boundary conditions are described indicates which electrode model is used [2, 106]. Assuming the simplest model, a continuous boundary, the forward problem can be defined by Equation (7.1) and Equation (7.2), where J represents the current density and $\partial/\partial n$ denotes the normal derivative. More accurate electrode models, which replace Equation (7.2), are given in more detail

in Section 7.3.

$$\nabla \cdot \big(\sigma(z)\nabla u(z)\big) = 0, z \in \Omega \tag{7.1}$$

$$\sigma \frac{\partial u}{\partial n}\bigg|_{\partial\Omega} = J \tag{7.2}$$

Equation (7.1) and Equation (7.2) can be derived from Maxwell's equations and the reader is referred to an article by Isaacson, *et al* [107] or the book by Mueller and Siltanen [2] for details. However, it is worth noting that several assumptions are made to obtain the forward problem, including the assumption that the bulk electric and magnetic properties of tissues in the body (or domain) are linear and isotropic [2]. Further any time delay that would exist as current travels through the domain is also neglected. The forward problem can also be posed in terms of the conductivity (σ) and permittivity (ε) of tissues, as shown in Equation (7.3) [2, 108].

$$\nabla \cdot \big((\sigma(z) + i\omega\varepsilon(z))\nabla u(z)\big) = 0, z \in \Omega \tag{7.3}$$

Accurate finite element and electrode models are required for creating absolute image reconstructions corresponding to human subject data, and a solution of the forward problem is generally used a reference for these images. However, the forward solution is dependent upon various factors, including: contact impedance, size of electrodes used, size and shape of the boundary and accurate knowledge of electrode placement [97]. If the model used for the forward problem is accurate enough, the forward problem should be able to be solved to at least the same precision as the measurement system [95, 97]. But, errors in the model

affect the solution to the forward problem, and subsequent use of such a poor model would decrease accuracy of reconstructed absolute images [97].

7.2. Finite Element Formulation

In 2-dimensional finite element method (FEM), the domain (Ω) or area of interest is divided into discrete parts or elements comprising the FEM mesh. It is common to use triangular elements in 2-D EIT. Finite element meshes in this chapter were constructed using Gmsh 2.4.8 software. Individual elements are used to make local conductivity matricies (Ω_i) and later assembled to form the global conductivity matrix ($\mathcal{Y}$). These matricies include conductivity and permittivity information about each element (ρ). Detailed information about use of finite elements for use in the forward problem is given in Appendix D and a brief summary is presented here.

Equation (7.4) describes whether a given node or vertice on the triangle belongs to a particular element. In this equation, n is the number of elements in the mesh, w_i indicates whether nodes are contained in an element ($w_i = 1$ when nodes are contained and $w_i = 0$ when they are not) and u_i is the voltage associated inside a given element.

$$\Omega_i(x, y) = \sum_{i=1}^{n} w_i u_i(x, y) \tag{7.4}$$

To form each local matrix, three basis functions (Equations (7.7) - (7.9)) are needed. For a triangular element, these functions are linear and are of the form given in Equation (7.5), where i is an index identifying an i-th element. In EIT, u_i represents the the voltage

associated with the i-th element.

$$u_i(x, y) = a_i + b_i x + c_i y \tag{7.5}$$

Equation (7.6) shows the 3x3 matrix that is formed for each element from the three nodes defining it. The coefficients used in the basis functions can be found by inverting the following matrix, which incorporates (x, y) locations of the element's three nodes and the unknown voltages at the nodes of the triangle (u_{i,n_1}, u_{i,n_2}, u_{i,n_3}).

$$\begin{bmatrix} 1 & x_1 & y_1 \\ 1 & x_2 & y_2 \\ 1 & x_3 & y_3 \end{bmatrix} \begin{bmatrix} a_i \\ b_i \\ c_i \end{bmatrix} = \begin{bmatrix} u_{i,n_1} \\ u_{i,n_2} \\ u_{i,n_3} \end{bmatrix} \tag{7.6}$$

Inversion of the matrix with nodal (x,y) locations results in the area of the i-th element (A_e), α, β, and γ.

$$f_1 = \frac{1}{2A_e}\left(\alpha_1 + x\beta_1 + y\gamma_1\right) \tag{7.7}$$

$$f_2 = \frac{1}{2A_e}\left(\alpha_2 + x\beta_2 + y\gamma_2\right) \tag{7.8}$$

$$f_3 = \frac{1}{2A_e}\left(\alpha_3 + x\beta_3 + y\gamma_3\right) \tag{7.9}$$

Derivatives of these functions are used in the calculation of the local conductivity matrix, shown in Equation (7.10), details for which are found in Appendix D.

$$\Omega_i = \frac{h}{4A_{e_i}\rho_i} \begin{bmatrix} \beta_1^2+\gamma_1^2 & \beta_1\beta_2+\gamma_1\gamma_2 & \beta_1\beta_3+\gamma_1\gamma_3 \\ & \beta_2^2+\gamma_2^2 & \beta_2\beta_3+\gamma_2\gamma_3 \\ sim. & & \beta_3^2+\gamma_3^2 \end{bmatrix} \tag{7.10}$$

To solve the finite element problem, local matrices are assembled into the global conductivity matrix. The psuedo-inverse of the global conductivity matrix multiplied by the a current matrix containing the imposed current patterns on nodes in the mesh yields voltage values for all nodes in the mesh. Voltages on nodes for the electrodes can be compared to voltages measured during ACE1 acquisition to determine how well the solved forward problem models the system.

7.3. Electrode Models

Without a good forward problem FEM model, simulated voltage results will not be similar to experimental measurements [95, 106]. Edge and shunt effects should be considered [93] because they are known properties of current flowing through materials with different conductivities.

7.3.1. The Gap Model. The simplest way to model current flowing into the domain through electrodes is to discretize the continuous model in Equation (7.2) which creates the gap model. In the gap model, the current density (J) over the area of the electrode (A_{e_l}) is uniform. Nodes are either considered to be part on an electrode or not. When current is

being injected, J is imposed only on injecting electrode nodes on the boundary [2, 106]:

$$J(z) = \begin{cases} \frac{I_l}{A_{e_l}} \text{ if z lies on electrode } e_l, l = 1, 2... \text{ L} \\ 0 \text{ off } \cup_{l-1}^{L} e_l \end{cases} \tag{7.11}$$

Although this model is not sufficient to model the electrode-saline interface of a tank phantom or electrode-skin interface on human subjects, it was studied in this work.

7.3.1.1. *Gap Model Simulations.* Two different meshes were tested to determine the best way to implement the gap model using finite elements. Both meshes contain two anatomically relevant layers, a more refined 0.25 cm upper skin layer and a lower layer assigned the admittivity of fat. The first mesh contains 24,320 elements including elements for an electrode. Current is imposed on 64 nodes on top of the electrode elements. The other mesh assumes that if the electrode is a perfect conductor, currents on boundary nodes defining the electrode are known. The second mesh contains 22,272 elements and 64 nodes where current is imposed on the skin surface. A plot of the nodal potentials for injecting nodes is given for the two meshes in Figure 7.1.

If the nodal potentials from Figure 7.1 are summed, the mesh with the gel has a voltage of 25.4 V and the mesh without the gel is 0.0729 V. The maximum voltage on a single node for the mesh with the gel is still too large when compared to measured data. The mesh that imposes currents directly on the skin boundary predicts values that are closer to measured data for the same amount of injected current, so this implementation is used in development of the anatomically inspired model.

7.3.2. The Shunt Model. The flow of electric current will preferentially take the path of least resistance. When a low resistance route is created for current to flow around an area

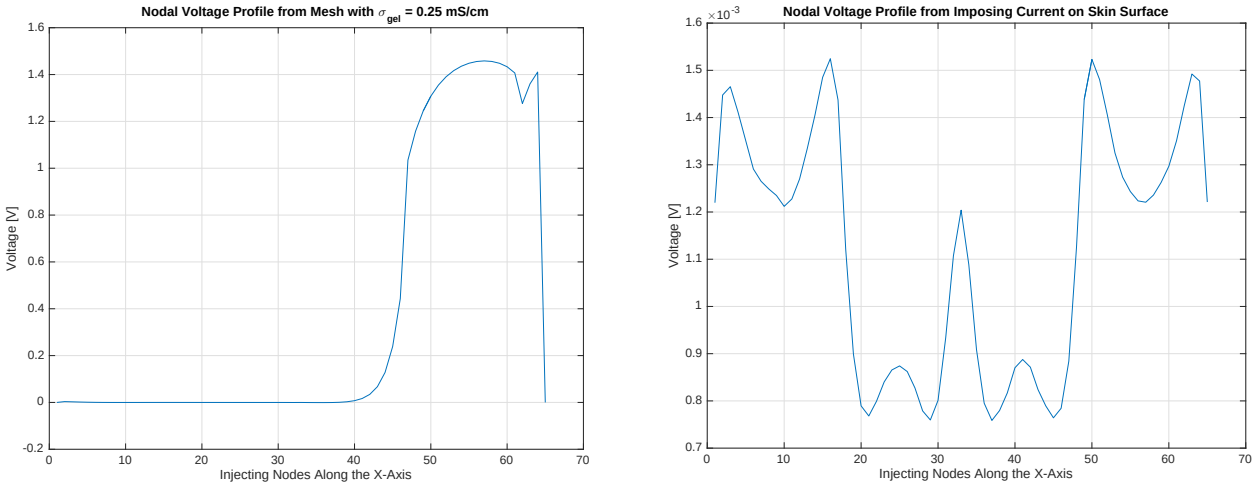

Figure 7.1. A plot nodal potentials for injecting nodes for the mesh with electrode element conductivities of 0.25 mS/cm (left) and the mesh where currents are imposed directly long the skin (right).

of higher resistance, this is sometimes referred to as a shunt. Adding the shunt condition to the gap model accounts for non-uniform distribution of current across an electrode. In the shunt model, the current density over the electrode is described as a function, shown by Equation (7.12) [2, 106]. Figure 7.2 shows an example of what the current density might look like over the cross-section of the electrode [95].

$$\int_{e_l} \sigma \frac{\partial u}{\partial \nu} dS = I_l^n, l = 1, 2...L \tag{7.12}$$

$$\sigma \frac{\partial u}{\partial \nu} = 0 \text{ off } \cup_{l-1}^{L} e_l \text{ on } \partial\Omega \tag{7.13}$$

7.3.3. The Complete Electrode Model (CEM). Solving the forward problem with the Complete Electrode Model (CEM) is acceptable for ACE1 system use on tank phantoms. The electrode-skin impedance is also somewhat accounted for in the CEM with the parameter Z_{e_l}, or the contact impedance on a given electrode e_l for L number of electrodes. The CEM changes the boundary conditions for voltage to the Robin boundary condition in Equation

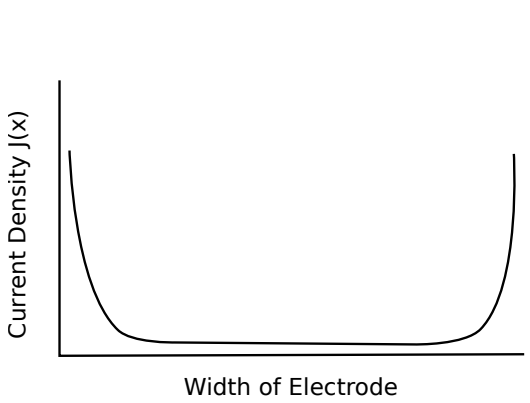

(a) A possible 'U" shape current density profile across a single injecting electrode.

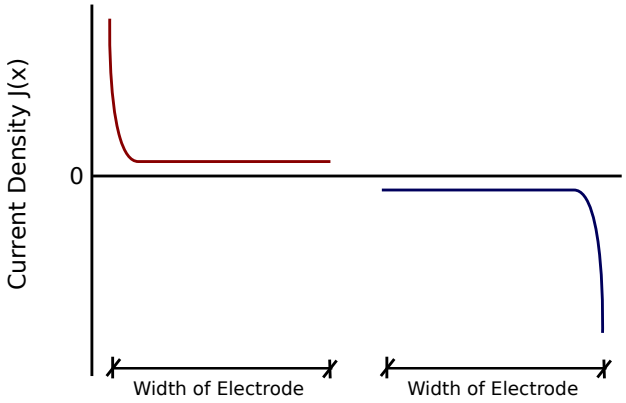

(b) Another possible "L" shape current density profile across adjacently injecting electrodes of a bipolar source.

Figure 7.2. Examples of shunt model current densities.

(7.14). The conductivity (σ) is assigned through elements in a FEM mesh and electrical potentials or voltages are recovered in the interior (u). Equation (7.12) and Equation (7.13) from the shunt model in addition to Equation (7.15) describe the CEM on the domain (Ω), where the injected currents (I) are known, and one solves for the measured voltages (U_l^n) on the boundary ($\partial\Omega$) [2].

$$u + Z_{e_l}\sigma\frac{\partial u}{\partial \nu} = U_l^n \text{ on } e_l, l = 1, 2, \ldots \text{ L} \tag{7.14}$$

Kirchhoff's voltage and current laws apply to ensure uniqueness of the solution:

$$\Sigma_{l=1}^{L} I_n^l = 0,\ \Sigma_{l=1}^{L} U_l^n = 0 \tag{7.15}$$

A common implementation of the CEM is the Hua model, which was originally proposed for use with rectangular elements [98]. However, assuming the thickness of the electrode is much less than the width, the rectangular elements can be simply mapped to triangular ones. When using the finite element method, the following conductivity matrix for a Hua

element can be incorporated into the global matrix for electrode elements [109]:

$$\nabla \mathcal{Y}_{hua_i} = \frac{ba}{6t\rho} \begin{bmatrix} 2 & 1 & -3 \\ & 2 & -3 \\ sim. & & 6 \end{bmatrix} \tag{7.16}$$

Often the thickness (t) and resistance of the electrode (ρ) of Equation 7.16 are combined into the electrode parameter $\rho' = \rho t$ [109]. Some groups have worked to improve upon this model. In 2009, the group at RPI proposed a method for computing a variable contact impedance with the CEM through a nonlinear optimization approach [94].

7.3.3.1. *CEM - Skin Interface Simulations.* A mesh with 22,336 elements and 64 electrode elements, shown in Figure 7.3, was constructed to investigate the flow of current through the skin. The mesh contains two layers, a 0.25 cm upper skin layer and a lower layer assigned the admittivity of fat. The admittivity of skin was varied from one to eight times the values given in Table 2.1.

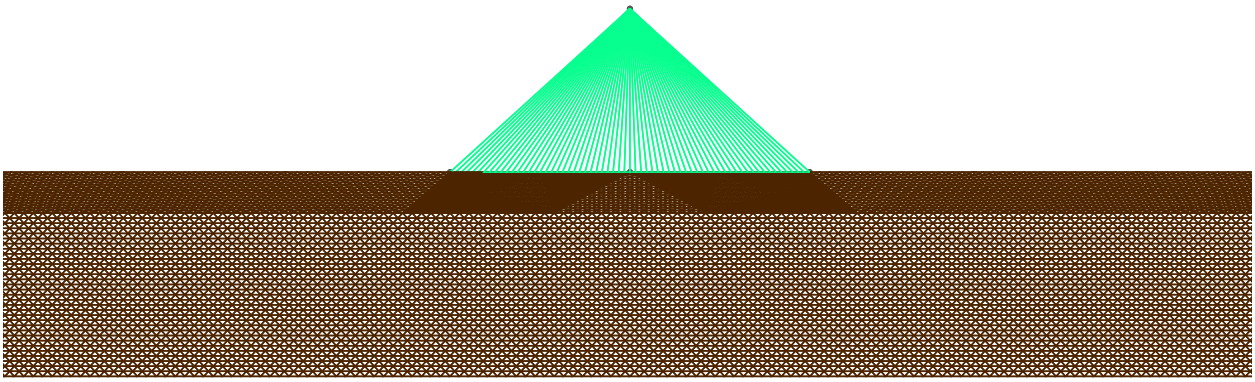

Figure 7.3. The finite element mesh with a single CEM electrode made of 64 elements on a layer of skin and fat.

A colormap of nodal potentials for FEM simulation results are shown in Figure 7.4 where the electrode is located on the skin boundary from 3.9 to 6.1 cm on the x-axis. The large electric potential drop created by the skin is shown by the plot with normal skin conductivity. The "skinning" effect can be observed in the horizontal spreading of the larger voltages (or yellow region) in the skin layer. An increase in conductivity of the skin lessens the skinning effect and allows for current to pass more easily from the skin to lower layers. Changes can in skin conductivity can occur for a variety of reasons, discussed in Section 6.4, so visualizing its effects through finite elements is helpful to provide intuition about how sensitive the simulated voltages are to these differences.

7.3.4. The Patacon Model. Another approach to contact impedance involves using many elements. In the dissertation of Olavo Luppi Silva, the Patacon model is suggested. In this approach, 3-dimensional electrode mesh elements are refined to approximately 700,000 elements. The electrode is divided into two layers. The outer most layer is assigned the resistivity value of stainless steel ($1.0\text{x}10^{-8}$ Ω/m) and inner layer is set to try to best mimic contact impedance [93].

In general, though refining the mesh in EIT forward models is computationally expensive, more accurate results can be obtained. Additionally, it is suggested for use with this model that a more refined mesh near the electrode will better represent electrical potentials associated with the edge and shunting effects of current [93].

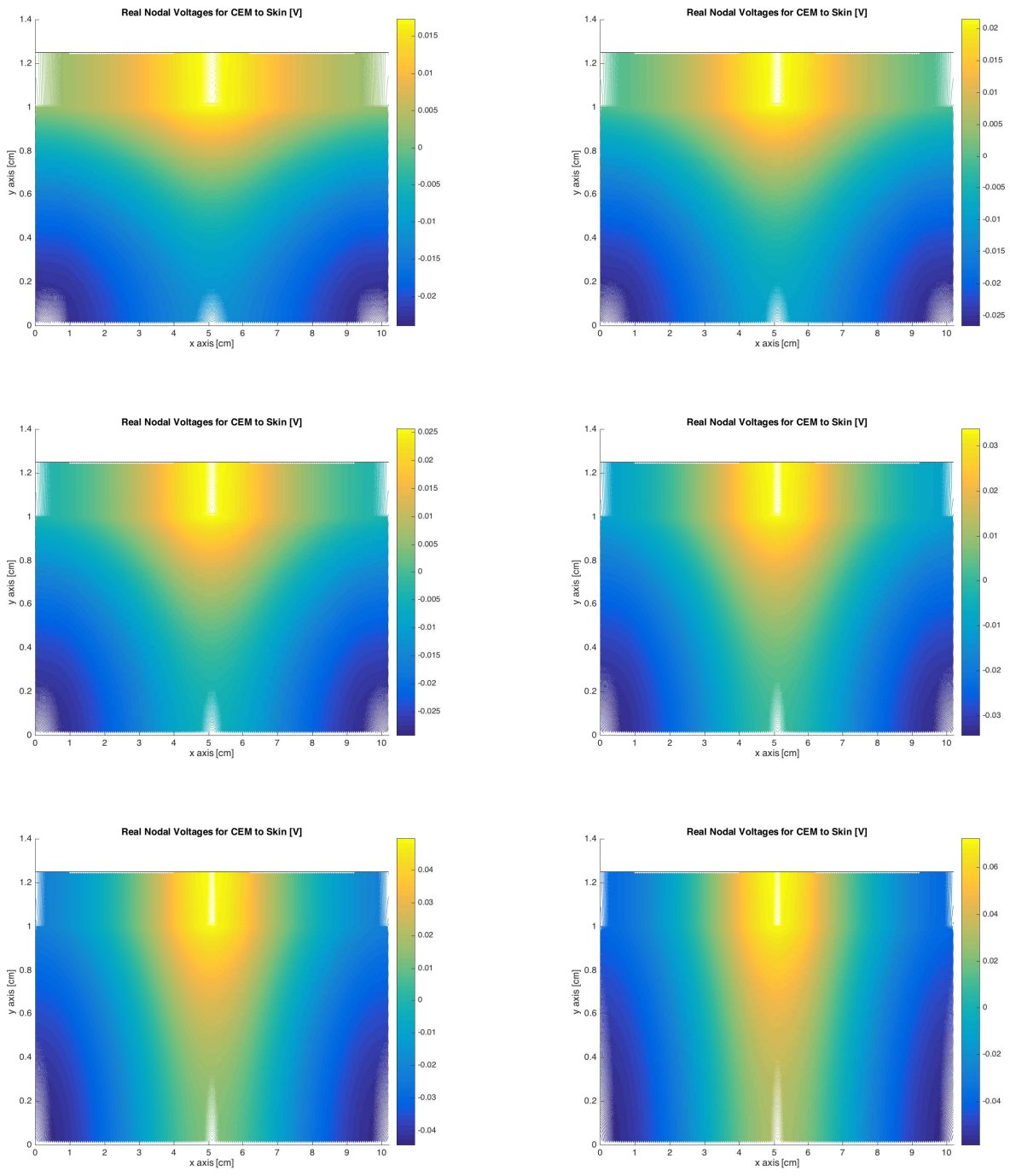

Figure 7.4. Nodal voltage potentials for electrode parameter of 3.84 mS/cm and varying skin conducitivites, from left to right: (Row 1) 0.0012 mS/cm, x 0.0018 mS/cm, (Row 2) 0.0024 mS/cm, 0.0036 mS/cm, (Row 3) 0.006 mS/cm and 0.0096 mS/cm. The electrode is located on the boundary from 3.9 to 6.1 cm on the x-axis.

7.4. Implementing an Anatomically Inspired Electrode Model

The proposed anatomically inspired model [10] that was modified for EIT applications and discussed in Section 6.5 is further described in this section in the context of integration into the finite element forward problem. Model parameters are restated here for convenience; they include: harmonic voltages ($\phi = \widetilde{\phi} e^{i\omega t}$) associated with each pore, currents ($J = \widetilde{J} e^{i\omega t}$) inside each the pore, specific capacitance of the pore wall (C_w), conductance of the pore wall (G_w), conductivity of solution filling the pore (σ_r), the cross-sectional area of a single pore (A_{cs}), a known density of the pores (n), and σ_r is assumed to be the electrode gel conductivity.

When solving the ODE, Equation (7.17) or a function for voltage along a pore is found. However, to easily implement this model in the forward problem, it is desirable to have boundary conditions in terms of current. The results from Section 6.5 are modified here to give $\widetilde{J}_{pore}$ in Equation (7.20), or the corresponding current imposed at a node in the FEM mesh. Equations (7.17) - (7.20) describe how the boundary conditions were modified to be in terms of current to best integrate with the forward problem EIT finite element code. Note that $\partial/\partial\nu$ refers to the outward normal derivative which is chosen to be parallel to the pore so that $\partial/\partial\nu = \partial/\partial x$.

$$\widetilde{\phi}(x) = \underbrace{\left(\frac{\widetilde{J}}{\sqrt{\widetilde{b}} A_{cs} \sigma_r} \right)}_{C} e^{-\sqrt{\widetilde{b}} x} \tag{7.17}$$

$$\text{where: } \widetilde{b} = \frac{2G_w}{\sigma_r} \left(\frac{C_w}{G_w} i\omega + 1 \right) \tag{7.18}$$

$$\frac{\partial \widetilde{\phi}}{\partial x} = -C \sqrt{\widetilde{b}} e^{-\sqrt{\widetilde{b}} x} \tag{7.19}$$

$$\widetilde{J}_{pore}(x) = \frac{-\widetilde{J}}{A_{cs}} e^{-\sqrt{\widetilde{b}}x} \tag{7.20}$$

Another important parameter to choose is the thickness of the skin (x_{sub}) or where subcutaneous tissue and fat begin. This information can be accurately obtained if ultrasound images of a subject's skin are obtained. In the finite element mesh, these boundary conditions are imposed at nodes dividing the skin and fat layers (or the *new boundary* with $\widetilde{m}$ nodes) as described in Equation (7.21).

$$J(x_{sub}) = \begin{cases} \widetilde{J}_{pore}(x_{sub}) \text{ where: x is a node on the } \textit{new boundary}\text{, x = 1, 2... } \widetilde{m} \\ 0 \text{ off the } \textit{new boundary} \end{cases} \tag{7.21}$$

Each node on the boundary corresponds to a single pore, and spacing nodes in the FEM mesh is determined using a typical pore density of 240 pores/cm^2. Figure 7.5 shows the 51 by 33 pore grid created from the 2.2 by 3.3 cm ECG electrode size. A single row used in the 2-D foward problem considers 33 pores and results are multiplied by "height" of the electrode, which is approximately 51 rows.

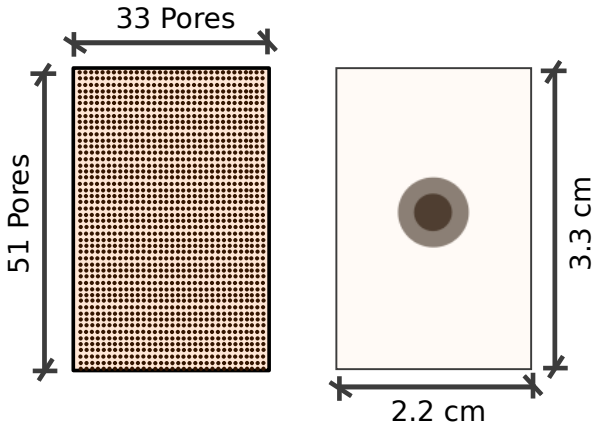

Figure 7.5. Spacing of pores (left) corresponding to an ECG electrode with size 2.2 cm by 3.3 cm (right).

7.4.1. Creation of an Anatomically Representative Mesh. The need for incorporating anatomical features into the EIT forward problem for various EIT applications has been investigated by many research groups. In 2001, Bayford and colleagues proposed using integrated design engineering analysis software to incorporate MRI brain scans into their forward models [110]. Later, Tizzard used registered medical images of patients to further customize head anatomical models to be specific to each subject [111]. A highly detailed anatomically realistic forward solver for the chest was proposed in 2013 by Yang which uses conductivity values only. Yang's work is most related to what is proposed in this section. However, no skin layer is included in the proposed model, nor is any information about a corresponding appropriate electrode model [112]. Anatomical information can also be incorporated into EIT reconstruction algorithms, such as use of an anatomical atlas by Camargo [51] and use of *a priori* data in the D-bar algorithm by Alsaker [113].

However, in this work, a detailed anatomical model reflecting the general bulk properties of organs is presented with information about electrode spacing or placement. To create a forward model that better matches measured voltages, accurate modeling of the boundary shape and placement of electrodes is needed [97]. Flexible rulers were used to obtain the best approximate chest shape of the subject and mark the position of electrode centers. In Figure 7.6, ACE1 placement is shown on an eight year old body and the corresponding cross-section used to create the FEM mesh.

Information about placement of human anatomy was used from a random CT scan of a healthy human subject to add lungs, heart, ribs and spinal column, corresponding to conductivity and permittivity values in Table 7.1. These organs were stretched to fit shape

of the cross section shown in Figure 7.6. A skin layer and fat layer were also added to model. The average thickness for human skin was used (0.254 cm) and 0.76 cm for the fat layer.

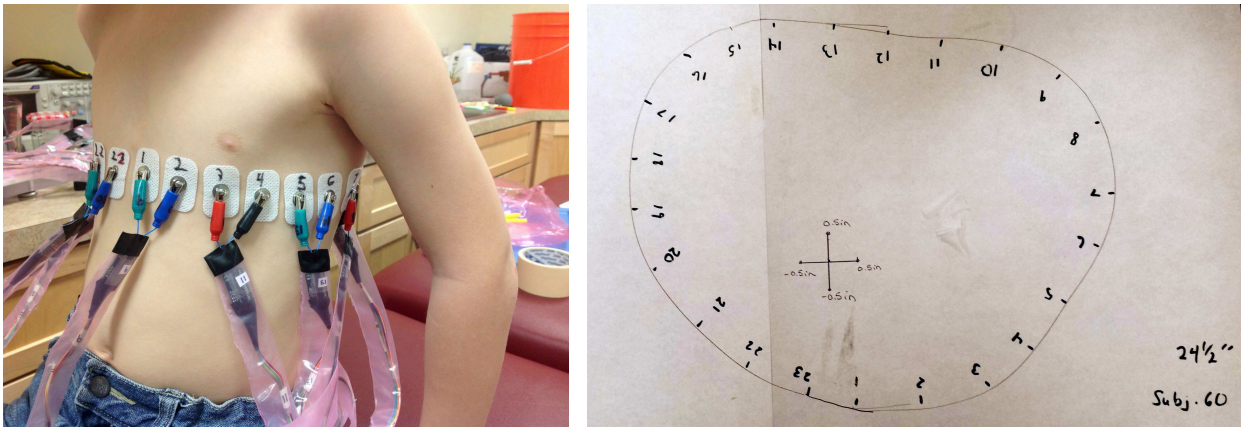

Figure 7.6. An image of the healthy human subject volunteer (left) and the cross-section of electrode placement obtained with use of flexible rulers (right).

Table 7.1. Values used (which are relevant at approximately 100 kHz) in the anatomical forward problem model for subject 60 [2].

Anatomy	Conductivity $[mS/cm]$	Permittivity $[\mu F/m]$
skin	0.0012	0.0144
fat	0.36	0.18
lung	0.7	0.22
bone	0.06	0.0027
aorta	6.7	0.05
spinal fluid	15.4	0
heart	4.3	0.62
background	2	0

7.4.1.1. *Set-up in the Finite Element Mesh.* In the lower image of Figure 7.7, a magnified image of the refined elements in the skin layer is shown. Shown in this image are the 33 equally spaced nodes defining the locations of pores conducting current for a given electrode along the outside boundary of the skin layer. In addition, 33 nodes are specified at the skin-fat interface. To incorporate the model into the forward problem, the skin layer was assumed

to be an additional fat layer and the model currents were imposed on the 33 electrode nodes of the outermost boundary.

7.4.2. Comparisons of Different Electrode Models and Human Subject Data. To best understand the limitations of this model, it was compared to the gap model, CEM model and measured data taken on a healthy human volunteeer. The finite element meshes in Figure 7.7 and Figure 7.8 contain a refined skin layer. Elements in the model were assigned admittivity values appropriate to the anatomy in the cross-section and are consistent with values stated in Table 7.1. To ensure that differences in the model were not due to refinement in skin and fat layers, the complete electrode model mesh (Figure 7.8) is identical to the mesh used for the anatomically-inspired and gap models, with the exception of additional Hua electrode elements.

7.4.2.1. *Implementing the Anatomically Inspired Model.* The best way to implement the anatomically inspired model into the mesh shown in Figure 7.7 is to assign the skin layer the same admittivity value as fat. Current is imposed on the 33 nodes on the outermost layer that define each electrode on the mesh. It should be noted that this method of implementing increases the fat layer in this test, so in future work, it would be recommended that one "strips" the skin layer from the mesh as it is not needed with this model. Figures containing plots of simulated real electrode voltages for a single current pattern is compared for the anatomically-inspired model, other electrode models and real data in this section.

The imposed currents $J_{imposed}$ that work best are given by Equation (7.22), where $I_{applied}$ is the total current applied to an electrode. n is the number of pores. This is more consistent

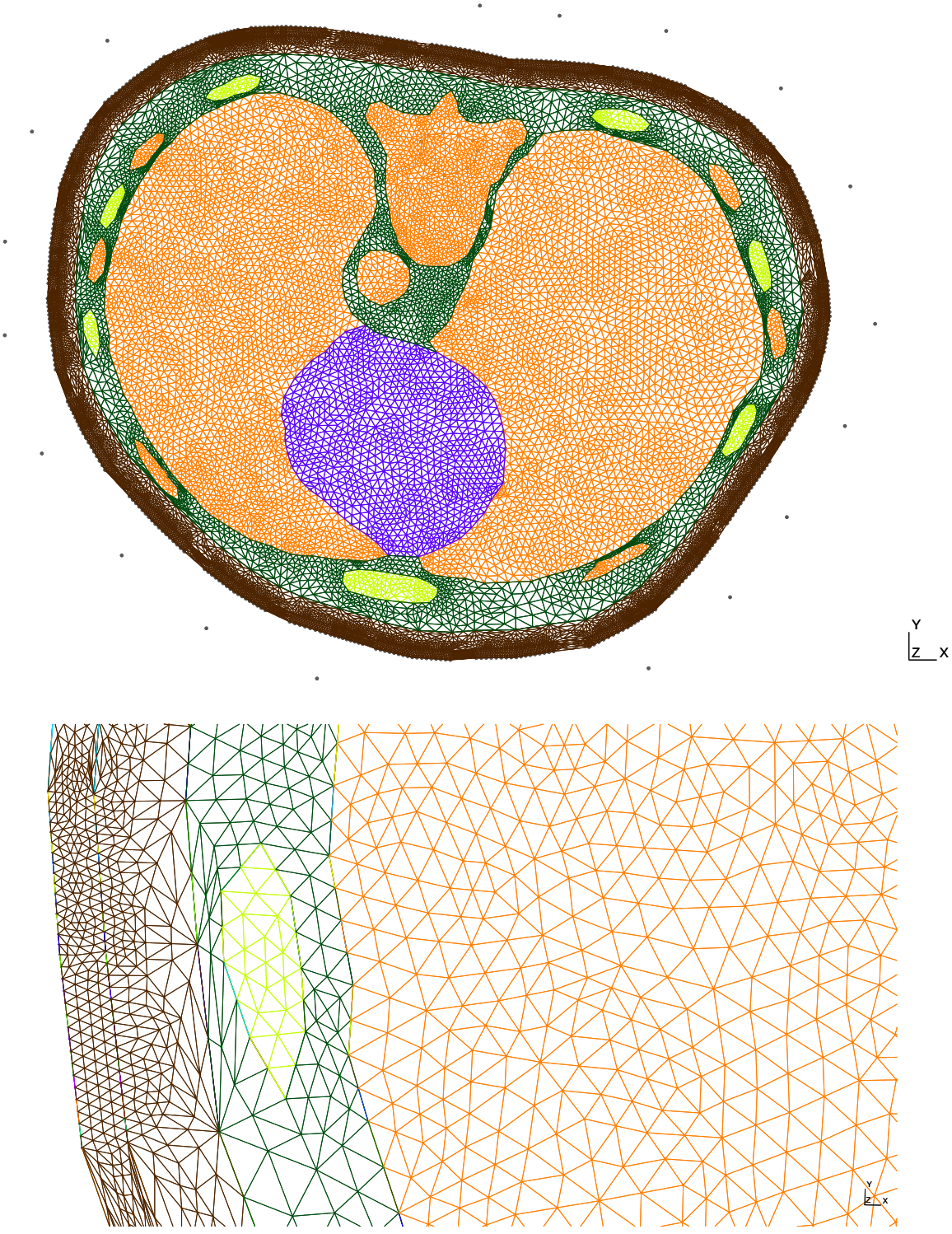

Figure 7.7. The mesh (top) used for both the antomically inspired model and gap model. The mesh elements are more refined near electrode nodes (bottom).

with the current used in the model in Section 6.5.

$$J_{imposed} = I_{applied}/n \tag{7.22}$$

The solution to the forward problem gives voltages at nodes on the outer fat layer corresponding to injecting electrodes ($V_{inj-node}$) and non-injecting electrodes ($V_{mease-node}$). Equations (7.23) - (7.24) describes how electrode voltages are calculated for injecting and non-injecting electrode nodes. Electrode voltage values for $V_{elect-inj}$ or $V_{elect-meas}$ are obtained by summing the corresponding predicted nodal electrode voltages ($V_{elect-node}$) over the number

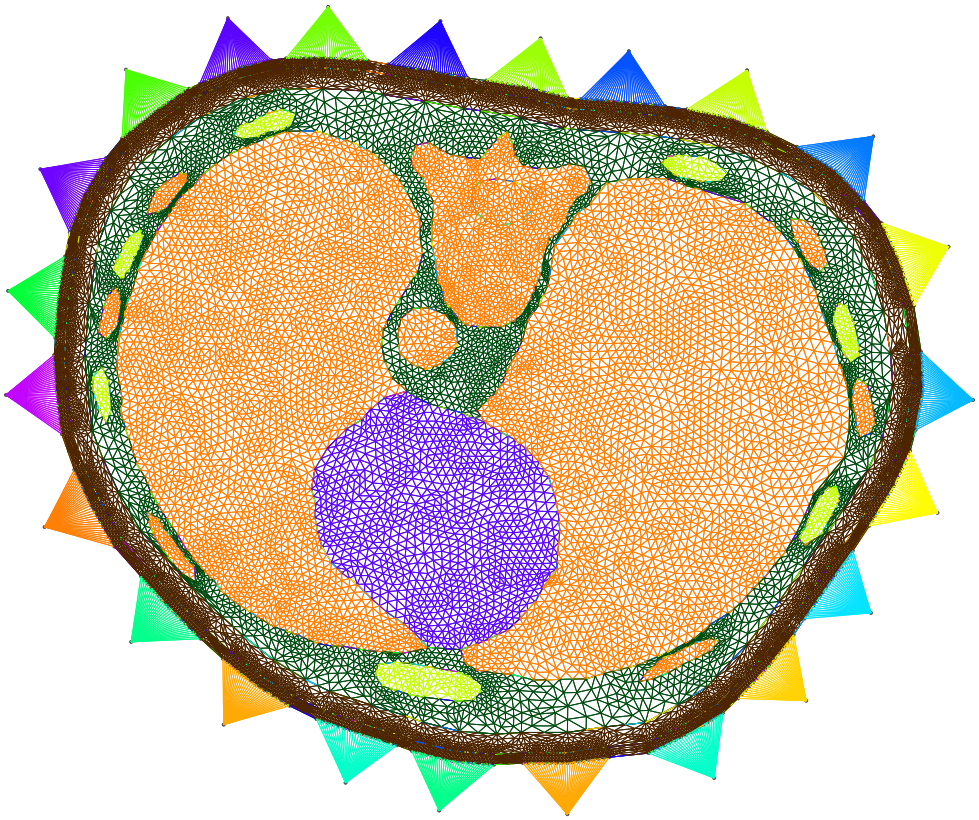

Figure 7.8. Incorporating 32 Hua elements onto the same mesh shown in Figure 7.7.

of nodes comprising each horizontal slice of the electrode ($\widetilde{m}$), shown in Equation (7.25).

$$V_{elect-inj} = V_{inj-node} e^{\sqrt{\tilde{b}} x_{sub}} \tag{7.23}$$

$$V_{elect-meas} = V_{m-node} e^{-\sqrt{\tilde{b}} x_{sub}} \tag{7.24}$$

$$V_{elect} = \sum_{m=1}^{\widetilde{m}} {V_{elect-node_l}}^{k}(m) \tag{7.25}$$

Table 7.2 lists parameters used to obtain some of the best initial results with this model. Figure 7.9 shows these results for a typical current pattern, where a uniform current distribution was used. The new model is good at predicting voltage values on injecting electrodes and the neighbors and either side. It displays consistent behavior for all current patterns.

Table 7.2. Parameters used in the proposed anatomically inspired skin model.

Model Parameter	**Recommended Range of Values**
Pore Wall Specific Capacitance (C_w)	0.05 - 0.08 μF/cm
Conductance of Pore (G_w)	0.01 mS/cm
Conductivity Inside Pore (σ_r)	0.3 - 0.6 mS/cm
Radius of the Pore (r)	20 μm
Thickness of the Epidermis (h)	10 μm

Error for each of the different models was calculated. The error (ε) is defined as the difference from the simulated data (${V_{e-sim}}_l^k$) to the real voltage measurements (${V_{e-meas}}_l^k$) for each electrode (l) and current pattern (k), shown in Equation 7.26. Figure 7.10 shows the error for several different current patterns. Percent error (ε_{per}) is given in Table 7.3. Figure 7.11 plots error for only the injecting electrodes for the CEM and new model.

$$\varepsilon = {V_{e-sim}}_l^k - {V_{e-meas}}_l^k \tag{7.26}$$

$$\varepsilon_{per} = \left(\left({V_{e-sim}}_l^k - {V_{e-meas}}_l^k \right) / {V_{e-meas}}_l^k \right) * 100 \tag{7.27}$$

Table 7.3. Percent error of the different electrode models with one standard deviation.

Model	**Percent Error on Injecting Electrodes**	**Percent Error on the 3 Neighboring Electrodes**
Gap	1.95 % ± 2.48 %	257 % ± 1392 %
CEM ($\rho' = 3.48$)	1.54 % ± 0.98 %	179 % ± 553 %
Anatomical ($\sigma_r = 0.525$ mS/cm, $C_w = 0.075$ μF/cm, uniform)	1.56 % ± 3.46 %	160 % ± 431%
Anatomical ($\sigma_r = 0.35$ mS/cm, $C_w = 0.05$ μF/cm, uniform)	1.56 % ± 3.46 %	160 % ± 431%

There are several conclusions that can be made of about this new electrode model. The anatomically-inspired model is about as good at predicting the voltages on injection electrodes as the CEM. It does slightly better at predicting voltages on neighboring electrodes to injecting electrodes than the other methods test. But, it is poor at predicting voltages on electrodes far from the injecting electrodes, and performs about as well as the gap model in this case. Testing in this section suggests that it is a viable method for predicting some electrode voltages in simulations for skip 0 current patterns. Future work using this model should consider combining the CEM with this new method to try to generate more accurate results.

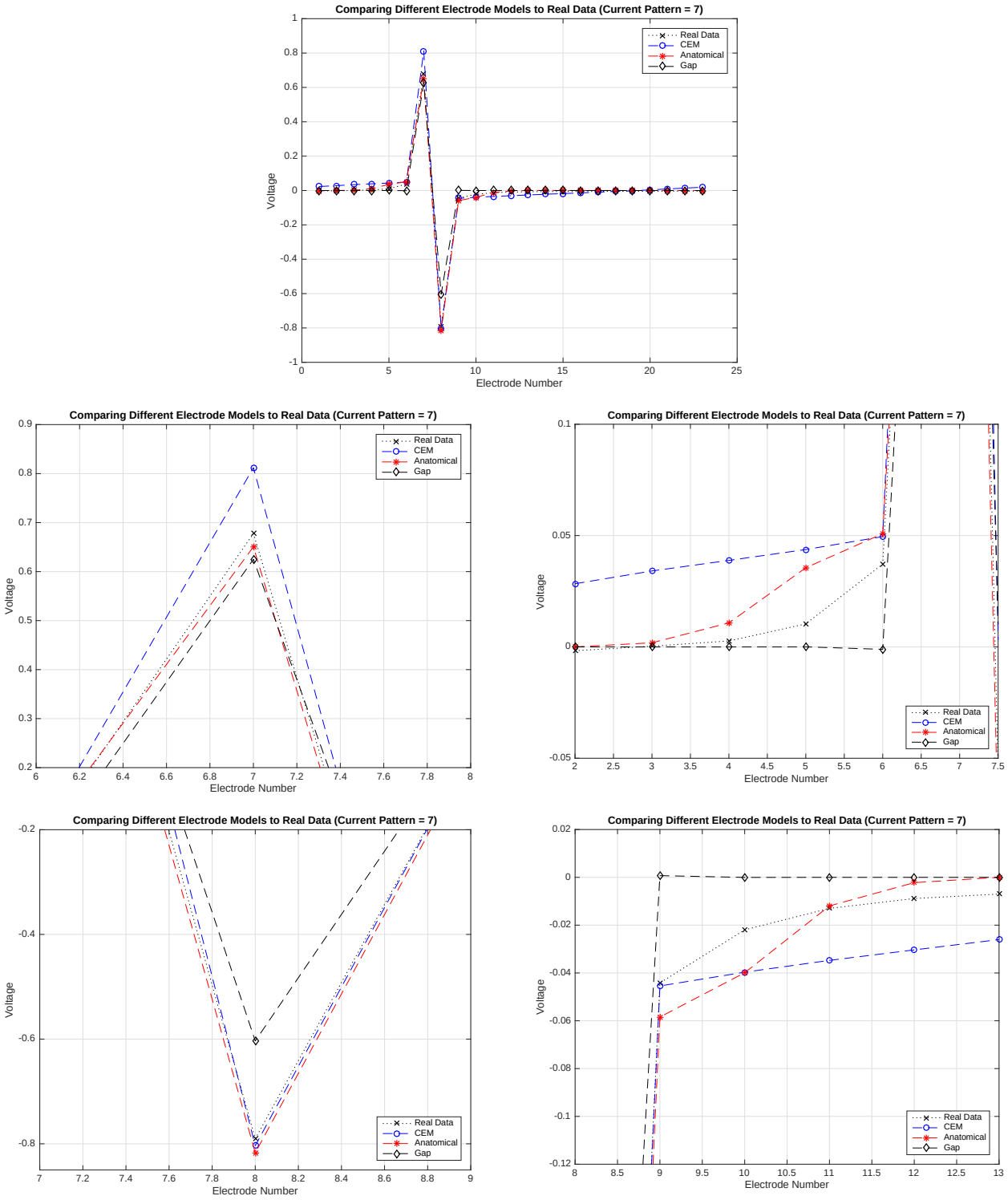

Figure 7.9. Real voltages on electrodes for measured data, the gap model, the CEM ($\rho' = 3.48$) and the anatomically inspired model which uses a uniform current density, $\sigma_r = 0.525$ mS/cm and $C_w = 0.075$ μF/cm (row 1). Row 2 shows voltages near the lagging injection electrode (7) and row 3 shows voltages on leading injection electrode (8).

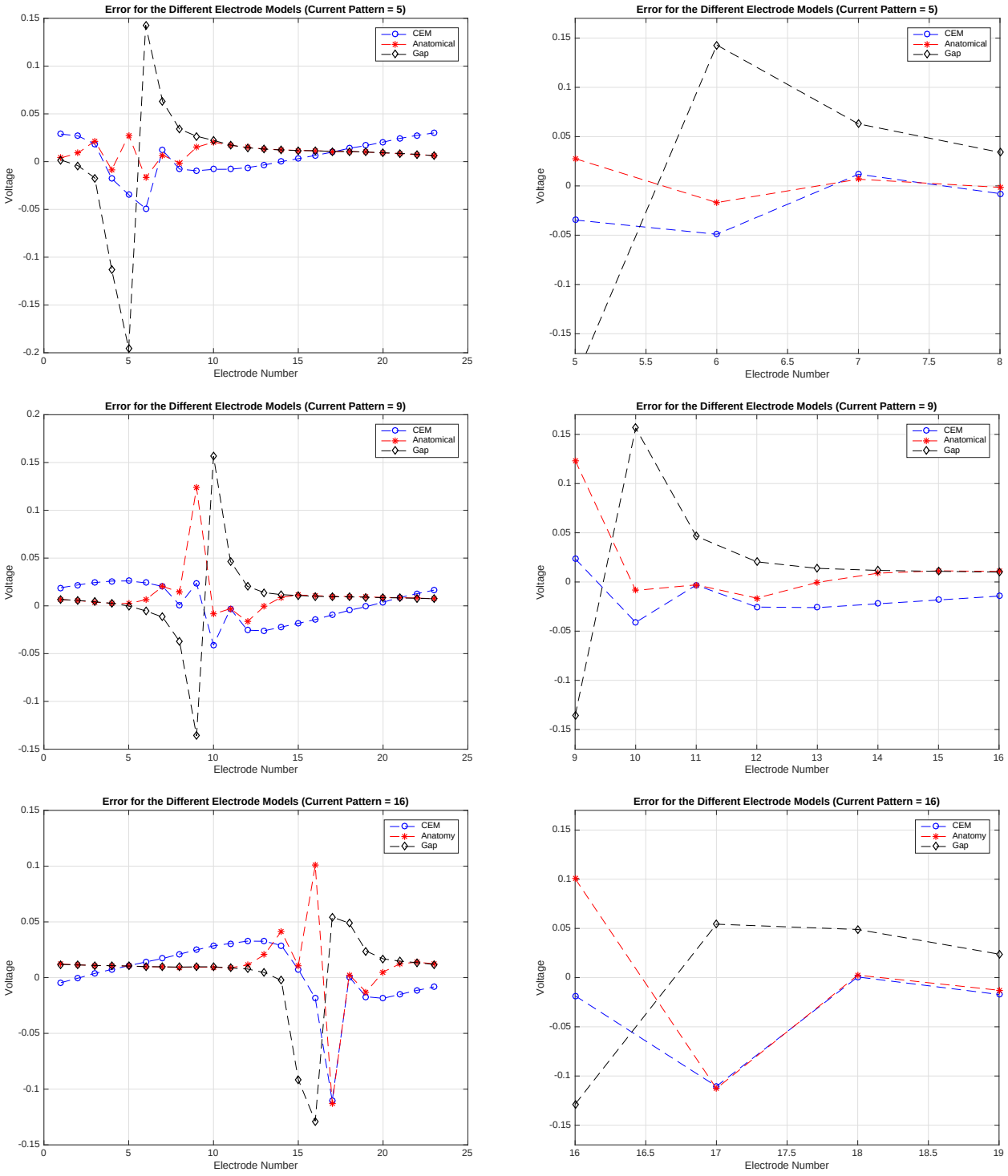

Figure 7.10. Comparison of error for different current patterns (5, 9, and 16) for the gap model, the CEM ($\rho' = 3.48$) and the anatomically inspired model ($\sigma_r = 0.525$ mS/cm and $C_w = 0.075$ μF/cm).

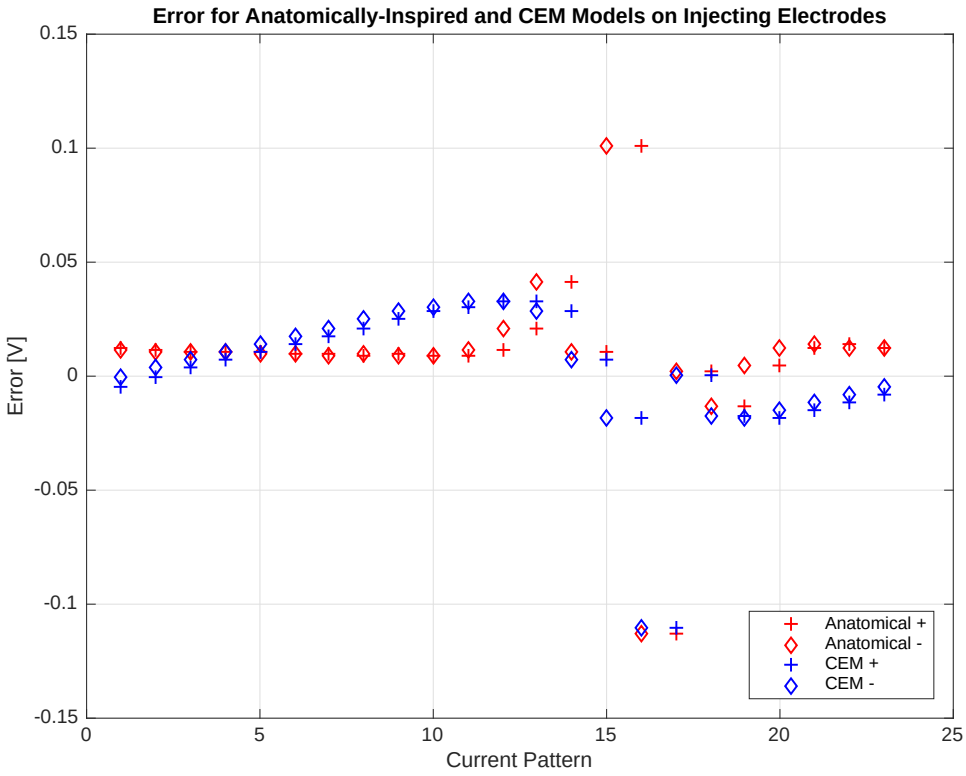

Figure 7.11. Comparison of error on injecting electrodes for the CEM and anatomically inspired model ($\sigma_r = 0.525$ mS/cm and $C_w = 0.075$ μF/cm) for each half of the bipolar, denoted by +/-.

CHAPTER 8

CONCLUSIONS

The previous chapters have described work related to the two aims of this dissertation. The first aim was to design an electrical impedance tomography system in which magnitude and phase of measured voltages and currents could be determined. This aim was achieved through the creation of the active complex electrode (ACE1) system. The second aim of this dissertation was to use the EIT forward problem to investigate the skin-electrode interface. This was achieved through implementation of an anatomically inspired model that describes current flow through the skin.

8.1. The ACE1 System

The design and testing of Colorado State University's first electrical impedance tomograph is given in this work. The initial development was part of a collaboration with the University of São Paulo, and data from this system has been used by both research groups. A description of ACE1 with reconstructed conductivity and permittivity ventilation images was presented in an extended abstract and an oral presentation at the 37^{th} Annual International Conference of the IEEE Engineering in Medicine and Biology Society [75]. The ACE1 system is presently being used in three different IRB approved human subject research studies at: Colorado State University, the Medical Center of the Rockies and the Children's Hospital Colorado. This includes human subject research comparing pulmonary function tests (PFTs) on children with cystic fibrosis to reconstructed EIT images [44]. At this time, there are several publications in preparation that showcase images and other results obtained from data taken with this system.

The ACE1 system design contains small advances that ensure consistent and quality data can be obtained. Its modular structure will allow for easy implementation of small changes as future iterations are developed. In addition, this dissertation describes several tests that can be repeated to quantify future improvements in: current source performance, precision, accuracy, reproducibility, distinguishability and the signal-to-noise ratio (SNR) of measured data. Future work might include adding more current sources, injecting multiple frequencies and incorporating digitally controlled components into the current source. The addition of active electrodes with negative or general impedance converters to reduce stray capacitance at the electrode would also be beneficial. Another improvement should include controlling current injection through logic circuits requiring USB signals.

8.2. The Anatomically Inspired Model

The second aim of this dissertation was also met. The model for current flow through the skin by Chizmadzhev [10] was successfully combined with a finite element solution to the EIT forward problem. Testing demonstrates that when assuming a single contact impedance for all electrodes and skip 0 current patterns, the anatomically inspired model predicts voltages consistent with real data on injection and neighboring electrodes. The errors in the predicted voltages when using this new model are approximately as low as the errors when using the complete electrode model (CEM) on several of the electrodes in each current pattern. However, the CEM seems to be more accurate on electrodes that are far from the injecting electrodes, since the anatomically inspired model simulated values are zero.

There is a lot of future work that could be done to better understand the limitations of the anatomically inspired model. The effects of nonuniform current densities across the pores or nodes comprising the electrodes in the mesh should be studied. Different skip patterns and

human subject meshes should be tested to determine the robustness of model parameters. Additionally, both this model and the complete electrode model should be compared when the contact impedance for each electrode is different and carefully considered. It is also possible that the two models could be combined to further reduce error in simulated voltages. Testing a mesh that incorporates prior information about skin thickness and comparing the anatomically inspired model results to measured data would also be informative about the usefulness of this model.

REFERENCES

[1] D. C. Barber, *The Biomedical Engineering Handbook*, ch. 68: Electrical Impedance Tomography. CRC Press LLC, 2nd ed., 2000.

[2] J. L. Mueller and S. Siltanen, *Linear and Nonlinear Inverse Problems with Practical Applications*. Society for Industrial and Applied Mathematics, 1st ed., 2012.

[3] L. F. Fuks, M. Cheney, D. Issacson, D. G. Gisser, and J. C. Newell, "Detection and imaging of electric conductivity and permittivity at low frequency," *IEEE Transactions on Biomedical Engineering*, vol. 38, no. 11, pp. 1106–1110, 2002.

[4] E. McAdams, J. Jossinet, A. Lackermeier, and F. Risacher, "Factors affecting electrode-gel-skin interface impedance in electrical impedance tomography," *Medical & Biological Engineering & Computing*, vol. 34, pp. 397–408, 1996.

[5] "Layers of the skin." `http://training.seer.cancer.gov/melanoma/anatomy/layers.html`, 2016. NIH: National Cancer Institute Seer Training Modules.

[6] W. M. Haynes, *CRC Handbook of Chemistry and Physics*. CRC Press LLC, 96th ed., 2016.

[7] R. Edelberg, "Electrical properties of skin," in *Biophysical Properties of the Skin* (H. R. Elden, ed.), ch. 15, pp. 513–550, Wiley-Interscience, 1971.

[8] P. Bertemes-Filho, A. Felipe, and V. C. Vincence, "High accurate howland current source: Output constraints analysis," *Circuits and Systems*, vol. 4, pp. 451–458, 2013.

[9] U. S. Government, "Anatomy of the skin." `http://web.archive.org/web/20090114060549/http://training.seer.cancer.gov/ss_module14_melanoma/images/illu_skin01.jpg`, June 2008.

[10] Y. A. Chizmadzhev, P. I. Kuzmin, J. C. Weaver, and R. O. Potts, "Skin appendageal macropores as a possible pathway for electrical current," *The Journal of Investigative Dermatology Symposium Proceedings*, vol. 3, no. 2, pp. 148–152, 1998.

[11] D. S. Holder, *Electrical Impedance Tomography: Methods, History and Applications*. Institute of Physics (IOP) Publishing Ltd, 2005.

[12] R. D. Cook, *ACT3: A High-Speed, High-Precision Electrical Impedance Tomograph*. PhD thesis, Rensselaer Polytechnic Institute, Troy, New York, July 1992.

[13] S. Franco, *Design with Operational Amplifiers and Analog Integrated Circuits*. McGraw-Hill, 1st ed., 1988.

[14] B. H. Brown, "Electrical impedance tomography (eit): a review," *Journal of Medical Engineering and Technology*, vol. 27, pp. 97–108, 2003.

[15] E. L. V. Costa, R. G. Lima, and M. B. P. Amato, "Electrical impedance tomography," *Current Opinion in Critical Care*, vol. 15, pp. 18–24, 2009.

[16] A. Adler, M. B. Amato, J. H. Arnold, R. Bayford, M. Bodenstein, S. H. Böhm, B. H. Brown, I. Frerichs, O. Stenqvist, N. Weiler, and G. K. Wolf, "Whither lung eit: Where are we, where do we want to go and what do we need to get there?," *Physiological Measurement*, vol. 33, pp. 679–694, 2012.

[17] F. T. Ulaby, *Electromagnetics for Engineers*. Pearson Education, Inc, 2005.

[18] P. O. Gaggero, *Miniaturization and Distinguishability Limits of Electrical Impedance Tomography for Biomedical Application*. PhD thesis, University of Neuchatel, Neuchatel, Switzerland, June 2011.

[19] A. Borsic, R. Halter, Y. Wan, A. Hartov, and K. D. Paulsen, "Electrical impedance tomography reconstruction for three-dimensional imaging of the prostate," *Physiological Measurement*, vol. 31, no. 8, pp. S1–16, 2010.

[20] Y. Wan, A. Borsic, J. Heaney, J. Seigne, A. Schned, M. Baker, S. Wason, A. Hartov, and R. Halter, "Transrectal electrical impedance tomography of the prostate: Spatially coregistered pathological findings for prostate cancer detection," *Medical Physics*, vol. 40, no. 6, pp. 063102–1–063102–11, 2013.

[21] O. V. Trokhanova, Y. A. Chijova, M. B. Okhapkin, A. V. Korjenevsky, and T. S. Tuykin, "Using of electrical impedance tomography for diagnostics of the cervix uteri diseases," in *Journal of Physics: Conference Series*, vol. 224, (Gainesville, FL), p. 012068, 2010 XIVth International Conference on Electrical Bioimpedance and the 11th Conference on Biomedical Applications of EIT (ICEBI), 2010.

[22] S. V. Ghandi, D. C. Walker, B. H. Brown, and D. O. C. Anumba, "Comparison of human uterine cervical electrical impedance measurements derived using two tetrapolar probes of different sizes," *Biomedical Engineering Online*, vol. 5, no. 62, 2006.

[23] "Introducing a new standard in colposcopy and cervical cancer diagnostics - ZedScan I." `http://zilico.co.uk/files/downloads/7jq70gXZQT/1397481561/zilico-zedscan-4pp-v-1-2-june-13.pdf`, Jul 2015. Zilico Brochure.

[24] "Gynecologic impedance tomograph git." `http://medimpedance.com/products.html`, Jul 2015. Impedance Medical Technologies Company Website.

[25] F. Ferraioli, A. Formisano, and R. Martone, "Effective exploitation of prior information in electrical impedance tomography for thermal monitoring of hyperthermia treatments," *IEEE Transacations on Magnetics*, vol. 45, no. 3, pp. 1554–1557, 2009.

[26] R. J. Halter, A. Hartov, S. P. Poplack, R. diFlorio Alexander, W. A. Wells, K. M. Rosenkranz, R. J. Barth, P. A. Kaufman, and K. D. Paulsen, "Real-time electrical impedance variations in women with and without breast cancer," *IEEE Transactions on Medical Imaging*, vol. 34, pp. 38–48, 2015.

[27] L. Fabrizi, M. Sparkes, L. Horesh, J. F. Perez-Juste, A. McEwan, R. H. Bayford, R. Elwes, C. D. Binnie, and D. S. Holder, "Factors limiting the application of electrical impedance tomography for identification of regional conductivity changes using scalp electrodes during epileptic seizures in humans," *Physiological Measurement*, vol. 27, pp. S163–S174, 2006.

[28] J. Engel, "Surgery for seizures," *New England Journal of Medicine*, vol. 334, pp. 647–653, 1996.

[29] D. S. Holder, "Electrical impedance tomography with cortical or scalp electrodes during global cerebral ischaemia in the anaesthetised rat," *Clinical Physics and Physiological Measurement*, vol. 13, p. 8798, 1992.

[30] D. S. Holder, "Detection of cortical spreading depression in the anaesthetised rat by impedance measurement with scalp electrodes: implications for non-invasive imaging of the brain with electrical impedance tomography," *Clinical Physics and Physiological Measurement*, vol. 1, p. 7786, 1992.

[31] K. Boone, A. M. Lewis, and D. S. Holder, "Imaging of cortical spreading depression by eit: implications for localization of epileptic foci," *Physiological Measurement*, vol. 15, pp. A189–A198, 1994.

[32] D. S. Holder, A. Rao, and H. Y., "Imaging of physiologically evoked responses by electrical impedance tomography with cortical electrodes in the anaesthetized rabbit," *Physiological Measurement*, vol. 17, p. A179A186, 1996.

[33] L. Fabrizi, L. Horesh, , C. D. McEwan, and D. S. Holder, "A feasibility study for imaging of epileptic seizures by eit using a realistic fem of the head," in *World Congress on Medical Physics and Biomedical Engineering 2006*, vol. 14, (Seoul, Korea), pp. 3874–3877, August 2006.

[34] D. D. Pak, N. I. Rozhkova, M. N. Kireeva, M. V. Ermoshchenkova, A. A. Nazarov, D. K. Fomin, and N. A. Rubstova, "Diagnosis of breast cancer using electrical impedance tomography," *Biomedical Engineering*, vol. 46, pp. 154–157, Nov 2012.

[35] "Breast cancer statistics." `http://www.wcrf.org/int/cancer-facts-figures/data-specific-cancers/breast-cancer-statistics`, 2014. World Cancer Research Fund International.

[36] J. McCann, D. Stockton, and S. Godward, "Impact of false-positive mammography on subsequent screening attendance and risk of cancer," *Breast Cancer Research*, vol. 4, no. 5, pp. 1–9, 2002.

[37] H. Fricke and S. Morse, "The electric capcity of tumors of the breast," *Journal of Cancer Research*, vol. 10, pp. 340–376, 1926.

[38] J. Jossinet and M. Schmitt, "A review of parameters for the bioelectrical characterization of breast tissue," *Annals of the New York Academy of Sciences*, vol. 873, pp. 30–41, Apr 1999.

[39] M. H. Choi, T.-J. Kao, D. Isaacson, G. J. Saulnier, and J. C. Newell, "A reconstruction algorithm for breast cancer imaging with electrical impedance tomography in mammography geometry," *IEEE Transactions on Biomedical Engineering*, vol. 54, pp. 700–710, April 2007.

[40] Y. Zou and Z. Guo, "A review of electrical impedance techniques for breast cancer detection," *Medical Engineering & Physics*, vol. 25, pp. 79–90, 2003.

[41] V. Cherepenin, A. Karpov, A. Korjenevsky, V. Kornieko, A. Mazaletskaya, D. Mazourov, and D. Meister, "A 3d electrical impedance tomography (eit) system for breast cancer detection," *Physiological Measurement*, vol. 22, pp. 9–18, 2001.

[42] B. H. Brown, D. C. Barber, A. H. Morice, and A. D. Leathard, "Cardiac and respiratory related electrical impedance changes in the human thorax," *IEEE Transactions on Biomedical Engineering*, vol. 41, pp. 729–734, Aug 1994.

[43] D. C. Agnus, A. F. Shorr, A. White, T. T. Dremsizov, R. J. Schmitz, and M. A. Kelley, "Critical care delivery in the United States: Distribution of services and compliance with leapfrog recommendations," *Critical Care Medicine*, vol. 6, pp. 1016–1024, 2006.

[44] J. Mueller, M. M. Mellenthin, P. Muller, R. R. Deterding, and S. D. Sagel, "Electrical imaging of patients with cystic fibrosis," in *NIH-IEEE Strategic Conference on Healthcare Innovations and Point of Care Technologies for Precision Medicine (HI-POCT'15)*, (Bethesda, MD), November 2015.

[45] J. H. Li, C. Joppek, and U. Faust, "Fast eit data acquisition system with active electrodes and its application to cardiac imaging," *Physiological Measurement*, vol. 17, pp. A25–A32, 1996.

[46] A. V. Noordegraaf, P. W. Kunst, A. Janse, J. T. Marcus, P. E. Postmus, T. J. Faes, and P. M. de Vries, "Pulmonary perfusion measured by means of electrical impedance tomography," *Phyisological Measurement*, vol. 19, pp. 263–273, 1998.

[47] T. M. T. Pham, M. Yuill, C. Dakin, and A. Schibler, "Regional ventilation distriubtion in the first 6 months of life," *European Respiratory Journal*, vol. 37, pp. 919–924, 2011.

[48] P. W. A. Kunst, A. V. Noordegraaf, E. Raaijmakers, B. Jan, A. B. J. Groeneveld, P. E. Postmus, and P. M. J. M. de Vries, "Electrical impedance tomography in the assessment of extravascular lung water in noncardiogenic acute respiratory failure," *Chest*, vol. 116, pp. 1695–1702, 1999.

[49] N. D. Harris, A. J. Suggett, D. Barber, and B. Brown, "Applications of applied potential tomography (apt) in respiratory medicine," *Clinical Physics and Physiological Measurement*, vol. 8, p. 155165, 1987.

[50] E. Costa, C. N. Chaves, S. Gomes, M. A. Beraldo, M. S. Volpe, M. R. Tucci, I. A. L. Schettino, S. H. Bohm, C. R. R. Carvalho, H. Tanaka, R. G. Lima, and M. B. P. Amato, "Real-time detection of pneumothorax using electrical impedance tomography," *Critical Care Medicine*, vol. 36, pp. 1230–1238, 2008.

[51] E. Darío León Bueno de Camargo, *Desenvolvimento de algoritmo de imagens absolutas de Tomografia por Impedância Elétrica para uso clínico*. PhD thesis, Escola Politécnica da Universidade de São Paulo, São Paulo, Brazil, 2012.

[52] J. G. Webster and R. P. Henderson, "An impedance camera for spatially specific measurements of the thorax," *IEEE Transactions on Bioemdical Engineering*, vol. 3, pp. 250–254, 1978.

[53] B. H. Brown and A. D. Seagar, "The sheffield data collection system," *Clinical Physics and Physiological Measurement*, vol. 8, pp. 91–97, 1987.

[54] A. Romsauerova, A. McEwan, L. Horesh, R. Yerworth, R. H. Bayford, and D. S. Holder, "Multi-frequency electrical impedance tomography (eit) of the adult human head: initial findings in brain tumours, arterivenous malformations and chronic stroke, development of an analysis method and calibration," *Physiological Measurement*, vol. 27, pp. S147–S161, 2006.

[55] R. Bayford, "Eit research groups." `http://www.eit.org.uk/groups.html`, Jun 2015.

[56] G. J. Saulnier, N. Liu, C. Tamma, H. Xia, T.-J. Kao, J. C. Newell, and D. Isaacson, "An electrical impedance spectroscopy system for breast cancer detection," in *Proceedings of the 29th Annual International Conference of the IEEE EMBS*, (Cité Internationale, Lyon, France), August 2007.

[57] "Inverse problems center: Electrical impedance tomography." `http://www.iprpi.rpi.edu/res_tomography.html`, 2015. Renesselaer Politechnic Institute IPRPI Project Website.

[58] "Multifrequency electrical impedance mammography system MEM." `http://medimpedance.com/products.html`, Jul 2015. Impedance Medical Technologies Company Website.

[59] M. S. Campisi, C. Barbre, A. Chola, G. Cunningham, V. Woods, and J. Viventi, "Breast cancer detection using high-density flexible electrode arrays and electrical impedance tomography," in *Annual International Conference of the IEEE Engineering in Medicine and Biology Society*, pp. 1131–1134, Aug 2014.

[60] D. G. Gisser, D. Isaacson, and J. C. Newell, "Current topics in impedance imaging," *Clinical Physics and Physiological Measurement*, vol. 8, pp. 39–46, 1987.

[61] R. Harikumar, R. Prabu, and S. Raghavan, "Electrical impedance tomography (eit) and its medical applications: A review," *International Journal of Soft Computing and Engineering*, vol. 3, no. 4, p. 193198, 2013.

[62] A. J. Wilson, P. Milnes, A. R. Waterworth, R. H. Smallwood, and B. H. Brown, "Mk3.5l a modular, multi-frequency successor to the mk3a eis/eit system," *Physiological Measurement*, vol. 22, pp. 49–54, 2001.

[63] "Timpel enlight: technology." `http://www.timpel.com.br/technology`, 2010. Timpel Company Website.

[64] "Technical datasheet: Dräger pulmovista 500." `http://www.draeger.com/sites/assets/PublishingImages/Products/rsp_pulmovista500/Attachments/rsp_pulmovista_500_pi_9066475_en.pdf`, 2010. Dräger Manufacturer Brochure.

[65] "Swisstom BB^2 product information 2st100-112, rev. 000." `http://www.swisstom.com/wp-content/uploads/BB2_Brochure_2ST100-112_Rev.000_EIT_inside.pdf`. Swisstom AG Manufacturer Brochure.

[66] "Maltron sheffield mk 3.5." `http://www.maltronint.com/eit/msmk35.php`, 2014. Maltron Company Website.

[67] G. Hahn, A. Just, J. Dittmar, K. H. Fromm, and M. Quitel, "Synchronous absolute eit in three thoracic plances at different gravity levels," in *Journal of Physics: Conference Series*, vol. 434, XV International Conference on Electrical Bio-Impedance & XIV Conference on Electrical Impedance Tomography, Institute of Physics Publishing, 2013.

[68] S. Pulletz, G. Elke, G. Zick, D. Schädler, J. Scholz, N. Weiler, and I. Frerichs, "Performance of electrical impedance tomography in detecting regional tidal volumes during one-lung ventilation," *Acta Anaesthesiologica Scandinavica*, vol. 52, pp. 1131–1139, 2008.

[69] "High-speed electrical impedance tomography system." `http://engineering.dartmouth.edu/bioimpedance/high-speed-EIT.html`, Nov 2014. Thayer School of Engineering at Dartmouth Technology Research Projects.

[70] P. O. Gaggero, A. Adler, J. Brunner, and P. Seitz, "Electrical impedance tomography system based on active electrodes," *Physiological Measurement*, vol. 33, pp. 831–847, 2012.

[71] Analog Devices, `http://www.analog.com/en/analog-to-digital-converters/ad-converters/ad678/products/product.html`, *AD678: 12-Bit 200KSPS Complete Sampling ADC Data Sheet Rev C, 03/2000.*

[72] "Ni pxie-6341 x series data acquisition." `http://sine.ni.com/nips/cds/view/p/lang/en/nid/207415`. National Instruments.

[73] Analog Devices, `http://www.analog.com/en/analog-to-digital-converters/ad-converters/ad9433/products/product.html`, *AD9433: 12-Bit 105/125 MSPS Analog-To-Digital IF Sampling Converter Data Sheet Rev A, 06/2009.*

[74] Abaco Systems, `http://www.abaco.com/products/ics-1640/p3403`, *ICS-1640 16-channel 2.5 MHz, 24-bit, ADC PCI Express x4 Slot Card.*

[75] M. Mellenthin, J. Mueller, E. Dario León Bueno de Camargo, F. Silva de Moura, S. J. Hamilton, and R. Gonzalez Lima, "The ACE1 thoracic electrical impedance tomography system for ventilation and perfusion," in *37th Annual International Conference of the IEEE Engineering in Medicine and Biology Society*, (Milan, Itlay), August 2015.

[76] M. Dodd and J. L. Mueller, "A real-time D-bar algorithm for 2-D electrical impedance tomography," *Inverse Problems and Imaging*, vol. 8, no. 4, pp. 1013–1031, 2014.

[77] T. Helzel, F. Suarez Sipmann, and G. Kowalewski, "electrode of biomedical measurements." US Patent No. US 7,136,690 B2, November 2006.

[78] U. Pliquett, "Front end with offset-free symmetrical current source optimized for time domain impedance spectroscopy," *Physiological Measurement*, vol. 32, pp. 927–944, 2011.

[79] P. Bertemes-Filho, B. H. Brown, and A. J. Wilson, "A comparison of modified howland circuits as current generators with current mirror type circuits," *Physiological Measurement*, vol. 21, pp. 1–6, 2000.

[80] A. S. Ross, G. J. Saulnier, J. C. Newell, and D. Isaacson, "Current source design for electrial impedance tomography," *Physiological Measurement*, vol. 24, pp. 509–516, 2003.

[81] Analog Devices, `http://www.analog.com/en/products/interface-isolation/isolation/isopower/adum6404.html`, *ADuM6400/ADuM6401/ADuM6402/ADuM6403/ADuM6404: Quad-Channel, 5 kV Isolators with Integrated Dc-to-DC Converter Data Sheet Rev A*.

[82] Analog Devices, http://www.analog.com/media/en/technical-documentation/data-sheets/ADG441_442_444.pdf, *ADG441/ADG442/ADG444: LC²MOS Quad SPST Switches Data Sheet Rev B.*

[83] *ANSI/AAMI ES60601-1:2005 (IEC 60601-1:2005, MOD) Medical Electircal Equipment - Part 1: General Requirements for Basic Safety and Essential Performance*, 2006.

[84] R. M. Fish and L. A. Geddes, "Conduction of electrical current to and through the human body: A review," *Open Access Journal of Plastic Surgery*, vol. 9, pp. 407–421, October 2009.

[85] W. Wang, M. Brien, D.-W. Gu, and J. Yang, "A comprehensive study on current source circuits," in *IFMBE Proceedings*, vol. 17, (Austria), pp. 213–216, ICEBI 2007: XIII International Conference on Electrical Bio-Impedance & VIII Conference on Electrical Impedance Tomography, 2007.

[86] "AN-1515 a comprehensive study of the howland current pump." Application Report, Apr 2013. Texas Instruments.

[87] J. Steele and T. Green, "Proper compensation techniques will let the improved-howland and floating-load current sources perform up to par. tame those versatile current-source circuits.," *Electronic Design*, pp. 61–71, 1992.

[88] *Operating Manual and Programming Reference: Model DS360 Ultra Low Distortion Function Generator.* http://www.thinksrs.com/downloads/PDFs/Manuals/DS360m.pdf, 2 ed., 2008.

[89] J. G. Webster, *Medical Instrumentation: Application and Design.* John Wiley & Sons, Inc., 4th ed., 2010.

[90] D. G. Gisser, D. Isaacson, and J. C. Newell, "Theory and peformance of an adaptive current tomography system," *Clinical Physics and Physiological Measurement*, vol. 9, pp. 35–41, 1988.

[91] D. Isaacson, "Distinguishability of conductic current computed tomography," *IEEE Transactions on Medical Imaging*, vol. MI-5, pp. 91–95, June 1986.

[92] *Harmonic detection and filtering.* `http://electrical-engineering-portal.com/res/Harmonic-detection-and-filtering.pdf`, 4 ed.

[93] O. Luppi Silva, *Muscle Contraction Detection Using Electrical Impedance Tomography.* PhD thesis, Escola Politécnica da Universidade de São Paulo, São Paulo, Brazil, 2012.

[94] G. Boverman, D. Isaacson, G. J. Saulnier, and J. C. Newell, "Methods for compensating for variable electrode contact in eit," *IEEE Transactions on Bioemdical Engineering*, vol. 56, no. 12, pp. 2762–2772, 2009.

[95] K.-S. Cheng, D. Isaacson, J. C. Newell, and D. G. Gisser, "Electrode models fo electric current computed tomography," *IEEE Transactions on Biomedical Engineering*, vol. 36, pp. 918–924, September 1989.

[96] L. A. Geddes, C. P. Da Costa, and G. Wise, "The impedance of stainless-steel electrodes," *Medical and Biological Engineering*, vol. 9, pp. 511–521, 1971.

[97] V. Kolehmainen, M. Vauhkonen, P. A. Karjalainen, and J. P. Kaipio, "Assessment of errors in static electrical impedance tomography with adjacent and trionometric current patterns," *Physiological Measurement*, vol. 18, no. 4, pp. 289–303, 1997.

[98] P. Hua, E. J. Woo, J. G. Webster, and W. J. Tompkins, "Finite element modeling of electrode-skin contact impedance in electrical impedance tomography," *IEEE Transactions on Biomedical Engineering*, vol. 40, pp. 335–342, 1993.

[99] D. A. Burns, S. M. Breathnach, N. Cox, and C. E. Griffiths, *Rook's Textbook of Dermatology*. Blackwell Science, 7th ed., 2004.

[100] Y. A. Chizmadzhev, A. V. Indenbom, P. I. Kuzmin, S. V. Galichenko, J. C. Weaver, and R. O. Potts, "Electrical properties of skin at moderate voltages: Contribution of appendageal macropores," *Biophysical Jounral*, vol. 74, pp. 843–856, 1998.

[101] J. J. Achmann and M. A. Seitz, "Methods of complex impedance measurements in biologic tissue," *Critical Reviews in Biomedical Engineering*, vol. 11, pp. 281–311, 1984.

[102] E. A. White, M. E. Orazem, and A. L. Bunge, "Single-frequency lcr databridge impedance measurements as surrogate measures for the integrity of human skin," *Journal of The Electrochemical Society*, vol. 159, pp. G161–G165, 2012.

[103] P. Bertemes Filho, R. Gonzalez Lima, and H. Tanaka, "An current source using a negative impedance converter (nic) for electrical impedance tomography (eit)," in *Proceedings of COBEM 2003*, vol. 1014, (São Paulo, Brazil), 17th International Congress of Mechanical Engineering, 2003.

[104] K. Kontturi and L. Murtomäki, "Impedance spectroscopy in human skin. a refined model," *Pharmaceutical Research*, vol. 11, pp. 1355–1357, 1994.

[105] J. Beach, M. Orazem, and A. Bunge, "Evidence that pores are the primary conductive pathway in human skin," in *Perspectives in Percutaneous Penetration (PPP)*, vol. 10A, (La Grande Motte, France), pp. 2109–2116, Perspectives in Percutaneous Penetration Tenth International Conference, 2006.

[106] E. K. Murphy, *2-D D-Bar Conductivity Reconstructions on Non-Circular Domains*. PhD thesis, Colorado State University, Fort Collins, Colorado, February 2008.

[107] D. Isaacson, M. Cheney, and J. Newell, *Inverse Problems in Mathematical Physics: Proceedings of the Lapland Conference on Inverse Problems Held at Saariselk a, Finland, 14-20 June 1992*, ch. Problems in Impedance Imaging, pp. 62–70. Springer Berlin Heidelberg, 1993.

[108] S. J. Hamilton, *A Direct D-Bar Reconstruction Algorithm for Complex Admittivities in $W^{2,\infty}(\Omega)$ for the 2-D EIT Problem*. PhD thesis, Colorado State University, Fort Collins, Colorado, Summer 2012.

[109] F. Silva de Moura, *Estimação Não Linear de Estado Através do Unscented Kalman Filter na Tomografia por Impedância Elétrica*. PhD thesis, Escola Politécnica da Universidade de São Paulo, São Paulo, Brazil, 2012.

[110] R. H. Bayford, A. Gibson, A. Tizzard, T. Tidswell, and D. S. Holder, "Solving the forward problem in electrical impedance tomography for the head using ideas (integrated design engineering analysis software), a finite element tool," *Physiological Measurement*, vol. 22, pp. 55–64, 2001.

[111] A. G. Tizzard, *Improving the Forward Model for Electrical Impedance Tomography of Brain Function Through Rapid Generation of Subject Specific Finite Element Models*. PhD thesis, Middlesex University, London, England, 2007.

[112] F. Yang, J. Zhang, and R. Patterson, "Development of an anatomically realistic forward solver for thoracic electrical impedance tomography," *Journal of Medical Engineering*, vol. 2013, pp. 1–7, 2013.

[113] M. Alsaker, *Computational Advancements in the D-bar Reconstruction Method for 2-D Electrical Impedance Tomography*. PhD thesis, Colorado State University, Fort Collins, Colorado, Spring 2016.

[114] A. S. Tucker, R. M. Fox, and R. J. Sadleir, "Biocompatible, high precision, wideband imrpoved howland current source with lead-lag compensation," *IEEE Transactions on Biomedical Circuits and Systems*, vol. 7, no. 1, pp. 63–70, 2013.

[115] Analog Devices, `http://www.analog.com/en/specialty-amplifiers/differential-amplifiers/ad8132/products/product.html`, *AD8132: low Cost, High Speed Differential Amplifier Data Sheet Rev 1, 09/2009*.

[116] U. Pliquett and A. Barthel, "Interfacing the ad5933 for bio-impedance measurements with front ends providing galvanostatic or potentiostatic excitation," in *Proceedings of the First Latin American Conference on Bioimpedance*, (Joinville, Brazil), November 2012.

[117] R. D. Cook, G. J. Saulnier, D. G. Gisser, G. J. C., J. C. Newell, and D. Isaacson, "Act 3: A high-speed, high-precision electrical impedance tomography," *IEEE Transactions on Biomedical Engineering*, vol. 41, pp. 713–722, August 1994.

[118] J. Reddy, *An Introduction to the Finite Element Method*. Mcgraw Hil, 3rd ed., 2005.

APPENDIX A

CURRENT SOURCE DESIGN

One of the most commonly used current source designs in EIT is the Howland or Improved Howland, shown in Figure A.1. Both Howlands are unidirectional linear voltage controlled current sources that can apply AC currents. Their configurations are unique when compared to many other operational amplifier (op amp) configurations because feedback occurs to both the positive and negative input terminals [114, 86, 87]. Presented here are the design considerations and relevant theory for construction of an EIT current source.

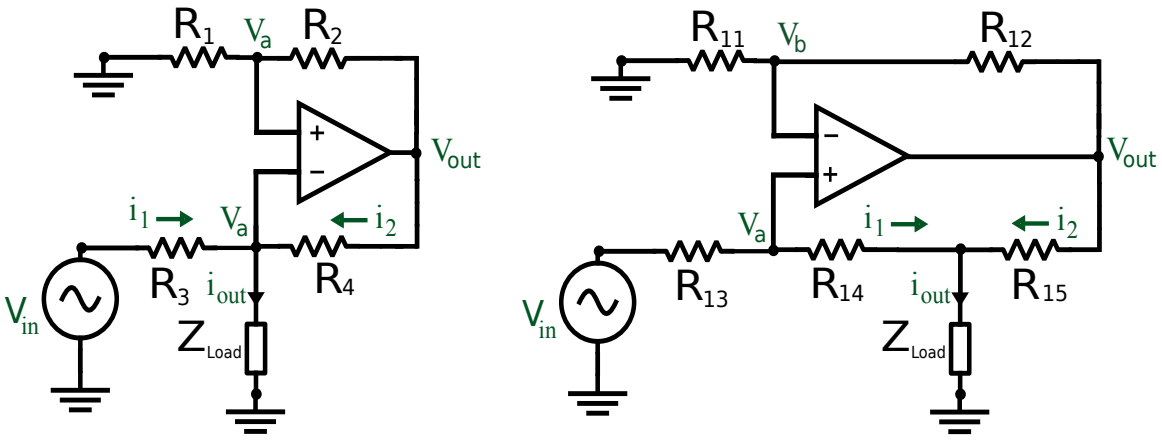

(A) Howland Current Source (B) Improved Howland Current Source

Figure A.1. The schematics of the two different Howland designs.

There are several design considerations that apply to both types of Howland circuits. Because an intended use of ACE1 was for data collection on human subjects, it was determined that the source should inject 1-10 mA of current for frequencies of 100 kHz to 200 kHz, where typical operation is considered to be approximately 5-6 mA at 125 kHz. To add additional safety, a direct current (DC) blocking capacitor was placed in series with the current output to ensure that no DC is accidentally injected in the subject. Op amp

choice should be limited to ones made from field-effect transistors (FETs) because of their high bandwidth. However, the input capacitance to FET terminals varies with the applied voltage, which can degrade output impedance in the range of EIT frequencies, so careful selection of the op amp is essential (Section 4.1.2). The performance of both sources is limited by component mismatches created by tolerances and degrades source output impedance [86]. Additional compensation for undesired capacitance and non-ideal behavior can improve source performance and is discussed in Section A.4.

A.1. Howland Design

There are a few points to consider in the Howland design. Increasing the value of both R_1 and R_2 is advantageous because it will increase output impedance, but when they are too great, op amp performance is affected and only very small currents can be applied. The Howland equations can be derived from Kirchhoff's Voltage Laws (KVL) [86]:

$$i_{out} = i_1 + i_2 \tag{A.1}$$

$$i_1 = \frac{V_{in} - V_a}{R_3} \tag{A.2}$$

$$i_2 = \frac{V_{out} - V_a}{R_4} \tag{A.3}$$

$$i_{out} = \frac{V_{in} - V_a}{R_3} + \frac{V_{out} - V_a}{R_4} \tag{A.4}$$

Generally it is assumed that $R_1 = R_2 = R_3 = R_4 = R$. Therefore i_{out} is as follows:

$$i_{out} = \frac{V_{in}}{R} \tag{A.5}$$

Depending on the choice of R and desired current, it can be impossible to get the desired i_{out} because the limitations imposed by the op amp supply voltages.

A.2. Improved Howland Design

To overcome challenges with the Howland design, the Improved Howland was created. The design equations for the Improved Howland can also be derived from KVL [86]:

$$i_{out} = i_1 + i_2 \tag{A.6}$$

$$i_1 = \frac{V_{in}}{R_{13} + R_{14}} \tag{A.7}$$

$$i_2 = \frac{V_{out}}{R_{15}} \tag{A.8}$$

$$i_{out} = \frac{V_{in}}{R_{13} + R_{14}} + \frac{V_{out}}{R_{15}} \tag{A.9}$$

Resistors should be chosen and trimmed such that: $R_{13} = R_{14} + R_{15}$. In addition, it is common to choose $R_{11} = R_{12} = R_{14}$ [86, 87]. To find V_{out} in terms of V_{in}:

$$V_a = i_1 R_{14} \tag{A.10}$$

$$V_{out} = 2V_a = 2i_1 R_{14} \tag{A.11}$$

$$V_{out} = \frac{2V_{in}}{R_{13} + R_{14}} \tag{A.12}$$

The ideal current delivered to the load is expressed by equation (A.13):

$$i_{out} = \frac{V_{in}}{R_{13} + R_{14}} \left(1 + \frac{2R_{14}}{R_{15}}\right) \tag{A.13}$$

There are several other considerations that should be made when designing this source. It is often recommended that a feedback capacitor be placed in parallel with R_{12} [86]. However, when tested with some of the ACE1 sources, no notable difference in performance was noted.

A.3. Bipolar Source from One AC Voltage Input

There are two different versions of the bipolar current source that have been successfully tested in the ACE1 system. Before using the bipolar output feature on the Stanford Research Systems Model DS360 Ultra Low Distortion Function Generator the design, Figure A.2 was implemented. This design may still be useful in future modifications to ACE1, especially if a smaller and less sophisticated AC voltage source was used. Figure A.2 uses an AD8132 low-cost, high speed, differential amplifier to to produce to two voltages that are 180 degrees out of phase from one another [115]. The resistors of Figure are not equal in value and must be adjusted to achieve circuit stability. The improved Howland current source is independently connected to each output of the AD8132, inspired by recent work of Pliquett, *et al* [78] [116].

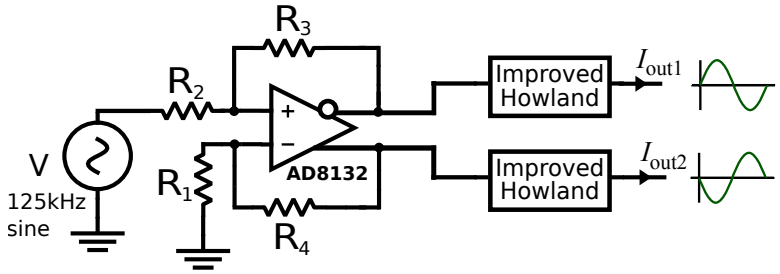

Figure A.2. The schematic diagram of the bipolar current source shows the incorporation of two improved Howland designs with an AD8132 differential amplifier.

Configurations were tested such that $R = R_{11} = R_{12} = R_{14} = 47\ k\Omega$ and $100\ k\Omega$. In simulation the $100\ k\Omega$ configuration had a higher output impedance, and had low levels of mismatch. However, during bench top testing, the $47\ k\Omega$ source was better matched.

A.4. Increasing Source Output Impedance

One of the challenges in designing a pairwise injection EIT system where the source is located physically far from the load is compensating for the presence of components or stray capacitance that are in parallel with the source. These impedances cause the output impedance and performance of the source to be degraded. To cancel out their effects, the use of additional active circuit components is necessary. The use of negative impedance converters (NIC)s and general impedance convereters (GIC)s can aid in reducing the extent to which the output impedance of the source is degraded by stray or capacitance from components in the tomograph box, cables and active electrode PCBs. For example, a NIC or GIC circuit could be used to cancel a portion of the capacitance from the switches or on the stray capacitance on a cable in between the tomograph box and electrode.

The design of a NIC and GIC should be rigorously tested as suggested by Ross and coworkers, whom reported instabilities in the current source with the NIC as designed by Cook [117] in RPI's ACT3 EIT system. It was reported that in the presence of a large capacitance (> 100 pF) and at higher frequencies relative to 28.8 kHz, the source was unable to perform in a manner that was both consistent and stable [80]. For systems that do not measure the current but rely on maintaining excellent source performance in a variety of conditions, variability in source behavior that effects performance is not acceptable. In ACE1, injected current values can be approximated from V_e and V_c electrode measurements. In this case, source performance is primarily a concern to ensure that a relationship between input voltage to the VCCS to output current is repeatable for a range of loads. This will ensure a more accurate estimate of injected current at the time of data acquisition.

A.4.1. NIC Design Theory. Negative Impedance Converters (NICs) work by adding or subtracting voltage at a specific point in a larger circuit. They can be appealing to use in a variety of situations because they behave like a negative capacitor. Their implementation also requires fewer components and is simpler than a GIC. The schematic in Figure A.3 is a proposed NIC implementation for use in EIT in a book chapter written by Saulnier [11]. It is also the implementation used by Betermes with a monopolar howland current source [103].

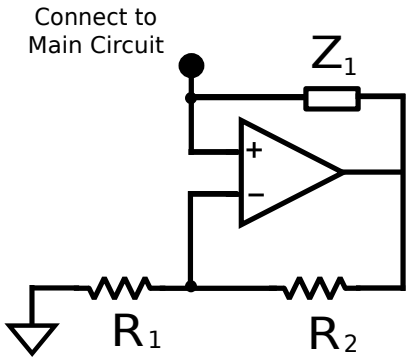

Figure A.3. Implementation of a basic NIC design [11].

The impedance of the NIC (Z_{NIC}) as seen from the main circuit is [11]:

$$Z_{NIC} = -Z_1 \frac{R_1}{R_2} \tag{A.14}$$

The negative capacitance is created by choosing Z_1 to be a capacitor and is adjusted by varying R_1 and R_2. Additionally, Z_1 could be a resistor to create a negative resistance or R_2 could be replaced by a capacitor with Z_1 as a resistor to create a negative inductance. However, a negative capacitance is typically what is wanted for EIT applications.

NICs can be particularly desirable when multiple frequencies are used or it is desirable for the system to work over a range of frequencies. However, it is important to test current

source designs that incorporate NICs carefully because certain loads can cause them to oscillate and exhibit unstable behavior [11].

The proposed NIC design by Cook is shown in Figure A.4. The corresponding NIC impedance ($Z_{NIC_{Cook}}$) is is described by Equation A.15, where A is the open loop gain of the op amp, C_2 is a capacitor chosen for feedback-lead compensation, and Z is a scaling factor based on current amplitude [12].

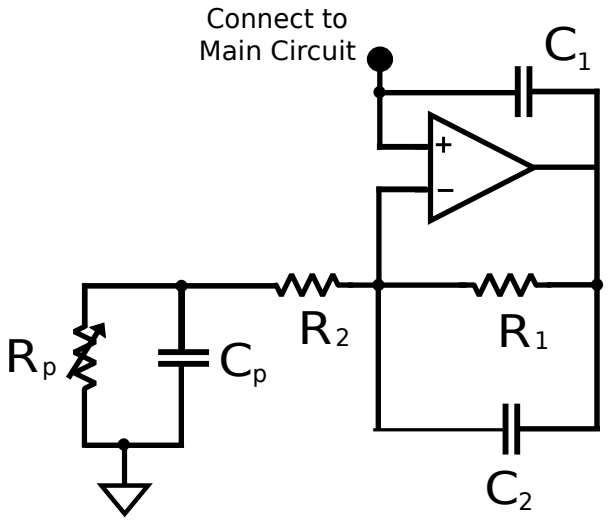

Figure A.4. Implementation of the NIC design proposed by Cook [12].

(A.15) $$Z_{NIC_{Cook}} = \frac{Z(1+A) + R_1||C_2}{j\omega(Z + (1+A)R_1||C_2)}$$

A.4.2. GIC Design Theory. In certain situations, general impedance converters (GICs) are a more appropriate choice than NICs. GICs tend not to suffer from oscillatory behavior like NICs can and are better suited to single frequency or narrow range multi-frequency EIT systems [11]. An article by Wang and group presents an EIT current source design that was able to achieve a 120 MΩ peak output impedance, but rapidly degraded to approximately 2

MΩ above 100 kHz using a GIC configuration [85]. The group at RPI reported the output impedance characteristics of their Improved Howland with a GIC in detail. With the GIC design, the group achieved a peak output impedance of approximately 2 GΩ which was degraded when the GIC was not adjusted to about 90 MΩ. The reported output capacitance for the source with the GIC was less than 2.5 fF, which allowed the source to maintain such an high ouput impedance. To achieve this level of performance, digitally controlled components were used in the GIC implementation. Figure A.5 depicts a commonly used GIC.

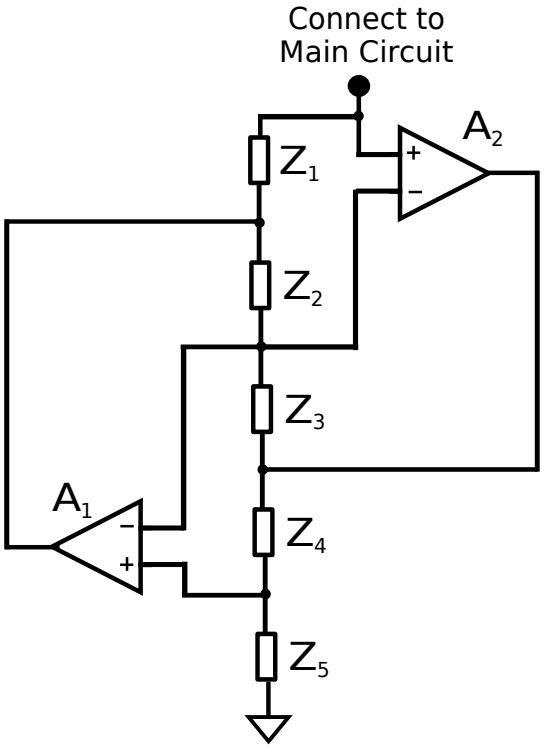

Figure A.5. Implementation of a basic GIC design [13].

For a given voltage at the attachment point to the main circuit (V_s) and its associated current with respect to the GIC (I_s) in Figure A.5 one can determine the overall effective impedance of the GIC (Z_{GIC}) [13]. The output voltages of the op amp are denoted by V_{outA1} and V_{outA2}. By Kirchhoff's Current Law (KCL), Equation A.16 can be written to describe

node which joins the negative input op amp terminals to Z_2 and Z_3. Equation A.17 describes the node where Z_4 and Z_5 connect the positive input terminal to op amp A_2 [13].

$$\frac{V_{outA1} - V_s}{Z_2} = \frac{V_s - V_{outA2}}{Z_3} \tag{A.16}$$

$$\frac{V_{outA2} - V_s}{Z_4} = \frac{V_s}{Z_5} \tag{A.17}$$

By substituting Equation A.16 into Equation A.17, Z_{GIC} is determined [13, 11]:

$$Z_{GIC} = \frac{V_s}{I_s} = \frac{Z_1 Z_3 Z_5}{Z_2 Z_4} \tag{A.18}$$

Saulnier suggests that a GIC topology be used to create an LC resonant circuit, where the parallel synthetic inductance created by the GIC acts to cancel undesired capacitance at a specific resonant frequency [11]. To do this, one can choose Z_2 or Z_4 to be a capacitor [13]. In this design, $Z_1 = R_1$, $Z_2 = R_2$, $Z_3 = R_3$, $Z_4 = C_4$, and $Z_5 = R_5$. Substitution into Equation A.18, where $X_{c_4} = 1/(j\omega C_4)$, is shown by:

$$Z_{GIC_{LC}} = \frac{j\omega R_1 R_3 R_5 C_4}{R_2} \tag{A.19}$$

With any GIC or NIC, the use variable resistors and/or capacitors can allow the circuit to more easily compensate for setup specific differences and improve performance.

APPENDIX B

ADDITIONAL SYSTEM TEST RESULTS

Figures in this Appendix follow the discussion presented in both sections for the convenience of the reader.

B.1. Additional Precision Figures & Discussion

To calculate precision and accuracy, all channels of the ACE1 system were connected to the same voltage source and 100 frames of data was acquired, shown in Figure 4.12. Plots of amplitude and phase precision are given in figures of this appendix section for 25 kHz, 75 kHz, 100 kHz, 125 kHz, 150 kHz and 175 kHz. These additional figures are supplementary to Section 4.3.2, which discusses ACE1 precision, but primarily includes plots at individual frequencies for a 0.25 V_{peak} applied voltage at the 1024 point acquisition rate (or 16 frames/second). The purpose of this section is to present results for other applied voltages acquired at the 512 point and 1024 point acquisition rate. The following applied voltages were considered at the 512 point acquisition rate: 0.125 V_{pk}, 0.25 V_{pk} and 0.375 V_{pk}. 0.375 V_{pk} is also considered at the 1024 point acquisition rate.

In this appendix, amplitude precision (${P_{pk}}_l^k$) or one standard deviation for measured voltage amplitudes as defined by Equation (4.18) is given in Figures B.1 - B.3 for 0.125 V_{pk}, 0.25 V_{pk} and 0.375 V_{pk} data collected at the 512 point acquisition rate, respectively. Figures B.4 - B.6 plot mean phase precision ($({P_\theta}^k)_{mean}$) as defined by Equation (4.22) for 0.125 V_{pk}, 0.25 V_{pk} and 0.375 V_{pk} data collected at the 512 point acquisition rate, respectively.

Figure B.7 plots overall mean precision for amplitude $(P_{pk})_{mean}$ and phase $(P_\theta)_{mean}$ given be Equation (4.20) and Equation (4.23), respectively. This plot shows that the amplitude precision with which voltages ranging from 0.125 V_{pk} to 0.375 V_{pk} is not greatly influenced

by magnitude of the applied voltage. However, plots of $(P_\theta)_{mean}$ suggest that phase precision improves for larger applied voltages.

Figure B.8 shows overall percent mean precision for amplitude Percent $(P_{pk})_{mean}$ and phase Percent $(P_\theta)_{mean}$ for different skip patterns and frequencies taken at the 512 point acquisition rate. These percentages, give by Equation (4.26) and Equation (4.30) respectively, reveal results that are consistent with Figure B.7. Because the overall mean amplitude precision remains constant for different applied voltages, the overall mean percent amplitude precision improves as applied voltage increases. Overall mean percent phase precision is also better for some frequencies and skip patterns as applied voltage increases, but the trend is less clear than overall mean percent amplitude precision.

Figures B.9 - B.10 measuring a 0.375 V_{pk} applied voltage can be compared to Figure 4.13 and Figure 4.14 which measure a 0.375 V_{pk} applied voltage. Figure B.11 plots the overall mean precision for amplitude $(P_{pk})_{mean}$ and phase $(P_\theta)_{mean}$ for different skip patterns and frequencies taken at the 1024 point acqusition rate for 0.25 V_{pk} and 0.375 V_{pk}. Similar to the 512 point acquisition results, the overall mean amplitude precision is not greatly influenced by an increase in magnitude of the applied voltage. Although less clear, plots of $(P_\theta)_{mean}$ suggest that phase precision may improve for larger applied voltages.

B.2. Additional Distinguishability Figures

Plots of distinguishability of single current patterns for frequencies at 25 kHz, 100 kHz, 125 kHz and 175 kHz. Figure B.12, Figure B.14, Figure B.16 and Figure B.18 show voltage difference measurements during a single current pattern used to determine distinguishability of conductor targets, or copper pipes described in Figure 4.28. Figure B.13, Figure B.15, Figure B.17 and Figure B.19 show voltage difference measurements during a single current

pattern used to determine distinguishability of insulator targets, or plastic pipes described in Figure 4.28. Figures in this section show that the voltage different profiles generated for each current pattern are consistent for different frequencies used in this test.

All figures in this section show the effects of contact impedance on the injecting electrodes. Differences between all tank phantom targets are larger on non-injecting electrodes.

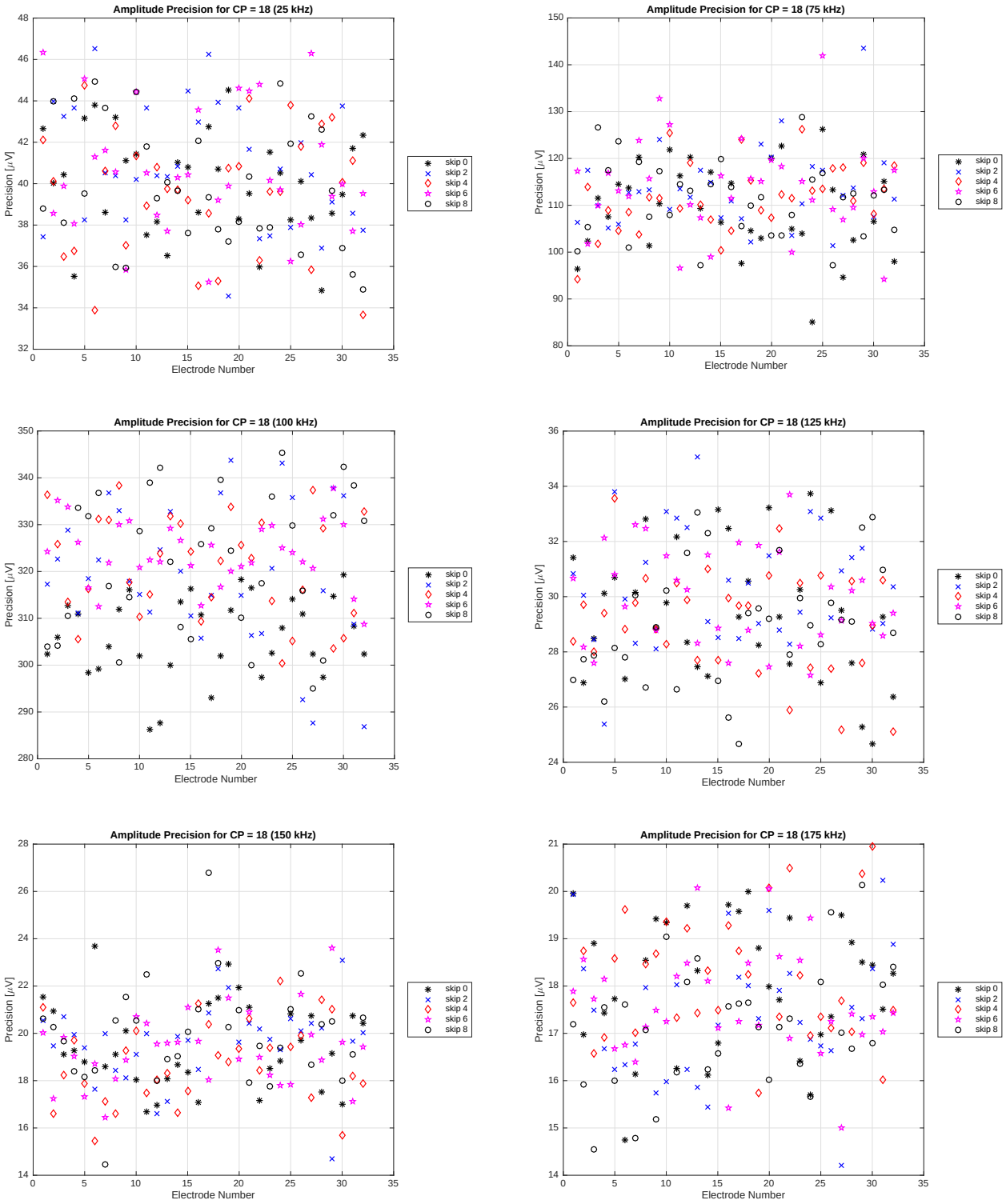

Figure B.1. The precision $(P_{pkl}^{\ k})$ or one standard deviation for measured voltage amplitudes of a 0.125 V_{pk} applied voltage at various frequencies for 100 frames of data acquired at the 512 point acquisition rate.

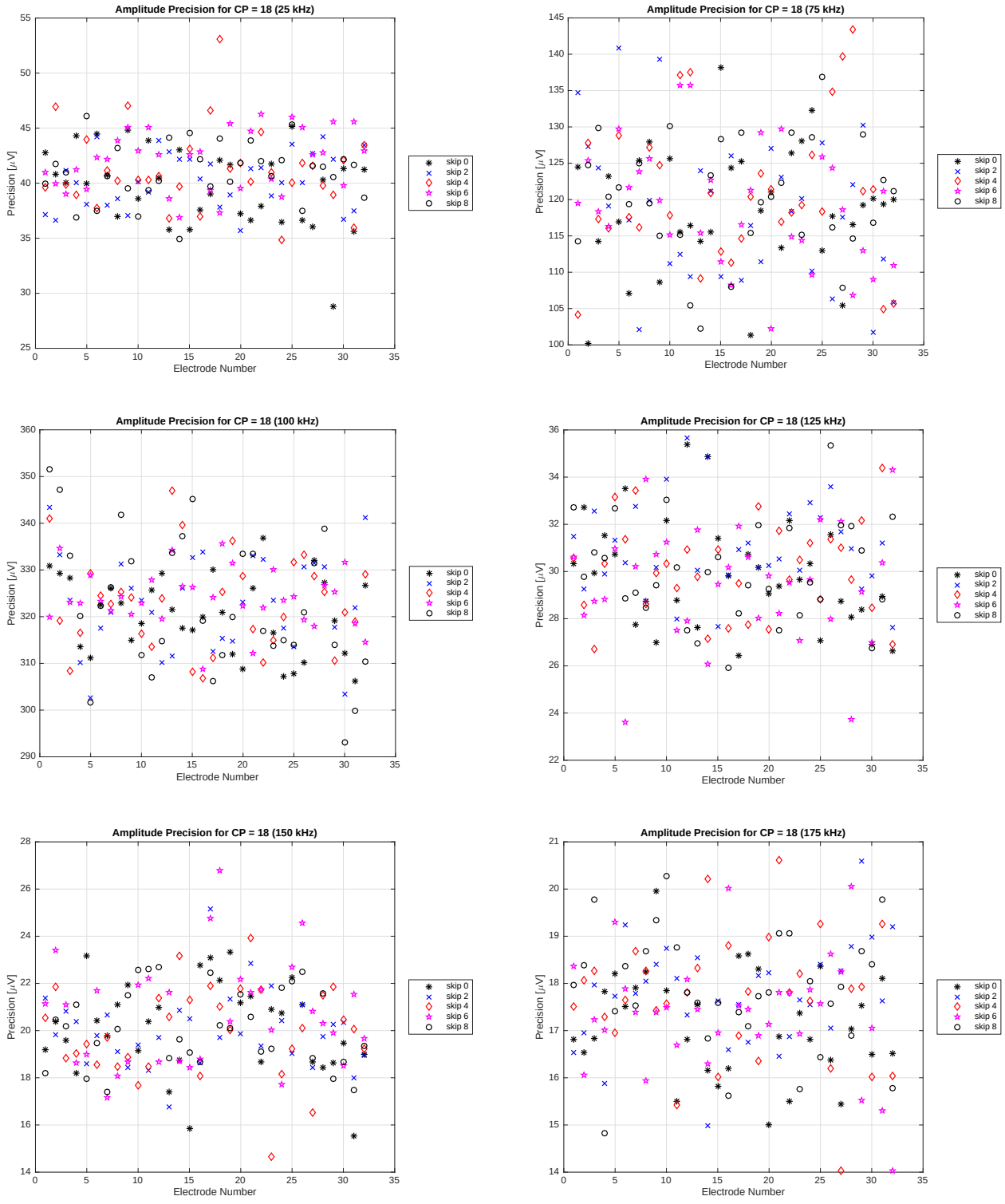

Figure B.2. The precision $(P_{pkl}{}^{k})$ or one standard deviation for measured voltage amplitudes of a 0.25 V_{pk} applied voltage at various frequencies for 100 frames of data acquired at the 512 point acquisition rate.

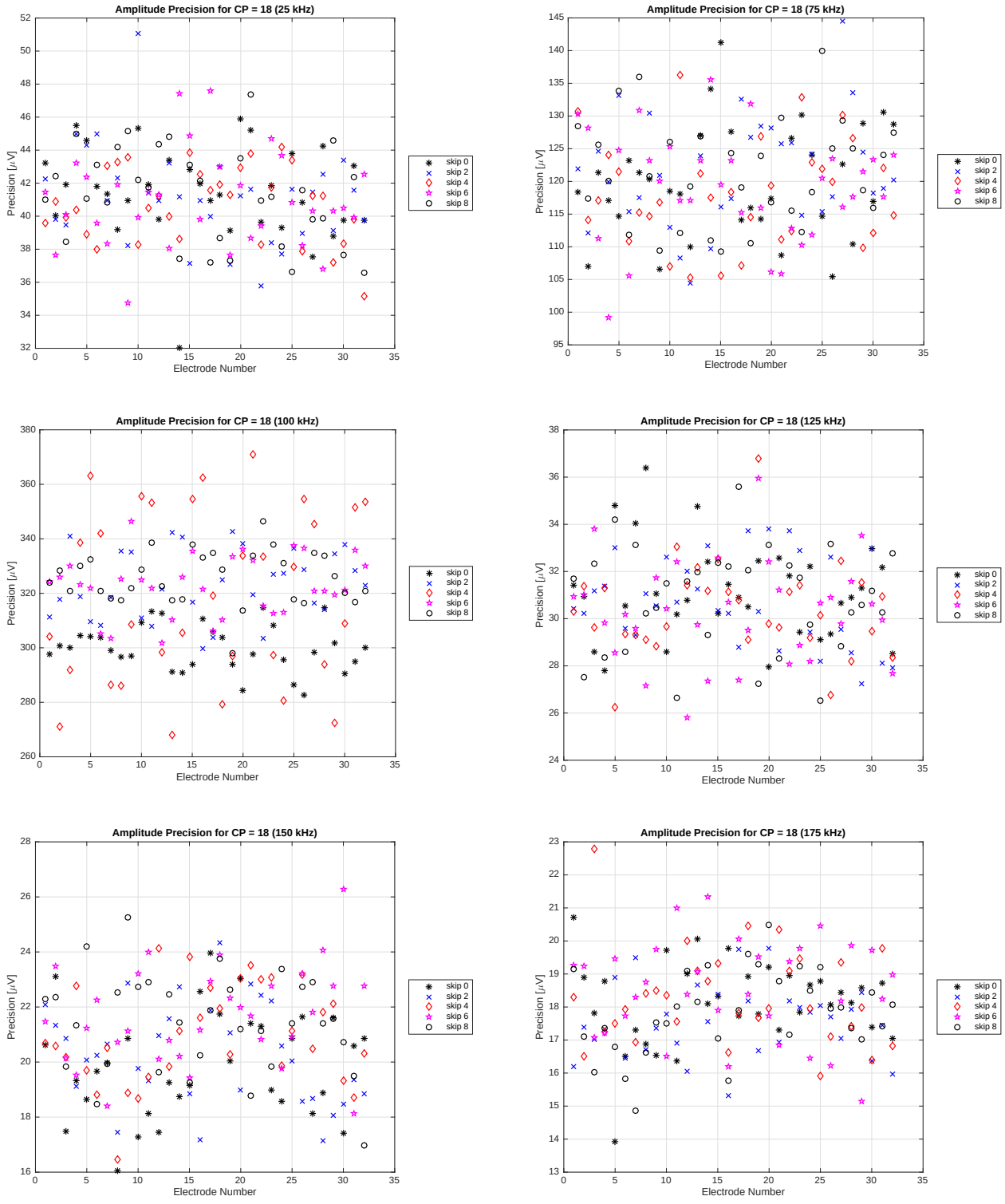

Figure B.3. The precision $(P_{pkl}{}^{k})$ or one standard deviation for measured voltage amplitudes of a 0.375 V_{pk} applied voltage at various frequencies for 100 frames of data acquired at the 512 point acquisition rate.

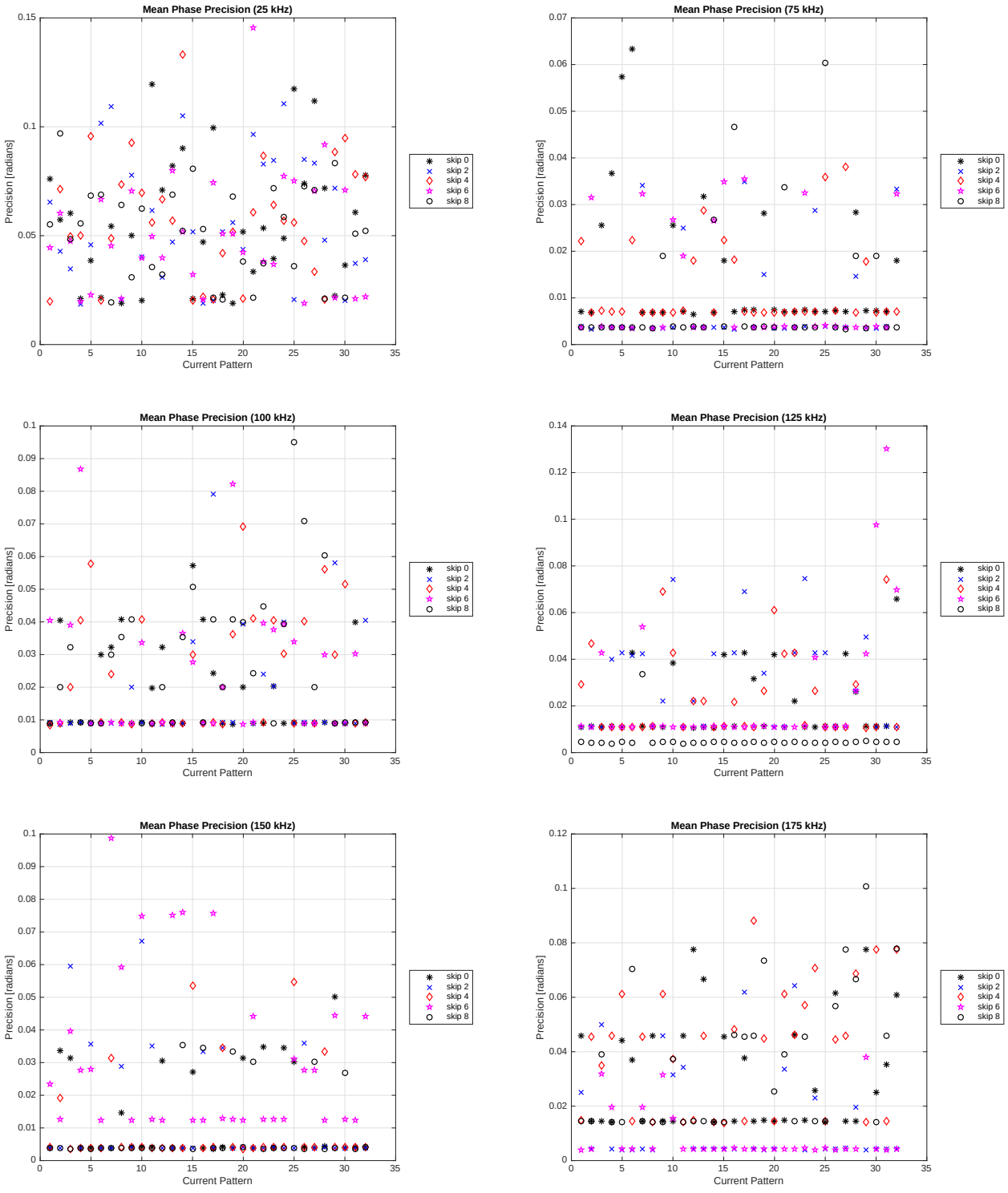

Figure B.4. Mean phase precision for each current pattern ($(P_\theta{}^k)_{mean}$) for measured voltage phases corresponding to a 0.125 V_{pk} applied voltage at various frequencies for 100 frames of data acquired at the 512 point acquisition rate.

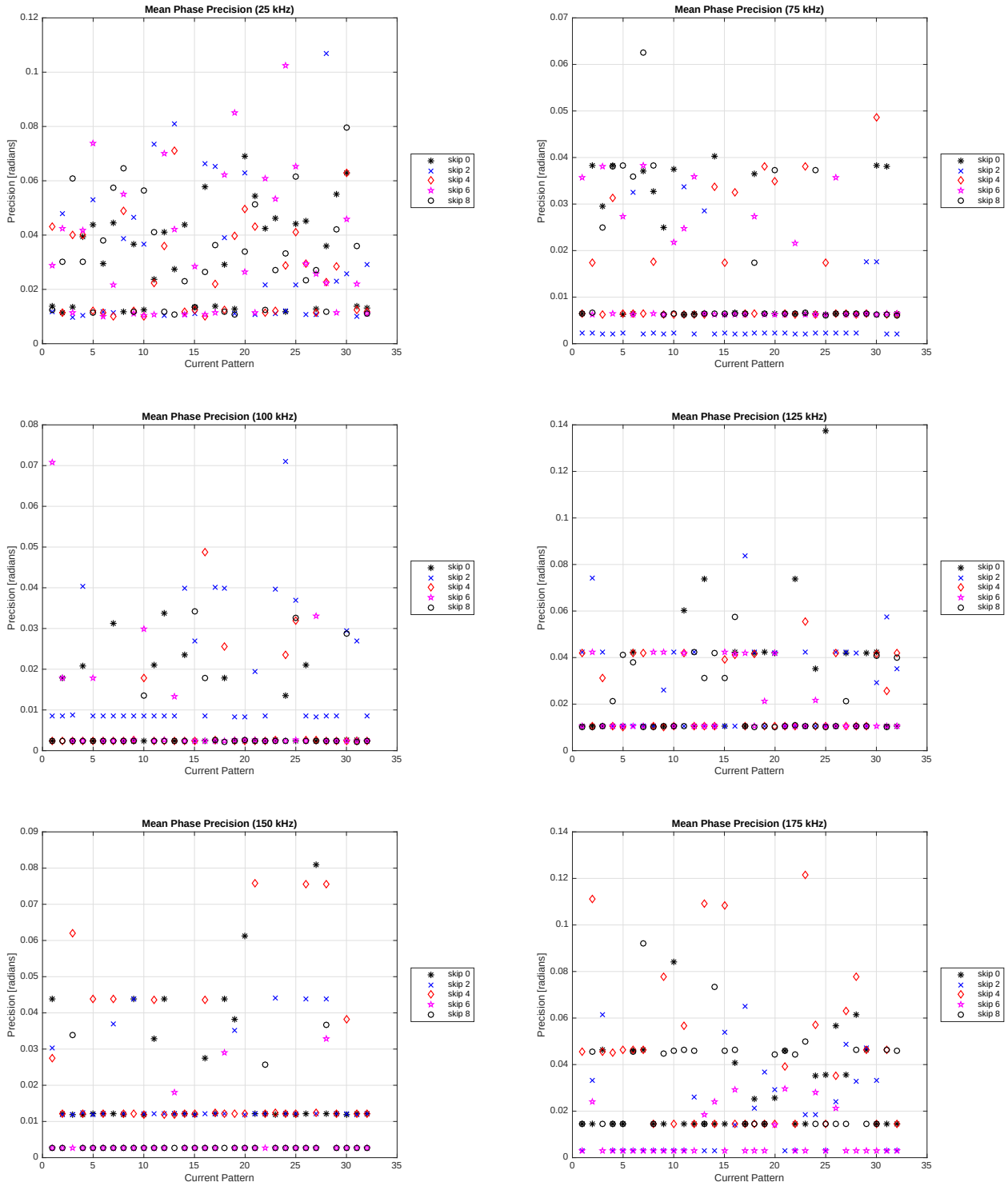

Figure B.5. Mean phase precision for each current pattern ($(P_\theta{}^k)_{mean}$) for measured voltage phases corresponding to a 0.25 V_{pk} applied voltage at various frequencies for 100 frames of data acquired at the 512 point acquisition rate.

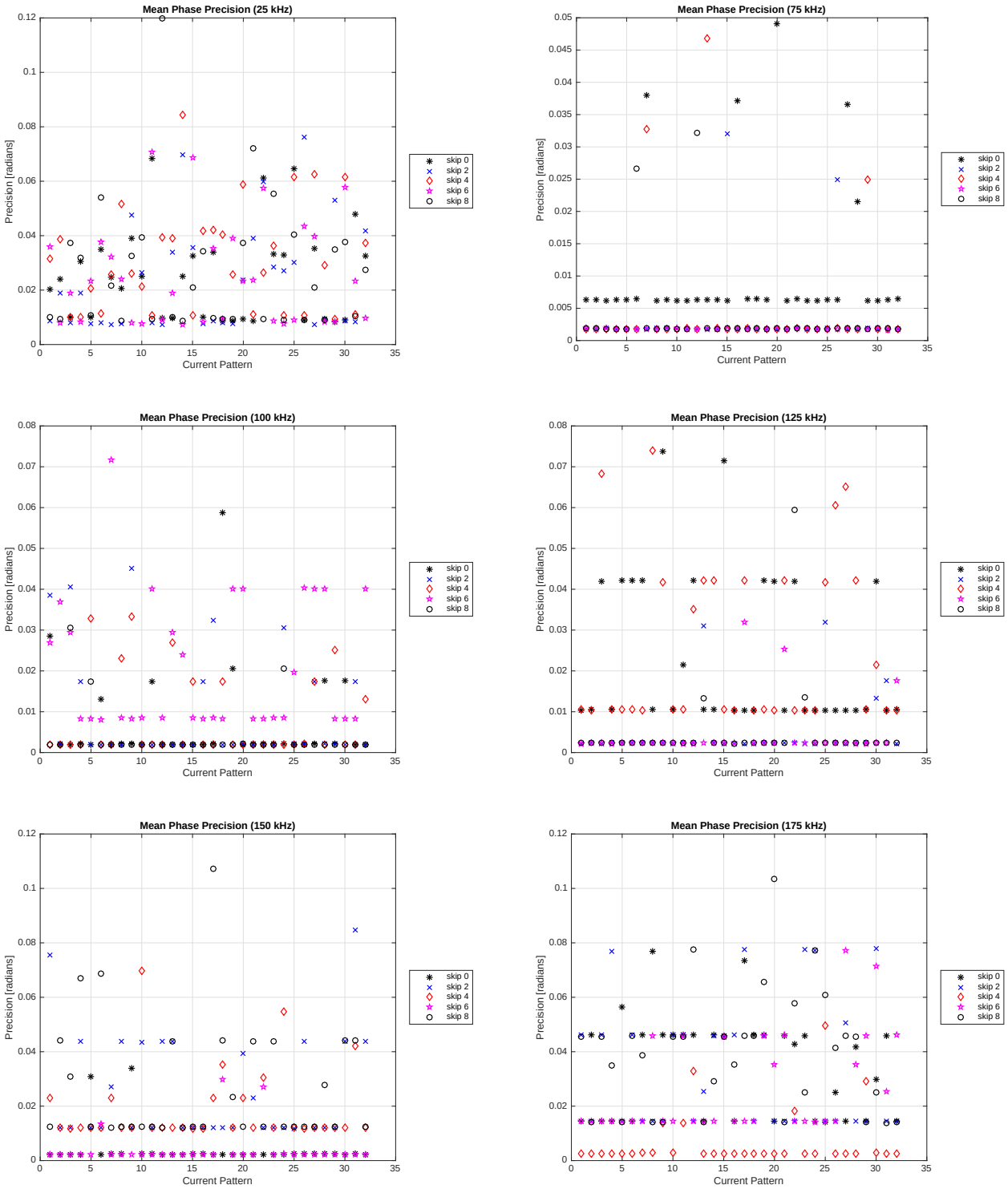

Figure B.6. Mean phase precision for each current pattern ($(P_\theta{}^k)_{mean}$) for measured voltage phases corresponding to a 0.375 V_{pk} applied voltage at various frequencies for 100 frames of data acquired at the 512 point acquisition rate.

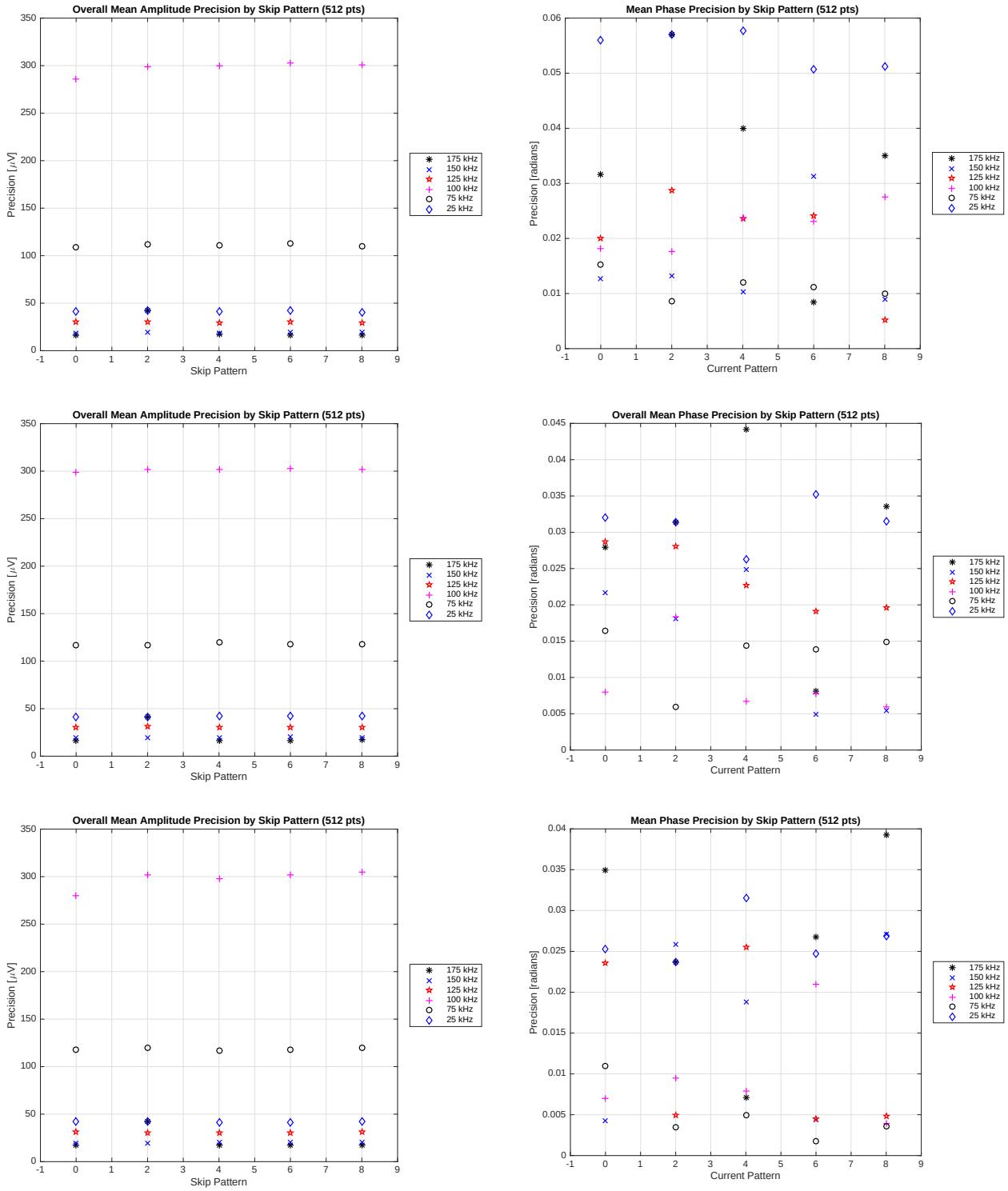

Figure B.7. Overall mean precision for amplitude $(P_{pk})_{mean}$ (left) and phase $(P_{\theta})_{mean}$ (right) for different skip patterns and frequencies taken at the 512 point acqusition rate for: 0.125 V_{pk} (row 1), 0.25 V_{pk} (row 2) and 0.375 V_{pk} (row 3).

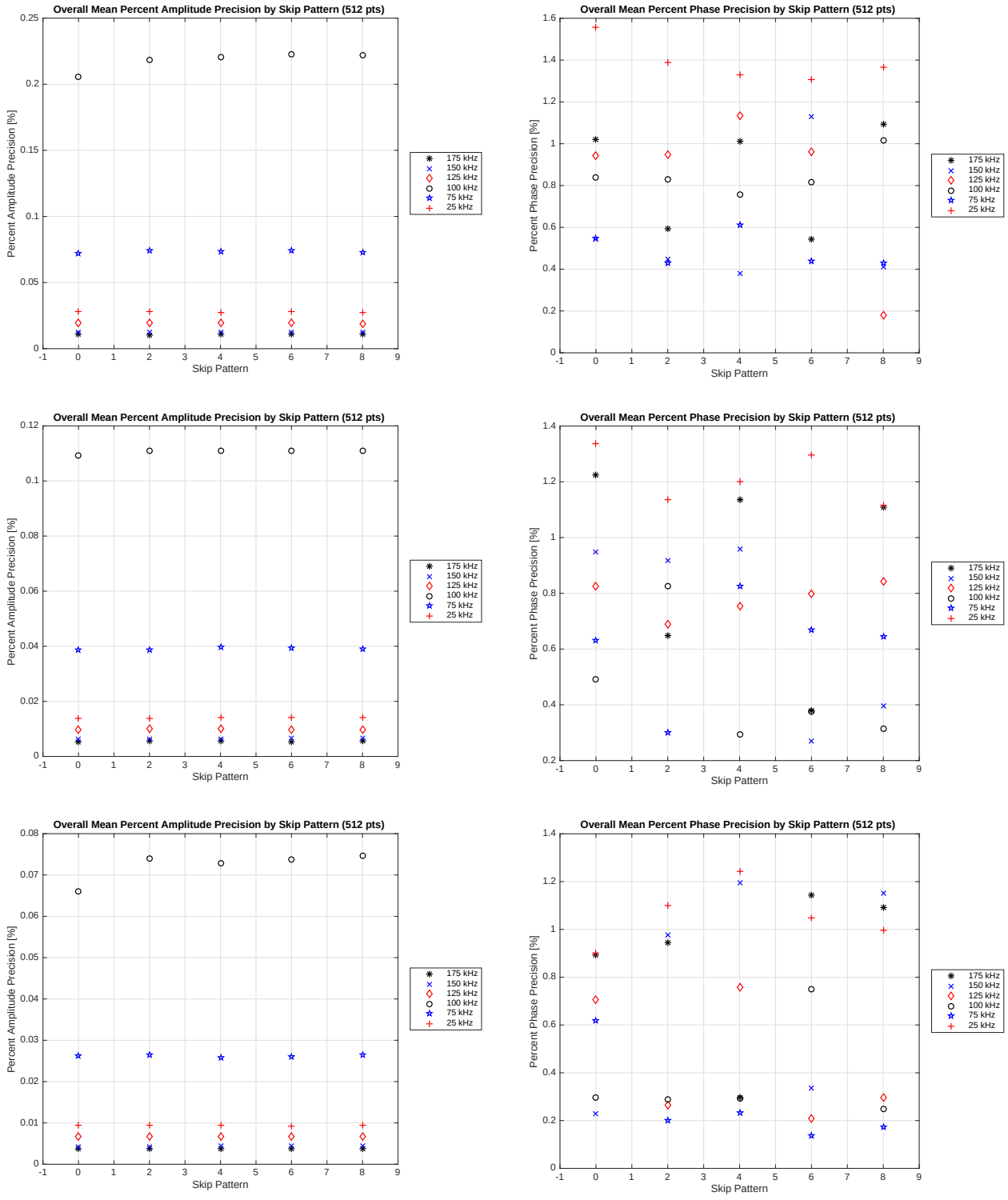

Figure B.8. Overall percent mean precision for amplitude Percent $(P_{pk})_{mean}$ (left) and phase Percent $(P_{\theta})_{mean}$ (right) for different skip patterns and frequencies taken at the 512 point acqusition rate for: 0.125 V_{pk} (row 1), 0.25 V_{pk} (row 2) and 0.375 V_{pk} (row 3).

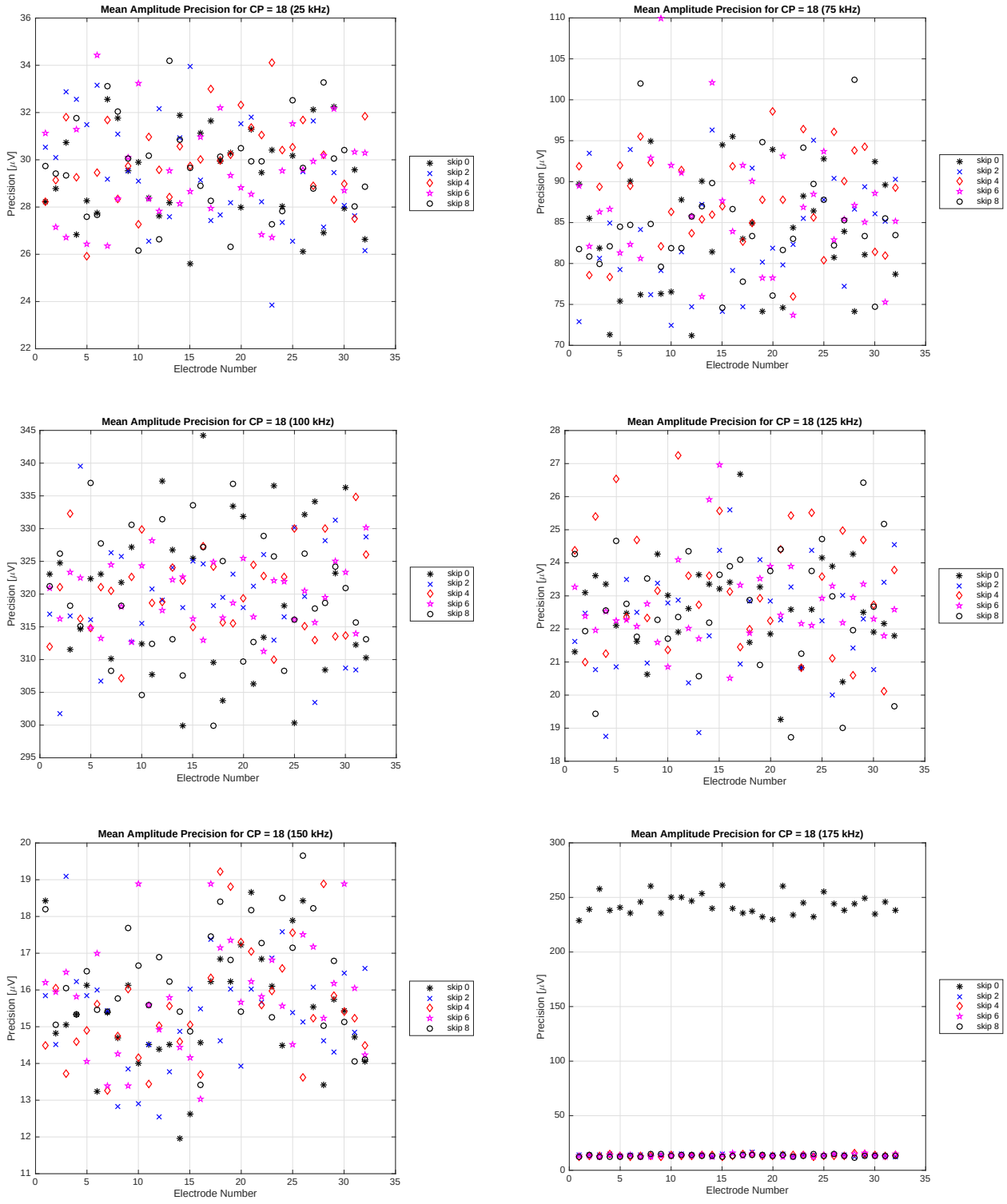

Figure B.9. The precision $(P_{pk}{}_l^k)$ or one standard deviation for measured voltage amplitudes of a 0.375 V_{pk} applied voltage at various frequencies for 100 frames of data acquired at the 1024 point acquisition rate.

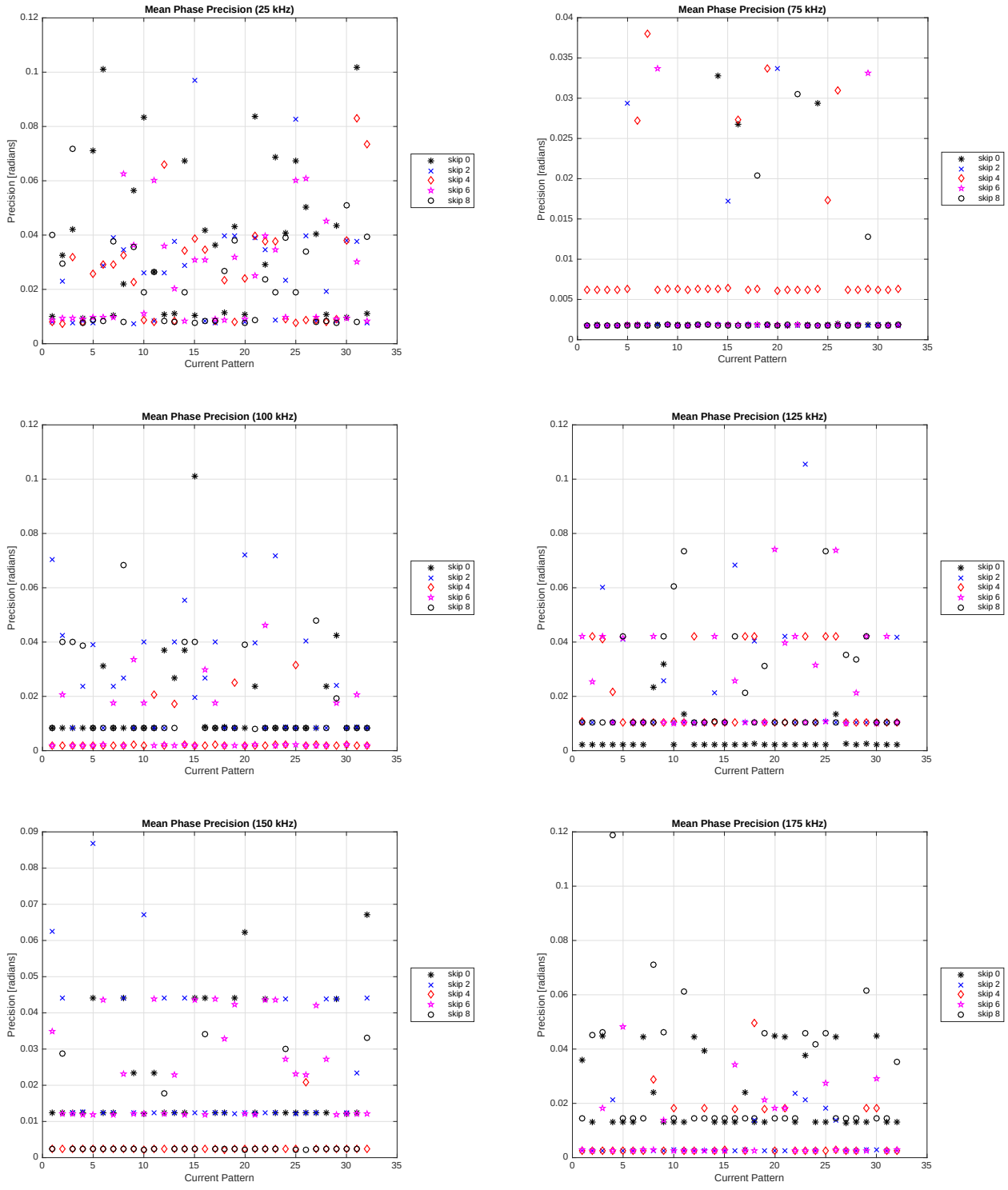

Figure B.10. Mean phase precision for each current pattern ($(P_\theta{}^k)_{mean}$) for measured voltage phases corresponding to a 0.375 V_{pk} applied voltage at various frequencies for 100 frames of data acquired at the 1024 point acquisition rate.

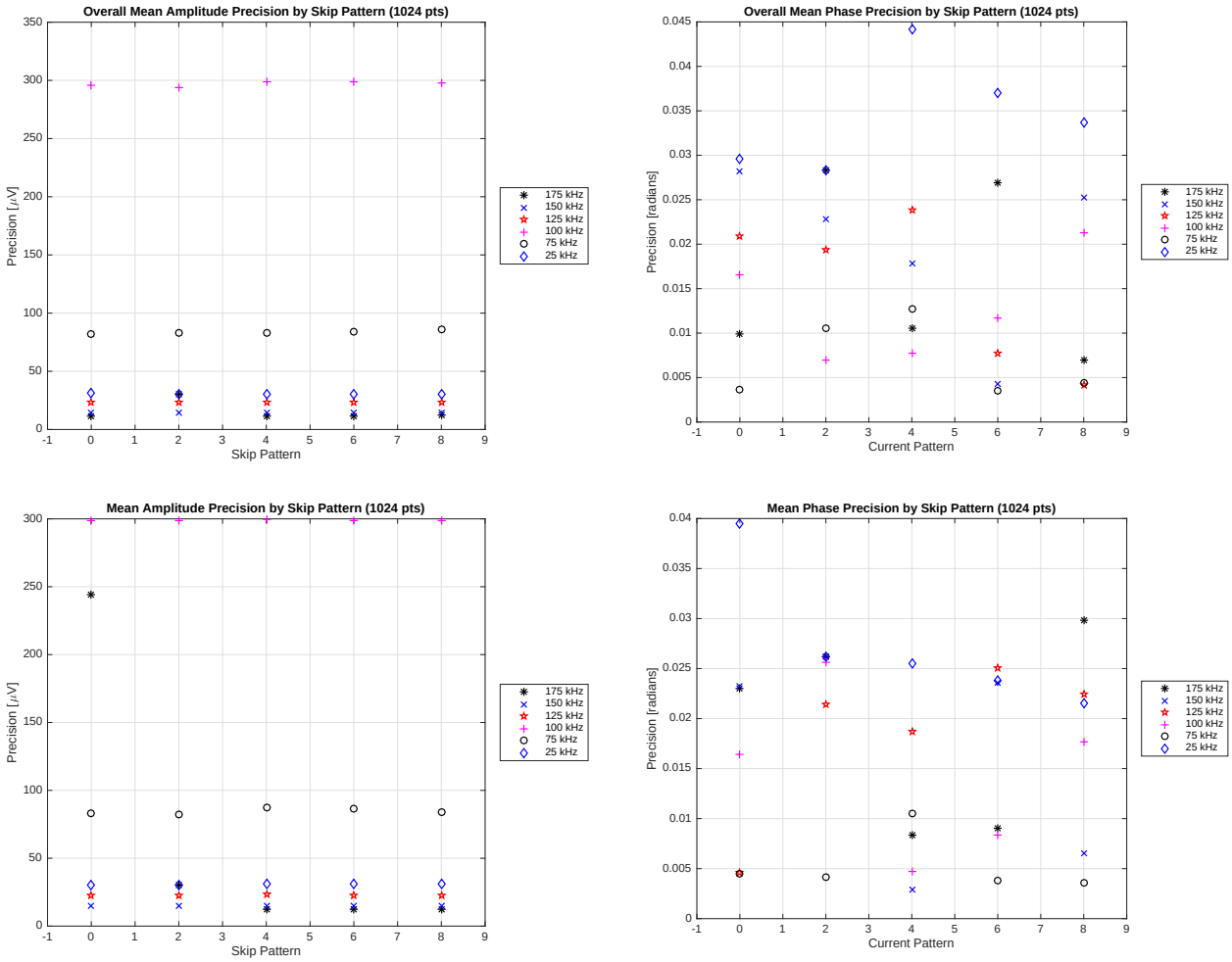

Figure B.11. Overall mean precision for amplitude $(P_{pk})_{mean}$ (left) and phase $(P_\theta)_{mean}$ (right) for different skip patterns and frequencies taken at the 1024 point acqusition rate for: 0.25 V_{pk} (row 1) and 0.375 V_{pk} (row 2).

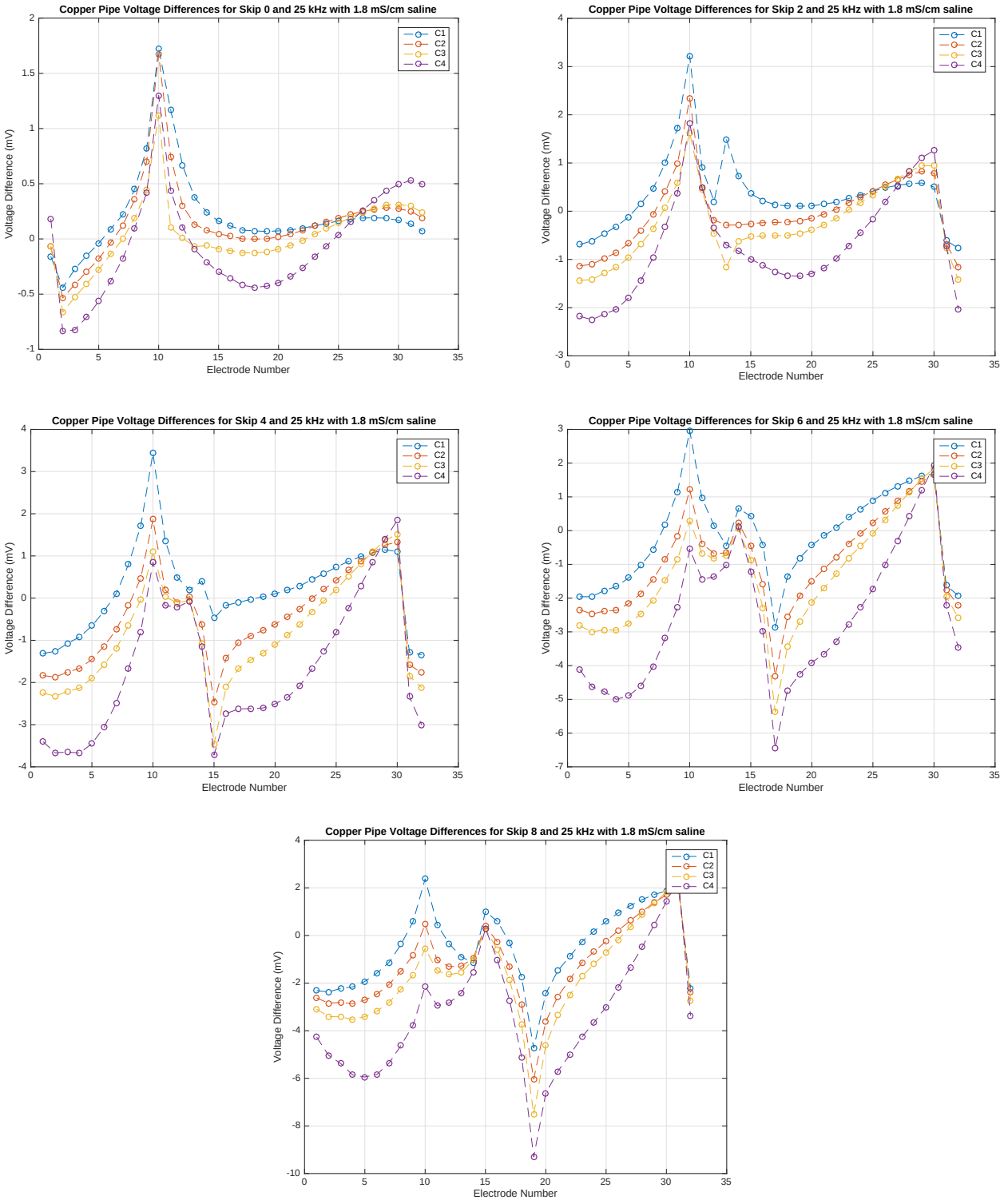

Figure B.12. Mean distinguishability plots at 25 kHz for current pattern 10 and skip patterns 0, 2, 4, 6, and 8 where C1, C2, C3 and C4 are the copper pipe targets.

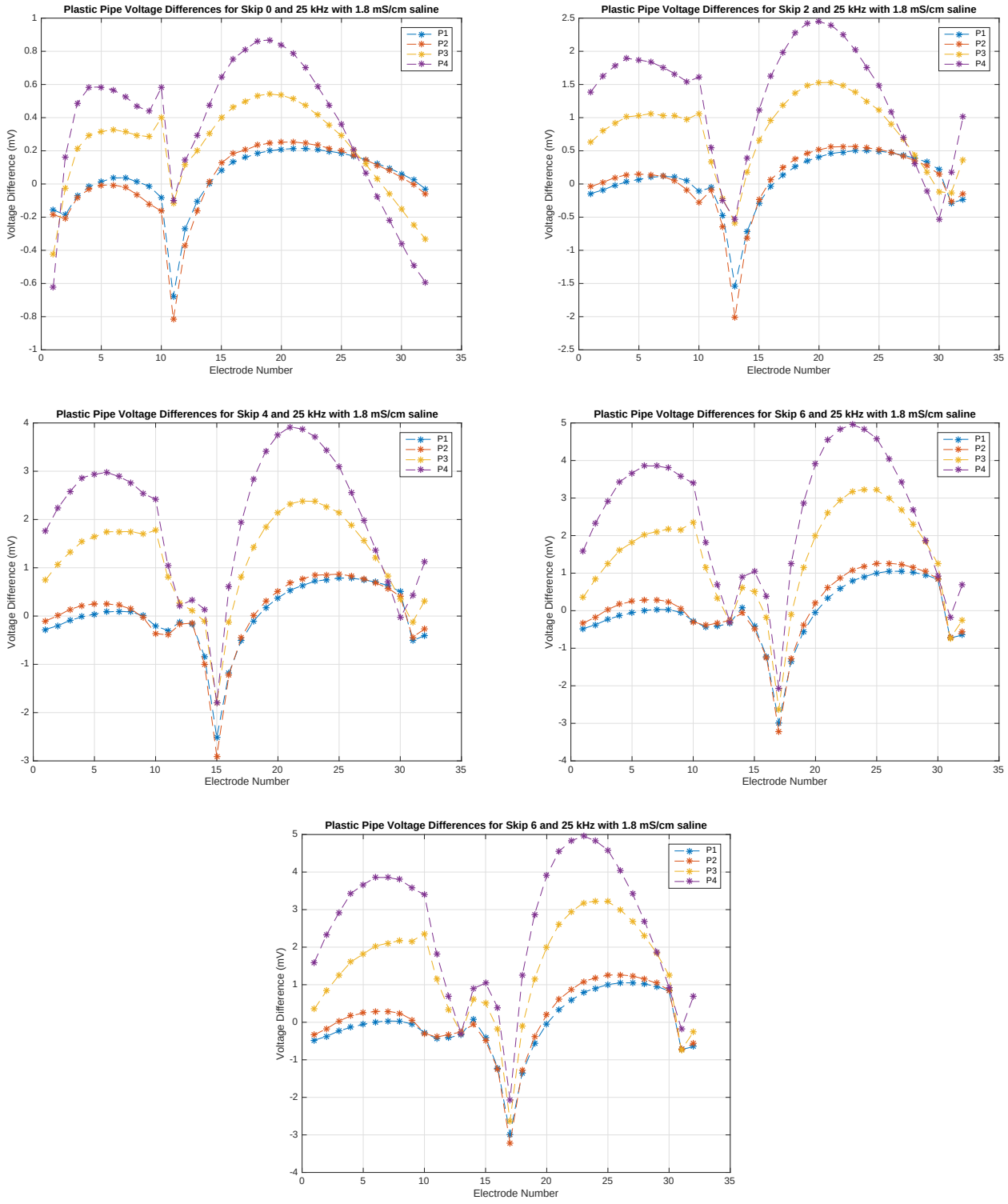

Figure B.13. Mean distinguishability plots at 25 kHz for current pattern 10 and skip patterns 0, 2, 4, 6, and 8 where P1, P2, P3 and P4 are the plastic pipe targets.

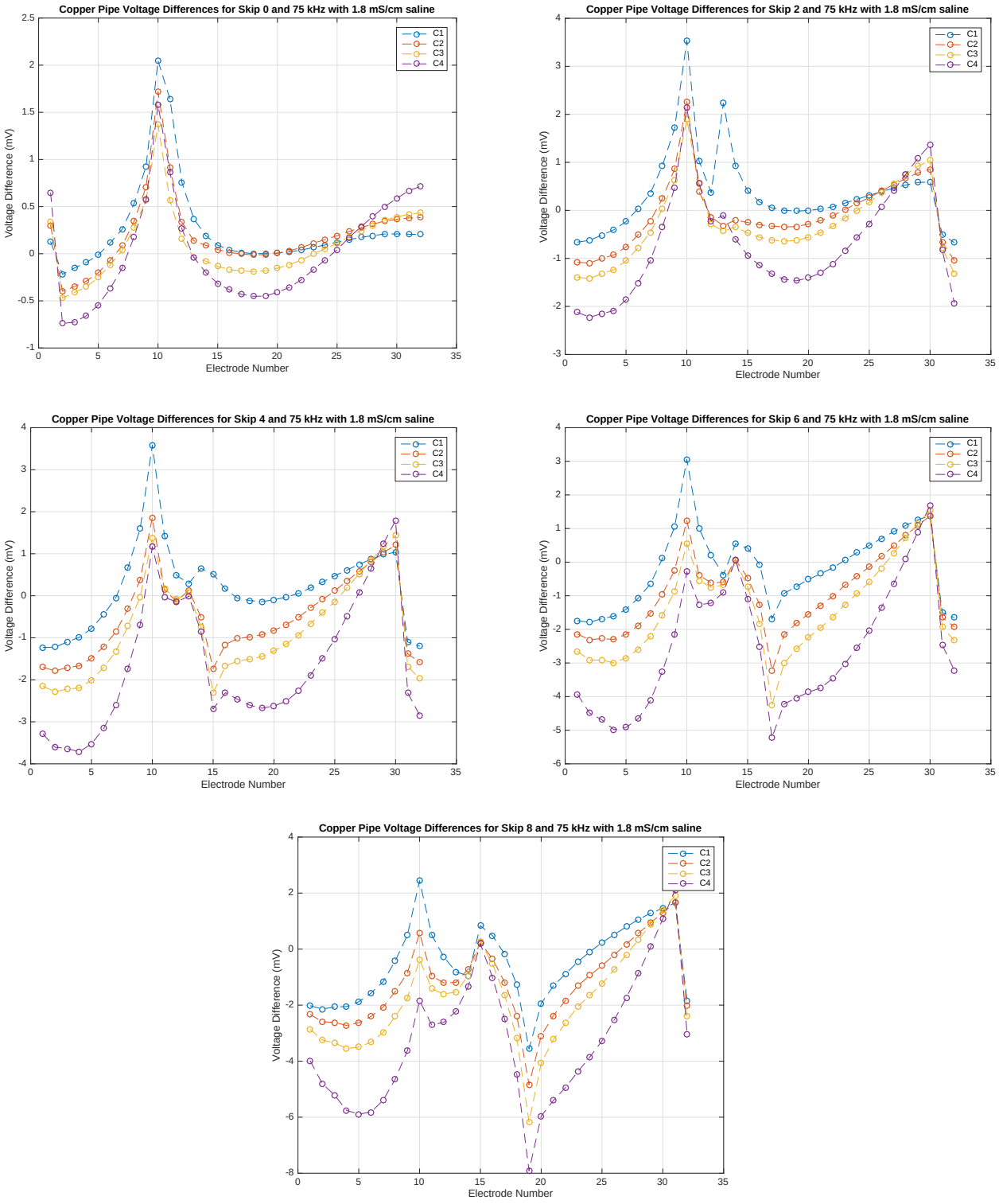

Figure B.14. Mean distinguishability plots at 75 kHz for current pattern 10 and skip patterns 0, 2, 4, 6, and 8 where C1, C2, C3 and C4 are the copper pipe targets.

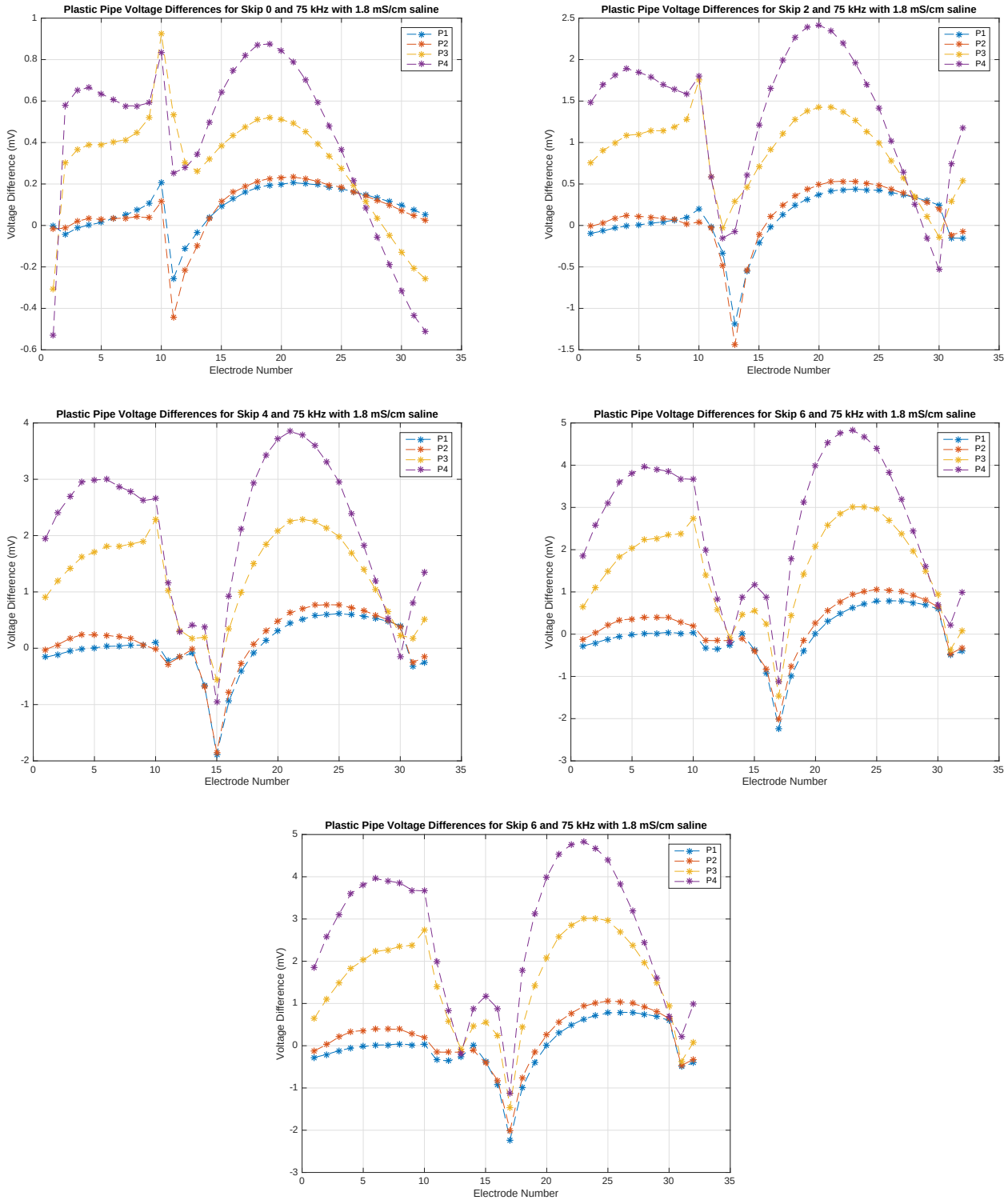

Figure B.15. Mean distinguishability plots at 75 kHz for current pattern 10 and skip patterns 0, 2, 4, 6, and 8 where P1, P2, P3 and P4 are the plastic pipe targets.

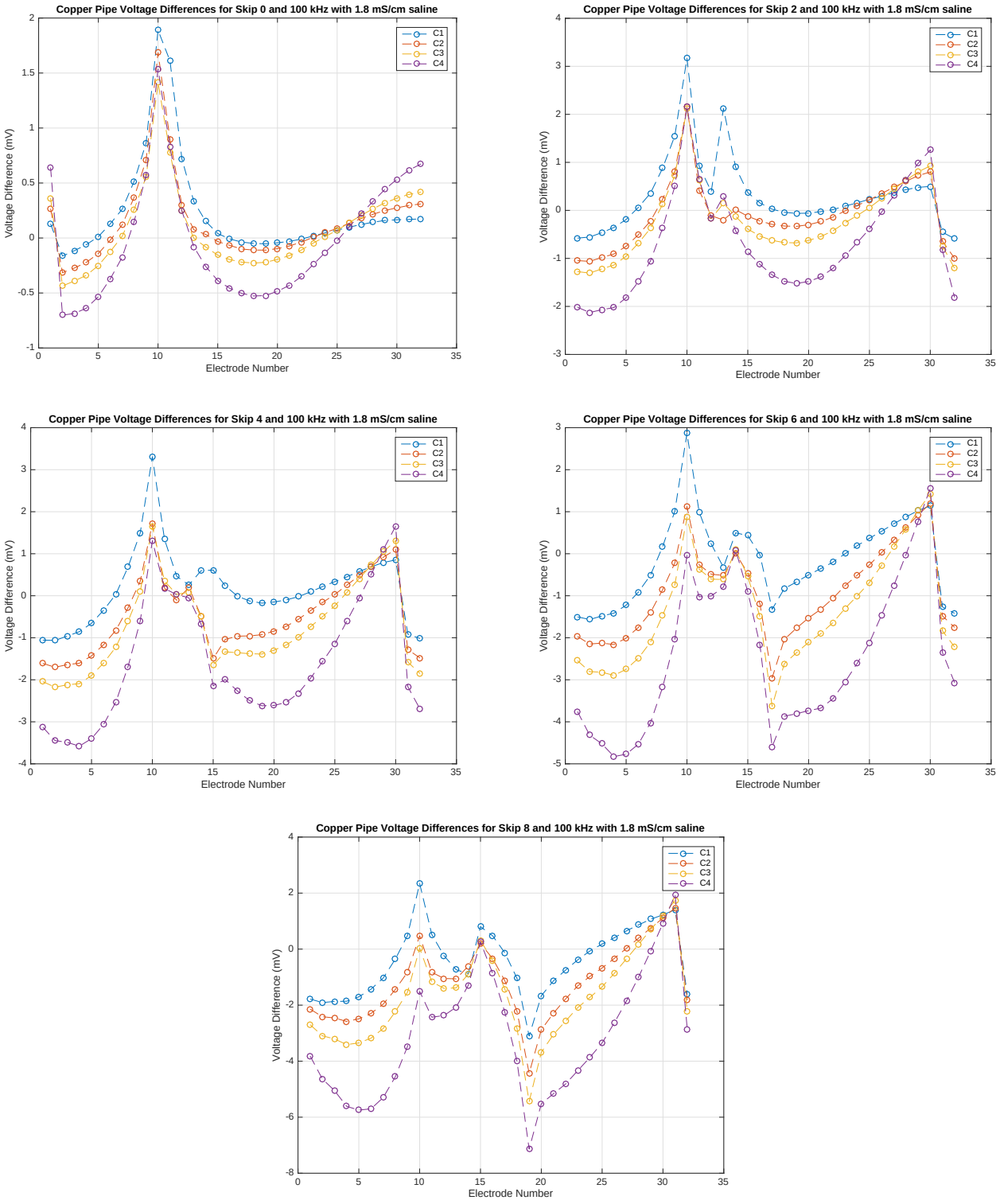

Figure B.16. Mean distinguishability plots at 100 kHz for current pattern 10 and skip patterns 0, 2, 4, 6, and 8 where C1, C2, C3 and C4 are the copper pipe targets.

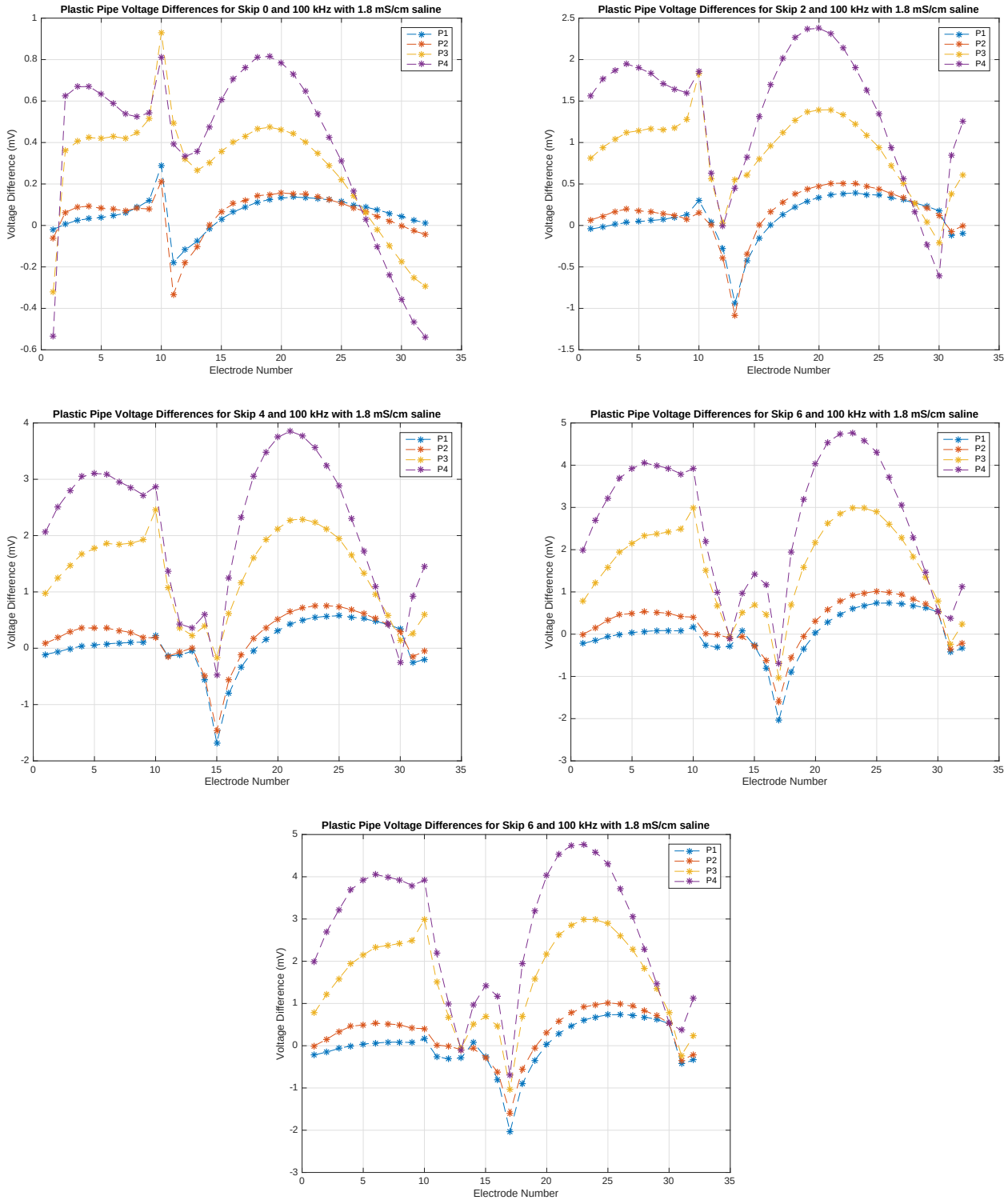

Figure B.17. Mean distinguishability plots at 100 kHz for current pattern 10 and skip patterns 0, 2, 4, 6, and 8 where P1, P2, P3 and P4 are the plastic pipe targets.

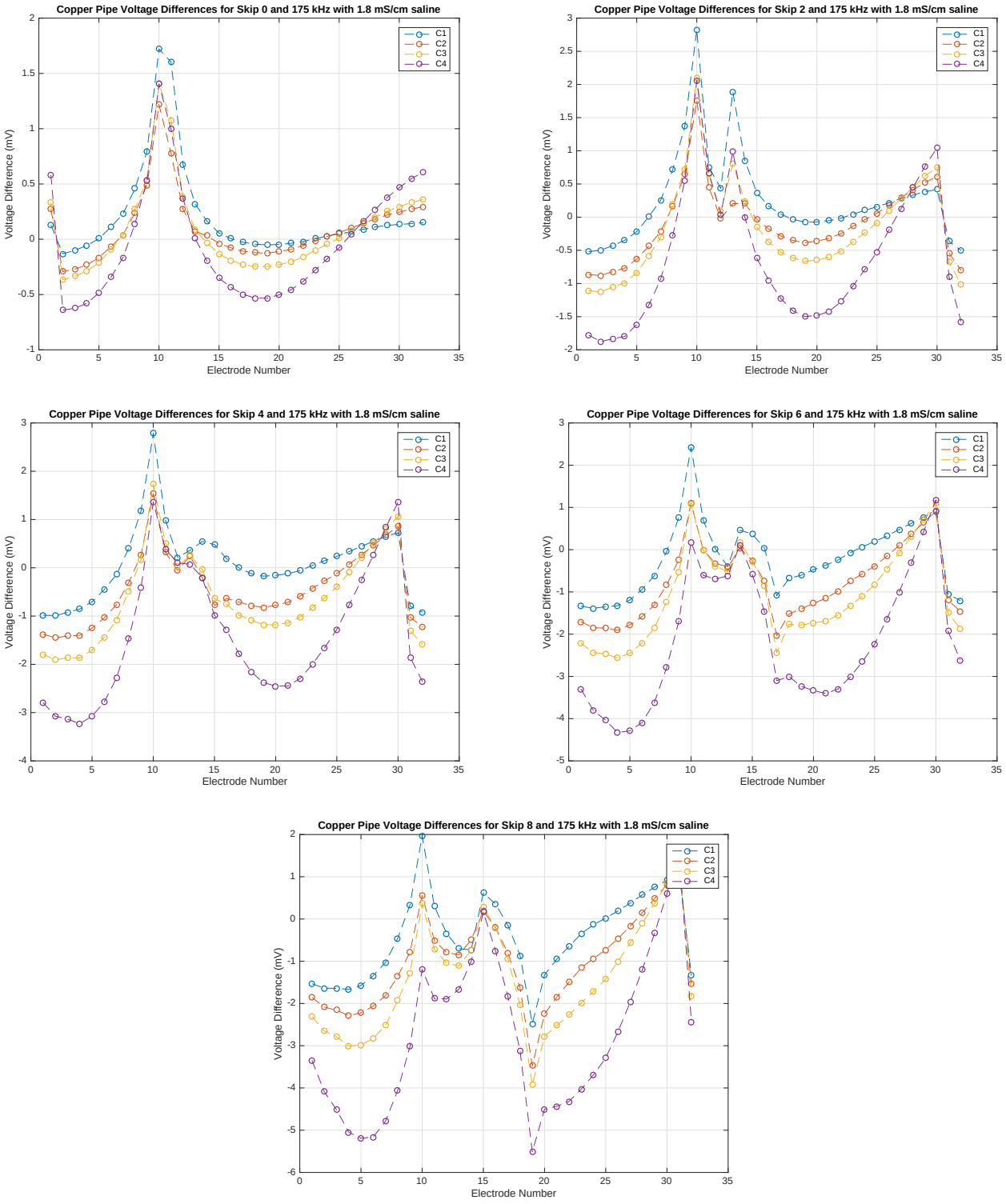

Figure B.18. Mean distinguishability plots at 175 kHz for current pattern 10 and skip patterns 0, 2, 4, 6, and 8 where C1, C2, C3 and C4 are the copper pipe targets.

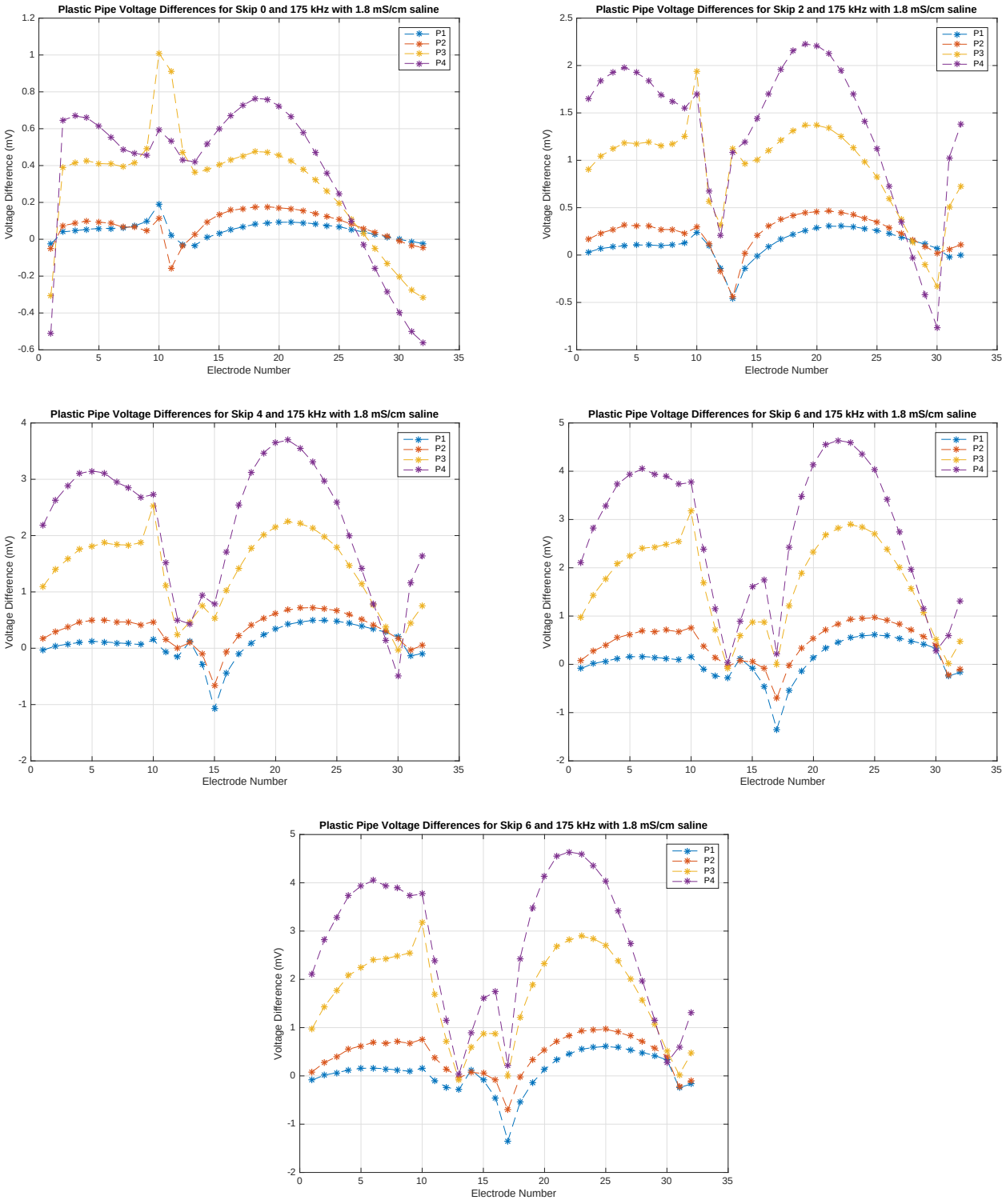

Figure B.19. Mean distinguishability plots at 175 kHz for current pattern 10 and skip patterns 0, 2, 4, 6, and 8 where P1, P2, P3 and P4 are the plastic pipe targets.

APPENDIX C

ADDITIONAL RESULTS FROM TESTS RELATING TO NOISE

C.1. SNR on a Homogeneous Tank

Table C.1 and Table C.2 contain SNR testing results for 75 kHz and 100 kHz, respectively. In both tests, no ground was placed in the center, and 8 V_{pp} input to the VCCS in general yielded worse SNR than 6 V_{pp}. It may be inferred from these tables that skip patterns 4-8 should yield data with a higher SNR. They also suggests that a frame rate of 33.2 frames/second (or the 256 point acquisition rate) would be sufficient to achieve tank data with an SNR of at least 80 dB, but approximately 5 dB can be gained by decreasing the frame rate or increasing acquisition rate to 1024 points.

Figure C.1 shows plots of SNR for even numbered skip patterns at a variety frequencies. Figure C.2 plots both even and odd numbered skip patterns at 125 kHz for different input voltages to the VCCS. It is clear from comparing 6 V_{pp} to 8 V_{pp} plots in Figure C.2 that the SNR is reduced without a ground to absorb mismatched current.

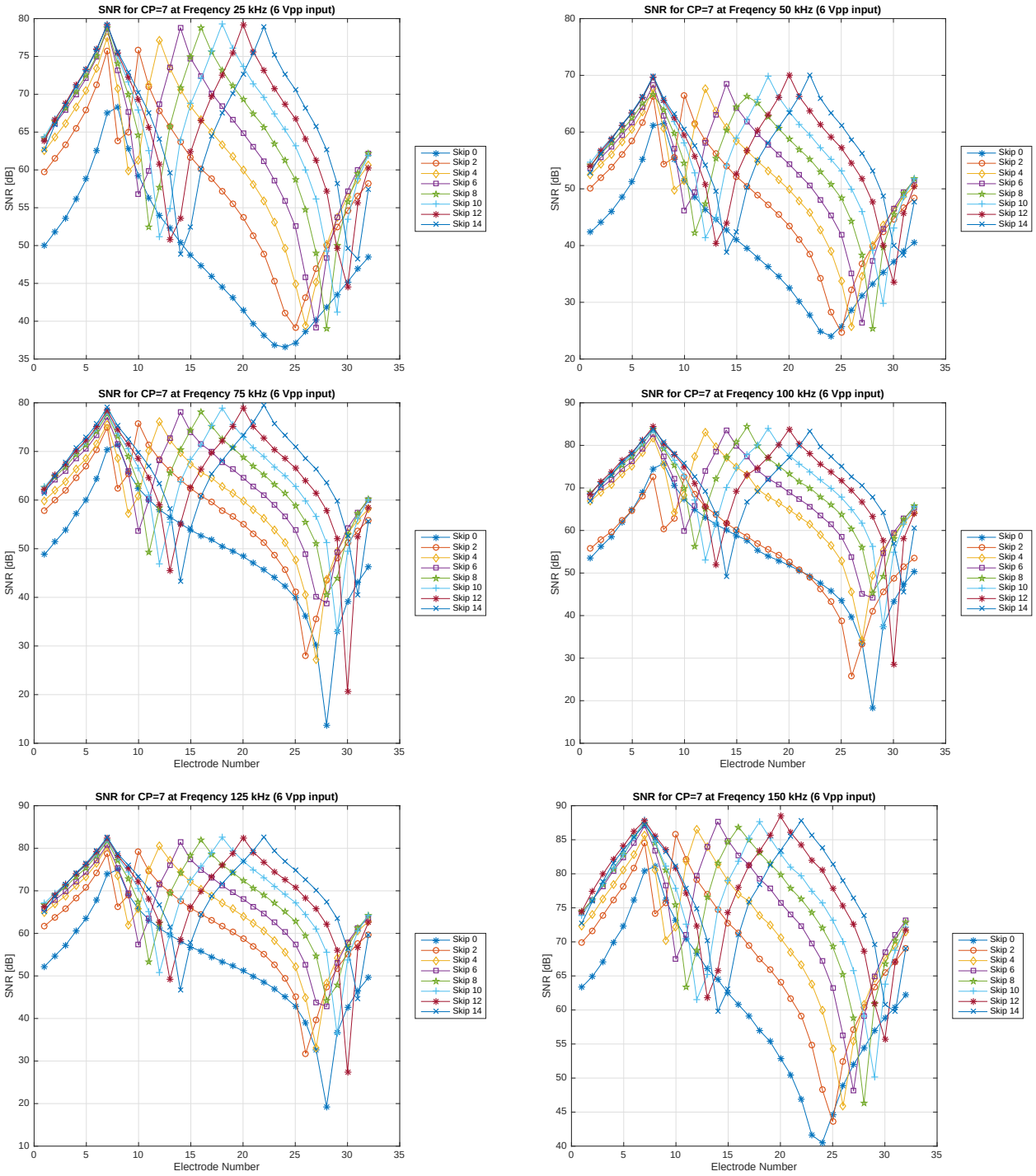

Figure C.1. Single current pattern SNR for 250 frames at the 256 point acquisition rate for 6 V_{pp} input voltage to the VCCS. (Row 1) 25 kHz, 50 kHz. (Row 2) 75 kHz, 100 kHz. (Row 3) 125 kHz, 150 kHz.

Table C.1. A comparison of the average SNR of V_e measurements for injecting electrodes is presented. 251 frames of data was taken on a tank phantom filled with a saline solution with no ground in the center. Current was injected at 75 kHz. The peak-to-peak voltages correspond to function generator settings of the VCCS. 256, 512, or 1024 indicate the number of samples acquired.

Skip	2Vpp 256	2Vpp 512	2Vpp 1024	4Vpp 256	4Vpp 512	4Vpp 1024	6Vpp 256	6Vpp 512	6Vpp 1024	8Vpp 256	8Vpp 512	8Vpp 1024
0	60.4	63.5	66.6	66.5	69.5	73.6	70.3	73.0	75.4	70.7	73.1	77.8
1	63.9	67.0	69.9	70.0	72.8	76.6	73.7	76.2	78.8	75.5	79.1	**81.4**
2	65.6	68.5	71.5	71.6	74.3	78.1	75.3	77.7	**80.8**	77.2	**80.9**	**82.5**
3	66.7	69.5	74.6	72.5	75.5	79.0	76.2	78.9	**81.6**	77.8	76.2	**80.1**
4	67.4	70.2	74.5	73.3	76.4	79.7	76.9	79.8	**82.2**	77.2	74.4	71.3
5	67.8	70.8	74.7	73.8	76.7	**80.1**	77.4	**80.0**	**82.8**	76.1	75.4	76.0
6	68.3	71.2	74.0	74.2	77.0	**80.1**	77.9	**80.5**	**83.4**	75.0	76.3	**80.5**
7	68.6	71.6	74.1	74.6	77.5	**80.5**	78.1	**80.8**	**83.9**	76.2	77.2	61.1
8	69.0	72.8	74.4	75.0	77.6	**80.8**	78.2	**80.9**	**83.8**	71.7	71.9	77.7
9	69.1	73.0	75.6	75.4	77.9	**80.6**	78.3	**81.5**	**83.5**	68.0	72.7	71.2
10	69.3	73.0	75.6	75.5	78.0	**80.8**	78.5	**81.7**	73.0	67.3	52.8	68.7
11	69.4	72.7	75.3	75.6	78.0	**80.8**	78.6	**81.8**	**84.4**	65.3	52.6	71.9
12	69.4	72.8	75.6	75.5	77.8	**81.5**	78.7	**81.8**	**84.1**	63.7	67.2	70.1
13	69.5	72.7	75.4	75.5	78.0	**81.3**	78.8	**81.5**	**84.5**	62.3	65.9	68.3
14	69.5	72.6	75.4	75.6	78.1	**82.7**	78.8	**81.8**	**84.5**	67.3	64.5	53.4
15	69.4	72.6	75.6	75.5	78.0	**81.2**	79.0	**81.8**	**83.5**	67.6	63.0	56.5

Table C.2. A comparison of the average SNR of V_e measurements for injecting electrodes is presented. 251 frames of data was taken on a tank phantom filled with a saline solution with no ground in the center. Current was injected at 100 kHz. The peak-to-peak voltages correspond to function generator settings of the VCCS. 256, 512, or 1024 indicate the number of samples acquired.

Skip	2Vpp 256	2Vpp 512	2Vpp 1024	4Vpp 256	4Vpp 512	4Vpp 1024	6Vpp 256	6Vpp 512	6Vpp 1024	8Vpp 256	8Vpp 512	8Vpp 1024
0	66.0	67.7	69.1	71.7	73.7	75.0	75.1	77.1	77.7	75.2	79.3	**80.7**
1	60.3	71.0	72.3	75.1	77.2	78.1	78.4	**80.7**	**81.2**	**80.5**	**82.6**	**82.7**
2	70.9	72.7	74.1	76.6	78.7	79.8	74.8	**82.1**	**82.8**	**81.3**	71.6	**83.2**
3	71.9	73.7	75.1	77.7	79.6	**81.0**	70.1	**83.2**	**83.5**	**82.9**	77.8	**80.8**
4	72.6	74.4	75.4	78.5	**80.4**	**81.7**	**81.7**	**83.7**	**84.6**	78.2	78.9	74.6
5	73.1	75.0	75.9	78.9	**80.9**	**82.0**	**82.4**	**84.4**	**85.4**	77.9	77.9	78.0
6	73.5	75.3	76.3	79.2	**81.2**	**82.6**	**82.8**	**84.8**	**85.1**	77.3	78.0	78.8
7	73.7	75.5	75.7	79.7	**81.5**	**82.6**	**83.0**	**82.8**	**83.9**	79.5	76.5	51.2
8	74.0	76.2	76.9	79.8	**81.7**	**82.7**	**83.2**	**85.1**	**84.8**	71.3	51.9	72.6
9	74.3	76.4	77.0	**80.0**	**81.9**	**83.2**	**83.5**	**85.3**	**85.6**	54.8	66.1	51.9
10	74.5	76.6	76.7	**80.3**	**81.8**	**83.5**	**83.6**	**84.7**	**85.5**	52.5	51.8	73.9
11	74.5	76.6	76.9	**80.3**	**82.1**	**83.5**	**83.2**	**85.4**	**85.8**	52.2	50.5	63.4
12	74.6	76.7	77.5	**80.3**	**82.1**	**83.6**	**83.7**	**85.6**	**85.1**	63.2	67.8	60.7
13	74.6	76.7	78.0	**80.4**	**82.2**	**83.5**	**83.3**	**85.9**	**86.4**	65.5	66.5	54.1
14	74.5	76.7	77.8	**80.5**	**82.2**	**83.7**	**83.8**	**85.1**	**84.5**	62.5	56.4	55.9
15	74.7	76.8	77.7	**80.5**	**82.2**	**83.6**	**80.5**	**85.1**	**85.7**	57.9	58.2	53.5

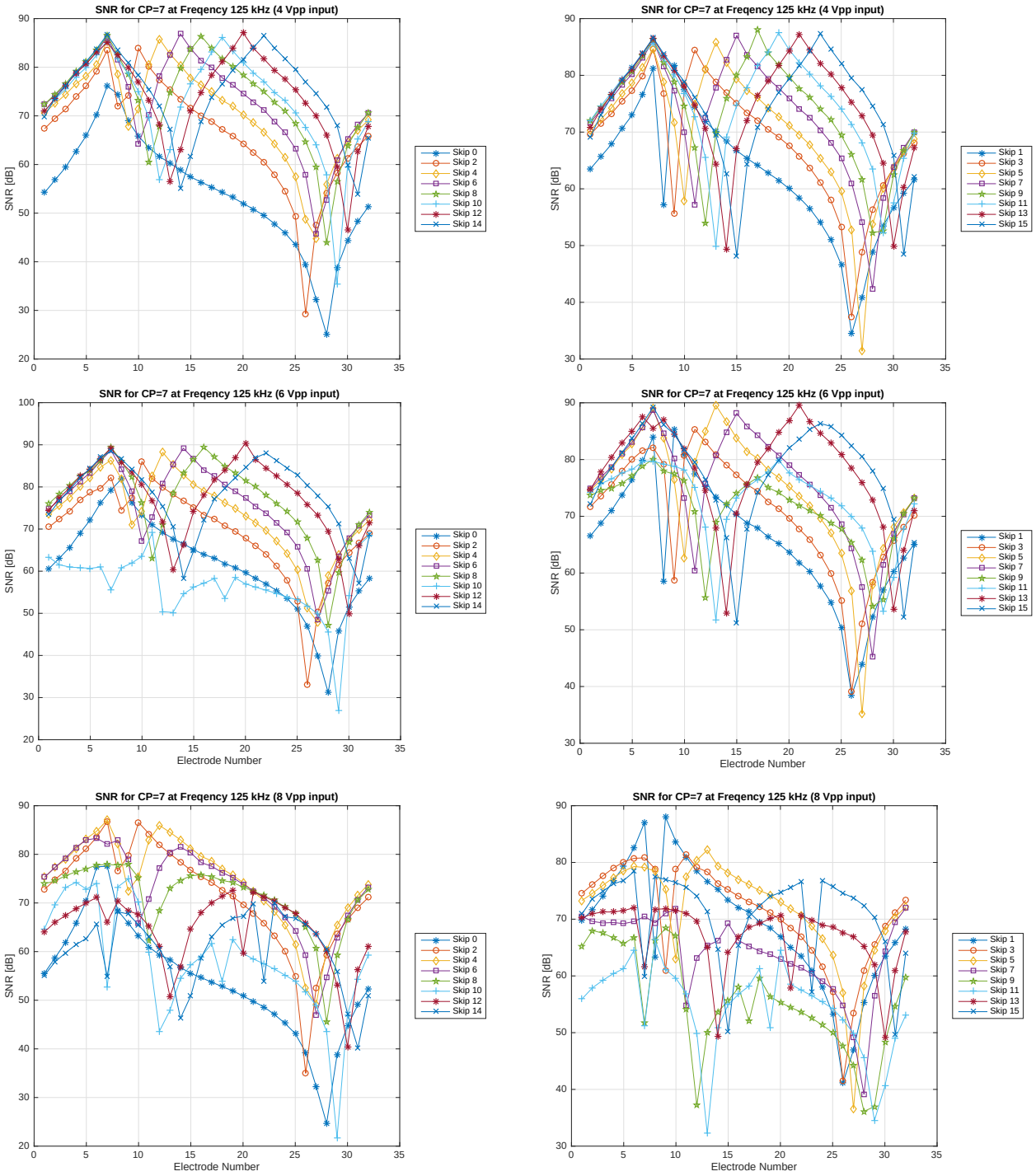

Figure C.2. Single current pattern SNR for 250 frames at 125 kHz where the voltage input to the VCCS is set to 4 V_{pp} (Row 1), 6 V_{pp} (Row 2), 8 V_{pp} (Row 3) for the 1024 point acquisition rate.

C.2. Additional FFTs of ACE1 Raw Data at Multiple Frequencies

Presented in this section are Fast Fourier Transforms (FFTs) for raw data (prior to demodulation) taken at 125 kHz on a healthy human subject for skip 0 and skip 2. Figure C.3 overlays FFTs of different channels during the first current pattern, more greatly emphasizing the noise and smaller magnitudes of voltages measured as distance from injection electrodes increases. Figure C.4 and Figure C.5 show raw data and corresponding FFTs. These results are consistent with what one might expect from SNR results presented in Section 5.1 and Section C.1. Additionally, in future modifications of the ACE1 system, it is recommended that the group avoid using 40 to 50 kHz or 65 kHz because of the higher levels of noise associated with those frequencies.

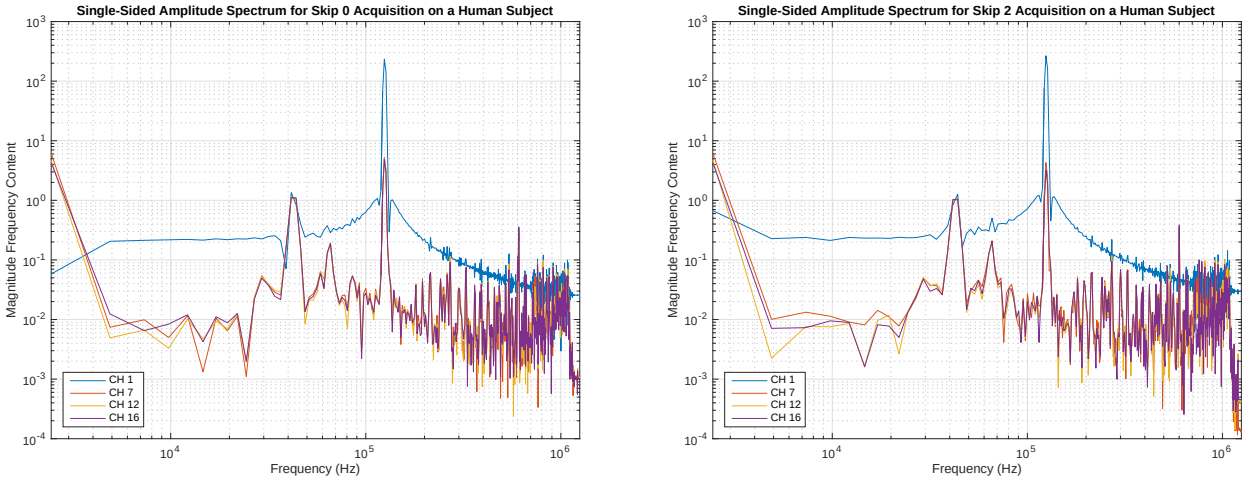

Figure C.3. FFTs of channel measurements for a skip 0 and 2 datasets taken on a human subject.

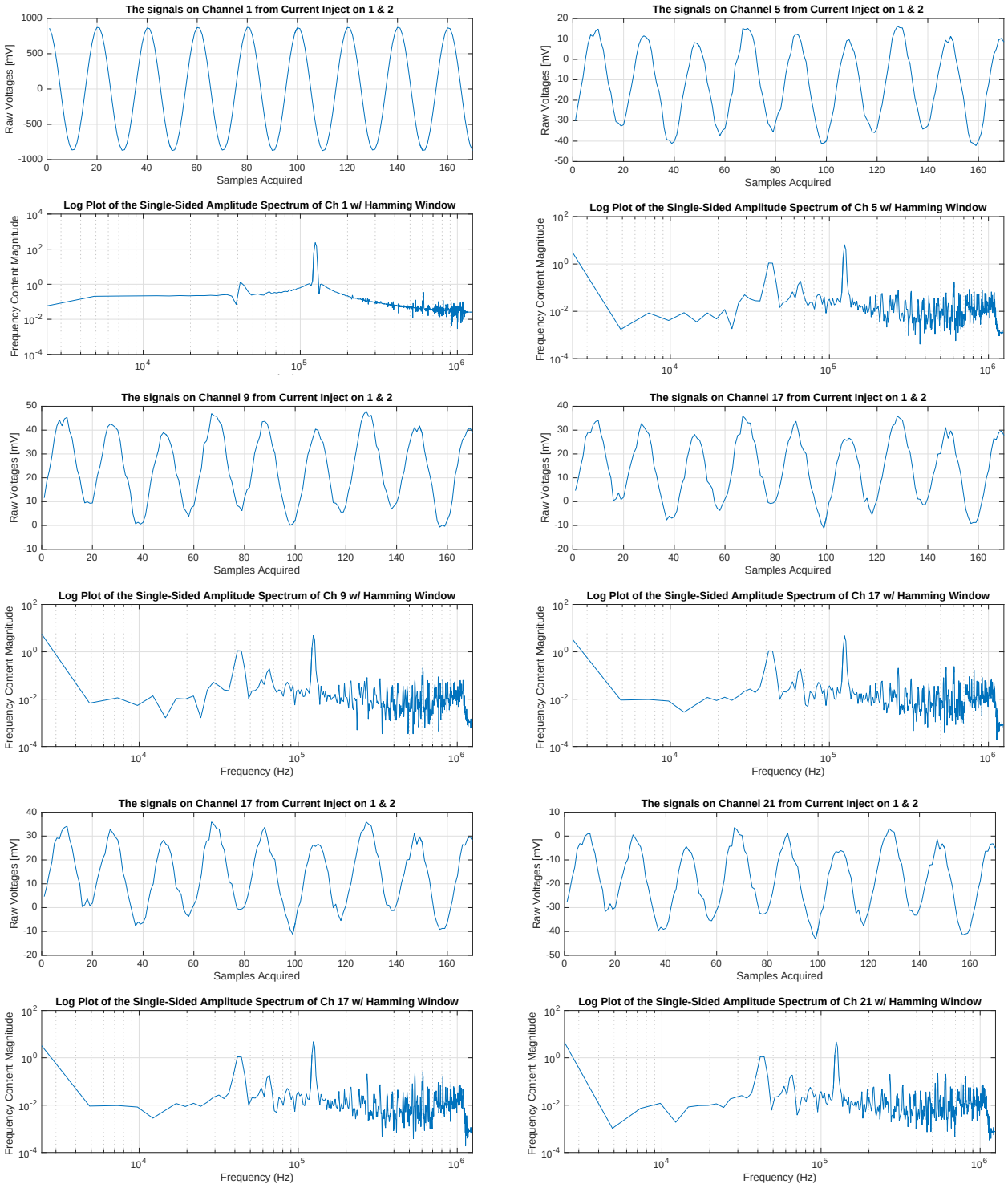

Figure C.4. Raw data measurements and corresponding FFTs of individual channels for a skip 0 dataset at 16.0 frames/second and 125 kHz taken on a human subject.

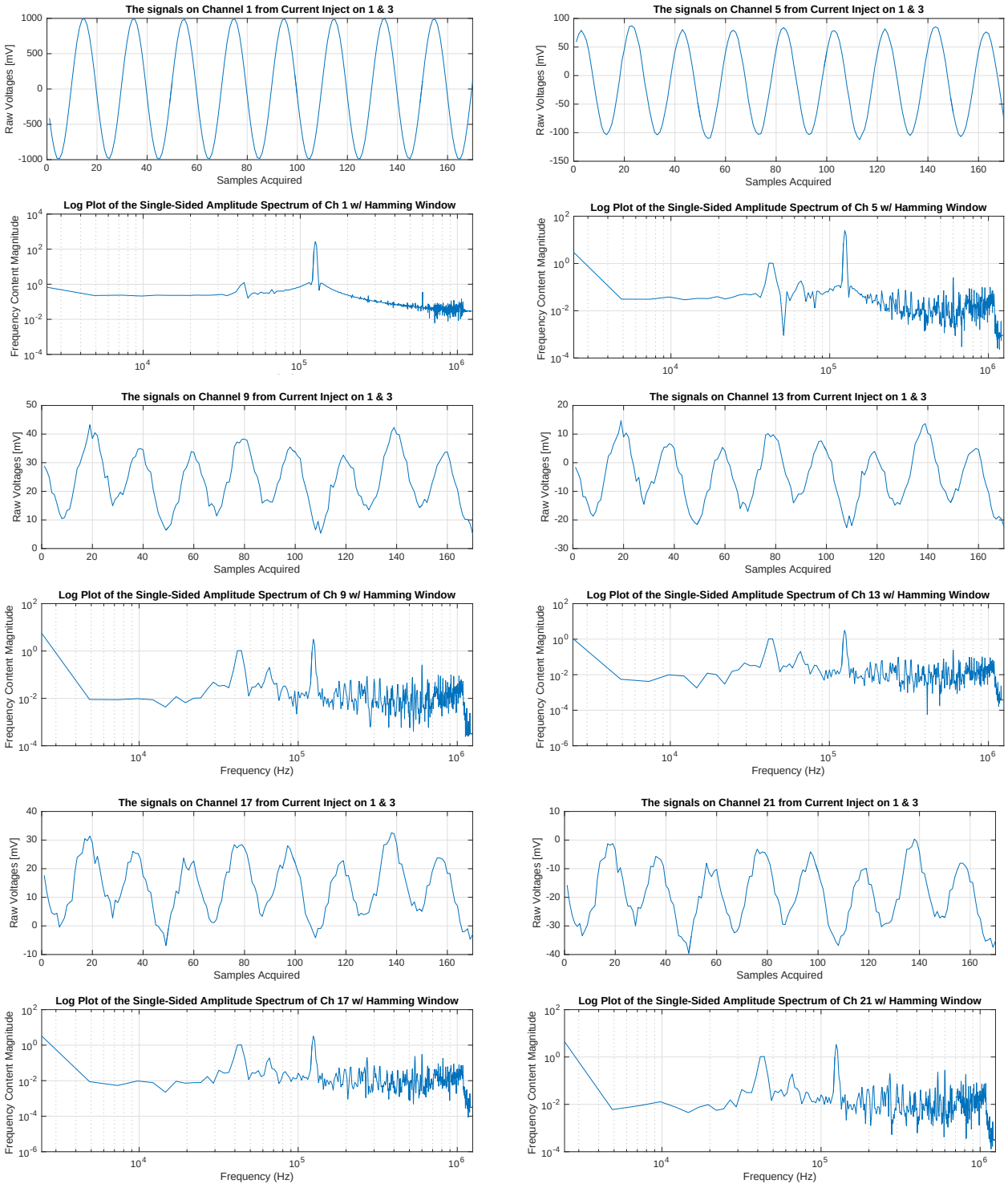

Figure C.5. Raw data measurements and corresponding FFTs of individual channels for a skip 2 dataset at 16.0 frames/second and 125 kHz taken on a human subject.

APPENDIX D

DETAILED FORMULATION OF 2-D TRIANGULAR FINITE ELEMENTS IN EIT

The EIT forward problem can be solved with triangular elements. Finite element properties are considered on the "local level" or properties unique to each individual element and at the "global level" which includes all of the properties of individual elements. To solve with this method, the model or domain is first discretized into elements. Elements are assigned an element number and verticies of the triangles or nodes are additionally indexed. Elements are assigned conductivity and/or permittivity values. Then a local conductivity matrix (Ω_i) is constructed for each element using conductivity and permittivity information assigned to each element (ρ). The derivation of the weak form for local elements described here follows the formulation in the dissertation text of Fernando Silva de Moura [109].

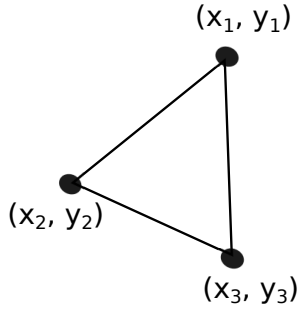

Figure D.1. A typical triangular element used in the forward problem where the x and y coordinates define locations of the nodes.

Equation D.1 describes whether a given node belongs to a particular element. In this equation, n is the number of elements in the mesh, w_i indicates whether nodes are contained in an element ($w_i = 1$ when nodes are contained and $w_i = 0$ when they are not) and u_i is

the voltage associated inside a given element [118].

$$\Omega_i(x,y) = \sum_{i=1}^{n} w_i u_i(x,y) \tag{D.1}$$

D.1. Shape Functions for Triangular Elements

To form each local matrix, three shape or basis functions (equations D.5 - D.7) are needed. For a triangular element, these functions are linear and are of the form given in Equation D.2, where i is an index identifying an i-th element. In EIT, u_i represents the the voltage associated with the i-th element.

$$u_i(x,y) = a_i + b_i x + c_i y \tag{D.2}$$

A 3x3 matrix is formed by (x,y) locations of the nodes defining each element. The coefficients related to a_i, b_i, and c_i can be found by solving Equation D.2. The other matrix is for the unknown voltages at the nodes of the triangle (u_{i,n_1}, u_{i,n_2}, u_{i,n_3}).

$$\begin{bmatrix} 1 & x_1 & y_1 \\ 1 & x_2 & y_2 \\ 1 & x_3 & y_3 \end{bmatrix} \begin{bmatrix} a_i \\ b_i \\ c_i \end{bmatrix} = \begin{bmatrix} u_{i,n_1} \\ u_{i,n_2} \\ u_{i,n_3} \end{bmatrix} \tag{D.3}$$

Solving for a_i, b_i and c_i requires inversion of the matrix with nodal (x,y) locations. This inversion gives the area of the i-th element A_{e_i}, α, β, and γ:

$$\begin{bmatrix} 1 & x_1 & y_1 \\ 1 & x_2 & y_2 \\ 1 & x_3 & y_3 \end{bmatrix}^{-1} = \frac{1}{2A_e} \begin{bmatrix} \alpha_1 & \beta_1 & \gamma_1 \\ \alpha_2 & \beta_2 & \gamma_2 \\ \alpha_3 & \beta_3 & \gamma_3 \end{bmatrix} \tag{D.4}$$

The results is the generic triangular EIT basis functions.

$$f_1 = \frac{1}{2A_e}\left(\alpha_1 + x\beta_1 + y\gamma_1\right) \tag{D.5}$$

$$f_2 = \frac{1}{2A_e}\left(\alpha_2 + x\beta_2 + y\gamma_2\right) \tag{D.6}$$

$$f_3 = \frac{1}{2A_e}\left(\alpha_3 + x\beta_3 + y\gamma_3\right) \tag{D.7}$$

Substituting Equation D.4 into Equation D.3, a equation for the electrical potential or voltage (u_i)for an element can be written. It is equal to the basis functions multiplied by the voltages on each node.

$$u_i(x,y) = \begin{bmatrix} f_1 & f_2 & f_3 \end{bmatrix} \begin{bmatrix} u_{i,n_1} \\ u_{i,n_2} \\ u_{i,n_3} \end{bmatrix} = \mathbf{f_i^T u_i} \tag{D.8}$$

D.2. Weak Form Derivation for Local Conductivity Matrix

To calculate the local conductivity matrix, the weak form must be derived. To do this, it is assumed that the material is isotropic and that the current flowing through an element is conserved and can be described through the divergence theorem. The divergence theorem states that for a well behaved vector field, the flux through a closed surface is equal to the volume integral of the divergence over the region inside the surface. In Equation D.9, the first integral represents the electrical energy stored within an element and the other is the energy that crosses the boarders of the element due to imposed currents.

$$\frac{1}{2}\int_{\Omega_i} \frac{1}{\rho_i} || - \nabla u_i||^2 d\Omega = \int_{\partial\Omega_i} u_i(-\mathbf{J_i}\hat{\mathbf{n}}_\mathbf{i})\mathrm{dA} \tag{D.9}$$

Substitute Equation D.8 into Equation D.9:

$$\frac{1}{2}\int_{\Omega_i}\frac{1}{\rho_i}||-\nabla u_i||^2 d\Omega = \int_{\partial\Omega_i}\mathbf{f_i^T u_i}(-\mathbf{J_i}\hat{\mathbf{n}}_\mathbf{i})\mathrm{dA} \tag{D.10}$$

where:

$$\nabla u_i = \begin{bmatrix}\frac{dU_i}{dx}\\ \\ \frac{dU_i}{dy}\end{bmatrix} = \begin{bmatrix}\frac{df_1}{dx} & \frac{df_2}{dx} & \frac{df_3}{dx}\\ \\ \frac{df_1}{dy} & \frac{df_2}{dy} & \frac{df_3}{dy}\end{bmatrix}\begin{bmatrix}u_{i,n1}\\ \\ u_{i,n2}\\ \\ u_{i,n3}\end{bmatrix} \tag{D.11}$$

$$\nabla u_i = \mathbf{F_i u_i} \tag{D.12}$$

Before substituting Equation D.12 into Equation D.10, use the following: $||-\nabla u_i||^2 = \nabla u_i^T \nabla u_i$.

$$\frac{1}{2}\mathbf{u_i^T}\left[\int_{\mathbf{\Omega_i}}\frac{\mathbf{1}}{\rho_\mathbf{i}}\mathbf{F_i}^\mathbf{T}\mathbf{F_i}\mathrm{dV}\right]\mathbf{u_i} = \mathbf{u_i^T}\int_{\partial\mathbf{\Omega_i}}\mathbf{f_i}(-\mathbf{J_i}\hat{\mathbf{n}}_\mathbf{i})\ \mathrm{dA} \tag{D.13}$$

$$\Omega_i \mathbf{u_i} = \mathbf{I_i} \tag{D.14}$$

Simplifying,

$$\frac{1}{2}\left[\int_{\Omega_i}\frac{1}{\rho_i}\mathbf{F_i}^\mathbf{T}\mathbf{F_i}\mathrm{dV}\right]\mathbf{u_i} = \int_{\partial\Omega_i}\mathbf{f_i}(-\mathbf{J_i}\hat{\mathbf{n}}_\mathbf{i})\ \mathrm{dA} \tag{D.15}$$

In Equation D.15, $\mathbf{I_i}$ is the current matrix. For ACE1, $\mathbf{I_i}$ is implemented as a matrix where the number of columns represents the number of current patterns, and the number of rows is equal to the number of nodes.

In EIT, local element conductivity matrices are of the form:

$$\Omega_i = \frac{h}{4A_{e_i}\rho_i}\begin{bmatrix} \beta_1^2+\gamma_1^2 & \beta_1\beta_2+\gamma_1\gamma_2 & \beta_1\beta_3+\gamma_1\gamma_3 \\ & \beta_2^2+\gamma_2^2 & \beta_2\beta_3+\gamma_2\gamma_3 \\ sim. & & \beta_3^2+\gamma_3^2 \end{bmatrix} \tag{D.16}$$

D.3. Example of Assembling Local Matrices

After all of the local element conductivity matrices are formed, they can be assembled into the global matrix. An example of this is shown in Figure D.2. This example assumes the local conductivity matrices for a generic triangular element contained in the mesh is as follows:

$$\Omega_i = \begin{bmatrix} k_{11}^{(i)} & k_{12}^{(i)} & k_{13}^{(i)} \\ k_{21}^{(i)} & k_{22}^{(i)} & k_{23}^{(i)} \\ k_{31}^{(i)} & k_{32}^{(i)} & k_{33}^{(i)} \end{bmatrix} \tag{D.17}$$

The global matrix is square matrix equal to the size of the number of nodes.

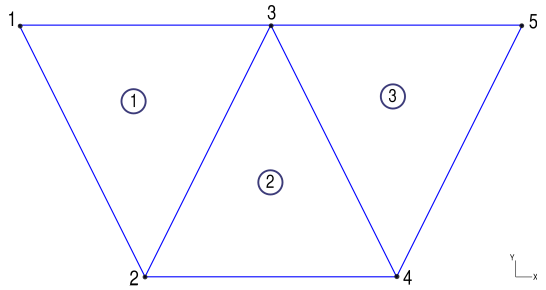

Figure D.2. An example of a simple three element mesh.

The global matrix for Figure D.2 can be found by combining local matrices. It is important to keep track of the connectivity. For Figure D.2 the connectivity for each element is: Ω_1: node 1, node 3, node 2; Ω_2: node 2, node 3, node 4; Ω_3: node 3, node 5, node 4. These

elements can be assembled into a global matrix as described by Equation D.18. In practice, both the local and global matrices are symmetric. The global matrix is also sparse.

$$\mathcal{Y}_{global} = \begin{bmatrix} k_{11}^{(1)} & k_{13}^{(1)} & k_{12}^{(1)} & 0 & 0 \\ k_{31}^{(1)} & k_{33}^{(1)} + k_{11}^{(2)} & k_{32}^{(1)} + k_{12}^{(2)} & k_{13}^{(2)} & 0 \\ k_{21}^{(1)} & k_{23}^{(1)} + k_{21}^{(2)} & k_{22}^{(1)} + k_{22}^{(2)} + k_{11}^{(3)} & k_{23}^{(2)} + k_{13}^{(3)} & k_{12}^{(3)} \\ 0 & k_{31}^{(2)} & k_{32}^{(2)} + k_{21}^{(3)} & k_{33}^{(2)} + k_{23}^{(3)} & k_{22}^{(3)} \\ 0 & 0 & k_{31}^{(3)} & k_{33}^{(3)} & k_{32}^{(3)} \end{bmatrix} \tag{D.18}$$

APPENDIX E

TESTING OF THE FORWARD PROBLEM CODE

In this appendix, results for the initial testing of the forward problem on code on tank data in Section E.1 and on a less refined human subject mesh in Section E.2 are presented.

E.1. Comparison of the Forward Problem to Tank Data

The CEM works reasonably well with little adjustment to model ACE1 tank data. The finite element model of the tank phantom is shown in Figure E.1 and includes 32 Hua elements. The inside of the tank model is divided into two sections to reduce the number of elements, since for a homogeneous phantom, a refined mesh is not necessary for the center. This finite element mesh was used in a custom solution to the forward problem programmed in Matlab. Figure E.2 compares simulated results to a measured dataset.

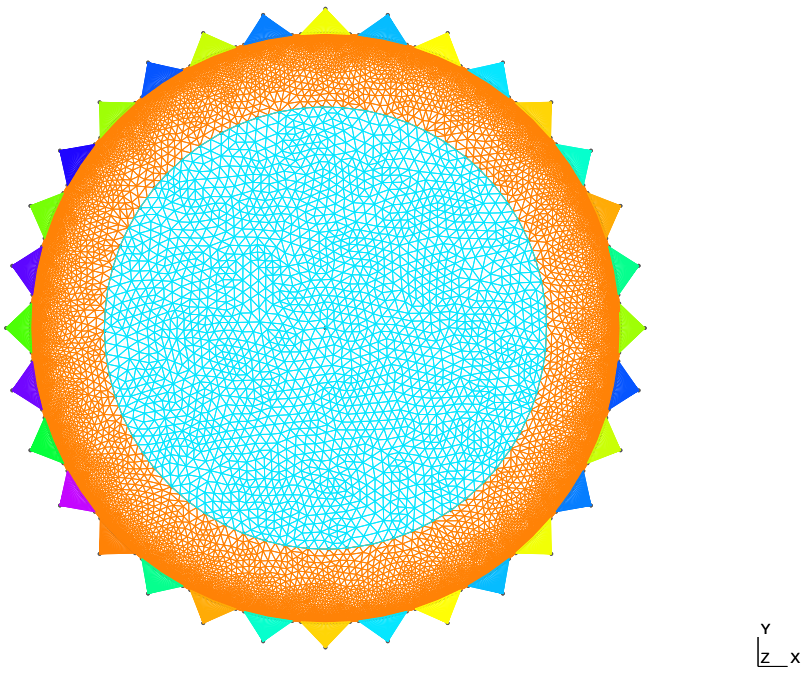

Figure E.1. A 32 triangle element Hua model corresponding to the placement of the ACE1 tank phantom's 32 electrodes.

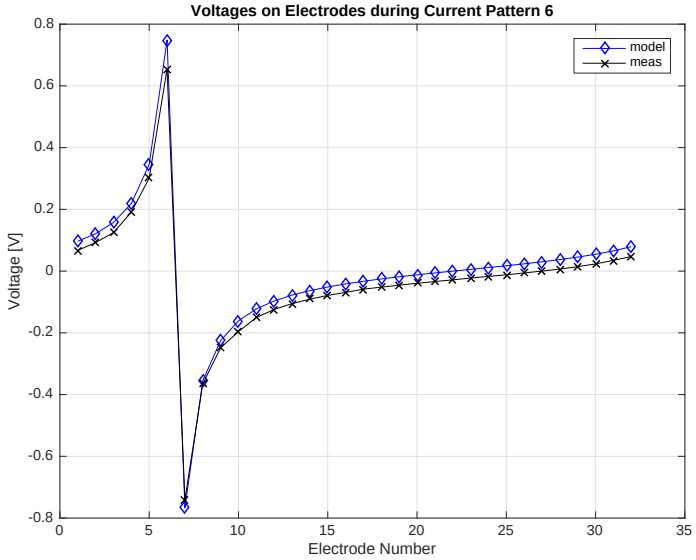

Figure E.2. Comparing voltages all all electrodes during a single current pattern for simulated and measured data.

E.2. Comparison of Anatomical Cross-Section Forward Problem Model to Human Data

Since it is know that skin conductivity can vary based on multiple factors, the electrode parameter in the Hua model and skin conductivity were varied to determine how their values change the shape of the voltage curve for different current patterns. Table E.1 shows used electrode parameter values for the different values conductivity skin values. For skin conductivity values closest to the cited value, electrode parameters did not change much between skip 0 and skip 3 simulations. The electrode parameter values were chosen by running multiple simulations and comparing the voltages on injection electrodes to measured data. When the voltages were close for most current patterns, the corresponding electrode parameter was chosen. The mesh used to investigate this is shown in Figure E.3.

Table E.1. Skin and electrode parameter values tested.

Skin	Skip 0 Electrode Parameter	Skip 3 Electrode Parameter
1 x skin value	2900 x skin value	2500 x skin value
1.5 x skin value	2900 x skin value	2500 x skin value
2 x skin value	2800 x skin value	2200 x skin value
3 x skin value	2700 x skin value	2000 x skin value
5 x skin value	2700 x skin value	1200 x skin value
8 x skin value	2500 x skin value	800 x skin value

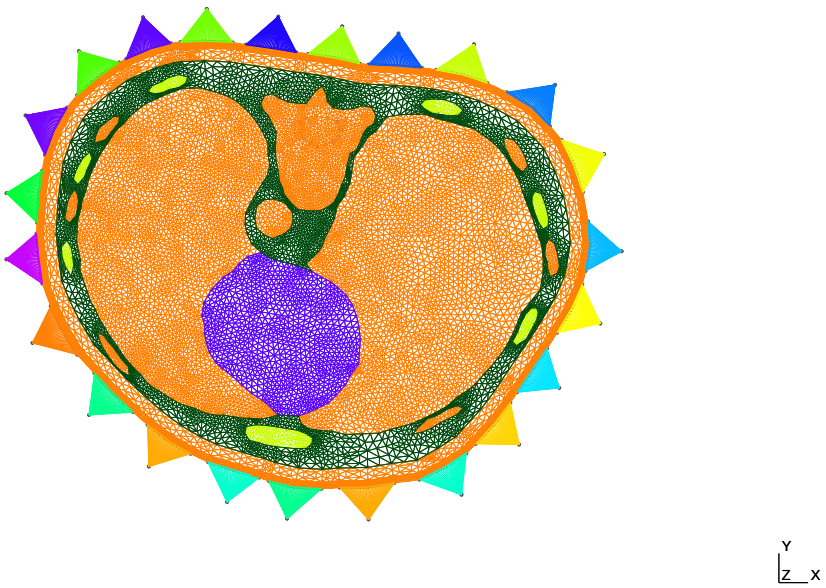

Figure E.3. A 32 element Hua model representing electrodes is consistent with placement marked in Figure 7.6

Although the CEM model does account for contact impedance, the high impedance of the skin should still be included in the model to produce a voltage curve during a single current pattern similar in shape to the measured data. As seen in Figures E.4 - E.5 the conductivity of skin does change the shape of the curve. If the skin becomes more conductive, the voltage curve is more similar to that produced by a tank phantom in Figure E.2. The main difference between voltage curves on the tank and humans is that voltage measurements decrease more

gradually as one moves away from injecting electrodes on a tank. The low conductivity of the skin relative to other tissues causes voltages on electrodes near injecting electrodes to decrease rapidly. The most difficult potentials to predict with a simulation are those adjacent to injecting electrodes.

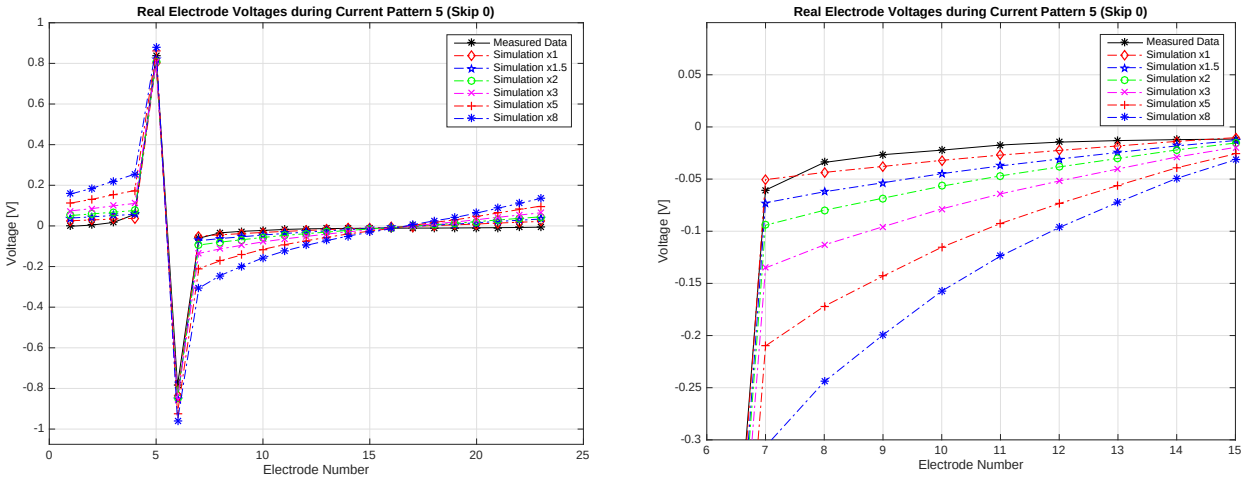

Figure E.4. Comparisons to skip 0 measured data using parameters in Table 7.1. The simulation used values for inspired lung since measured data trace corresponds an average for 301 frames of breath holding at 24.9 frames/sec.

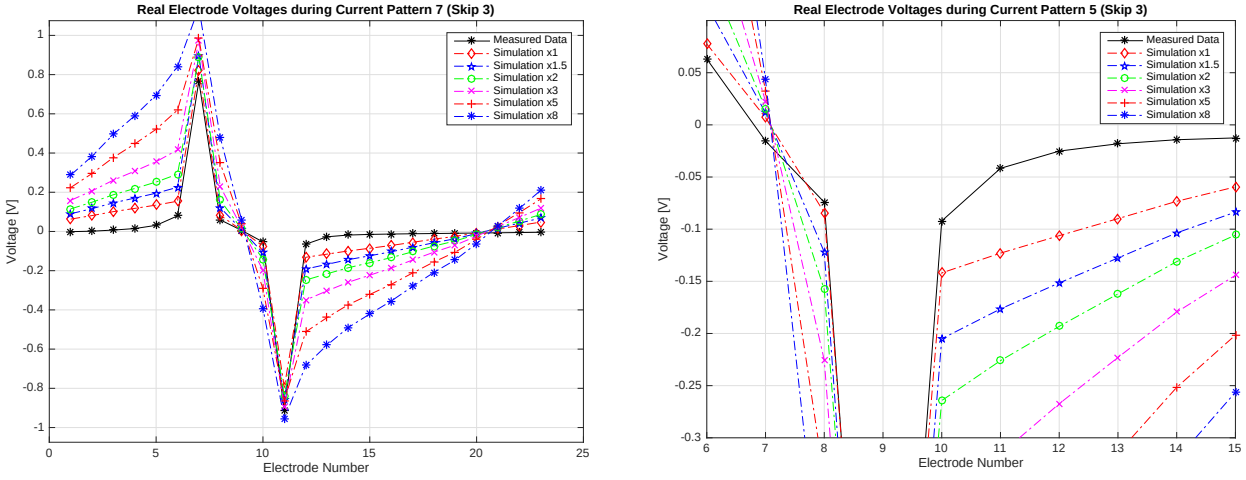

Figure E.5. Comparisons to skip 3 measured data using parameters in Table 7.1. The simulation used values for lung that were an average of inspiration and expiration because the measured data trace corresponds to 301 frames of tidal breathing at 16.0 frames/second

For the mesh used, the CEM predicts voltage values that are closer to measured data for skip 0 when compared to skip 3. This is show by comparing Figure E.4 (skip 0) to Figure E.5 (skip 3). It is likely that in this Section using a more refined mesh would improve CEM results, and that the contact impedance on all electrodes cannot be modeled with a single electrode parameter.